ON THE CONCEPT OF EARTHQUAKE RESISTANT

HYBRID STEEL FRAMES

by

SEYED MOHAMMAD RAZAVI

Presented to the Faculty of the Graduate School of

The University of Texas at Arlington in Partial Fulfillment

of the Requirements for the Degree of

DOCTOR OF PHILOSOPHY

THE UNIVERSITY OF TEXAS AT ARLINGTON

May 2013

Dedication

This dissertation is dedicated to my father, my mother, and my wife,

who supported me each step of the way.

ACKNOWLEDGEMENTS

March 01, 2013

ABSTRACT

ON THE CONCEPT OF EARTHQUAKE RESISTANT

HYBRID STEEL FRAMES

SEYED MOHAMMAD RAZAVI, PhD

The University of Texas at Arlington, 2013

Supervising Professor: ALI ABOLMAALI

The concept of hybrid steel frame system is presented in which mixtures of fully-rigid and semi-rigid steel connections are used in the 3-, 9- and 20-story SAC frames. Several different patterns and locations of semi-rigid connection replacements within the frame are examined in order to identify hybrid frames with the best seismic performance. The effective connection stiffness is identified by performing a parametric study on the initial stiffness of the semi-rigid connections. Then, the cyclic behavior of the connections with the most effective stiffness is obtained using nonlinear finite element analysis. Inelastic dynamic analyses are conducted on the proposed selected frames by subjecting them to Los Angeles earthquake records characterized as those with 2% and 10% probabilities of exceedance in fifty years. The maximum story drift for the hybrid frames are determined and compared with the "life safety" and "collapse prevention" performance limits as recommended by FEMA 356. The story drift and member forces for the hybrid frames are reported and compared with those of conventional SAC frames without semi-rigid connections. The nonlinear incremental modal analysis is also introduced as a tool for assessment of the behavior of frames under seismic loading. Finally, a reliability analysis utilizing the collapse margin ratio presented in FEMA P695 is performed to quantify and compare the collapse performance of the selected hybrid and rigid frames.

The mid- and high-rise hybrid frames showed improved performance compared with rigid frames, especially under maximum credible earthquake (MCE) ground motions.

TABLE OF CONTENTS

LIST OF ILLUSTRATIONS

LIST OF TABLES

CHAPTER 1

INTRODUCTION

Seismic performance of structural systems has been at the forefront of research for many years. Occurrences of several severe earthquakes in the state of California in a 15-year period from 1979 to 1994; particularly, the 1994 Northridge Earthquake motivated researchers to look beyond conventional design philosophies. One of the safest lateral load resisting systems known is the fully restrained welded steel moment frame (WSMF) and it has been known to sustain large plastic deformations, which made it the dominant design choice in seismic regions. The confidence to this type of construction has been decreased by observations of cracks in more than 150 WSMF' welded connections after the Northridge earthquake of 1994. The premature brittle failures of welded connections have also been noticed after the Kobe earthquake of 1995.

After the 1994 Northridge earthquake, many owners tried to upgrade their buildings' seismic performance. They also wanted to know, how their buildings would behave at various earthquake hazard levels if any of the proposed rehabilitation design alternatives by engineers were implemented. There was no such a tool for engineers at the moment to quantify or qualify the performance of structures subjected to a given seismic record.

To fulfill this shortcoming, the U.S. Federal Emergency Management Agency (FEMA) initiated a 6-year program to develop and verify reliable and cost-effective methods for inspection, evaluation, repair, rehabilitation, design, and construction of steel moment frame structures (Mahin et al. (2002)). This program was managed and administrated by the FEMA/SAC joint venture which examined connection and frame performances under earthquake loads. The SAC steel project was funded by FEMA and is a joint venture of the

1

Structural Engineers Association of California (SEAOC), the Applied Technology Council (ATC), and the Consortium of Universities for Research in Earthquake Engineering (CUERR).

The above program has resulted in several valuable publications and guidelines such as NEHRP 1997 and FEMA 356 in which the concept of Performance Based Earthquake Engineering (PBEE) was introduced. PBEE can be defined as "Design for the achievement of specified results rather than adherence to particular technologies or prescribed means" (May 2004). In PBEE, multiple performance objectives are met when structure is subjected to different levels of hazard, which is an iterative procedure between design and performance evaluation.

In the above-mentioned documents, four different building performance levels and four different earthquake hazard levels were introduced and these are summarized in Table 1.1. The first two hazard levels are typically used for serviceability controls while the third and fourth levels are generally used for strength checks.

According to current seismic design codes, buildings should fulfill a performance level of "Life Safety" under Design Base Earthquakes (DBE) that are earthquake records with 10% probabilities of exceedance in 50 years or a return period of 474 years. Although providing life safety is a major objective in seismic design of structures; however, the socio-economic impacts of damage could outweigh the cost of the structures (Gupta 1999).

The performance objectives are selected based on structural functionality expectations. As an example, hospitals should be designed for operational performance to serve patients after a severe earthquake; however, providing performance level of life safety would be satisfactory for small residential buildings.

In the past few decades, several research investigations have been conducted to improve the seismic performance of steel frames by introducing more ductile connections as well as new lateral resistant systems and energy dissipating technologies such as base isolators, frictional or visco-elastic dampers, and active control elements.

2

Table 1.1 Rehabilitation Objectives Building Target Performance Level

Earthquake Hazard Level	Operational	Immediate Occupancy	Life Safety	Collapse Prevention
50% in 50 yr RP:72 yr	a	b	c	d
20% in 50 yr RP:225 yr	e	f	g	h
10% in 50 yr RP:474 yr	i	j	k	l
2% in 50 yr RP:2475 yr	m	n	o	p

This study draws motivation from the presented issue to introduce a new lateral resistant steel moment frame called "Earthquake Resistant Hybrid Steel Frame (ERHSF)." This system is based on introducing energy dissipating mechanisms in the structural frame systems by replacing selected rigid connections with ductile energy dissipating semi-rigid connections. This concept, even though at first glance is similar to the eccentrically braced frame introduced by Engelhardt and Popov (1989), is quite different in behavior. In the eccentrically braced frames, isolated "links" are commonly introduced throughout the frame, while in the proposed method; semi-rigid connections are placed at selected locations and/or particular patterns. Indeed, hybrid frames may experience relatively high story drifts, which may become problematic in meeting serviceability requirements. This problem will be addressed and discussed in this dissertation. The story drift angle is defined as the ratio of the relative displacement of a story to the story height. A schematic definition of the drift angle is shown in Figure 1.1.

The idea of the hybrid frame instigated from a simple assumption that if a high-rise building is seen as a single cantilever beam, theoretically, an indefinite number of mode shapes is considered for this system. The idealized simple model of rigid frame and its first, second, and third mode shapes are shown in Figure1.2.

Replacing rigid connections with flexible semi-rigid connections at certain stories simulates spring development within the beam as shown in Figure 1.3. These simplified models explains why the two cases of rigid and hybrid frame have a significant difference in seismic

behavior, where the newly formed springs may help to decouple the earthquake acceleration into two mode shapes as shown in Figure 1.3.

In general, story drifts at the semi-rigid connection levels are translated into connection rotations. Thus, for a properly designed connection that behaves in a ductile manner, this cyclic rotation is absorbed into angle/plate yielding without bolt or weld fracture. This would lead to excessive end-plate or angel distortion at ultimate rotation that can be retrofitted at the semi-rigid connection levels. These types of connections have successfully been tested by Astaneh et al. (1991), Abolmaali et al. (2003, 2009). To achieve the above goal, thin plate/angle and overdesigned bolts should be used.

Los Angeles SAC frames will be used as case studies in this research. Selected rigid connections will be replaced by ductile semi-rigid connections. SAC earthquake records for the Los Angeles site with different frequencies will be applied for inelastic dynamic analyses. The results of displacement time history, story drift, and member forces will be compared with the corresponding responses of the fully rigid SAC frames. The SAC 20-story rigid frame and two proposed hybrid frame models for primary investigations are shown in Figure1.4.
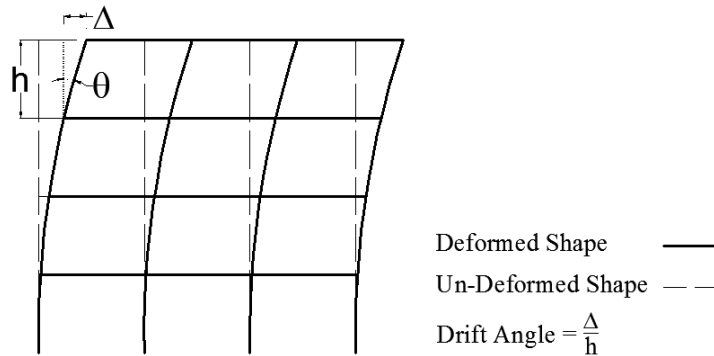
Figure 1.1 Schematic definition of a story drift angle
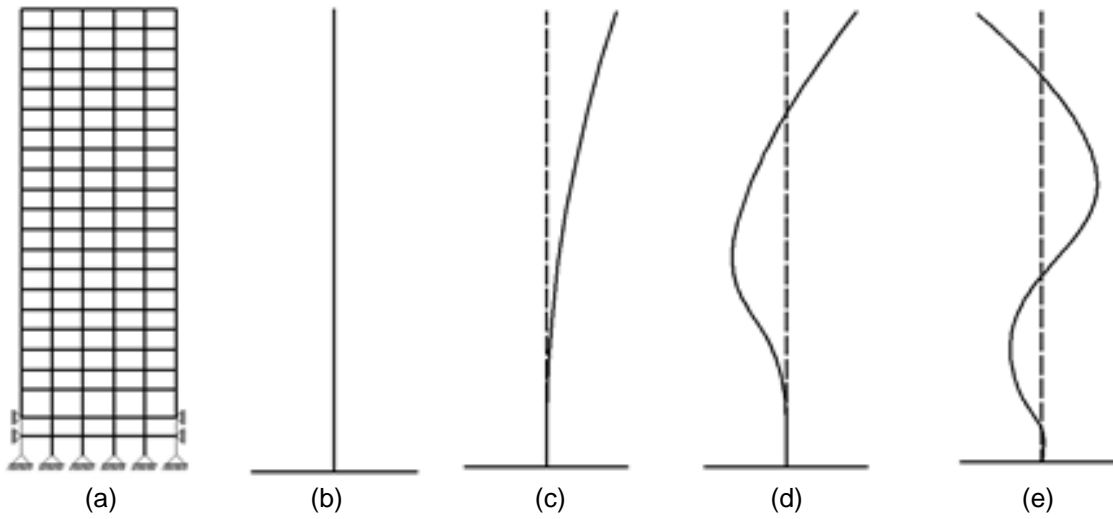
Figure 1.2 The simplified Model of a rigid frame (a) Rigid Frame, (b) Simplified Model,
(c) First Mode, (d) Second Mode, and (e) Third Mode
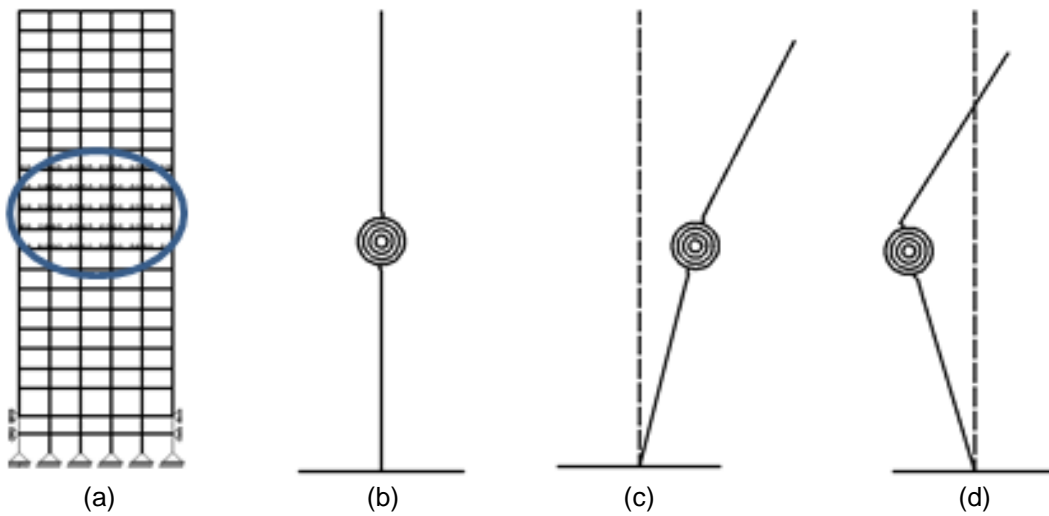
Figure 1.3 The simplified Model of a hybrid frame (a) Hybrid Frame, (b) Model,
(c) First Mode, and (d) Second Mode

(a) (b) (c) (d)
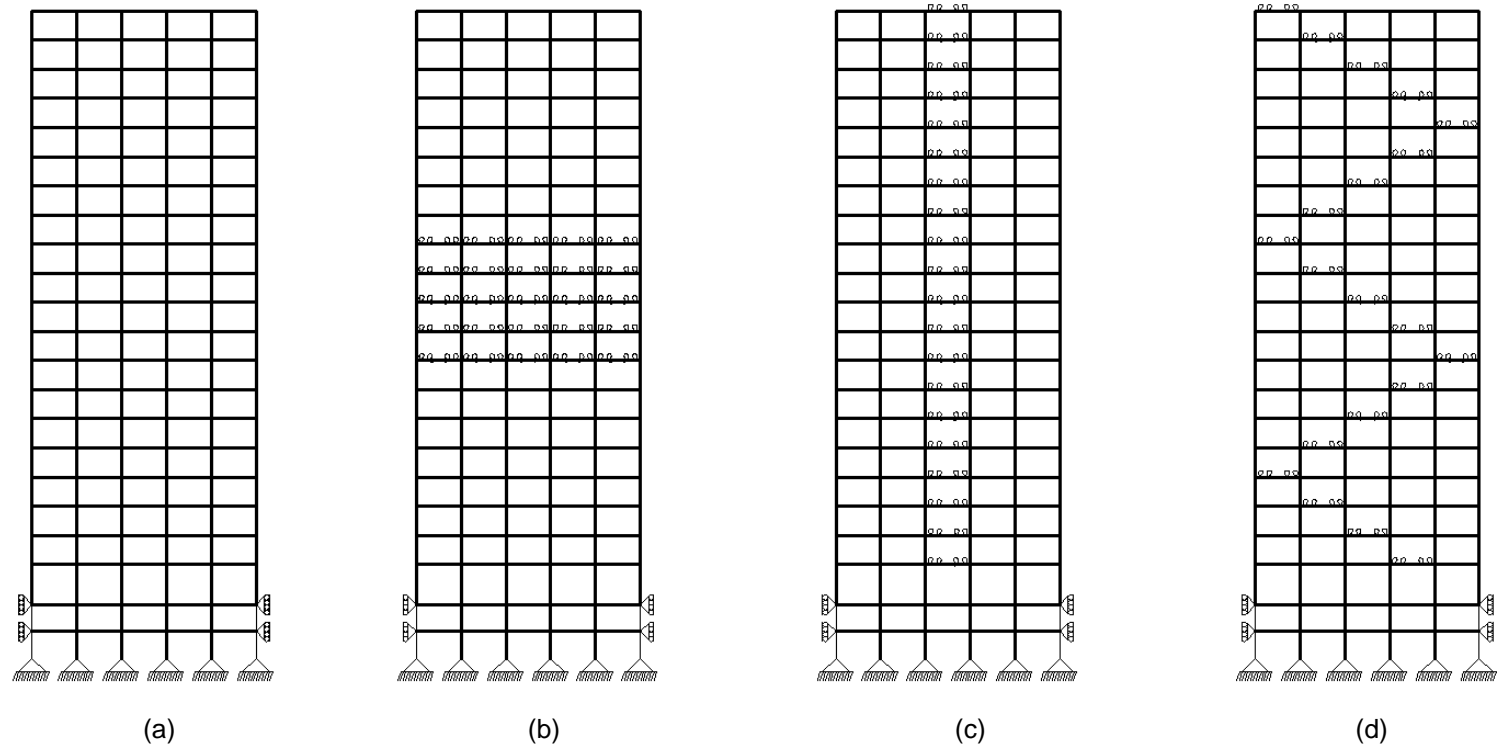
Figure 1.4 The SAC 20-story frame and the proposed hybrid frames for primary studies
(a) Sac Rigid Frame, (b) Hybrid Model #1, (c) Hybrid Model #2, and
(d) Hybrid Model #3

1.1 Goals

The primary goal of this study is to develop a pattern consisting of semi-rigid ductile connections coupled with rigid connections to enhance the seismic performance of steel moment frame structures. To accomplish this goal, several semi-rigid connection patterns are applied to the SAC frames for the Los Angles site. The seismic behavior of the hybrid frames subjected to different levels of earthquake hazard will be investigated and compared to the corresponding fully rigid SAC frame.

1.2 Objectives

Related to this research, the objectives are to advance on the following forefronts:

1. To determine the most effective pattern of semi-rigid connections in hybrid frame

2. To understand the behavior of hybrid frames subjected to various levels of earthquake hazard

3. To investigate the nonlinear incremental modal shapes and frequencies of frames

4. To evaluate and compare story drifts and member forces for proposed hybrid frame systems and conventional SAC frame systems using inelastic dynamic analysis..

5. To study effects of the effective pattern on inelastic response on low-, mid-,and high-rise hybrid frames

6. To employ reliability-based analysis utilizing Collapse Marginal Ratio (CMR) proposed by FEMA P695

7. To design a ductile semi-rigid connection which can accommodate the hybrid frames for optimum performance and satisfy the objective of the research

8. To develop computational benchmarks in simulation of cyclic performance of steel connections using a three-dimensional nonlinear finite element method

1.3 Outline for Dissertation

In *Chapter 2*, motivations of this study are explored. The background of the research work done is presented in both structural level such as story drifts, performance, and reliability evaluation of the structures and component levels including member forces and semi-rigid connection behavior.

In *Chapter 3*, the initial concept of seismic resistance hybrid frame is tested. The concept is presented and applied to a 9-story and a 20-story steel frame. Linear elastic models are used for beams and columns in this phase of study. The demands of hybrid frames resulted from incremental time history analysis of hybrid frames subjected to eight different earthquakes are then compared with demands of the corresponding rigid frames.

In *Chapter 4*, the behavior and modeling assumptions of steel moment resisting frame structures in both structural and element levels are described. Different material models for the simulation of the nonlinear behavior of the frame elements (Beams, Columns, Connections, and Panel Zones) are summarized. The ground motions and nonlinear analyses assumptions used in this study are described in this chapter.

In *Chapter 5*, different patterns of semi-rigid connections are applied to 3, 9, and 20-story frames on a trial basis and two of the most effective patterns are selected for each frame. Then, the optimized connections stiffness is identified by performing a sensitivity study on the initial stiffness and post yield stiffness of semi-rigid connections.

In *Chapter 6*, first the computational benchmarks in simulation of cyclic performance of steel connections using three-dimensional nonlinear finite element method are presented. Then, connections with optimum stiffness, which have been identified in Chapter 5, are simulated and analyzed under cyclic loading. Finally, a tri-linear model is fitted to the moment-rotation hysteresis curve of optimum semi-rigid connections. These results are used in the global analysis of frames.

In *Chapter 7*, global (story and roof drifts) and local response parameters (member forces, energy dissipation in plastic hinges and semi-rigid connections) of the optimum hybrid frames are investigated and discussed. The results of pushover and nonlinear time history analysis under different levels of ground motion are also presented.

The incremental modal analysis is introduced in *Chapter 8*. The procedure and its application as a tool for assessment of structures during a seismic loading are presented. The results of incremental modal analysis for different hybrid frames and their corresponding rigid frame are also discussed.

In *Chapter 9*, a reliability-based analysis utilizing the Collapse Margin Ratio (CMR), proposed in FEMA P695 is performed on the selected hybrid and rigid frames. The results of the Incremental Dynamic Analysis (IDA) along with the CMR calculation on the frames are presented and discussed in this chapter.

In *Chapter 10* the findings of this study are summarized, the conclusions are presented, and the issues that need further investigations are introduced.

The framework of the conducted research work is presented in Figure 1.5.

Development of Hybrid Frames

Structural Level

Component Level

Initial Concept

Pattern Selection

Implementing the Selected patterns on low-rise, mid-rise, and high-rise frames

Sensitivity study on effects of connection properties on structural performance of effective pattern

Initial Development of verified FEM Model of Connections

Initial Pattern Selection

Implementing Different Patterns on 3-Story, 9-Story ,and 20 Story frames

Modeling and Analyzing of 3-Story, 9-Story ,and 20 Story frames using Incremental Inelastic Time History Analysis

Identify Required Connections' Strength and Stiffness

FEM Modeling of Optimum Connections

9-Story
20-Story

Fitting tri-linear material model for semi-rigid connections

Story Drift
Roof Displacement
Member Forces

Development of the Final Effective Models

Performance Assessment of the Final Effective Models

incremental modal analysis

reliability-based analysis using

Summary and Conclusion

Figure 1.5 Framework of the conducted research work

CHAPTER 2

BACKGROUND

<u>2.1 Background on Earthquake Engineering</u>

Traditionally, lateral resisting systems against an earthquake is designed via a strength-based approach, which prescribes that a building should remain safe for a rare earthquake and its significant aftershocks (Moehle 2008).

Development of seismic codes has generally been a reaction to catastrophic events. The Messina earthquake of 1911 and the Tokyo earthquake of 1923 were the reasons for the development of earthquake resistant design guidelines that includes designing buildings for a lateral force of about 10 % of the building's weight. These simple developments aimed to reduce life and economic losses in future earthquakes (Holmes et al. 2008).

In the US, the first building code incorporating a voluntary Lateral Bracing Appendix was the Uniform Building Code of 1927. This code provision states that although the design of buildings to resist against earthquake shaking is a moot question, following this provision will provide adequate additional lateral strength for structures (UBC 1927).

The 1933 Long Beach earthquake resulted in mandatory seismic design for buildings in the state of California (the Riley Act). This rule initiated a vast code development activity. Structural Engineers Association of California (SEAOC) wrote the first widely used design publication called "*Recommended Lateral Force Requirements and Commentary*" which was commonly known as the "*Blue Book*" (Holmes et al. 2008). The Blue Book contained relatively clear performance objective as follow:

1. "Resist minor earthquakes without damage;"

2. "Resist moderate earthquakes without structural damage, but with some non-structural damage"; and

3. "Resist major earthquakes, of the intensity of severity of the strongest experienced in California, without collapse, but with some structural as well as non-structural damage." (SEAOC 1960)

Since 1960, the Blue Book terms and criteria evolved but the objectives almost remained the same. For example, the term "earthquake" is referred as "ground motion" in later design books.

In the 1970s, the Applied Technology Council (ATC), which was funded by the federal government, published the Tentative Provisions for the Development of Seismic Regulations for Buildings (commonly known as ATC 3). According to ATC 3, if the design ground motion were to occur, one to two percent of buildings might be exposed to life threatening damages and if the ground motion is two or three times as strong as the design ground motion, damage might rise to 10 to 50 percent, respectively (ATC 1978). Although there is no evidence on how these probabilities are calculated, the fact of inherent uncertainty of ground motions was introduced in this document.

Definition of the ground motion level was vague in the Blue Book. Although the severity of ground motions were categorized as minor, moderate, and major, these levels were not translated into engineering terms. The term "code ground shaking" was finally adopted by both ATC 3 and the Blue Book that was a ground motion with a 10 % probability of exceedance in 50 years. This level of ground motion, known as "Designed Basis Earthquake (DBE)" ground motion, has only been introduced into ground motion by codes since 1997 when a new national mapping program was completed and the Maximum Considered Earthquake (MCE) was introduced. The MCE was defined as a ground motion with a 2% chance of exceedance in 50 years. The code design philosophy was then to provide a margin of safety against MCE simply by implementing the traditional methods for a ground motion of 2/3 of the MCE. The 2/3 factor was adopted because of the presumed safety factor of 1.5 which was traditionally used for DBE.

DBE and MCE may also be defined as ground motions with return periods of 475 and 2475 years, respectively. The common strength-based practice is to design structural members

to withstand demands associated with these ground motions. The design codes are still following this philosophy.

2.2. Background of Performance Based Design.

The Northridge earthquake of 1994 unveiled the vulnerability of the buildings being subjected to strong ground motions. Several structural and non-structural damage to buildings, especially to hospitals that should remain operational to serve victims after earthquake, forcing engineers to look beyond conventional strength-based design methods. Engineers realized that serviceability after an earthquake should be included in design methods; therefore, a building's performance can be predicted.

SEAOC was the first professional society to respond to this shortage in these engineering building codes. The result of this attempt was a publication known as Vision 2000 (SEAOC) in 1995, which initiated the Performance Based Earthquake Engineering (PBEE). This document introduced a different level of performance objectives that can be selected for rehabilitation of a building depending on the needs and resources of the owner.

SEOAC's Vision 2000 performance objectives descriptions are as follows:

1- "Fully functional: No significant damage has occurred to structural and non-structural components. Building is suitable for normal intended occupancy and use."

2- "Operational: No significant damage has occurred to structures, which retains nearly all of its pre-earthquake strength and stiffness. Non-structural components are secure and most would function, if utilities available. Building may be used for intended purpose, albeit in an impaired mode."

3- "Life Safety: Significant damage to structural elements, with substantial reduction in stiffness; however, margin remains against collapse. Non-structural elements are

secured but may not function. Occupancy may be prevented until repairs can be instituted."

4- "Near Collapse: Substantial structural and non-structural damage. Structural strength and stiffness substantially degraded. Little margin against collapse. Some falling debris hazards may have occurred." (SEOAC 1995)

SEOAC's Vision 2000 performance objective chart is shown in Figure 2.1. Buildings' performance objectives are categorized in three different groups of "Performance for Ordinary Buildings," "Performance for Essential Buildings," and "Performance for Hazardous Facilities." Each performance objective is shown by a line in Figure 2.1 that shows the building performance level subjected to different ground motion levels.
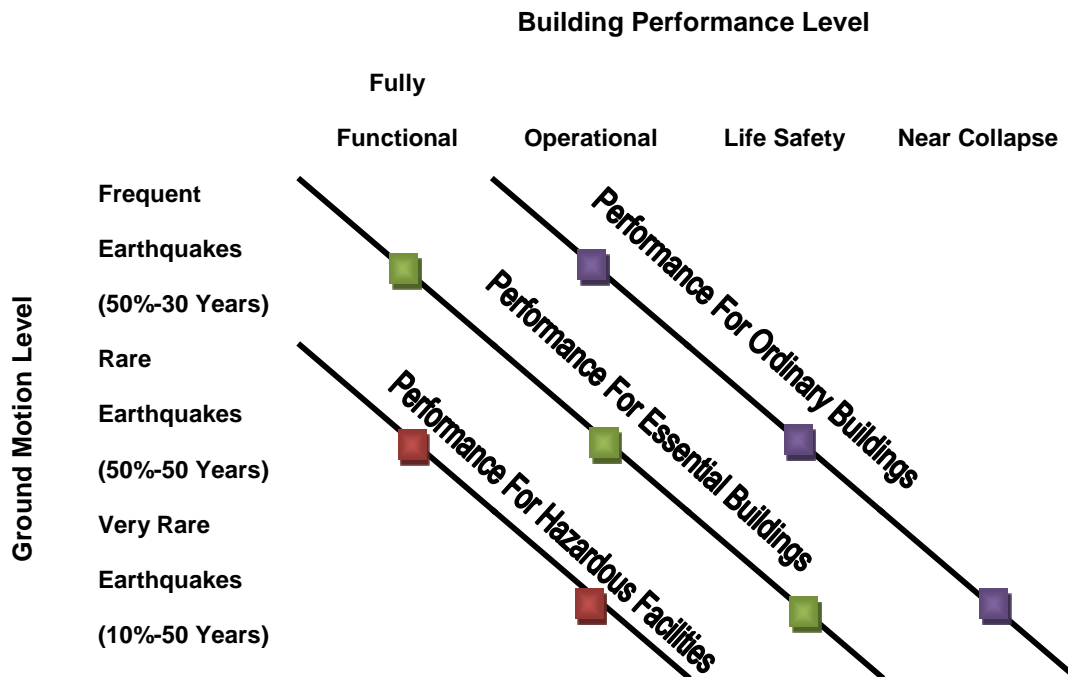
Figure 2.1 Vision 2000 recommended seismic performance objectives chart

For example, the performance for hazardous facilities might be selected for hospitals that are expected to serve patients after a very rare earthquake. In this case, a hospital should

satisfy the requirements for "Fully Functional" and "Operational" performance levels when it is subjected to a "rare" or "very rare" ground motion, respectively.

FEMA 273 (1997) was another attempt to standardize PBEE methodology. This document expresses design objectives adopting a similar framework with a slightly different performance level description and levels of ground motion. Primary performance levels are defined as Immediate Occupancy (IO), Life Safety (LS), and Collapse Prevention (CP). Moreover, the performance levels are considered for both structural and non-structural systems. Each global performance objective is detailed in terms of the performance of individual elements. It was believed that if all individual frame elements meet the predefined strength and serviceability criteria, the global performance of building is satisfied. This method was deterministic and did not define any quantified probability.

Other pioneer PBEE documents published include ATC-32 (1996a), ATC-40 (1996b), and FEMA 356 (2000). These documents have also followed a similar framework. The recommended building performance objectives chart based on FEMA 365 is presented in chapter 1 of this dissertation.

2.3. Next Generation of Seismic Performance-Based Design

The Pacific Earthquake Engineering Research (PEER) Center, which is a federally-funded earthquake engineering research center, is focused on the development of the next generation of seismic performance-based design.

The primary difference of the next generation PBEE in comparison with the previous generation is the output of the analysis. The principal outputs of the new approach are system level performance in terms of losses including repair cost, casualties, and loss-of- used duration (Porter 2003). These outputs, rather than traditionally engineering technical terms such as story drift and element forces, assist stakeholders (owners, insurance companies, etc.) in making decisions based on the performance objectives.

Undoubtedly, inherent uncertainty and variability of ground motions prevent engineers from coming to a design, which withstands any earthquake. In the new approach, the uncertainties in the calculation parameters are explicitly considered (Holmes et al. 2008).

Figure 2.2 shows PEER's analysis methodology for next generation PBEE. This methodology results in a reasonable decision making after performing 4 stages of analysis on a facility's basic information. These four stages are hazard, structural, damage, and loss analyses. The outcomes of these analyses are expressed using four variables of Intensity Measure (IM), Engineering Demand Parameter (EDP), Damage Measure (DM), and Decision Variable (DV). Considering the fact of inherent uncertainties in measurement of these variables, they are expressed in terms of conditional probability of exceedance, namely, $p[A/B]$ is the probability of exceedence of A if B is given. Moreover, this methodology assumes that the assessment components can be treated as a discrete Markov process where the conditional properties between variables are independent (Moehle 2004).
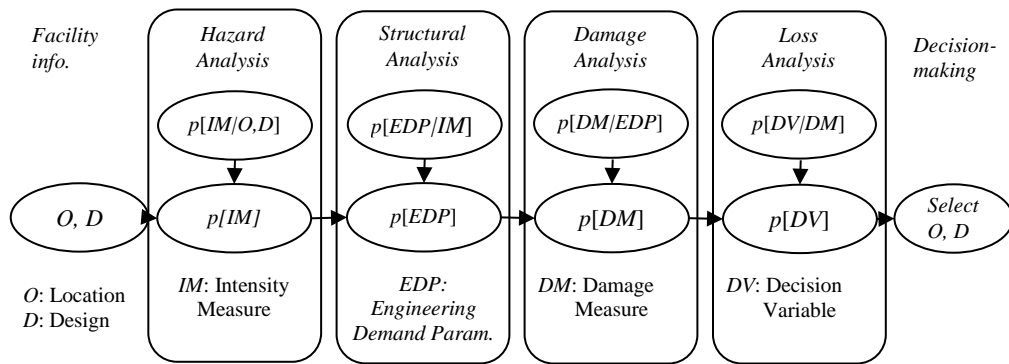
Figure 2.2 PEER Probabilistic Framework (Porter 2003)

The first step of the assessment is the hazard analysis. The result of this step is the Intensity Measurement (IM) of ground motions. A common IM for earthquakes is the Spectral Acceleration (Sa). Hazard analysis is commonly expressed as the mean annual probability of exceedance of a given Sa for a given building, p(IM), which is a function of the building's

location (*O*) parameters such as soil type and distance from active faults and also is a function of design parameters (*D*) including the first natural period of vibration, height, material properties, and analysis assumptions of the building. In the present study, this step is done by selecting two groups of ground motions which Sa(T:first period of building) matches 10% and 2% of probability of exceedance in 50 years.

The second step is structural analysis that yields the probability of exceedance of Engineering Demand Parameters p(*EDP|IM)* such as story drifts and member forces for a building when it is subjected to IMs that have been found in the first step. The IMs and EDPs are generally related using a nonlinear inelastic analysis. Development of the Incremental Nonlinear Analysis (IDA) was an attempt to express the EDPs in term of probability of exceedance. This method will be comprehensively explained in chapter 9 of this dissertation.

In the next step, the relation between EDPs and Damage Measures (DM) are obtained using a damage analysis, which in turn quantifies the physical damage to the facility. These can be categorized as damages to structural and non-structural components. The functions of damages to buildings components are commonly expressed with a fragility curve. Fragility curves express the probability of exceedance of damage to a structural member such as beams and columns, as a function of EDPs such as member forces and story drifts. These fragility curves are commonly obtained using experimental tests.

The last step of the analysis is to obtain the Decision Variable base on a loss analysis. Decision variable is defined as the variable that has the most interest for the stakeholder such as the amount of money, which is needed for repairing the facility, or the risk of earthquake to human's life.

The procedure can be formulated as shown in the Equation 2.1.

$$v(DV) = \iiint G\langle DV|DM\rangle |dG\langle DM|EDP\rangle |dG\langle EDP|IM\rangle |d\lambda\langle IM\rangle \qquad (2.1)$$

<u>2.4. Summary of Related Research Works</u>

In recent years, many research works have been performed to improve the behavior of the steel moment resistant frames (SMRF) subjected to seismic loadings. These attempts included experimental studies on frame components such as beams, columns, and connections as well as cyclic or dynamic tests on full- or reduced-scale SMRF models. In addition, analytical research focused on introducing new design methods or energy dissipating systems to enhance the seismic behavior of SMRFs. The focus of this literature review is on two recent analytical investigations, which had the most effect on the present study.

2.4.1. Performance Based Plastic Design

Performance Based Plastic Design (PBPD) is an innovative seismic design method that introduced and developed by S.C.Goel and his associates at the University of Michigan (Leelataviwat et al., 1999; Lee and Goel, 2001; Dasgupta et al., 2004; Chao and Goel, 2005; Chao and Goel, 2006; Goel and Chao, 2008). Development of this method was a response to limitations in existing seismic design codes on satisfying a performance objective in a direct manner. These shortages can be categorized as follows:

1- The current design methods are based on elastic structural behavior and the inelastic structural behavior is taken into account implicitly by applying modification factors.

2- Story drifts are not considered in design methods directly; thus, satisfying drift limits provided by codes, requires an iterative design and evaluation procedure.

3- The structure's yield mechanism which plays an important role in collapse analysis is not a part of current seismic design practice.

In PBPD, the inelastic behavior of structures is explicitly considered in the design methodology; therefore, it eliminates any iteration for satisfying a pre-defined performance limit. In this method, selection of target drift and yield mechanism for a

18

specific hazard level is a part of the design process. In PBPD, the base shear is calculated by equating the work done by pushing the structure to a predefined target drift monotonically to the work done by an equivalent elastic-perfectly plastic single degree of freedom system as shown in Figure 2.3.
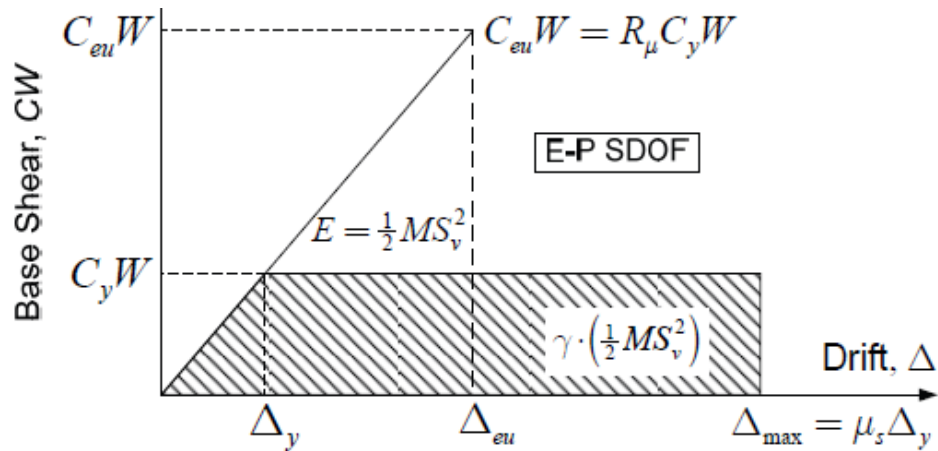
Figure 2.3 Structural Idealized Response and Energy (Work) Balance Concept for SDOF(Bayat 2010)

This method also introduces a new lateral distribution based on the relative distribution of maximum story shears from inelastic dynamic analysis (Chao et al., 2007). In PBPD, an assumed target yield mechanism as shown in Figure 2.4, beams are considered as designated yielding members (DYM) and are designed using the plastic design approach. Then columns, which are not designated to yield, are designed to remain elastic against a combination of a factored gravity load and maximum expected strength of the DYMs connected to the columns. This methodology ensures the formation of the intended mechanism of strong column-weak beam.
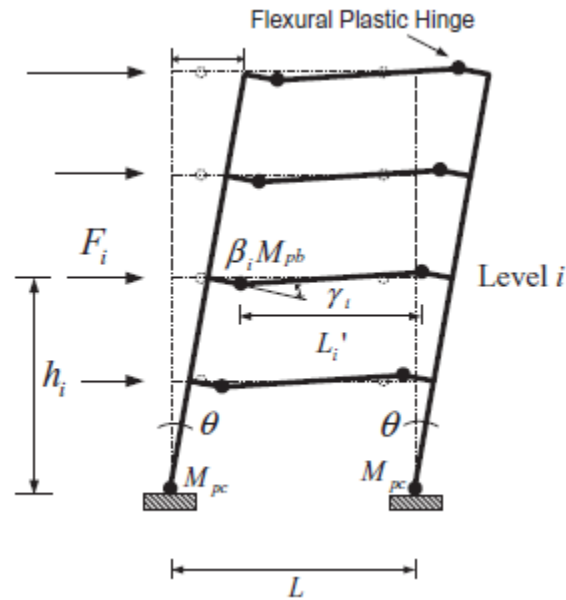
Figure 2.4 Target yield mechanism for moment frames (Bayat 2010)

Bayat (2010) implemented the PBPD method on tall SMRFs. He redesigned a 20-story SAC frame using the PBPD approach. Comparison of the results of redesigned SAC frame with the original SAC frame showed that the PBPD approach enhances the seismic behavior of tall SMRFs. Figures 2.5 and 2.6 show the plastic hinge formation of the original SAC frame and the redesigned one using PBPD subjected to LA38 ground motion, respectively. Comparing these two figures, shows the redesigned frame has a better distribution of plastic hinge formation. Plastic hinges in SAC frame are concentrated in the lowest 5 stories of the building while they are distributed in all stories in the PBPD design. In addition, PBPD eliminates the formation of plastic hinges in columns, which is a desirable seismic behavior. Figure 2.5, shows plastic hinge locations in a hybrid frame with a zigzag pattern. The proposed hybrid frame is capable of distributing plastic hinge in the frame height and eliminating their concentration in the lowest 5 stories. It also reduces the formation of plastic hinges in columns.

Column Plastic
Hinges

Gravity
Column

Gravity
Column

(a)

(b)

(c)
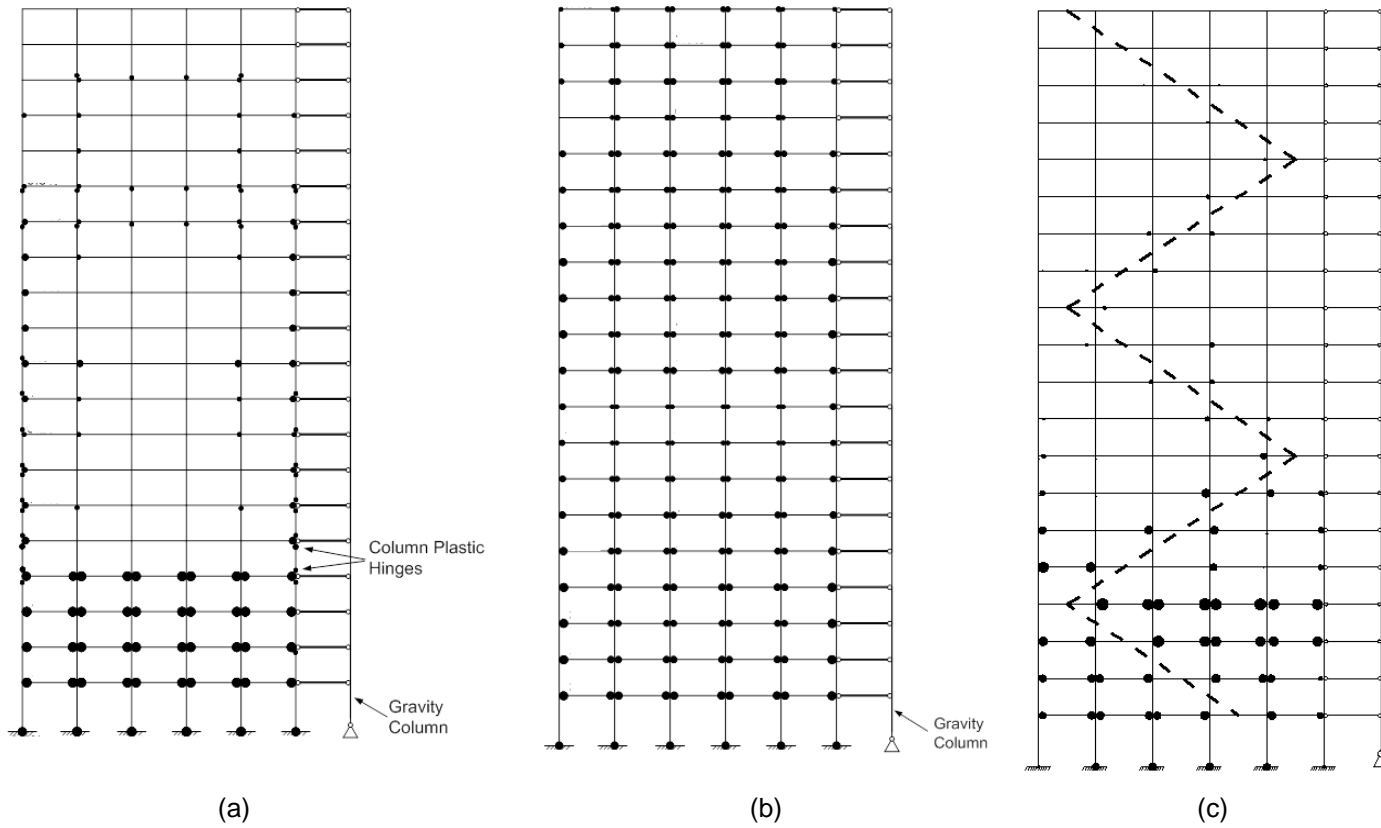
Figure 2.5 Plastic Hinge Locations for a) SAC Frame (Bayat 2010), b) PBPD Frame (Bayat 2010), and c) Hybrid Frame under LA38 Ground Motion. (The dashed-line shows the pattern of semi-rigid connections)

2.4.2. Seismic eccentrically braced frames

The development of seismic eccentric braced frames (EBF) was another attempt to enhance the seismic behavior of steel frames. Well-designed EBFs constructed with shear links provide high elastic stiffness and strength under low to moderate ground motions combined with high ductility and energy dissipation capacity in severe ground motions (Popov and Englehardt 1988). Typical bracing configurations of EBFs are shown in Figure 2.6.

The bracing members in EBFs provide high stiffness and allow the drift requirement of codes to be met economically. On the other hand, the high ductility of this system comes from two factors. First, shear links are designed to sustain large deformation without significant loss of strength. The second factor is that bracings are designed not to buckle regardless of severity of ground motion. The amount of compression force in bracings is limited to the force required for yielding of the shear links. Thus, the ultimate strength of the shear links is designed to be less than the buckling force of the bracings. In fact, this design methodology assures that the bracings will not buckle.
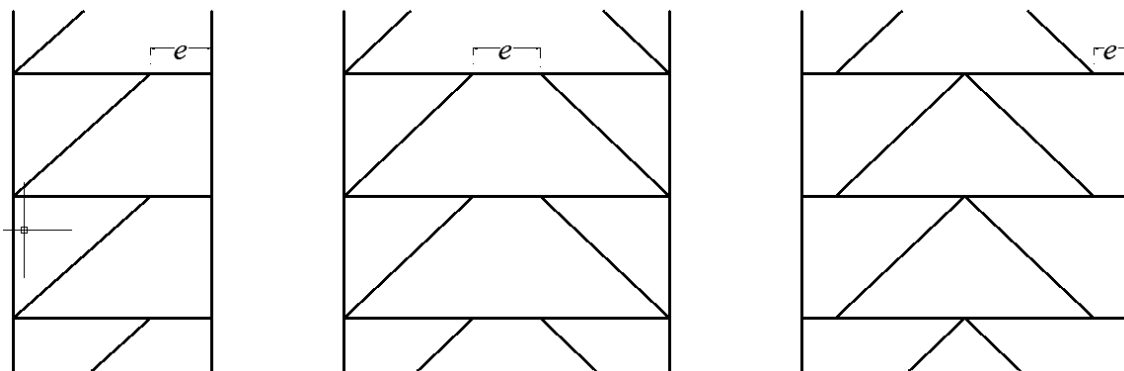
Figure 2.6 Typical bracing arrangements for EBFs

The seismic behavior of EBFs will be better understood by comparing the behavior of three different lateral resistant systems of Moment Resistant Frame (MRF), Centrically Braced Frame (CBF), and EBF. The experimental lateral force versus displacement plot of these three systems is shown in Figure 2.7. The stable hysteresis loop of MRF shows the high-energy dissipation capacity in MRFs. In addition, it shows that a MRF can sustain large deformations without considerable reduction in strength and stiffness. In contrast, pinching in a CBF's loop as shown in Figure 2.7(b) illustrates the low energy dissipation of capacity of CBF system. This pinching is due to the buckling of brace members in CBF system. Finally, Figure 2.7(c) shows that for a well-designed EBF, a full and stable hysteresis loop is obtained that is indicative of the high energy-dissipation capacity of the frame.

Similar to the shear links in EBF, research works (Abolmaali 2009; Astaneh 1989) showed that a well-designed semi rigid connection, could also sustain large deformation (up to 5% drift) without considerable deterioration. In the proposed hybrid frame, energy dissipative semi-rigid connections are used to enhance the seismic behavior of the steel moment frames.
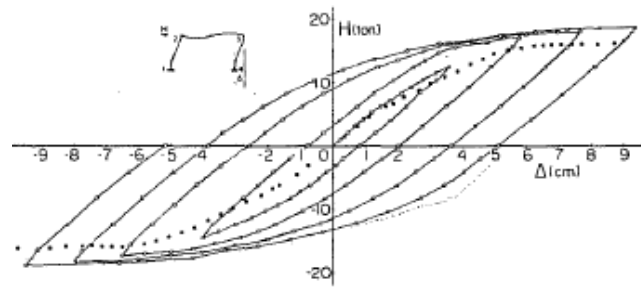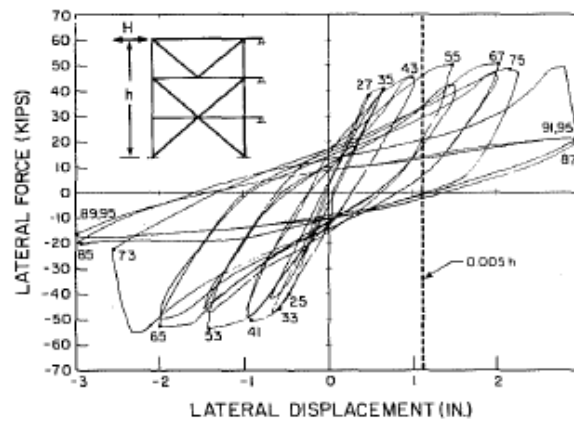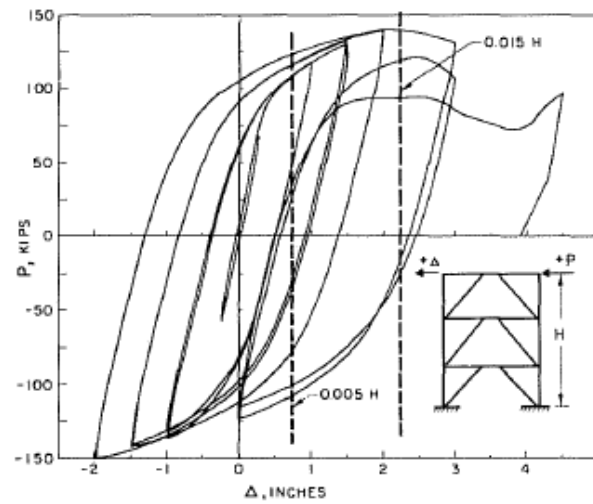
Figure 2.7 Typical experimental frame behaviors under cyclic lateral load. (a) MRF (after Wakabayashi 1974), (b) CBF (Maison 1980), and (c) EBF (Manheim 1982)

24

2.5. Background on semi-rigid connections

In general, bolted-bolted or welded-bolted connections with slip critical bolts, which are pre-tensioned to 70% of their minimum tensile strength, are known as semi-rigid connections. Static and dynamic characteristic of semi-rigid connections are categorized by their moment rotation (M-θ) curves and hysteresis loops, respectively.

Theoretically, the M-θ behavior of semi-rigid connections falls in between the shear and fully-restrained all-welded moment connections. Shear connections are traditionally designed to transfer shear force from beams to connecting columns with their bolts being bearing type for which high slip resistance is not required. Thus, relative rotation of the beam end with respect to the column is ensured, which results in insignificant transfer of the moment. Typical examples of shear connections are single plate, single web angle, double web angle, and top and seat angle connections with snug tight bolts. Moment connections on the other hand, transfer the moment from the beam end to the column with slip critical bolts requiring high slip resistance at the service load. Some examples of moment connections are the family of end-plate connections such as flush end-plate connections and un-stiffened or stiffened extended end-plate connections.

Seismic behavior of MRSFs with semi-rigid connection has been investigated in several studies theoretically and experimentally such as Nader and Astaneh (1991, 1992, 1996); Maison and Kasai (2000). Excessive inter-story drift was a major concern for using semi-rigid connections in steel frames. These studies showed that when connection stiffness increases, base shear increases; however, inter-story drift does not decrease proportionally. They have also show that MSRFs with semi-rigid connections can also be used in highly seismic regions.

The implementation of semi-rigid connections in a static or dynamic frame analysis algorithm is achieved by using a nonlinear rotational spring element, which connects the beam end to the column web and flange. The connection element has the same translational degrees-

of-freedom (D.O.F) and different rotational D.O.F. at each end to account for the relative rotation of the beam with respect to that of column. The element nonlinearity is due to the intrinsic nonlinear M-θ of the connection obtained from experimental testing (Ackroyed and Gretle (1982), Bjorhovde (1990), Astaneh et al. (1991), Astaneh et al. (1995), Kukreti and Abolmaali (1999), Abolmaali et al. (2003), and Abolmaali et al. (2009)). This nonlinearity is due to the inelastic action of end-plate or angle materials which prevents sudden fracture of connection parts such as bolts and/or welds. Thus, the parameters being affected are connection initial stiffness, yield moment, and connection's post yield stiffness which govern the nonlinear M-θ characteristics.

Astaneh et al. (1989) and Abolmaali et al. (2009) studied the energy dissipation characteristics of different types of semi-rigid connections and showed that they are capable of undergoing large inelastic rotation (in excess of 0.05 radians) given the connection is designed such that the angle or plate yielding governs the behavior. In other words, if the plate or angle thickness is relatively small compared to bolt diameter, bolt yielding and fracture are prevented and plate yielding results in a ductile connection behavior by undergoing large inelastic rotation.

Current design codes have mostly eliminated partially restrained connections in high seismic zones. However, there are several studies that show high energy dissipation of the semi-rigid connections with high stiffness and strength as reported by Ackroyed and Gretle (1982), Bjorhovde (1990), Astaneh et al. (1989), Astaneh et al. (1991), Astaneh et al. (1995), Kukreti and Abolmaali (1999), Abolmaali et al. (2003), Abolmaali et al. (2005), and Abolmaali et al. (2009).

2.5.1 Finite element modeling of Semi-Rigid Connections

Numerical simulation and the finite element method are at their peak of accuracy and capable of simulating the behavior of engineering systems under complex loading. Time consuming and costly full-scale structural testing can be minimized for efficiency. Steel connections are among those whose cyclic testing and finite element modeling have attracted several researchers. This is due to the fact that connections are critical ingredients of seismic resistant design and their cyclic behavior impacts directly the performance of structures subjected to earthquake vibrations. Steel connections commonly consist of end-plate or angles which are bolted/welded to beam web/flange and bolted or welded to column flange. The combination of bolts and welds has also been used.

Several challenges arise in the numerical modeling of steel bolted connections. Bolted surfaces commonly consist of two plates connected by means of bolts, which are either snug tight (frictionless) or fully pre-tensioned. Bolt pre-tensioning in combination with contact between different surfaces lead to complexity in numerical simulation of semi-rigid connections.

The relationship between the beam end moment versus the connection relative rotation (M–θ) plays an important role in identifying the ductility and energy dissipation characteristics of bolted or bolted/welded connections. This M–θ relationship, which is highly sensitive to the connection's geometric variables, can typically be obtained by cost prohibitive full-scale experimental testing (Abolmaali et al. 2003).

Several standardized models ranging from the simplest linear form to bilinear and more complicated polynomial formulas has been fitted to experimental data; however, due to the limited parameters used in these models, there is still a need for a reliable tool to produce the moment-rotation curve or moment-rotation hysteresis loops for any arbitrary designed connection.

To eliminate the need for experiments for obtaining static or cyclic M–θ of connections, the nonlinear finite element method can be used as a powerful tool for modeling the cyclic moment-rotation behavior of semi-rigid connections.

Finite element investigations on the behavior of the steel bolted connections started as early as 1976. The majority of the early studies were focused on the correlation of the results from 2-D models with actual 3-D specimens. Computation capability, time dependency of old computers in addition to the substantially high cost of creating and running the 3-D model was the main reason that many researches were conducted in the 2-D model. With the advancement of the computer technology, highly sophisticated 3-D models are allowed to be executed without substantial penalties in computation time or cost.

Krishnamurty et al. (1976, 1979, 1980) developed a finite element method for analysis of end-plate connections. Due to the computational limitations, they utilized a 2-D constant strain triangle element and a 3-D eight-node brick element to determine adequate correlation between the results.

Ghassemieh (1983) incorporated the nonlinear material behavior in finite element modeling of extended end plate connections. Comparison of the finite element model developed in this study with full-scale experimental test, showed a good agreement between the moment-rotation hysteresis loops.

Kukreti et al. (1990) utilized finite element modeling to develop an equation to characterize the behavior of the extended stiffened end-plate connections. They introduced material nonlinearity by using a bilinear material law the algorithm. However, modeling of contact surfaces was neglected.

Kukreti and Biswas (1997) modeled the behavior and failure of end plate connections under cyclic hysteretic loading using the finite element method. The inelastic behavior of the materials was modeled by using incremental plasticity theory described by the Von Mises yield criterion and the Mroz kinematic hardening model.

28

Kishi et al. (2001) studied four finite element models to determine the moment rotation characteristics of the top- and seat-angle with double web angle connections under monotonic loading. Effects of bolt pretension were also considered in the finite element model.

Limited studies are reported with regard to numerical modeling of connection subjected to cyclic loading.

Takhirov and Popov (2002) conducted cyclic tests on 48 T-stub test specimens; however, they reported numerical nonlinear analysis of the connection subjected to static loads only.

Nie et al. (2006) studied the behavior of three types of steel-concrete composite connection under monotonic and cyclic loading. They reported a fairly good agreement between numerical and experimental study in terms of strength and loading stiffness; however, the reloading stiffness did not match the experimental results and no pinching phenomenon was seen in numerical hysteresis curves because the punching shear failure mode was not accounted in the FEM model.

Kiamanesh et al. (2012) worked on the effect of the circular bolt pattern on the behavior of the extended end-plate connection; they showed the FEM can precisely predict the experiment results.

In the study outlined in chapter 6 of this dissertation, essential parameters for modeling bolted connection are presented. Two different contact and friction properties between flat surfaces such as angle/beam and bolt head/beam and for bolt shank/bolt holes and an approach to apply the pre-tensioning bolt force is explained. Since the approach is general it can be applied to any arbitrary bolted connection; however, in order to verify the accuracy of the procedure, five different types of bolted connections are modeled, analyzed ,and compared with the experimental test results. This work has also been presented in Razavi et al. (2012).

CHAPTER 3

INTRODUCTION TO THE CONCEPT OF SEISMIC RESISTANCE HYBRID FRAME

3.1. Introduction

The concept of the proposed hybrid frame systems is based on introducing energy dissipating mechanisms in the structural frame systems (Abolmaali et al. (2012)). This is achieved by replacing selected rigid connections with ductile energy dissipating semi-rigid connections in order to enhance frame's seismic performance. This concept, even though at first glance is similar to the eccentrically braced frame introduced by Engelhardt and Popov (1989), the behavior is quite different. In the eccentrically braced frames, the isolated "links" are commonly introduced throughout the frame, while in the proposed method; the semi-rigid connections are placed at the selected locations and/or particular patterns (Radulova (2009)).

In general, with this concept, the story drifts at the semi-rigid connection levels are translated into connection rotation. Thus, for a properly designed connection that behaves in a ductile manner, this cyclic rotation is absorbed into angle/plate yielding without bolt or weld fracture. This would lead to excessive end-plate or angel distortion at ultimate rotation that can be retrofitted at the semi-rigid connection levels.

This concept is implemented in two SAC model buildings of 9 and 20-story (FEMA-355F) in which rigid connections are replaced with semi-rigid connections at different story levels with different patterns. In the 20-story building, all the exterior connections are rigid connections and box columns are used at the corners to resist bi-axial bending. In the 9-story building, one of the exterior bays has only one moment resisting connection to avoid bi-axial bending in the corner column as shown in figure 3.1. Most of the girder sizes are controlled by drift rather than strength considerations.
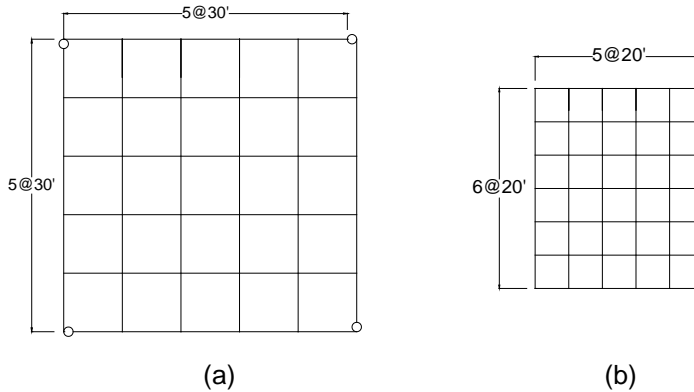
30

Figure 3.1 Floor plans showing layout of MRFs for LA model buildings (a) 9-story and (b) 20-strory

The proposed frames are called Hybrid SAC (H-SAC) frames. To identify the optimum H-SAC frame with respect to its energy dissipation, initially several 20-story frames were proposed and detailed investigations were conducted by Radulova (2009). The standard descriptions used were based on the following nomenclature:

FRAME TYPE-STORY (BS:ES)-LSRC (A-E-M)— ΘY - MY, where:

FRAME TYPE: (1) H-SAC for Hybrid SAC frame or (2) SAC for conventional SAC frame.

STORY (BF:EF)--represents the "STORY" numbers where semi-rigid connections are placed, and a range of stories is notated with "BF" and "EF" representing the "Beginning Floor" and "End-Floor," respectively. When BF=B, it represents the "Basement."

LSRC (A-E-M)--stands for the "Location of Semi-Rigid Connections" in which "A," "E," and "M" represent "All-Bays," "End-Bays," and "Middle Bays," respectively.

ΘY and MY--are the "Yield rotation" and "Yield moment," respectively.

For example, the frame designated as H-SAC-20–B:5-A-0.004-1,000 represents a Hybrid SAC frame with semi-rigid connections in all bays (LSRC = A) from the basement to the fifth (5th) floor (B:5). The yield rotation, ΘY =0.004rad and the yield moment, MY =1,000 kip-in (113 kN-m).

The hybrid frames by Radulova (2009) were subjected to a cyclic displacement history designed to be capable of producing 30 in. (76 cm) lateral sway in order to ensure yielding and subsequent inelastic hysteresis behavior in all the semi-rigid connections. The energy dissipation of each frame was examined by plotting the building's lateral force- sway hysteresis loops as shown in Figure 3.2. It should be noted that the source of the dissipating mechanism is merely the semi-rigid connections and their hysteresis behavior. For this particular analysis, a semi-rigid connection with yield rotation, $\Theta Y = 0.004$ rad and yield moment, $MY= 1000$ kip-in (113 kN-m) (Abolmaali et al. (2009)) was considered. This connection was a welded/bolted double web angle connection in which the angles were welded to the beam web and bolted to the column flange, and its bolts were pre-tensioned to the proof load. The mode of failure for this connection was excessive angle yielding with its ultimate rotation was in excess of 0.04 radians from the experimental testing reported by Abolmaali et al. (2009).
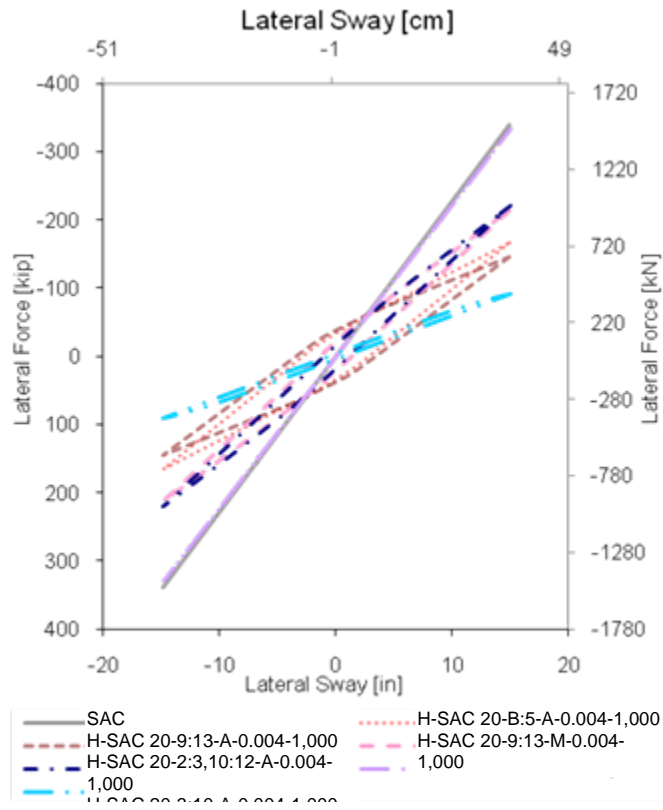

Figure 3.2 Outer loop hysteresis plots of the hybrid frames

32

for energy dissipation detection

The area under the outer loop was calculated for each hysteresis plot of Figure 3.2 which indicates the effectiveness of the semi-rigid pattern and frame's energy dissipation capability as shown in Table 3.1. It was shown that H-SAC-20-9:13-A-0.004-1000 and H-SAC-20-B:5-A-0.004-1000 frames with the energy dissipation values of 1,267 kip-in (143.00 kN-m) and 1,111 kip-in. (125.50 kN-m), respectively, were superior the other frames.

Table 3.1 Energy dissipation of the hybrid frames of Figure 3.1

Frame	AREA (kips.in)	AREA (kN.m)
SAC	0	0
H-SAC 20-9:13-M-0.004-1000	722	81.60
H-SAC 20-3:10-A-0.004-1000	202	22.80
H-SAC 20-B:5-A-0.004-1000	1111	125.50
H-SAC 20-9:13-A-0.004-1000	1267	143.0
H-SAC 20-9:13-E-0.004-1000	0.24	0.030
H-SAC 20-2:3,10:12-A-0.004-1000	640	72.30

During the selection of the locations of the semi-rigid connections, first the energy dissipation of beam ends were obtained by calculating the area under M-θ hysteresis obtained from the inelastic dynamic analysis. Thus, the high energy dissipation zones were selected and their rigid connections were replaced with semi-rigid. This concept yielded to semi-rigid connections for Floors 4, 5, and 6 for the 9-story frame and Floors 9 to 13 for the 20-story frame. Both frames are shown in Figure 3.3.
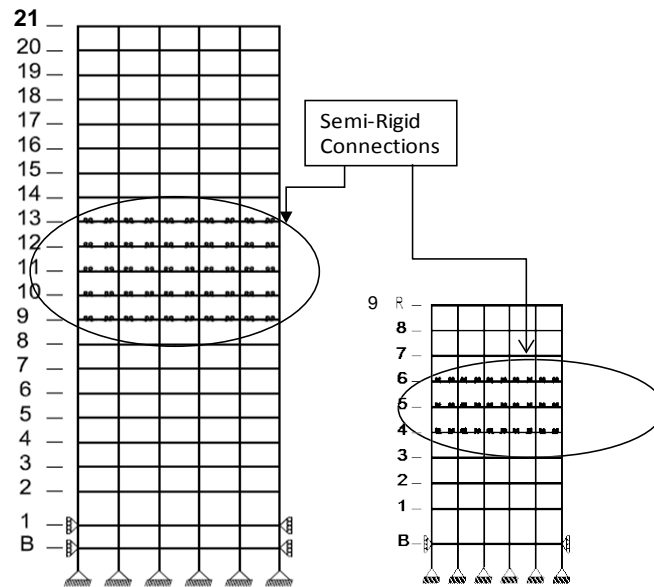
Figure 3.3 Selected Hybrid SAC frames for inelastic dynamic analysis

3.2. Inelastic dynamic analysis

Inelastic dynamic analyses were conducted on the selected hybrid frames of Figure 3.3. The beams and columns were considered to remain elastic while the semi-rigid connections elements were the only source of nonlinearity as defined by their inelastic bilinear moment rotation hysteresis constitutive relation. The semi rigid connection used for this study was a flush end-plate moment connection as shown in Figure 3.4. The end-plate thickness (tp= ½ in.) and bolt diameter (db=1.0 in.) were selected to ensure end-plate yielding as observed during the full-scale cyclic experimental testing by Abolmaali et al. (2009). To avoid weld fracture, high strength fully penetrated welds were used. The enveloping bilinear M-θ hysteresis is shown in Figure 3.4 (c) which is defined by four parameters: yield moment (MY); yield rotation (θY); ultimate moment (MU); and ultimate rotation (θu).Since the initial connection stiffness in general is not well defined, the connection stiffness was calculated by the ratio of KI = MY/ θY. To calculate the above hysteresis parameters, the following three-parameter Ramberg-Osgood functions (1943) for loading and unloading were fitted to the experimental data:

34

$$\frac{(\theta - \theta_1)}{2\theta_Y} = \frac{(M - M_1)}{2M_Y}\left(1 + \left|\frac{M - M_1}{2M_Y}\right|\right)^{r-1} \tag{1}$$

$$\frac{(\theta + \theta_2)}{2\theta_Y} = \frac{(M + M_2)}{2M_Y}\left(1 + \left|\frac{M + M_2}{2M_Y}\right|\right)^{r-1} \tag{2}$$

Where: θ_1 = rotation at the instant of unloading; θ_2 = rotation at the instant of reloading; M_1= moment at the instant of unloading; M_2 = moment at the instant of reloading; θ_Y = yield rotation; M_Y = yield moment; and r = rigidity parameter which defines the degree of flexibility or rigidity of the curve. The parameters θ_1 and M_1 are indeed the ultimate rotation and moment once the entire data are fitted. The Ramberg-Osgood functions are fitted to the experimental data by using the method of least squares and Newton iteration to find the three parameters (M_Y, θ_Y, and r). Once the values of M_Y, θ_Y, M_u, and θ_u are known, the enveloping bilinear hysteresis for the connection is constructed which defines the constitutive material law for the connection element used in the numerical analysis of the proposed hybrid frame system.
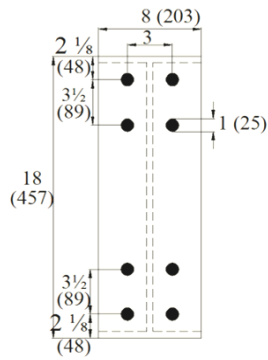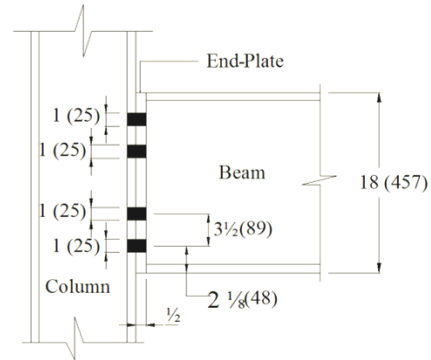
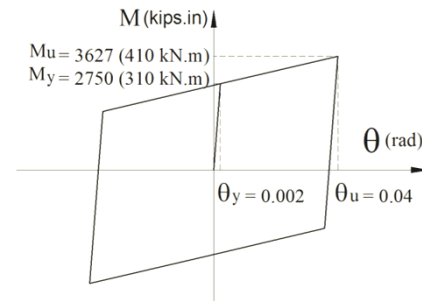(a)   [All units are in inches (mm)]
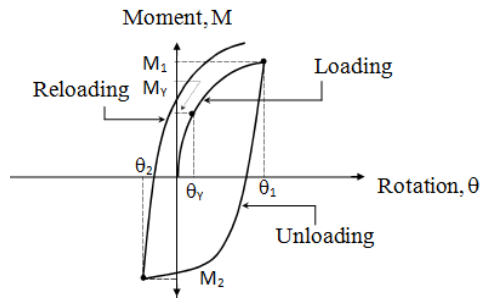
(b)   (c)

Figure 3.4 The configuration and properties of the connection used in the hybrid frame
(a) Details of the semi-rigid connection used in hybrid frames for inelastic dynamic analysis,
(b) Parameters of Ramberg-Osgoog function, and (c) Enveloping Hysteresis Model

The computer software Open System for Earthquake Engineering Simulation (OpenSees) was used for all the analyses. The Opensees is a software framework for simulating the seismic response of structural systems with computational platform for research in performance-based earthquake engineering. OpenSees has advanced capabilities for modeling and analyzing the nonlinear response of systems using a wide range of material models, elements, and solution algorithms.

The Los Angeles earthquake records used in this study are shown in Table 2. In this table, the LA01, LA02, LA11, and LA12 are categorize as those with 10% probabilities of

exceedence in 50 years while LA20, LA22, LA 27, and LA28 are listed as records with 2% probabilities of exceedence in 50 years.

Table 3.2 Details of Los Angeles Ground Motion Records

SAC Name	Record	Earthquake Magnitude	Distance (km)	Scale Factor	Number of Points	DT (sec)	Duration (sec)	PGA (cm/sec^2)
LA01	El Centro 1940	6.9	10	2.01	2674	0.02	39.38	452.03
LA02	El Centro 1940	6.9	10	2.01	2674	0.02	39.38	662.88
LA11	Loma Prieta, 1989	7	12	1.79	2000	0.02	39.38	652.49
LA12	Loma Prieta, 1989	7	12	1.79	2000	0.02	39.38	950.93
LA21	Kobe 1995	6.9	3.4	1.15	3000	0.02	59.98	1258.00
LA22	Kobe 1995	6.9	3.4	1.15	3000	0.02	59.98	902.75
LA27	Northridge 1994	6.7	6.4	1.61	3000	0.02	59.98	908.70
LA28	Northridge 1994	6.7	6.4	1.61	3000	0.02	59.98	1304.10

The non-linear p-δ effects were also coupled with the connection nonlinearities. Each semi-rigid connection was modeled as a 2-noded rotational spring connecting the beam end to the column with two identical translational degrees-of-freedom (d.o.f) and two different rotational d.o.f as shown in Figure 3.5. For the conventional SAC frame all members were assumed to remain elastic and 2% damping was introduced into the analysis.
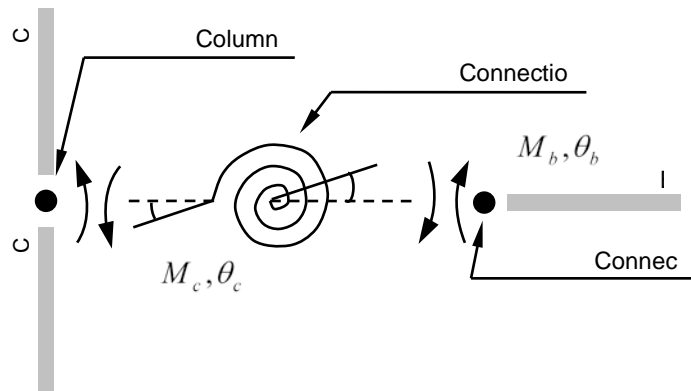

Figure 3.5 Analytical model of Semi-Rigid connection

3.3. RESULTS AND DISCUSSIONS

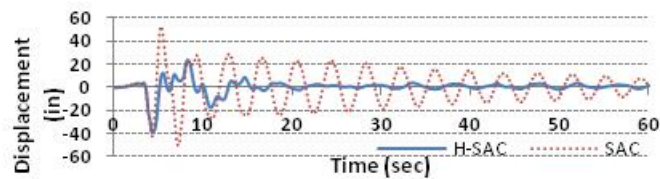*3.3.1 Roof Displacement Time History*

The H-SAC and SAC frames were subjected to all the earthquake records of Table 2, but only the roof-displacement time history plots of the two extreme (LA 11 and LA 28) and one mid-range (LA 22) records are presented in this study. Figures 3.6 (a), 3.6 (b), and 3.6 (c) present the roof displacement time history for the 20-story H-SAC and SAC frames subjected to the LA11, LA22, and LA28 records, respectively. These figures show that the displacement history of the 20-story H-SAC frames have decreased significantly for all the applied records. The average decrease for the LA11, LA22, and LA 28 records are 81%, 332%, and 346%, respectively. The displacement time history for the LA11 record shows a closer co-relation between H-SAC and SAC. However, for the higher frequency earthquakes (LA20 and LA 27), the benefit of the H-SAC over the SAC frame is profoundly evident. It should be noted that the H-SAC has a higher natural period of vibration (lower frequency) when compared with the SAC frame due the reduced frame stiffness which persuades it to perform superior when subjected to higher frequency earthquakes.
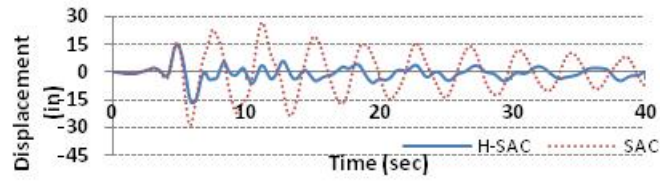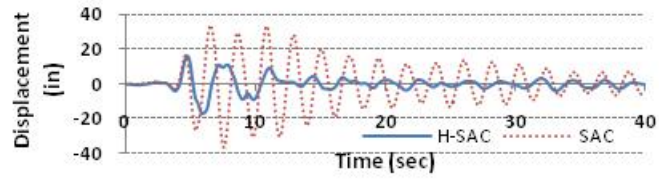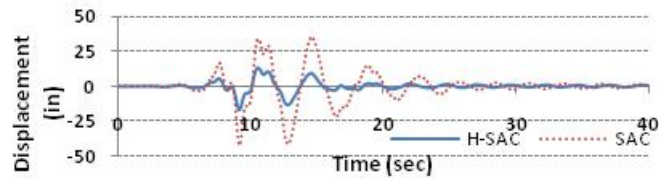
(a)
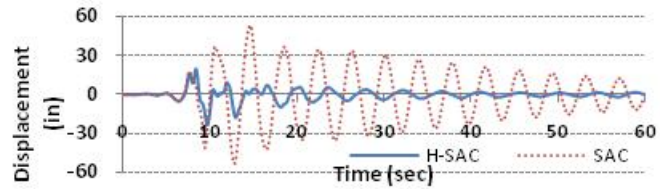
(b)

(c)

Figure 3.6 Roof-displacement-time-history for the 20-Story H-SAC versus SAC frames (a) Roof displacement history for the 21 Story H-SAC and SAC subjected to LA11 earthquake, (b) Roof displacement history for the 21 Story H-SAC and SAC subjected to LA22 earthquake, and (c) Roof displacement history for the 21- Story H-SAC and SAC subjected to LA28 earthquake

Similar plots for the nine 9- story H-SAC frame, shown in Figure 3.7, reveal the decrease in the roof displacement within each time step with the average decrease of 98%, 165%, and 144% for the LA11, LA22, and LA27 records, respectively. It is noted that the effect of the semi-rigid connections in the H-SAC for the 9-story frame is less than the 20-story frame. However, the overall positive effect of the reduction of the roof sway is hereditary in the proposed hybrid frame system.

(a) Roof displacement history for the 9 Story
H-SAC and SAC subjected to LA11 earthquake

(b) Roof displacement history for the 9 Story
H-SAC and SAC subjected to LA22 earthquake
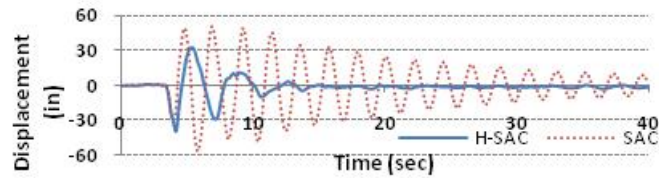
(c) Roof displacement history for the 9 Story
H-SAC and SAC subjected to LA28 earthquake

Figure 3.7 Roof-displacement-time-history for the 9 Story H-SAC versus SAC frames

3.3.2 Beam Axial, Shear, and Bending

To compare the axial, shear, and bending moments of the H-SAC versus SAC frames, the ratios of the absolute value of maximum forces for the H-SAC were normalized with respect to the forces of the SAC frame. Thus, a ratio of unity indicates that the H-SAC forces are equal to the SAC forces, and the ratio of less than unity implies a reduction in a given force for the H-SAC (lower demand).

Figure 3.8 shows the ratios of the beam axial, shear, and moment for the H-SAC versus SAC for each floor of the 20 story frame. A solid vertical line (ratio = 1) is drawn as the indicator

for comparing the forces of the H-SAC relative to the SAC. These figures show that, with the exception of a few cases, the shear and moment demands of the members of the H-SAC are significantly lower than SAC for all the floors as shown in Figures 3.8(b) and 3.8(c). The dashed lines indicating the average of the ratios show that the average of the ratios for shear and bending moment of 0.539 and 0.536 (Table 3.3), respectively. This means that the average decrease in shear and moment demands for the beams is approximately 46% when H-SAC frame is used.   Table 3.3 shows the averages of above ratios of the forces for all the Los Angeles Earthquake records of Table 3.2.

Table 3.3 Average of H-SAC/SAC Responses Ratio

Response	Statistics	Axial Force	Shear Force	Moment
21 Story Beams	Average	1.401	0.539	0.536
	Max	7.945	1.027	1.055
	Min	0.307	0.120	0.120
9 Story Beams	Average	0.930	0.469	0.484
	Max	2.437	0.902	0.903
	Min	0.116	0.074	0.072
21 Story Columns	Average	0.327	0.567	0.622
	Max	0.592	0.933	1.164
	Min	0.044	0.284	0.311
9 Story Columns	Average	0.445	0.496	0.566
	Max	1.536	0.738	1.089
	Min	0.065	0.118	0.126
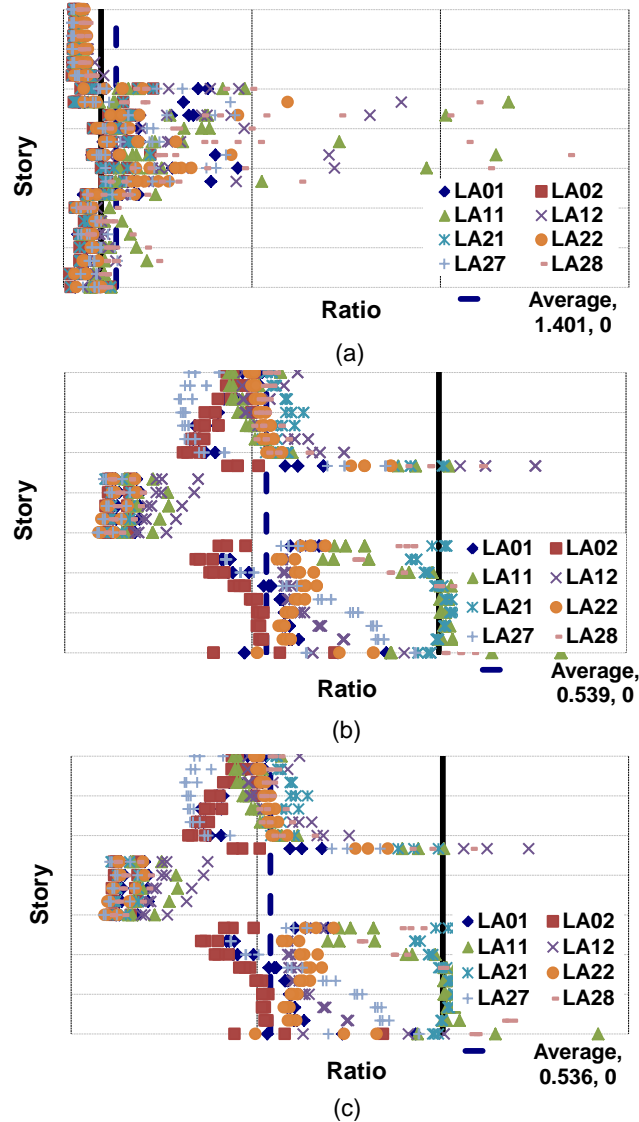
Figure 3.8 The ratios of the member forces in beams for the 20-Story H-SAC/SAC
(a) Beams Axial Force Ratio: H-SAC/SAC, (b) Beams Shear Ratio: H-SAC/SAC,
and (c) Moment Ratio in Beams: H-SAC/SAC

The beams axial forces, however, is shown to increase (Figure 3.8(a)) mostly at the

locations of the semi-rigid connections with an average ration of 1.401 (Table 3.3) which

indicates an average increase of 40%. It should be noted that this average increase is merely at

the semi-rigid connection levels, and indeed the axial forces in non-semi-rigid levels are

decreasing (Figure 3.8(a)). This observations lead to the fact that the semi-rigid floor levels act

as a "truss mechanism" to decouple the motions of the members above and below the semi-

rigid levels. This is supported based on the difference in high axial beam forces within the semi-rigid floor levels and low axial forces elsewhere.

Similar results are obtained for the ratios of the beam forces of the 9-story H-SAC versus SAC frames. The average reduction in shear and moment values for all members of the H-SAC frame is 51.7% which is obtained from ratios of 0.469 (53% reduction) and 0.484 (52% reduction) for shear and bending moment, respectively (Table 3.3). Similar to the 20-story frame, the ratios of beams axial force for the 9-story hybrid frame jump at the locations of semi-rigid connections, but on average the axial force in beams reduces with the average reduction of 7% (average ratio = 0.930) as shown in Table 3.3. Once again, a "truss mechanism" is formed to decouple the motions of the semi-rigid levels from the other levels.

3.3.3 Column Axial, Shear, and Bending

The reductions in column axial, shear, and bending moment are presented in Figures 3.9. In Figure 3.9 (a), the axial forces for all the members of the H-SAC frame are significantly less than the SAC frame. The average reduction in the column axial forces is shown to be 67.3 % which is taken from the average ratio of 0.327 presented in Table 3.3. Figures 3.9 (b) and (c) show similar plots for the column shear and bending moments of the 20-story H-SAC frame. Almost all the shear ratios and most of the moment ratios fall to the left of the line drawn at the ratio = 1. The averages of the shear and moment ratios for all the earthquake records are 0.567 and 0.622, respectively. This implies reductions in shear and moment of 43.3% and 37.8%, respectively. Figure 3.9 (c) shows that the column moment ratios exceed the ratio=1 at the floor levels where semi-rigid connections are placed for most earthquake records. This is due to the increase in the beam axial forces in these levels.

Similar results for the ratios of the column forces of the 9-story H-SAC to SAC are observed with the overall pattern as the 20-story frame. The averages of the ratios of the axial, shear, and moment are 0.445, 0.496, and 0.566, which indicates average reductions of 55.50%, 50.04%, and 43.40% in axial, shear, and moment, respectively. Except, the ratios of the column axial force at the locations of semi-rigid connections shift to the right of ratio=1 for the LA12 and LA22 earthquake records indicating higher axial force demand at these locations for the 9-story H-SAC. This is attributed to the closer relationship between the natural frequency of the 9-story frame and the above two earthquake records. The average value of moment ratios also exceeds unity at the locations of the semi-rigid connections, however, less of the ratios are higher than ratio=1 for the case of the 9-story H-SAC as compared to the 12-story H-SAC.
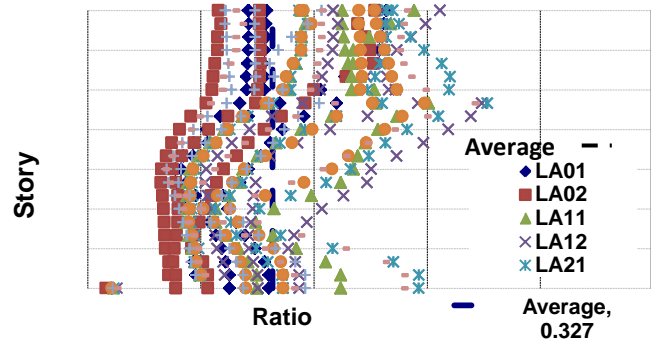
(a)
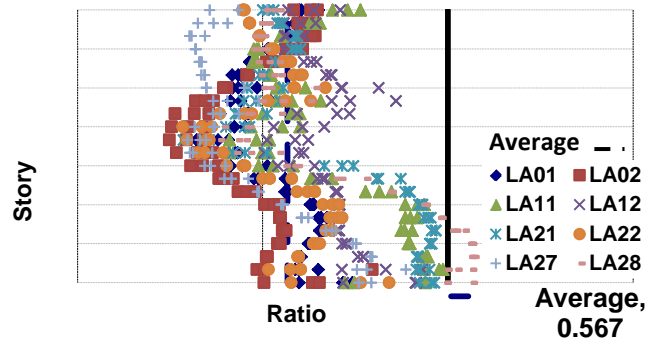
(b)
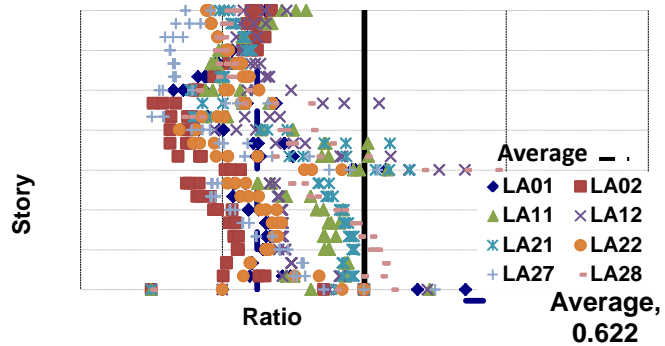
(c)

Figure 3.9 The ratios of the member forces in columns for the 20-Story H-SAC/SAC
(a) Columns Axial Force Ratio: H-SAC/SAC, (b) Columns Shear Ratio:
H-SAC/SAC, and (c) Columns Moment Ratio : H-SAC/SAC

3.3.4. Story Drift

Plots of the maximum story drift for the 20 and 9-story H-SAC frames are presented for the earthquake records of Table 3.2 in Figures 3.10 and 3.11, respectively. These plots also include the life "safety" and "collapse prevention" limits as defined by the FEMA 356. Figures 3.10 (a) and 3.11 (a) present the averages of the maximum story drift for all the LA earthquake records. It is observed that the drift values reduce in the H-SAC frame at all the floors with the exception of the semi-rigid floors, but they remain below the collapse prevention limit in the 20-story frame and slightly exceeds this limit in the 9-story frame. It is interesting to note that the roof drift also reduces in the proposed hybrid frame.

3.Figure 10 (b) and shows the analyses results for the 20-story frame subjected to LA01 through LA12 records with 10% probabilities of exceedence in 50 years, while Figure 3.10 (c) includes the plots of LA21 through LA28 records (2% probabilities of exceedence in 50 years). Similarly, Figures 3.11 (b) and 3.11 (c) present the individual drift plots of the 9 story H-SAC. These figures show that the roof drift values of the 9 and 20-story H-SAC are below the life safety" and "collapse prevention" limits as recommended by the FEMA 356. It is interesting to note that the drift values for the floors other than the semi-rigid floors (including the roof) are reduced for the H-SAC frame when compared to the SAC frame for all the earthquake records, and in some cases this difference is significant. For certain earthquake records, the story drift values exceed the above limits at the floors with the semi-rigid connections. For example, for the 20-story H-SAC the LA21, LA27, and LA28 force the drift of semi-rigid floors to beyond the collapse prevention limits. Similarly, LA21, LA22, LA27, and LA28 records push the story drift to beyond the collapse prevention limit in the 9-story H-SAC. However, for both frames subjected to LA01 through LA12 records the story drifts remain below the collapse prevention limits.
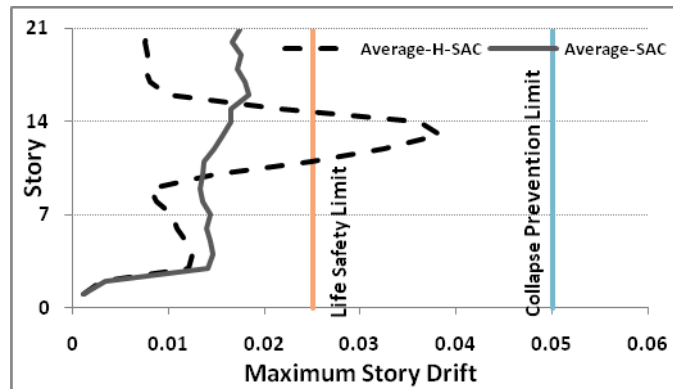
(a)
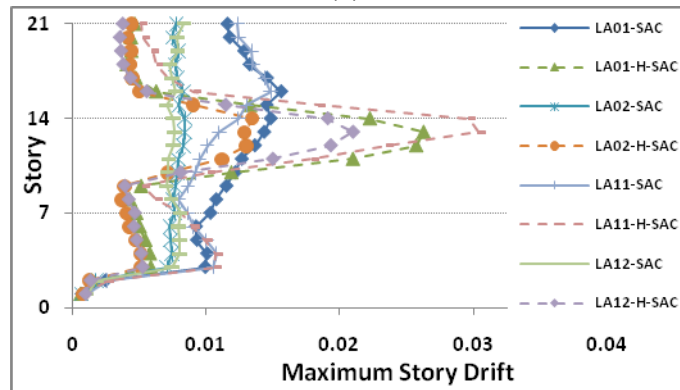
(b)
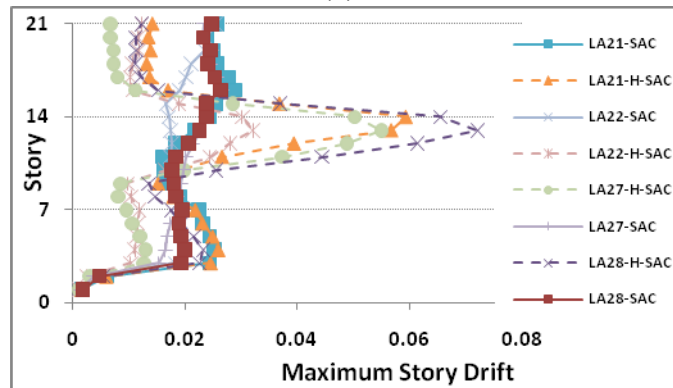
(c)

Figure 3.10 Story drift for the 20-story H-SAC (a) average story drift of all the earthquake records, (b) Story drift for LA01 through LA12 records, and (c) Story drift for LA21 through LA28 records
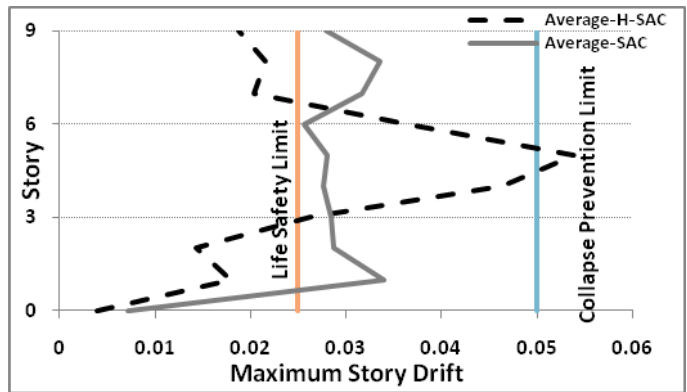
(a)
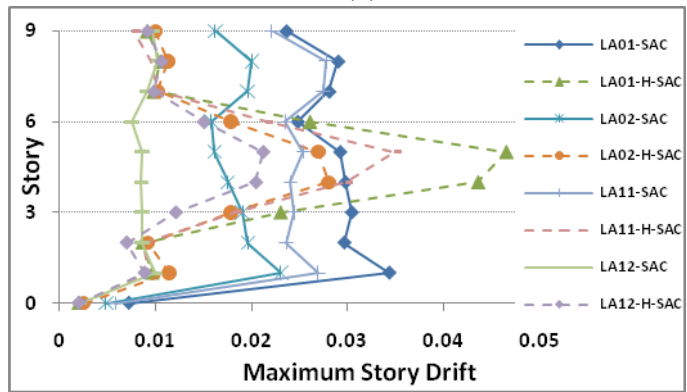
(b)
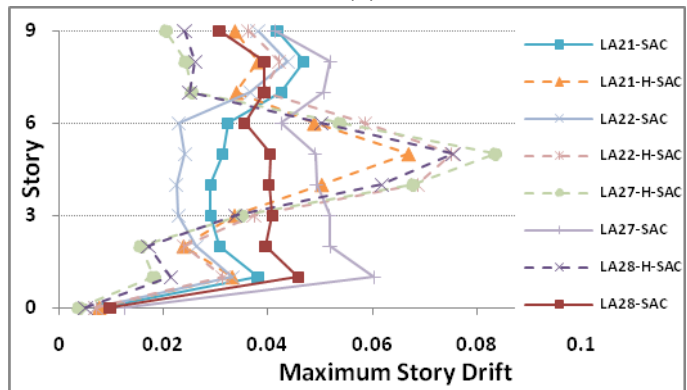
(c)

Figure 3.11 Story drift for the 9-story H-SAC (a) average story drift of all the earthquake records, (b) Story drift for LA01 through LA12 records, and (c) Story drift for LA21 through LA28 records

48

This increase in the story drift in the H-SAC frames at the floor levels with semi-rigid connections translates into connection rotation. This rotation forces the connections to behave in different manners depending on their geometric parameters such as bolt, angle/plate, beam, and column sizes. For example, if the bolt diameter is small compared to the end-plate/angle thickness, the story drift translates to bolt elongation, which causes plate separation that ultimately leads to connection failure. On the other hand, the desirable scenario is when the plate thickness is smaller than the bolt diameter in which the story drift translates into end-plate/angle yielding and causes "fat hysteresis loops" with or without pinching depending on the connection type. The capability of the semi-rigid connections to withstand large plastic rotation (in excess of 0.07 rad) without failure was observed by several researchers among which Astaneh et al. (1989) and Shen and Astaneh (2000) are noted here.

Cyclic connection tests in which the connection mechanism are isolated, in order to avoid the inclusion of the column flange deformation contributing to connection rotation, have shown that properly design semi-rigid connections can undergo rotations without bolt or weld fracture up to and exceeding 0.05 rad. with "fat" hysteresis (Astaneh et al. (1989)). Thus, the increased story drift at the semi-rigid connection levels in the proposed hybrid frames does not necessarily have a negative impact. Indeed, if the connection rotation is observed by the plate or angle cyclic deformation (yielding), some of the yielded connections are replaceable after an earthquake event.

In the current design philosophy, adequate strength, stiffness, and ductility are ensured by considering two alternatives which are included in connection provisions (AISC 2002). One choice is to adopt one of the suggested prequalified connections, and the other is to perform project-based testing which shows the appropriateness of the connection. The connections approved as prequalified by FEMA (2000) have an improved detailing so that the beam plastic hinge formation is shifted away from the column face. High demands at the beam-to-column interface (possibly the main reason for brittle failures during the Northridge earthquake) are

therefore significantly decreased. These connections are of two main categories; reinforced detailing and Reduced Beam Section (RBS) detailing. In the former, the formation of plastic hinge in the beam-column interface is hindered by providing reinforcement, while in the latter, lower strength of RBS shields the connection from high demands. The RBS connections require less welding and material than the reinforced connections which require thinner doublers and continuity plates.

By comparison, this study allows excessive yielding of the selected connections without fracture to dissipate the earthquake vibration through angle and/or plate yielding. Thus, high ductile demand is forced back in the semi-rigid connections of certain floor levels only. While limited number of connections would undergo yielding, the rest of the connections remain at low demand. This in turn eliminates the need for the reduced beam section.

The results of this study show that the hybrid frame concept presented in this manuscript can significantly enhance the seismic performance of the structural systems by reducing the member forces and story drifts. Finally, it should be noted that it is assumed that the connections in the non-semi rigid floors are welded connections.

3.4. Primary Study Findings

The concept of hybrid steel frame system is presented in which a mixture of fully-rigid and semi-rigid connections is used to enhance frame's seismic performance. The hybrid SAC frames were referred to as H-SAC throughout this manuscript. Several different patterns and locations of semi-rigid connection replacements within the frame are examined for the 20-story SAC frame in other to identify the H-SAC frame with the most energy dissipation capability. It was shown that replacing all the fully-rigid connections with semi-rigid connections between Floors 9 to 13 yielded to a frame with the most energy dissipation characteristics. Consequently,

for the 9-story SAC frame all the connections on Floors 4, 5, and 6 were also replaced with semi-rigid connections to form the 9-story H-SAC frame.

Inelastic dynamic analyses were conducted on both the H-SAC frames by using the Los Angeles earthquake records with 10% probabilities of exceedence in 50 years (LA01, LA02, LA11, and LA12) and 2% probabilities of exceedence in 50 years (LA21, LA22, LA27, and LA28). The general conclusions are summarized below:

1. The roof displacement-time history of the H-SAC frames decreased significantly ranging from -81% to -346%. The time-history plots show that the roof displacements of the H-SAC frames damp out and dissipate the roof sway when compared to the SAC frame. This, of course, is expected since semi-rigid connections with high energy dissipation ("fat" hysteresis) were used in the H-SAC frames.

2. The story drift of the H-SAC frames reduced noticeably when compared to the SAC frames with the exception of the story levels with semi-rigid connection. Particularly, the roof drift reduced for all the LA earthquake records for the H-SAC frame. The increased story drift values at the semi-rigid connection levels do not necessarily imply a negative effect. If ductile connections with fat hysteresis are selected, then, the story drift translates to the inelastic deformation of the connection through end-plate and/or angle yielding without bolt or weld fracture.

3. The column axial forces for the H-SAC frames reduced significantly (up to 67%) when compared with the SAC frames. The columns' shear and moment also reduced noticeably by employing H-SAC frames. Similarly, the beams' shear and moment demands also decreased. The axial forces in the beams of the semi-rigid connection floors increased in the H-SAC frames, which introduced a "truss mechanism." Given that the beams' axial forces decreased in the floors with fully rigid-connection, the above "truss mechanism" decoupled the dynamic motions and characteristics of the stories above and below the semi-rigid floors.

CHAPTER 4

MODELING ASSUMPTIONS

4.1 Introduction

Nonlinear finite element analysis of steel frame structures is highly sensitive to material nonlinearity models used for simulation of behavior of structural members. Especially, an accurate material nonlinearity model using state of the art techniques is necessary for collapse analysis.

This chapter presents the geometry, description, and loading of the SAC moment frames that are used in this study. Next, the modeling assumptions of the steel moment resisting frame structures in both structural and element levels are described. Different material models for the simulation of the nonlinear behavior of the frame elements (beams, columns, connections, and panel zones) are summarized. Finally, the ground motions and nonlinear analyses assumptions used in this study are described. For simulations the computer software Open System for Earthquake Engineering Simulation (OpenSees) and Perform 3-D are used for the nonlinear inelastic dynamic analyses of frames.

4.2. SAC Frames Description

Design of SAC special steel moment resisting frames (SMRF) was performed as a part of the FEMA/SAC joint venture Phase 2 studies on behavior of steel structures under seismic loading. These frames include a low-rise frame (3-story), a mid-rise frame (9-story), and a high-rise frame (20-story) which have been designed for three different locations that lie in seismic zones 2A (Boston), 3 (Seattle), and 4 (Los Angeles). The frames of the Los Angeles site, which have been designed for the most severe ground motions, are chosen for this study. Floor plans and elevations of SAC buildings for the Los Angeles site are shown in Figure 4.1. The sections

used in the 3-story, 9-story, and 20-story frames are presented in Table 4-1. These buildings are designed as standard office buildings situated on soil type 2 (stiff soil) according to UBC94.
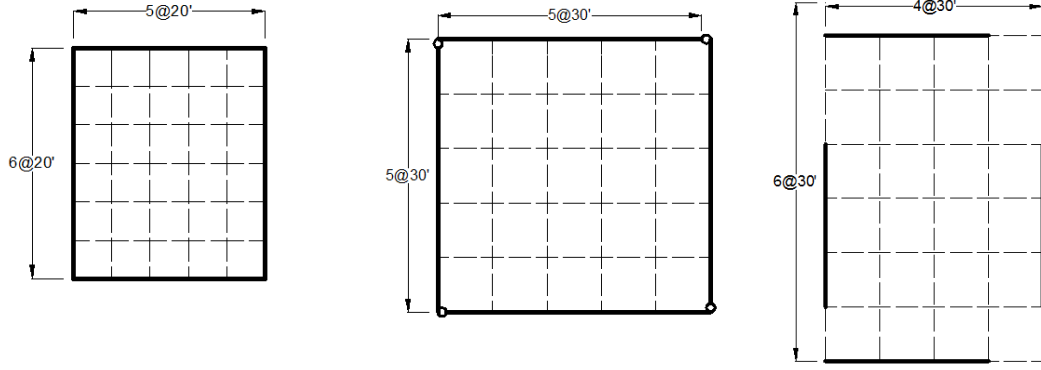
(a)
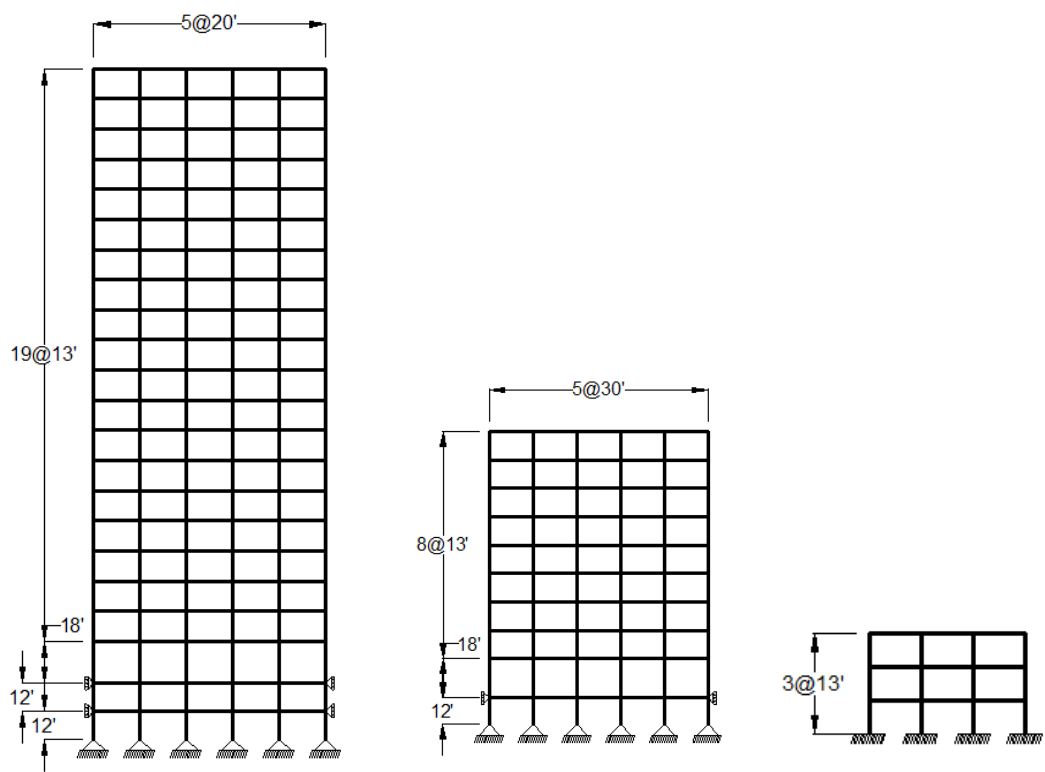
(b)

Figure 4.1 Floor plans and elevations for SAC Los Angeles buildings
(a)Floor plans and location of moment resisting frames and (b) elevations

Table 4.1 Beam and Column Sections, and Doubler Plate Thickness for Los Angeles Model Buildings

3-story Building	NS Moment Resisting Frame				NS Gravity Frames		
	COLUMNS		DOUBLER PLATES (in)	GIRDER	COLUMNS		BEAMS
Story/Floor	Exterior	Interior			Below penthouse	Others	
1/2	W14X257	W14X311	0,0	W30X116	W14X82	W14X68	W16X26
2/3	W14X257	W14X311	0,0	W30X116	W14X82	W14X68	W16X26
3/Roof	W14X257	W14X311	0,0	W24X62	W14X82	W14X68	W14X22

9-story Building	NS Moment Resisting Frame				NS Gravity Frames		
	COLUMNS		DOUBLER PLATES (in)	GIRDER	COLUMNS		BEAMS
Story/Floor	Exterior	Interior			Below penthouse	Others	
-1/1	W14X370	W14X500	0,0	W36X150	W14X211	W14X193	W18X35
1/2	W14X370	W14X500	0,0	W36X150	W14X211	W14X193	W16X26
2/3	W14X370, W14X370	W14X500, W14X455	0,0	W36X150	W14X211, W14X159	W14X193, W14X145	W16X26
3/4	W14X370	W14X455	0,0	W33X141	W14X159	W14X145	W16X26
4/5	W14X370, W14X283	W14X455, W14X370	0,0	W33X141	W14X159, W14X120	W14X145, W14X109	W16X26
5/6	W14X283	W14X370	0,0	W33X141	W14X120	W14X109	W16X26
6/7	W14X283, W14X257	W14X370, W14X283	0,1/2	W33X130	W14X120, W14X90	W14X109, W14X82	W16X26
7/8	W14X257	W14X283	0,0	W27X102	W14X90	W14X82	W16X26
8/9	W14X257, W14X233	W14X283, W14X257	0,1/2	W27X94	W14X90, W14X61	W14X82, W14X48	W16X26
9/Roof	W14X233	W14X257	0,0	W24X62	W14X61	W14X48	W14X22

20-story Building	NS Moment Resisting Frame				NS Gravity Frames		
	COLUMNS		DOUBLER PLATES (in)	GIRDER	COLUMNS	BEAMS	
Story/Floor	Exterior	Interior			Below penthouse	40 feet span	20 feet span
-2/-1	15X15X2.00	W24X335	0,0	W14X22	W14X550	W21X50	W14X22
-1/1	15X15X2.00	W24X335	0,0	W30X99	W14X550	W24X68	W16X26
1/2	15X15X2.00	W24X335	0,0	W30X99	W14X550	W21X50	W14X22
2/3	15X15X2.00, 15X15X1.25	W24X335, W24X335	0,0	W30X99	W14X550, W14X455	W21X50	W14X22
3/4	15X15X1.25	W24X335	0,0	W30X99	W14X455	W21X50	W14X22
4/5	15X15X1.25	W24X335	0,0	W30X99	W14X455	W21X50	W14X22
5/6	15X15X1.25, 15X15X1.00	W24X335, W24X229	0,0	W30X108	W14X455, W14X370	W21X50	W14X22
6/7	15X15X1.00	W24X229	0,0	W30X108	W14X370	W21X50	W14X22
7/8	15X15X1.00	W24X229	0,0	W30X108	W14X370	W21X50	W14X22
8/9	15X15X1.00, 15X15X1.00	W24X229, W24X229	0,0	W30X108	W14X370, W14X311	W21X50	W14X22
9/10	15X15X1.00	W24X229	0,0	W30X108	W14X311	W21X50	W14X22
10/11	15X15X1.00	W24X229	0,0	W30X108	W14X311	W21X50	W14X22
11/12	15X15X1.00, 15X15X1.00	W24X229, W24X192	0,0	W30X99	W14X311, W14X257	W21X50	W14X22
12/13	15X15X1.00	W24X192	0,0	W30X99	W14X257	W21X50	W14X22
13/14	15X15X1.00	W24X192	0,0	W30X99	W14X257	W21X50	W14X22
14/15	15X15X1.00, 15X15X0.75	W24X192, W24X131	0,5/8	W30X99	W14X257, W14X176	W21X50	W14X22
15/16	15X15X0.75	W24X131	0,5/8	W30X99	W14X176	W21X50	W14X22
16/17	15X15X0.75	W24X131	0,5/8	W30X99	W14X176	W21X50	W14X22
17/18	15X15X0.75, 15X15X0.75	W24X131, W24X117	0,5/8	W27X84	W14X176, W14X108	W21X50	W14X22
18/19	15X15X0.75	W24X117	0,5/8	W27X84	W14X108	W21X50	W14X22
19/20	15X15X0.75, 15X15X0.50	W24X117, W24X84	0,0	W24X62	W14X108	W21X50	W14X22
20/Roofs	15X15X0.50	W24X84	0,0	W21X50	W14X108, W14X43	W21X44	W12X16

The lateral load resisting system for all three frames is the perimeter moment resisting frames. The lateral resistant frames are shown with a bold line in Figure 4-1(a). All columns placed on perimeter frames bend about their strong axis. All beams located in the perimeter frame of the 9-story frame are connected to their adjacent columns using a rigid connection except the last beam, which is connected to the corner column using a pin connection to avoid bi-axial bending in the corner column. In the 20-story frame, all connections are rigid. The corner column, which has a box section, is designed for a bi-axial bending moment. In the 3-story frame, the moment resisting system consists of three bays in each side of the perimeter frames, as shown with bold lines in Figure 4-1(a). Gravity loads are transferred to the basement via gravity columns, which are located at the middle of the plan. The strong axis for the gravity columns is oriented in the North-South direction. The frames are designed to have a similar performance in both North-South and East-West directions. In this study, the N-S direction of the frame is modeled. Columns of the 3-story building are connected to the basement by using a rigid connection; while, the columns of the 9- and 20-story buildings are pin connected to the base plate. Dual Grade steel with a nominal yield stress of 50 ksi is used for both beam and column members. Moreover, the seismic mass of structures is summarized in Table 4.2. A more detailed report on design of these buildings is presented by Gupta 1999.

Table 4.2 Seismic mass for the SAC frames (All units are in kips-sec^2/ft.)

		Frames		
		3-story	9-story	20-story
Floors	**Floor 2**	65.53	69.04	38.63
	Middle Floors	65.53	67.86	37.76
	Roof	70.90	73.10	40.06

4.3. Type of Non-linear Models

In general, mathematical models for the simulation of non-linear frame components are categorized based on the degree of idealizations in the model. Figure 4.2, shows a schematic presentation of three common models for simulation of the component non-linearity.

Figure 4.2 (a) shows a detailed continuum finite element model, which explicitly simulates the nonlinear behavior of a component. The nonlinear component behavior is not enforced by a continuum model; nevertheless, the model is assumed capable of capturing the component nonlinearities using its associated constitutive material models explicitly during the analysis. For example, in a FEM model of a semi-rigid connection, the initial stiffness or yield moment of the connection is not enforced to the model; however, they are obtained from analysis.

On the other hand, Figure 4.2 (c) shows a lumped plasticity (concentrated hinge) model that is a complete phenomenological model. Concentrated hinge models are obtained from an experimental component tests. The phenomenological description of the force-deformation behavior of the components should be defined for a concentrated hinge model. For example, a plastic hinge might represent the moment-rotation behavior of a steel bolted connection with inelastic rules associated with the hysteretic test data of the connection.

The third category is the distributed inelasticity (fiber) model, which lies between the two aforementioned extremes. In fiber element models, some behavioral aspects are captured implicitly and some effects are captured explicitly. In distributed inelastic models, some behavior assumptions, such as plane sections remain plane, are dictated to the model; while some behaviors such as the uniaxial material behavior is explicitly modeled (ATC 72-2010).

The continuum and fiber models are very accurate for capturing some behaviors such as the initial stiffness and the yield force of a component; although, they might not precisely capture the strength degradation phenomena such as reinforcement buckling in a concrete beam. These models in practice need some calibrations based on experimental data.

The plastic hinge models can capture the strength losses in a more empirical manner. In addition, these models are more consistent with force and deformation limit states provided by codes.

In this study, the behavior of semi-rigid connections is obtained using calibrated continuum finite element models. More detailed modeling assumptions and techniques are presented in Chapter 6 of this dissertation.

Moreover, concentrated plasticity models are used for the simulation of the plastic hinges in beams and columns and for modeling of the semi-rigid connections in global structure models. Modeling of plastic hinges is described in detail in this chapter.

Physical ⟶ Phenomenological

(a)   (b)   (c)
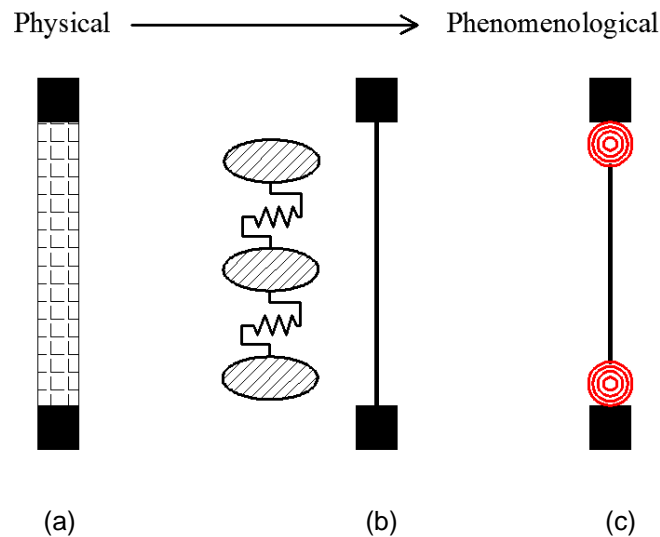
Figure 4.2 Comparison of the Nonlinear Model types (a) continuum FEM,
(b) Distributed inelasticity, and (c) concentrated hinge

4.4 Beams and Columns

As explained in the previous section, the concentrated plastic hinge model is adopted to introduce nonlinear behavior in beams with rigid connections, beams with semi-rigid connections, and columns of structures. Beams with rigid connections and columns, as shown

in Figure 4.3, are modeled as compound elements which consist of an elastic Bernoulli beam element at the middle confined by two plastic hinges and two end-zones that connects the member to the rigid connections. The assumption of the formation of plastic hinges at the two ends of beams and columns are adopted based on the hypothesis that the failure mechanism is governed by the seismic loading.
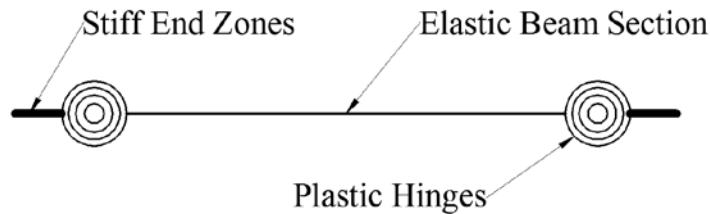
Figure4.3 Beam compound with stiff end zone and plastic hinges

Non-linear behavior is introduced to the compound element explained above by introducing non-linear moment-rotation behavior of the plastic hinges. Other components of the compound including elastic beam elements and stiff end zones are assumed elastic. Thus, the definition of the backbone curve of plastic hinge components, plays an essential role in the behavior of the frame members and consequently in the overall behavior of the frame. Different material models for simulation of plastic hinges are explained in detail in the following sections.

The semi-rigid beam compounds, as shown in Figure 4.4, are defined by replacing the two stiff end zones by two non-linear moment-rotation semi-rigid hinge in the rigid beam compounds. In this configuration, plastic hinges and semi-rigid connections are both sources of nonlinearity. However, since the plastic moment of semi-rigid connections are usually much smaller than the plastic moment of beam sections, the behavior of the beam compound is governed by the behavior of the semi rigid connections. In fact, the moment demand in beams cannot exceed the plastic moment of the semi-rigid connections; therefore, it will not reach the plastic moment of the beam section.
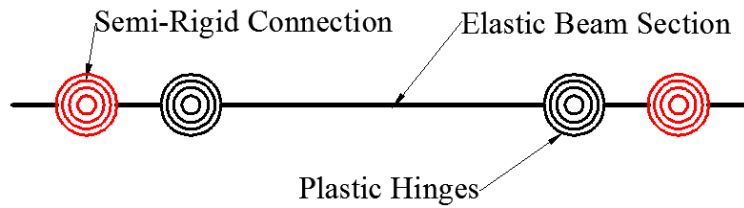
Figure 4.4 Beam compound with semi-rigid connections and plastic hinges

4.5. Bi-linear Backbone Curve with Strength Degradations

The nonlinear behavior of plastic hinges is commonly expressed by presenting their moment-rotation backbone-curves. The backbone curve is a force-deformation relation, which bounds the region where the force-deformation hysteresis loops of components are confined. If no deterioration occurs, the backbone curve is close to the monotonic loading and is referred to the initial backbone curve. On the other hand, if the cyclic deterioration occurs, the branches of the backbone curve move toward the origin. The updated backbone curve, which is a function of loading, is referred to the cyclic backbone curve. An example of the initial and cyclic backbone curve for a semi-rigid connection (Tremblay 1997) is shown in Figure 4.5.
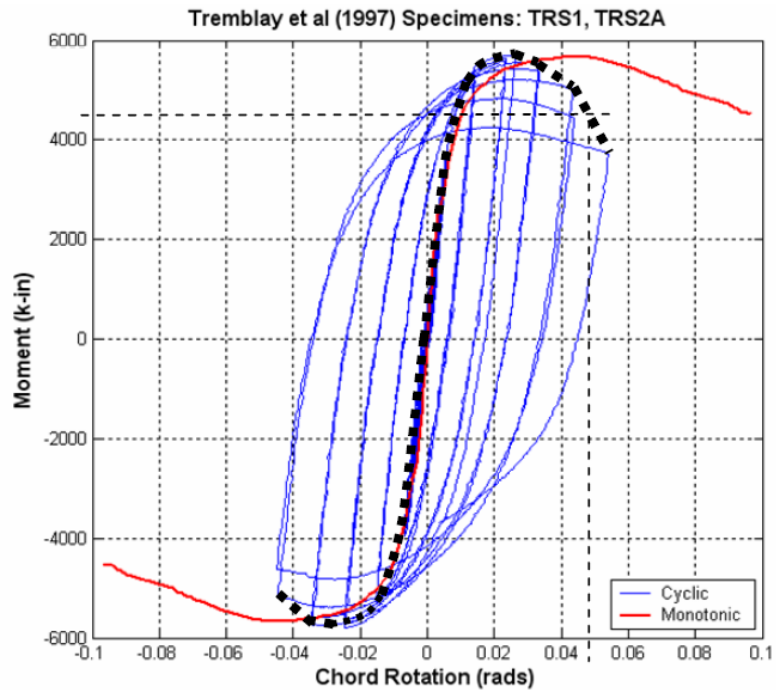
Figure 4.5 Monotonic and Cyclic backbone curve fitted to two identical beam sections
(Trembly 1997)

The key parameters for introducing a backbone curve for a concentrated plastic hinge model can be categorized in parameters such as stiffness, strength, and deformation. Stiffness parameters include pre-yielding stiffness (elastic, K_e), post yielding stiffness (hardening/softening, K_p), and post-capping stiffness (degradation, K_{pc}). Post yielding stiffness is commonly expressed as a fraction of the elastic stiffness. The key strength parameters are the yield strength (M_y), maximum strength (M_c), and the residual strength (M_r). Finally, the key deformation parameters are the deformations associated with the key strength parameters including the yield deformation (θ_y), capping deformation (θ_c), and the ultimate deformation (θ_u). A schematic presentation of the backbone curve is illustrated in Figure 4-6.

The cyclic deterioration in frame components should also be incorporated in backbone curve definition. Deterioration in steel frame members could happen due to local buckling of the flange or web, lateral torsional buckling, or ductile tearing of members. Moreover, other

60

phenomena such as bolt slippage or local plate bending may cause cyclic deterioration in connections' behavior. The effects of these deteriorations may appear in the backbone curve in different modes of basic strength degradation, capping strength degradation, unloading stiffness degradation, and accelerated reloading degradation.

In this study, the backbone curve for different beam and column members are constructed based on the beam deterioration modeling guideline provided in ATC72 (2010).

Eff. yield strength and rotation (M_y & θ_y)
Eff. elastic stiffness, $K_e = M_y/\theta_y$
Capping strength and rotation (M_c and θ_c)
Pre-capping plastic rotation, θ_p
Eff. post-yield tangent stiffness, $K_p = (M_c-M_y)/\theta_p$
Post-capping rotation range, θ_{pc}
Eff. post-capping tangent stiffness, $K_{pc} = M_c/\theta_{pc}$
Residual strength, $M_r = \kappa M_y$
Ultimate rotation, θ_u
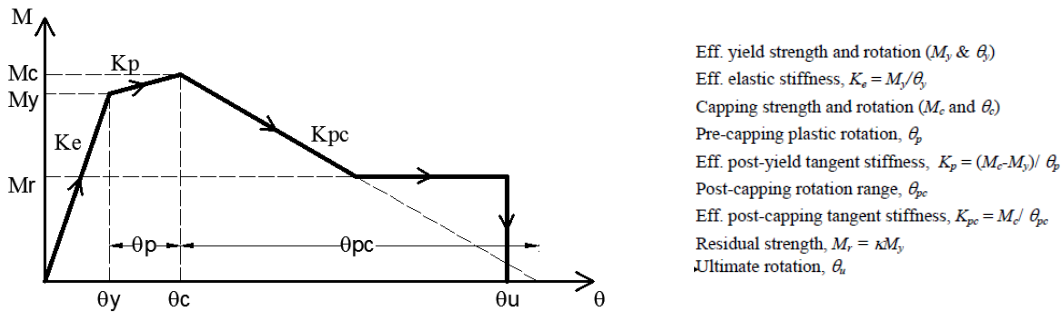
Figure 4.6 Parameters of the monotonic backbone curve of the modified Ibarra-Krawinkler model

A bilinear backbone curve with strength degradation similar to Figure 4-6 is used for modeling the concentrated plastic hinge behavior in beams and columns. The cyclic deterioration rules developed by Ibarra et al.(2005) and modified by Lignos and krawinkler (2009), which is presented in the ATC-72 (2010), is used for the calculations of the key parameters of plastic hinges' backbone curves.

These rules are presented in terms of empirical equations based on regression analysis on more than 300 steel component tests (Lignos and Krawinkler, 2007; Lignos and Krawinkler, 2009) that accounts for the geometric and material properties of the frame sections. This set of equations are derived for the modeling parameters of pre-capping plastic rotation (θ_p), post-capping rotation range (θ_{pc}), and the deterioration parameter (Λ). The definition of the two former parameters is shown in Figure 4-6. The reference cumulative plastic rotation parameter (Λ) is expressed as $E_t = \Lambda M_y$, with $\Lambda = \lambda\theta_p$ denoting the cumulative plastic rotation capacity.

Using these three parameters, the basic and post-capping strength deterioration, and the un-

loading stiffness deterioration are modeled. The equations presented in ATC72 (2010) are as

follow:

$$\theta_p = 0.087 \left(\frac{h}{t_w}\right)^{-0.365} \left(\frac{b_f}{2.t_f}\right)^{-0.14} \left(\frac{L}{d}\right)^{0.34} \left(\frac{d}{c_{unit}^1.21"}\right)^{-0.721} \left(\frac{c_{unit}^2 F_y}{50}\right)^{-0.23}$$ Equation 4.1

$$\theta_{pc} = 5.70 \left(\frac{h}{t_w}\right)^{-0.565} \left(\frac{b_f}{2.t_f}\right)^{-0.80} \left(\frac{d}{c_{unit}^1.21"}\right)^{-0.28} \left(\frac{c_{unit}^2 F_y}{50}\right)^{-0.43}$$ Equation 4.2

$$\Lambda = \frac{E_t}{M_y} = 500 \left(\frac{h}{t_w}\right)^{-1.34} \left(\frac{b_f}{2.t_f}\right)^{-0.595} \left(\frac{c_{unit}^2 F_y}{50}\right)^{-0.36}$$ Equation 4.3

where the parameters are defined as:

h/t_w = ratio of fillet-to-fillet depth to web thickness.

$b_f/2.t_f$ = ratio of flange width to thickness.

L/d= ratio of shear span to depth

d = depth of beam.

F_y= yield strength of the flange in ksi.

c_{unit}^1= (and c_{unit}^2) coefficients for units conversion. If d is in meters and F_y is in MPa,

c_{unit}^1=0.0254 and c_{unit}^2= 0.145. Both coefficients are 1.0 if inches and ksi are used.

The plastic hinge parameters for the beams used in this study are summarized in

Table 4-3.

Table4.3 Parameters used for modeling plastic hinges in beams

Section Name	θy	θp	θpc	My	Mu	Mr	Λ
W21X50	0.001272	0.031515	0.144247	6050	6655	2420	0.911012
W24X117	0.001051	0.02862	0.13431	17985	19783.5	7194	1.121186
W24X131	0.001047	0.029932	0.154909	20350	22385	8140	1.363264
W24X192	0.001016	0.034268	0.251071	30745	33819.5	12298	2.574784
W24X229	0.001004	0.036778	0.312908	37125	40837.5	14850	3.56026
W24X335	0.000975	0.04223	0.492401	56100	61710	22440	7.046369
W24X62	0.001123	0.027519	0.141778	8415	9256.5	3366	0.925926
W24X84	0.001076	0.028159	0.150593	12320	13552	4928	1.054636
W27X102	0.000959	0.024417	0.139434	16775	18452.5	6710	0.985227
W27X84	0.000974	0.022837	0.106695	13420	14762	5368	0.725497
W27X94	0.000967	0.022909	0.124601	15290	16819	6116	0.864289
W30X108	0.000881	0.021128	0.117753	19030	20933	7612	0.840001
W30X116	0.000872	0.021641	0.131185	20790	22869	8316	0.942266
W30X99	0.00089	0.020455	0.103769	17160	18876	6864	0.731785
W33X130	0.000792	0.018695	0.113615	25685	28253.5	10274	0.79902
W33X141	0.000785	0.019212	0.127438	28270	31097	11308	0.905832
W36X150	0.000731	0.017204	0.115387	31955	35150.5	12782	0.817314

Besides, other parameters for introducing the backbone curve are selected based on the suggested values in ATC72 (2010). These parameters include:

1- A value of My =1.1Mp is recommended for the effective yield strength. In which Mp, plastic moment of section, equals ZFy. Z is the plastic modulus of the section and Fy=55 ksi is the expected flange yield stress in this study.

2- A value of Mc= 1.1My is recommended for the capping-strength of the backbone curve.

3- The strength of steel members with deterioration behavior is typically stabilized in large deformations. A value of residual strength, Mr, equal to 0.4Mu is considered for frame members.

4- The ultimate rotation, θ_u=0.2 rad, is considered based on the suggested value by Zareian et al. (2010).

4.6. Panel Zone

When bending moment transfers from beams to columns in steel moment resisting frames, the connection panel zone is subjected to shear stresses. These stresses may cause shear deformation in panel zones which increases the story drifts at the frame stories. In this study, the shear deformation of the panel zones is simulated based on the mathematical model proposed by Krawinkler (1978) and presented in FEMA 355c. The tri-linear shear force-shear deformation of this model is presented in Figure 4.7.

The connection panel zone is modeled utilizing 8 rigid links, as shown in Figure 4.8, which are connected with hinges at three corners and with two bi-linear rotational springs in the fourth corner. The 8 links create a configuration that deforms in a parallelogram shape. The two rotational springs simulate a tri-linear rotational behavior. Deterioration in the material properties of the panel zone is not considered. Figure 4.9, shows how the tri-linear curve is constructed by combining two bilinear springs.
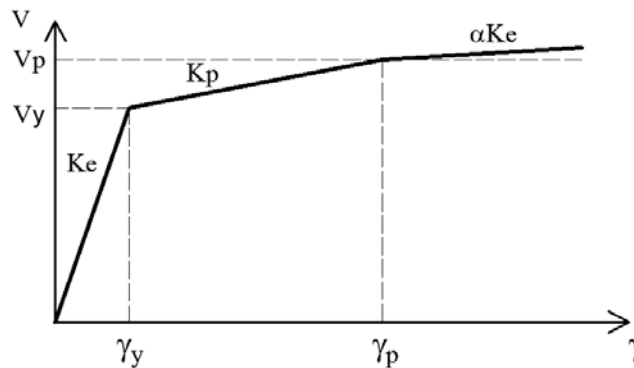
Figure 4.7 Tri-linear shear force-shear distortion relationship for panel zone
(Krawinkler 1978)
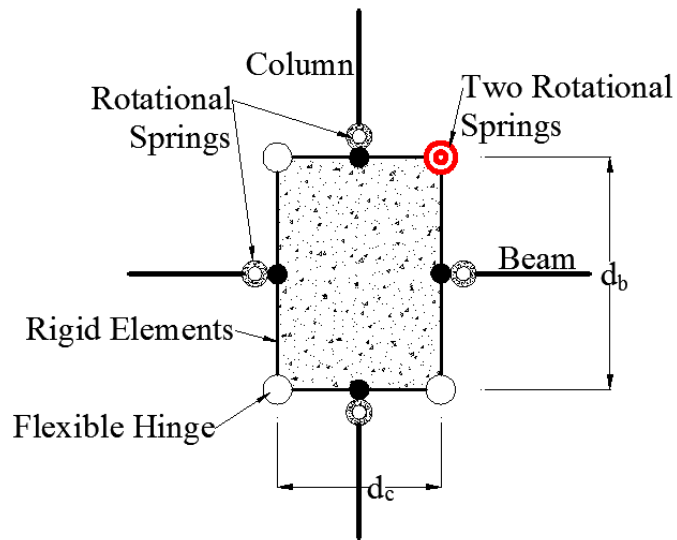
Figure 4.8 Analytical Model for Panel Zone (Gupta and Krawinkler 1999)
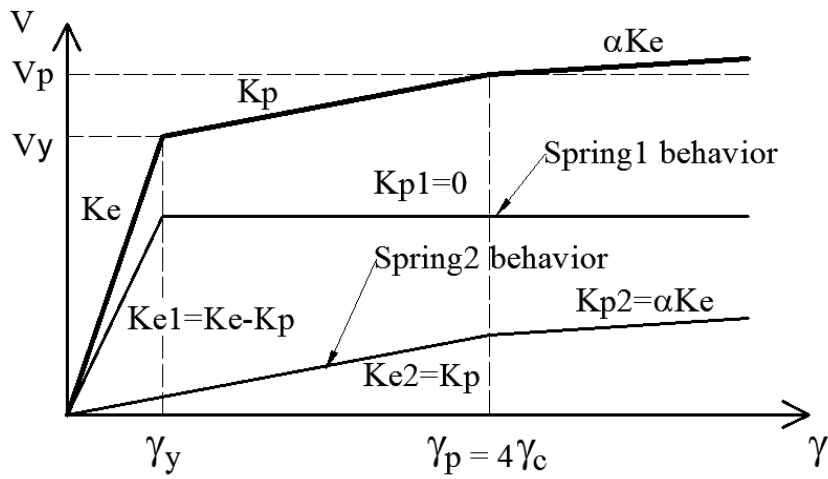
Figure 4.9 Use of two springs to model trilinear behavior
(Gupta and Krawinkler, 1999)

Mechanical properties of panel zones are determined by using following equations.

$$V_y = \frac{F_y}{\sqrt{3}} A_{eff} = \frac{F_y}{\sqrt{3}} \left(0.95 d_c t_p\right) \approx 0.55 F_y d_c t_p$$

$$\gamma_y = \frac{F_y}{\sqrt{3}G}$$

$$K_e = \frac{V_y}{\gamma_y} = 0.95 d_c t_p G$$

$$V_p = V_y \left(1 + \frac{3K_p}{K_e}\right) \approx 0.55 F_y d_c t_p \left(1 + \frac{3 b_c t_{cf}^2}{d_b d_c t_p}\right)$$

where,

V_y = the panel zone shear yield strength.

F_y = the yield strength of the material

A_{eff} = the effective shear area

d_c = the depth of the column

t_p = the thickness of the web including any doubler plates.

γ_y = yield distortion

K_e = elastic stiffness of the panel zone.

G = the shear modulus of the column material

V_p = the full plastic shear resistance of the joint

b_c = the width of the column flange

t_{cf} = the thickness of the column flange

4.7. Gravity Columns Modeling and P-Delta Effects

The P-Δ effects is caused by applying the gravity force on the deformed configuration of structures. The SAC buildings, moment resistant frames are located in the perimeter of the structure while gravity loads are carried by interior frames. Since moment resistant frames were modeled and analyzed in 2 dimensions, the effect of gravity load should have been taken into account for an accurate P-Δ analysis. For this purpose, gravity columns were modeled as a continuous column adjacent to the last column of the frame. The lateral displacement of the nodes on gravity columns is mathematically constrained to the lateral displacement of other nodes in each story; thus, the gravity columns follow the deflected shape of the frames. Moreover, the P-δ effect which reduces the bending moment capacity in members under compression is considered in the columns' formulation.

4.8. Seismic Loadings

The SAC earthquake records for Los Angeles site, presented by Somerville et al. (1997), were used in this study. These records are consisted of two sets of records of LA01 to LA20 which are categorized as those with 10% probabilities of exceedance in 50 years (DBE) while LA21 to LA40 are listed as records with 2% probabilities of exceedance in 50 years (MCE). These records consist of a series of real earthquakes, which have been scaled for the Los Angeles site, in addition to some simulated earthquakes to cover a wide range of frequencies that are able to excite frames with a variety of heights and structural systems. These records were applied to all low-rise, mid-rise, and high-rise steel frames without scaling. The basic characteristics of the Los-Angeles ground motion records for (DBE) and (MCE) records are presented in Tables 4.4 and 4.5, respectively. The pseudo acceleration spectra with 5% damping for the DBE and MCE records are also shown in Figures 4.10 and 4.11, respectively.

Table 4.4 The basic characteristics of the Los-Angeles ground motion records for DBE Records

10/50 Set of Records (475 years Return Period)						
Designation	Record Information	Duration (sec.)	Magnitude Mw	R (km)	Scale	PGA (in/sec^2)
LA01	Imperial Valley, 1940	39.38	6.9	10.0	2.01	178.0
LA02	Imperial Valley, 1940	39.38	6.9	10.0	2.01	261.0
LA03	Imperial Valley, 1979	39.38	6.5	4.1	1.01	152.0
LA04	Imperial Valley, 1979	39.38	6.5	4.1	1.01	188.4
LA05	Imperial Valley, 1979	39.38	6.5	1.2	0.84	116.4
LA06	Imperial Valley, 1979	39.38	6.5	1.2	0.84	90.6
LA07	Landers, 1992	79.98	7.3	36.0	3.20	162.6
LA08	Landers, 1992	79.98	7.3	36.0	3.20	164.4
LA09	Landers, 1992	79.98	7.3	25.0	2.17	200.7
LA10	Landers, 1992	79.98	7.3	25.0	2.17	139.1
LA11	Loma Prieta, 1989	39.98	7.0	12.4	1.79	256.9
LA12	Loma Prieta, 1989	39.98	7.0	12.4	1.79	374.4
LA13	Northridge, 1994, Newhall	59.98	6.7	6.7	1.03	261.8
LA14	Northridge, 1994, Newhall	59.98	6.7	6.7	1.03	253.7
LA15	Northridge, 1994, Rinaldi	14.95	6.7	7.5	0.79	206.0
LA16	Northridge, 1994, Rinaldi	14.95	6.7	7.5	0.79	223.9
LA17	Northridge, 1994, Sylmar	59.98	6.7	6.4	0.99	219.9
LA18	Northridge, 1994, Sylmar	59.98	6.7	6.4	0.99	315.5
LA19	North Palm Springs, 1986	59.98	6.0	6.7	2.97	393.5
LA20	North Palm Springs, 1986	59.98	6.0	6.7	2.97	380.9
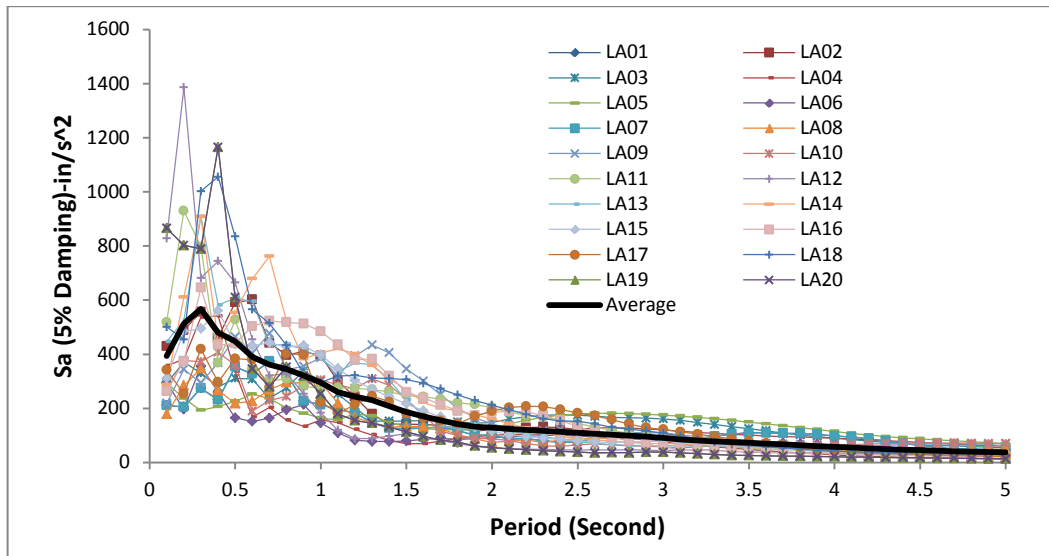
Figure 4.10 The pseudo acceleration spectra with 5% damping for the DBE records

Table 4.5 The basic characteristics of the Los-Angeles ground motion records for MCE Records

2/50 Set of Records (2475 years Return Period)						
Designation	Record Information	Duration (sec.)	Magnitude Mw	R (km)	Scale	PGA (in/sec^2)
LA21	Kobe, 1995	59.98	6.9	3.4	1.15	495.3
LA22	Kobe, 1995	59.98	6.9	3.4	1.15	355.4
LA23	Loma Prieta, 1989	24.99	7.0	3.5	0.82	161.4
LA24	Loma Prieta, 1989	24.99	7.0	3.5	0.82	182.6
LA25	Northridge, 1994	14.95	6.7	7.5	1.29	335.3
LA26	Northridge, 1994	14.95	6.7	7.5	1.29	364.3
LA27	Northridge, 1994	59.98	6.7	6.4	1.61	357.8
LA28	Northridge, 1994	59.98	6.7	6.4	1.61	513.4
LA29	Tabas, 1974	49.98	7.4	1.2	1.08	312.4
LA30	Tabas, 1974	49.98	7.4	1.2	1.08	382.9
LA31	Elysian Park (Simulated)	29.99	7.1	17.5	1.43	500.5
LA32	Elysian Park (Simulated)	29.99	7.1	17.5	1.43	458.1
LA33	Elysian Park (Simulated)	29.99	7.1	10.7	0.97	302.1
LA34	Elysian Park (Simulated)	29.99	7.1	10.7	0.97	262.8
LA35	Elysian Park (Simulated)	29.99	7.1	11.2	1.10	383.1
LA36	Elysian Park (Simulated)	29.99	7.1	11.2	1.10	424.9
LA37	Palos Verdes (Simulated)	59.98	7.1	1.5	0.90	274.7
LA38	Palos Verdes (Simulated)	59.98	7.1	1.5	0.90	299.7
LA39	Palos Verdes (Simulated)	59.98	7.1	1.5	0.88	193.1
LA40	Palos Verdes (Simulated)	59.98	7.1	1.5	0.88	241.4
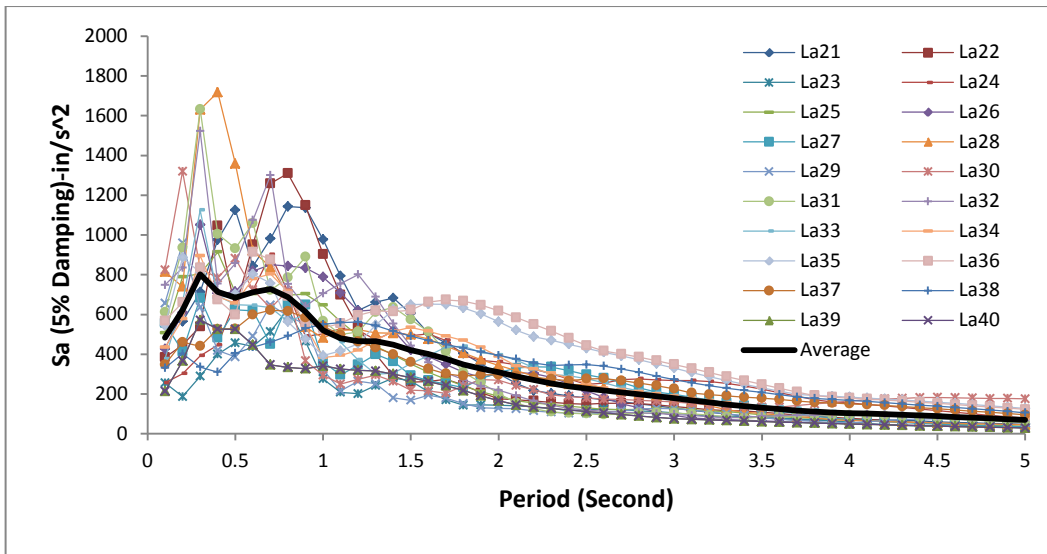
Figure 4.11 The pseudo acceleration spectra with 5% damping for the MCE records

4.9. Acceptance Criteria

Acceptance criteria for structural members are adopted from the ASCE-41 standard in order to assess the structural elements' performance. Hybrid and rigid frames in this study are evaluated by using two different acceptance criteria of Life Safety (LS) in Design Base Earthquakes (DBE) and Collapse Prevention (CP) in Maximum Credible Earthquakes (MCE). Moreover, the inter-story drift limits are considered to be 2.5% and 5% for LS and CP criteria, respectively. Structural collapse is also defined by plastic hinge formation of all columns in two different given stories.

CHAPTER 5

HYBRID FRAME PATTERNS

In this Chapter, first, the effects of semi-rigid connections on local and global responses of the hybrid frame under static and seismic loading are explained. Then, using these effects, three different approaches on selection of the semi-rigid connections are adopted. Five different patterns of semi-rigid connections are applied to the 20-story frame using the presented hypotheses and two of the most effective patterns are selected. The effective patterns on this basis are then applied to the 3- and 9-Story frames. Finally, the optimized connection stiffness is identified by performing a sensitivity study on the initial stiffness and post-yield stiffness of semi-rigid connections.

<u>5.1. Global and Local Effects of the Semi-rigid Connections on Structures</u>

Local and global effects of semi-rigid connection on hybrid frames are investigated in primary studies on 3- and 20-story rigid and hybrid frames. Results are as follows.

5.1.1. Moment Redistribution/Act as a Fuse

Since semi-rigid connections are modeled as rotational springs, they may change the distribution of moments between beams and columns. Moreover, the plastic moment of semi-rigid connections is generally less than the plastic moment in their adjacent frame members (beams/columns); thus, the moment cannot exceed the plastic moment of the connection and formation of plastic hinges in the adjacent structural members will be avoided.

Frame (a):

| -10630 | -10594 | -10601 | -10601 | -10594 | -10629 |

10630 · 21195 · 21195 · 10629

7484 · 17133 · 17132 · 7482

| -23039 | -22963 | -22980 | -22980 | -22962 | -23037 |

15554 · 28811 · 28810 · 15556

12326 · 26729 · 26728 · 12334

| -25575 | -25402 | -25411 | -25411 | -25402 | -25576 |

13249 · 24084 · 24085 · 13242

23709 · 30084 · 30085 · 23675

(a)

Frame (b):

| -1669 | -1605 | -10826 | -10732 | -10724 | -10817 |

1669 · 12431 · 21456 · 10817

7733 · 8374 · 12503 · 12333

| -23239 | -23450 | -1662 | -1659 | -23441 | -23215 |

15505 · 16737 · 12598 · 10882

18364 · 30083 · 19342 · 5522

| -25358 | -25042 | -25069 | -25468 | -1602 | -1681 |

6994 · 20028 · 7729 · -3840.7

23901 · 29983 · 30138 · 24063

(b)

Figure 5.1 Bending moment demands at global drift of 3% (kip-in)
(a) moment in fully rigid frame and (b) moment in hybrid frame

To study the effects of semi-rigid connections on moment redistribution, a pushover analysis is performed on a 3-story hybrid and the 3-story rigid frames. Moment demands of the fully rigid 3-story frame and its corresponding hybrid frame at roof drift of 3% are illustrated in Figures 5.1-a and 5.1-b, respectively. Semi-rigid connections of the hybrid frame are located on an inclined pattern as shown in Figure 5.1-b. Moment demands of the beams and columns adjacent to the semi-rigid connections in the hybrid frame are noticeably less than the moment demands on the corresponding rigid frame members, as shown in Figure 5.1. For example, the

moment of the beam and column located in the first span (from the left) of the third floor of the hybrid frame equals to 1669 kip-in while the moment demand on the corresponding members of the rigid frame equals 10630 kip-in. Indeed, in this case, the semi-connection acts like a fuse to prevent yielding of the adjacent beam and column.

This finding can be used in the design pattern selection to save columns in selected areas and control the structural stability.

5.1.2. Shifting Structures' Period and Changing their Mode Shapes

SAC 20-story rigid frame and HSAC20-5 frame (Figure 5.7.e) are used for this part of study. The mode shapes are identified for each time step increment during the solution of equation of motion by updating the system stiffness matrices for both the nonlinear semi-rigid connection elements and the beam column elements in addition to updating the nonlinearity due to geometry. A comprehensive flowchart and results of this study is presented in Chapter 8 of this presentation.

As an example, Figure 5.2a and Figure 5.2b show how the first mode period and its corresponding mode shape for the SAC 20-story frame change during the LA-35 (Elysian Park) ground motion. A comparison of the first mode period variation is shown in Figure 5.2b in which the maximum first period of structure is decreased by 30% in HSAC20-5, which in turn shows that the SAC rigid frame subjected to LA35 record, will behave more flexible than the hybrid SAC Model#3 frame. The same conclusion can be made by looking at the variation of the first mode shape during the earthquake in Figure 5.3 where in t=14.5 s, a higher modal stiffness in the hybrid frame is observed.

On the other hand, a semi-rigid connection may be used to shift the natural frequency of structure and to avoid resonance for a particular series of ground motions.

(a)

(b)
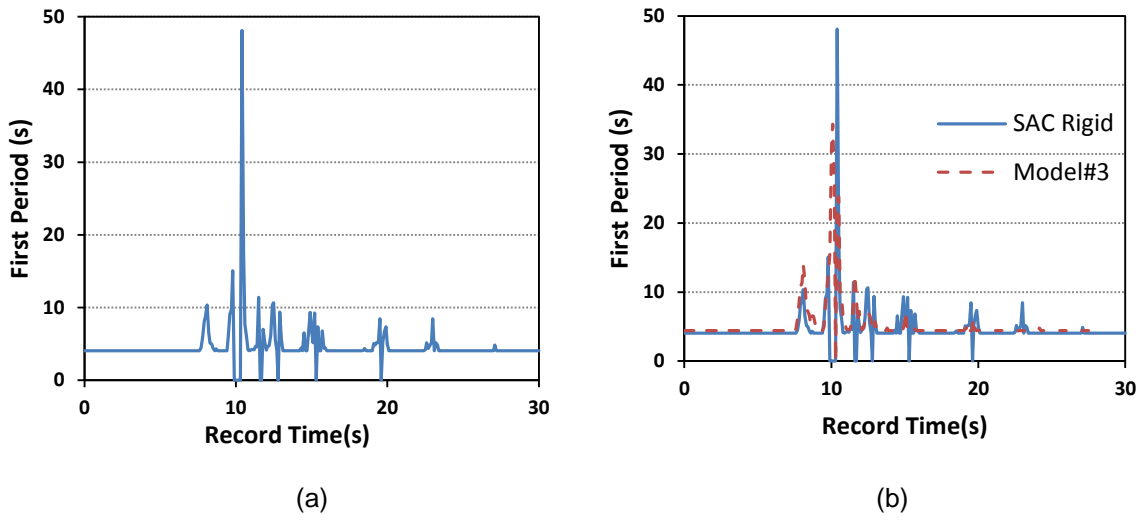
Figure 5.2 Variation of the first mode period of the L.A. SAC 20-Story and the Hybrid Model#3 frames during LA35 record excitation (a) SAC frame and (b) comparison

(a)

(b)
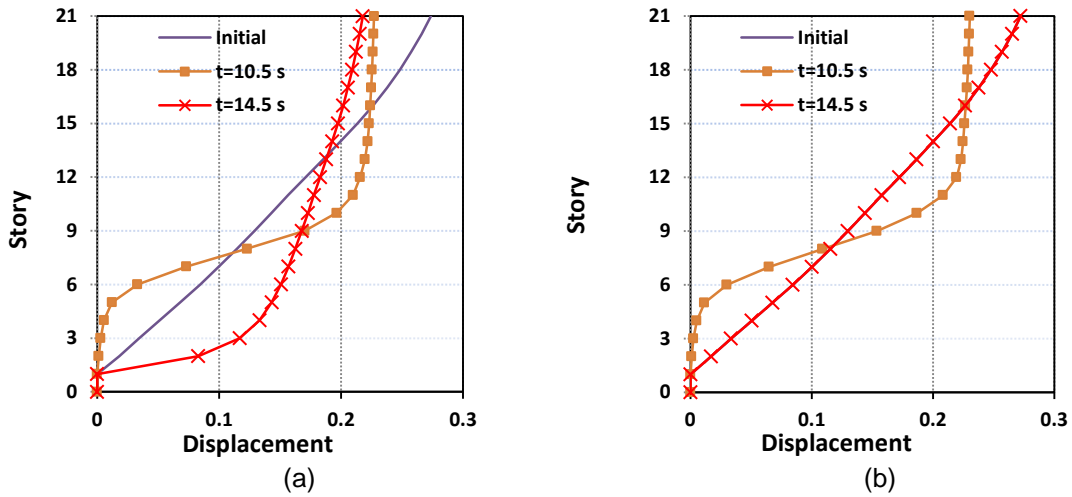
Figure 5.3 Variation of the first mode shape of the L.A. SAC 20-Story and the Hybrid Model#3 frames during LA35 record excitation (a) SAC frame and (b) hybrid frame

5.1.3. Decrease in Base Shear

As explained in the previous section, using semi-rigid connections in a steel frame increases the frame's period; therefore, considering the shape of the design spectra, the frame experiences a lesser amount of acceleration. For example, for the schematic design spectrum graph shown in the Figure 5.4, increasing the period of the structures from t_1 to t_2, decreases

the acceleration seen by the frame from Sa (t_1) to Sa (t_2). However, since using semi-rigid connection will reduce the system's stiffness, the optimum number and properties of semi-rigid connections should be determined to find the minimum base shear, which still satisfies the inter-story drift limits.
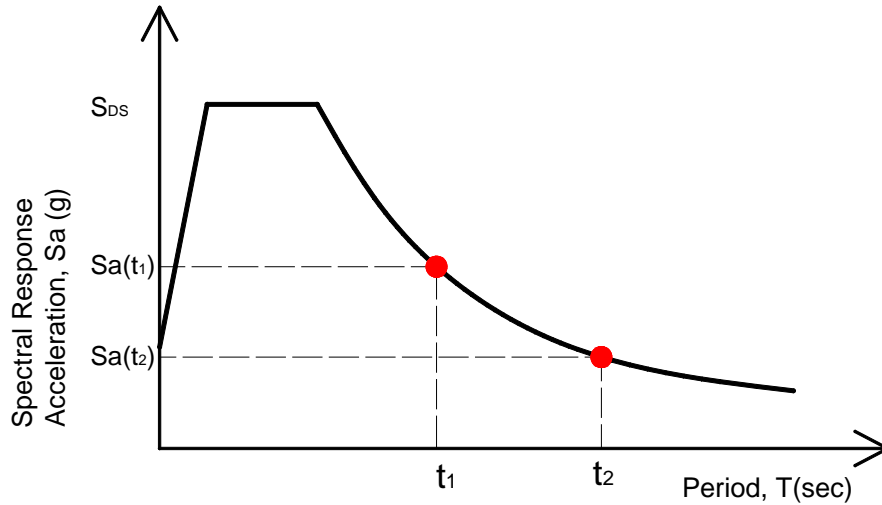
Figure 5.4 Schematic presentation of the Design Response Spectrum (ASCE 7-05)

5.1.4. Decrease Static Stiffness/Strength

Hybrid frames are obtained by replacing a selection of fully rigid connections with more flexible semi-rigid connections; consequently, a more flexible stiffness matrix for hybrid frames is expected. The hybrid and fully rigid three-story three-bay steel frames of Figure 5.1 are analyzed using a nonlinear static analysis up to roof drift of 10 percent. As shown in Figure 5.5, both initial stiffness and base shear are decreased in the hybrid frame. In this study, the NEHRP 1997 predefined pushover load pattern was used. Pushover analysis is able to identify the inelastic behavior and capacity of structures, which respond primarily to the first mode shape.
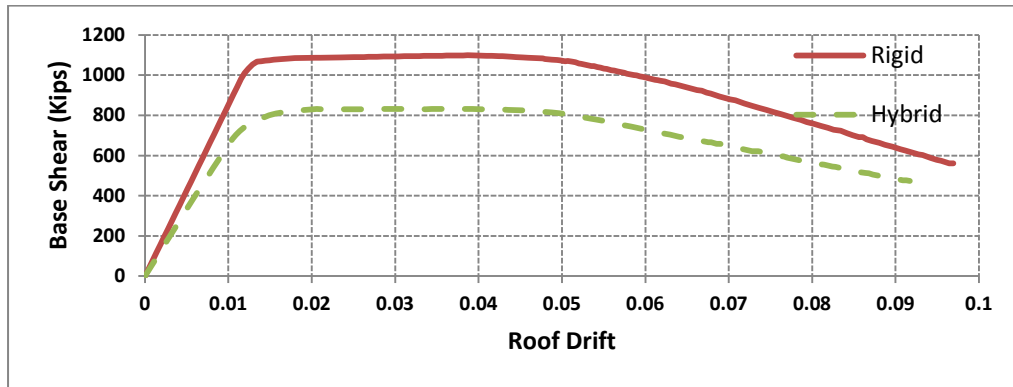
Figure 5.5 Pushover analysis results for hybrid and rigid 3-story 3-bay frames

.

5.1.5. Member Forces

To study the effects of utilizing the semi-rigid connections on the bending moment demands of frames, the bending moment demands of proposed HSAC20-5 frame and 20-story SAC frame are compared. The ratios of the absolute value of maximum forces for the hybrid frame were normalized with respect to the forces of the SAC frame. Thus, a ratio of unity indicates that the Hybrid frame forces are equal to the SAC forces, and the ratio of less than unity implies a reduction in a given force for the hybrid frame (lower demand).

Figures 5.6.a and 5.6.b show the ratios of the beam moment and column moment for the Hybrid frame versus the SAC frame, respectively, for each floor of the 20-story frame. The dashed lines indicate the unity ratio. The average of the ratios for bending moment of beams and columns end moments are 0.81 and 0.87, respectively.

There is one scattered point in the beams' bending moment demand ratio graph in each story, which corresponds to the semi-rigid beam in that story. The bending moment demands are noticeably reduced in these beams as expected.

(a) (b)
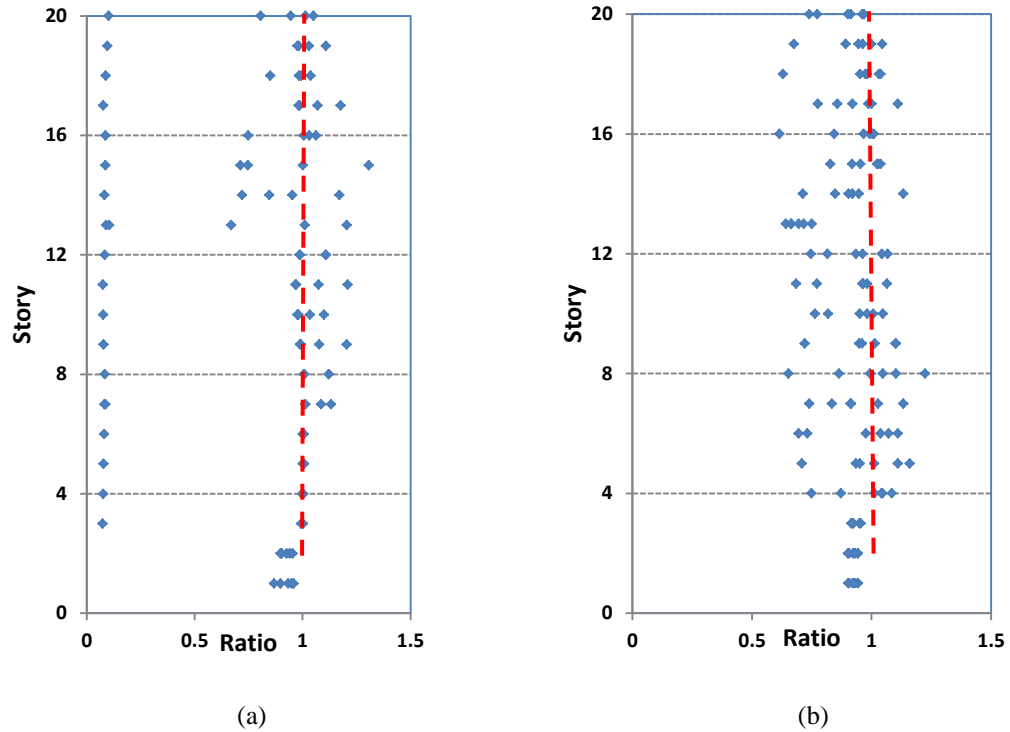
Figure 5.6 Hybrid/Rigid Bending Moment demands Ratio (a) beams and (b) columns

<u>5.2. Hypotheses on Semi-rigid Connection Pattern Selection</u>

Based on the aforementioned effects of the semi-rigid connections on the response of steel moment frames, three different approaches are utilized for the placement of semi-rigid connection in the 20-story hybrid frame.

The first approach, as explained in Chapter 1, is based on introducing a rotational spring at five middle stories of the frame. This approach will be utilized by replacing rigid connections with flexible semi-rigid connections in stories 9 to 13 as shown in Figure 5.7.a. The newly formed springs may help to decouple the earthquake acceleration into two mode shapes as it was shown in Figure 1.3. Although the performance of this system was tested with initial linear models in Chapter 3, in this chapter, the pattern will be tested using a comprehensive nonlinear model.

The second approach is based on the energy dissipation properties of the semi-rigid connections. In nonlinear models used in this study, as described in chapter 4, the seismic inelastic energy dissipation comes from two sources of plastic hinges in beams and columns and from the semi-rigid connections. The amount of the energy dissipated in each plastic hinge or semi-rigid connection is found by calculating the area confined by the outer loop of the moment-rotation hysteresis loop. Figure 5.8, shows the location and amount of energy dissipated in the plastic hinges of the SAC 20-story frame subjected to the LA35 ground motion. As shown in this figure, beams and columns located in stories 1 to 5 have the most contribution in the total inelastic energy dissipation. On the other hand, structural members of stories 6 to 20 are mostly remain elastic and have no contribution in the inelastic energy dissipation. Analysis result of the 20-story frame under other ground motions has commonly followed the same pattern of energy dissipation propagation over the height of frame. In the second approach, semi-rigid connections are placed in the beams, which are remained elastic. Thus, they could contribute in the energy dissipation of the beam. This approach resulted in two patterns of HSAC20-2 and HSAC20-3 as shown in Figures 5.7 b and 5.7 c, respectively. The former pattern has more energy dissipative members; however, the system is softer. Nevertheless, HSAC20-2 frame experienced less acceleration since it is softer and consequently has a larger period.

The last approach is based on maintaining stability of the structure under strong ground motions. Collapse occurs when plastic hinges form in all columns of two different stories. Semi-rigid connections, as explained in section 5.1.1 of this dissertation, might be used as a fuse to protect their adjacent columns. This approach aims to protect at least one column in each story level. Using this approach, two patterns of HSAC20-4 and HSAC20-5, as shown in Figures 5.7.d and 5.7.e, are proposed.
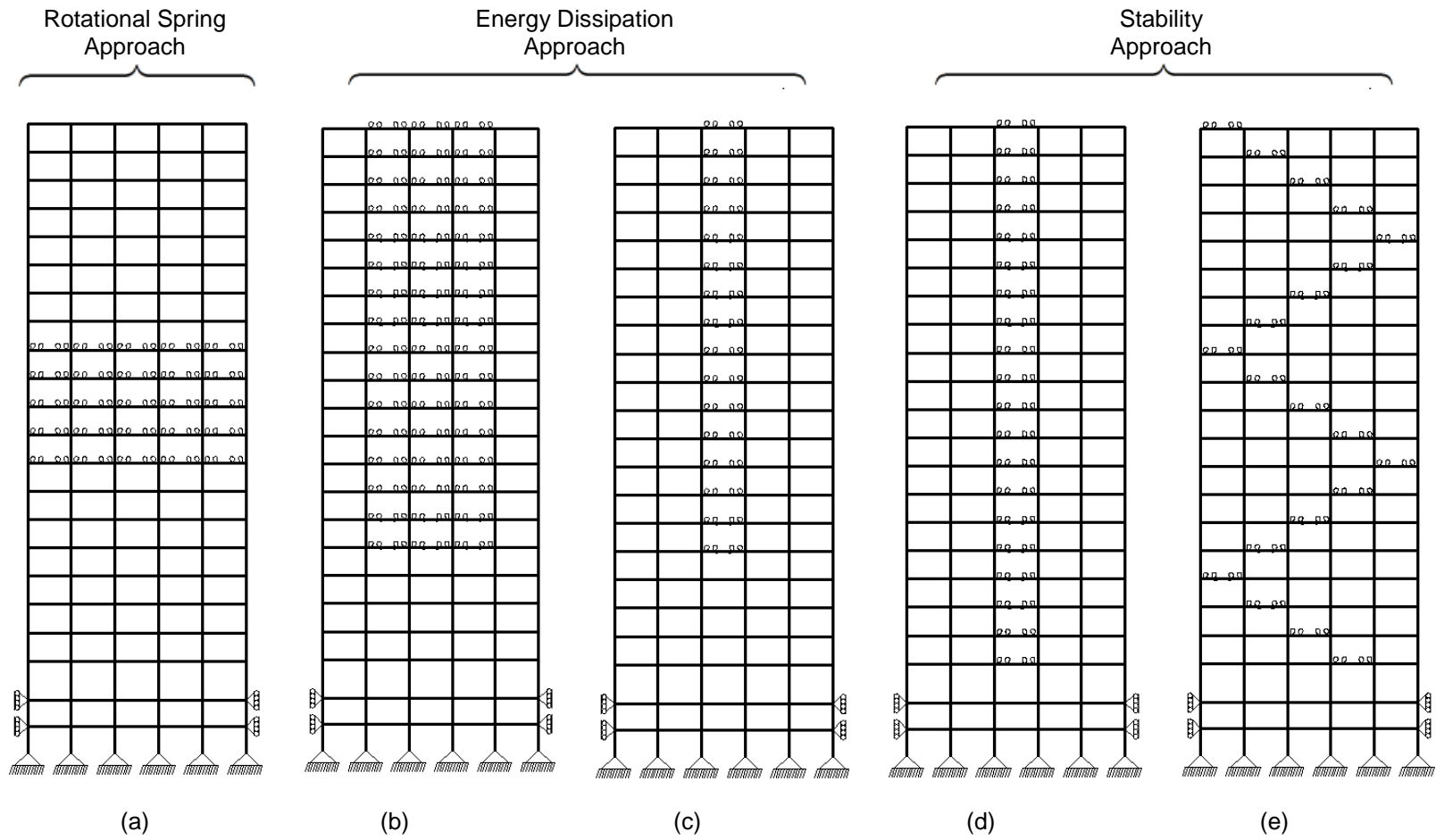
Figure 5.7 Hybrid Models Based on Three proposed approaches (a) HSAC20-1,
(b) HSAC20-2, (c) HSAC20-3, (d) HSAC20-4, and (e) HSAC20-5

Energy Dissipation:

Column = 5763 k-in

Beam = 18840 k-in

435.4 ●
373.2 ●
311 ●
248.8 ●
186.6 ·
124.4 ·
62.2 ·
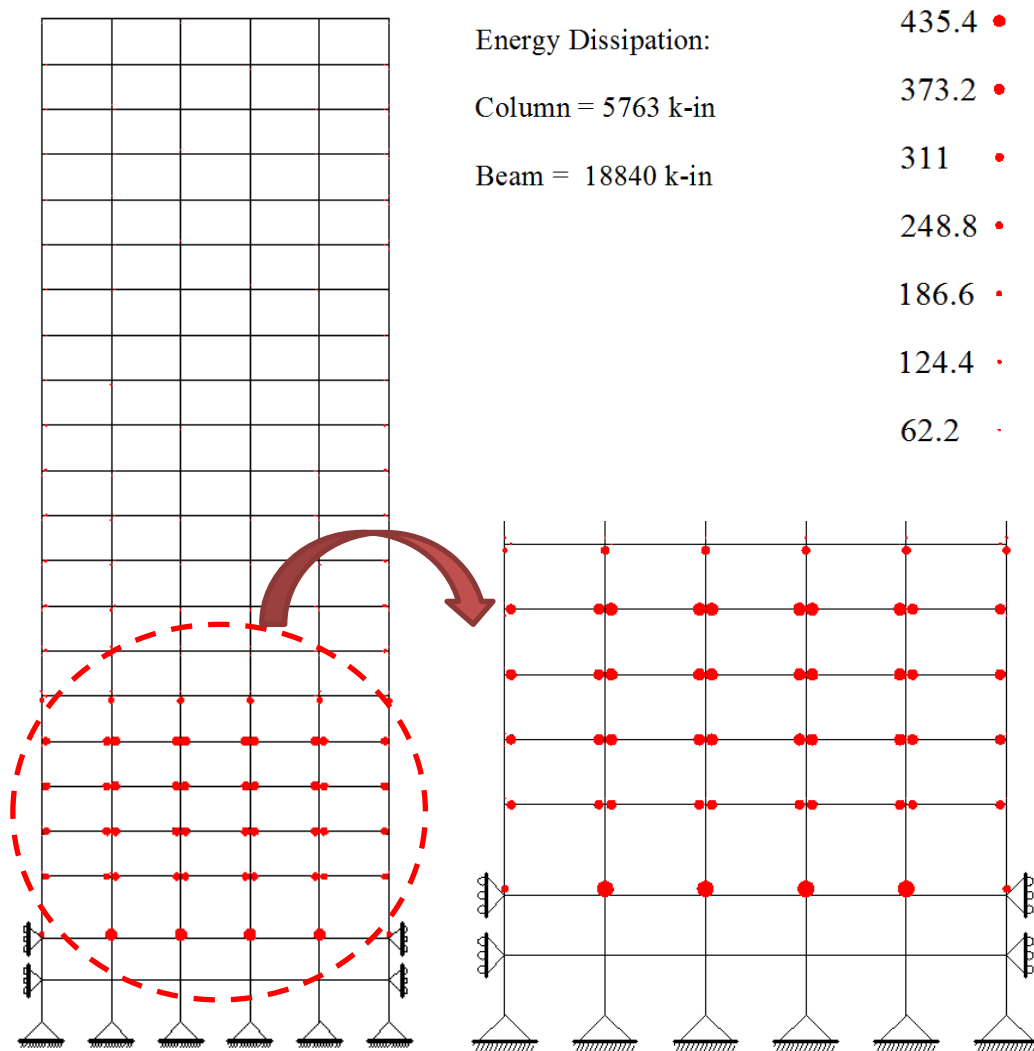
Figure 5.8 Energy dissipated in plastic hinges of the SAC20 frame under LA35

5.3. Evaluation of Proposed Patterns Based on Inter-story Drift Angle

Inter-story drift angle which is expressed as inter-story drift (δ) divided by the height of the story (h) is known as one of the best measures of seismic performance at the story level of steel moment resistant frames (SMRF). The story drift is a global parameter since it is related to the global drift angle (roof drift angle) which is defined as the roof displacement divided by the height of the roof and consequently to the spectral displacement demand. It is also a local

parameter since it provides a good estimation of member forces and deformation demands (Gupta 1999).

A major concern about using semi-rigid connection in steel frames is that it may cause the inter-story drifts to increase beyond acceptable limits. Although as shown previously in this study, the use of hybrid frame causes decrease in the initial stiffness; however, ground motions do not act similar to static lateral loads on the frame. Ground motions exert forces to frames by introducing acceleration to stories' mass in story levels. Since semi-rigid connections shift the period of structures, the amount of acceleration will not remain constant. On the other hand, although the initial stiffness of a SMRF is more than the initial stiffness of its corresponding hybrid frame, the system stiffness of the frame changes during an earthquake due to yielding in structural members and nonlinear moment-rotation behavior of semi-rigid connections

In order to determine the most effective pattern, the five proposed hybrid frames are modeled using a comprehensive nonlinear model and are subjected to the SAC ground motions for the Los Angeles site. As mentioned in Chapter 4 of this dissertation, these ground motions are categorized in two levels of Design Based Earthquakes (DBE) and Maximum Credible Earthquakes (MCE) based on their return period. The models are first subjected to the set of 20 DBE records, LA01 to LA21, to be evaluated for the first performance objective, which is to satisfy the Life Safety (LS) performance under DBE hazard level. The passing criterion for this performance objective is to maintain an average inter-story drift of less than 2.5%.

The drifts versus stories graphs for HSAC20-1 to HSAC20-5 models are shown in Figures 5-9 to 5-13, respectively. In addition, Figure 5-14 shows the drift results for the original rigid SAC frame. Each graph summarizes the story drifts resulted from 20 different analyses. The bold line in each graph shows the expected (average) story drift value. Moreover, the dashed-line shows the LS limit of 2.5% drift.
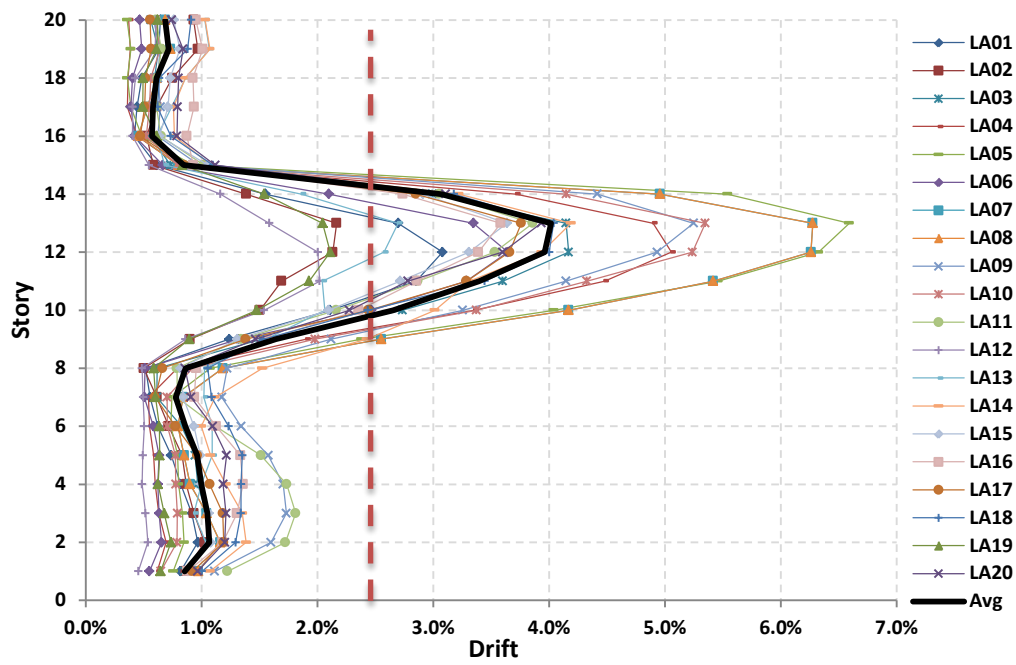
Figure 5.9 Story Drift Diagrams for HSAC20-1 Frame Subjected to L.A. DBE records
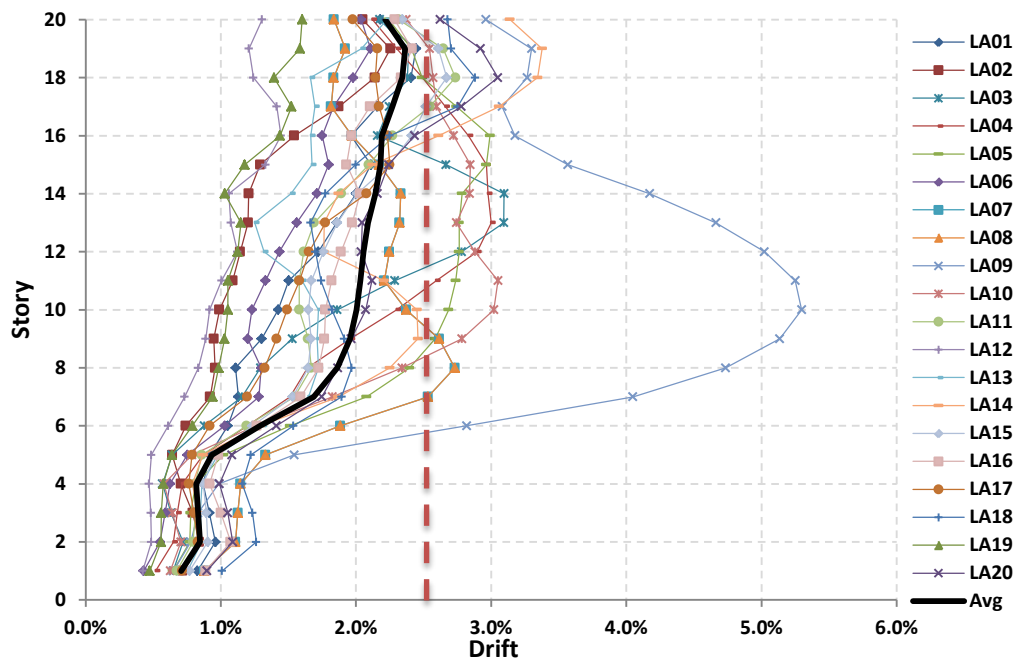
Figure 5.10 Story Drift Diagrams for HSAC20-2 Frame Subjected to L.A. DBE records
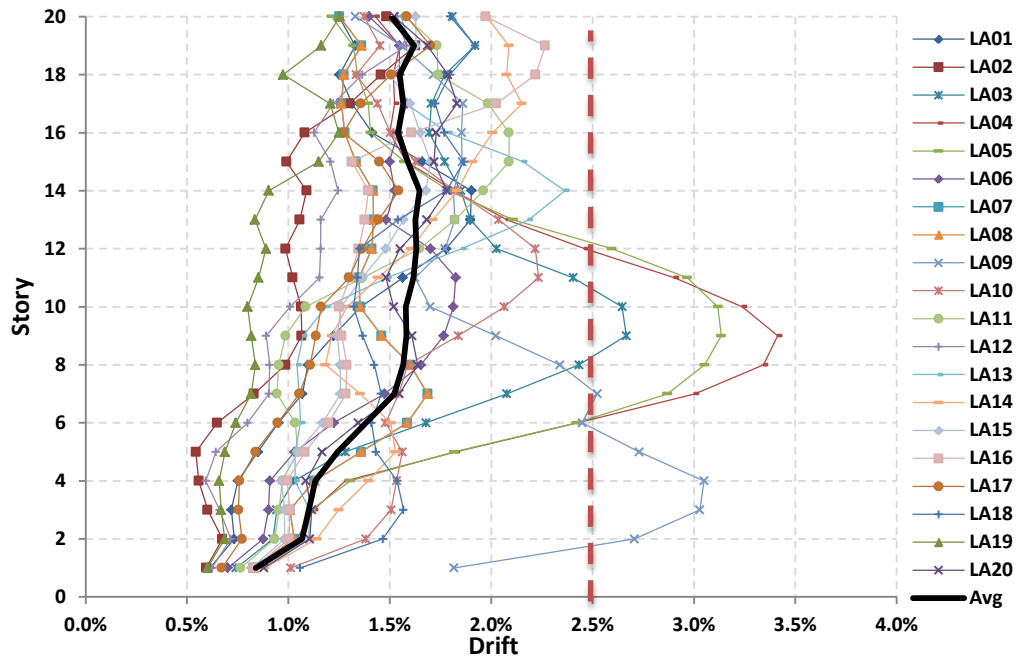
Figure 5.11 Story Drift Diagrams for HSAC20-3 Frame Subjected to L.A. DBE records
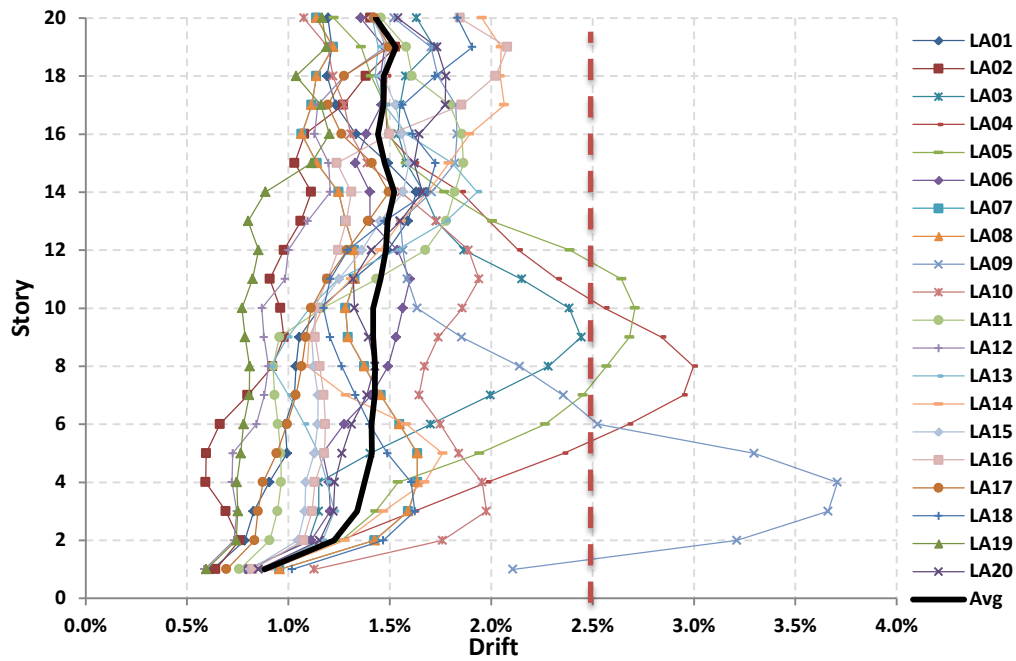
Figure 5.12 Story Drift Diagrams for HSAC20-4 Frame Subjected to L.A. DBE records
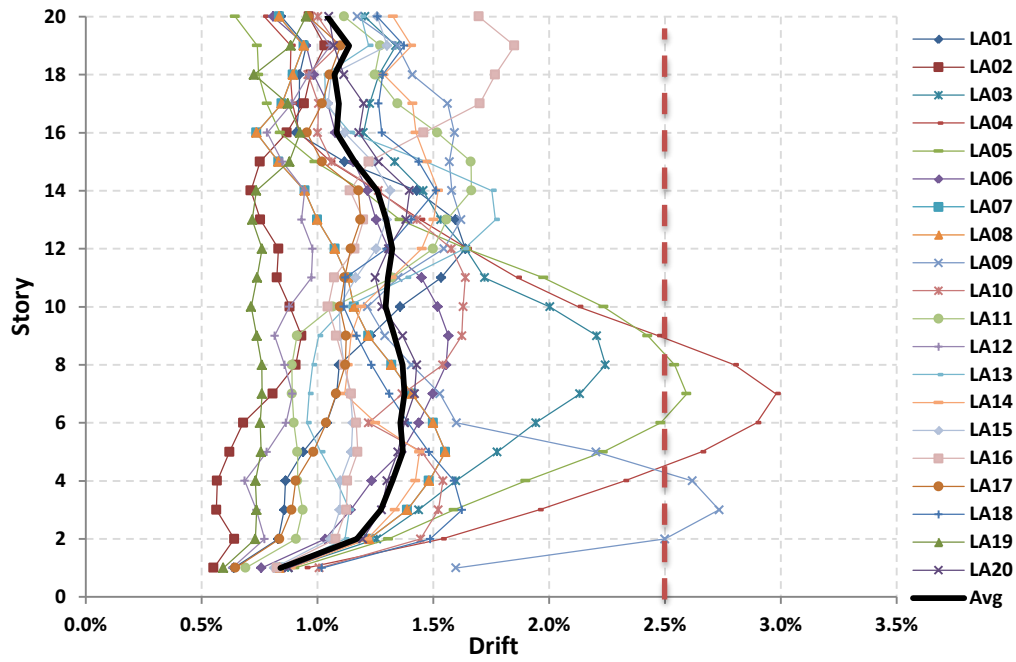
Figure 5.13 Story Drift Diagrams for HSAC20-5 Frame Subjected to L.A. DBE records
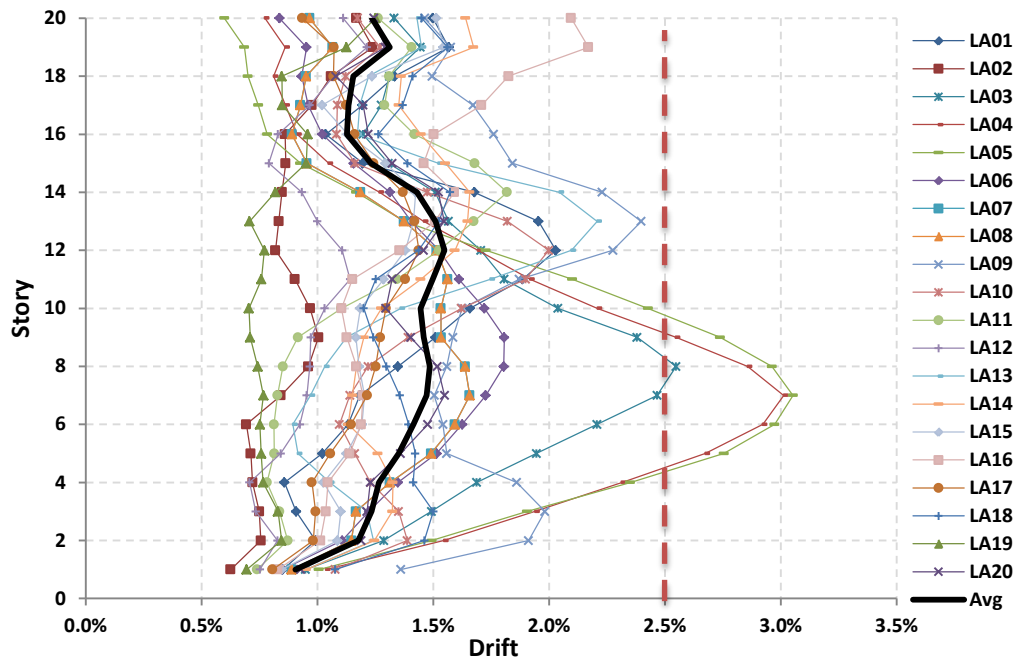
Figure 5.14 Story Drift Diagrams for Original Rigid SAC Frame Subjected to L.A. DBE records

The models are then subjected to the set of 20 MCE records, LA21 to LA40, to be evaluated for the second performance objective, which is to satisfy the Collapse Prevention (CP) performance under the MCE hazard level. The passing criterion for this performance objective is to maintain an average inter-story drift of less than 5%.

The drifts versus stories graphs for HSAC20-1 to HSAC20-5 models are shown in Figures 5-15 to 5-19, respectively. In addition, Figure 5-20 shows the drift results for the original rigid SAC frame subjected to MCE records. Each graph summarizes the story drifts resulted from 20 different analyses. The bold line in each graph shows the expected (average) story drift value. Moreover, the dashed-line shows the CP limit of 2.5% drift.
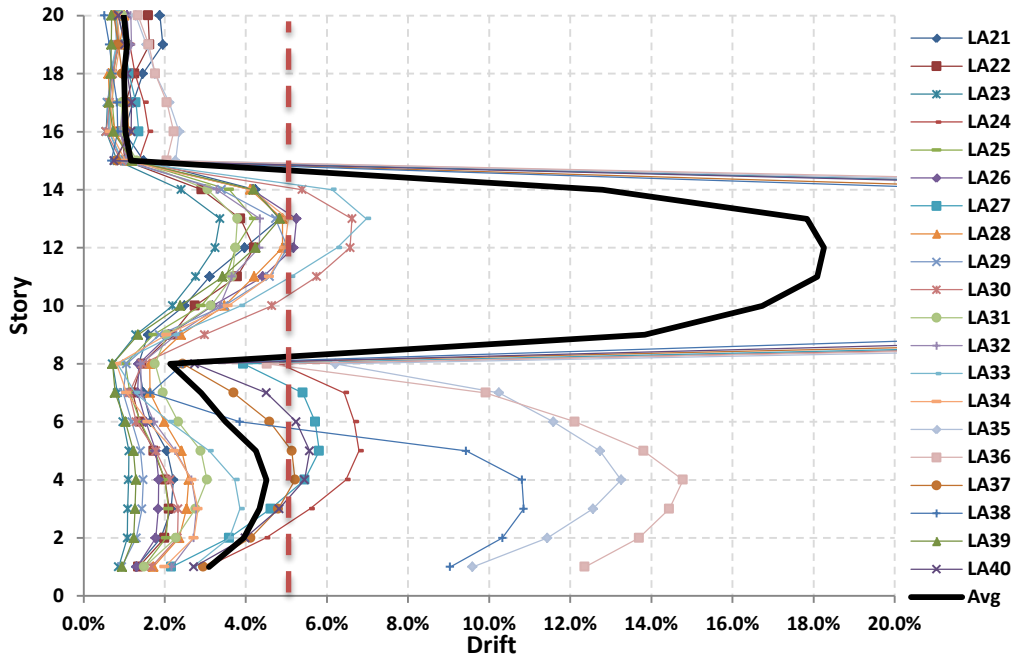
Figure 5.15 Story Drift Diagrams for HSAC20-1 Frame Subjected to L.A. MCE records
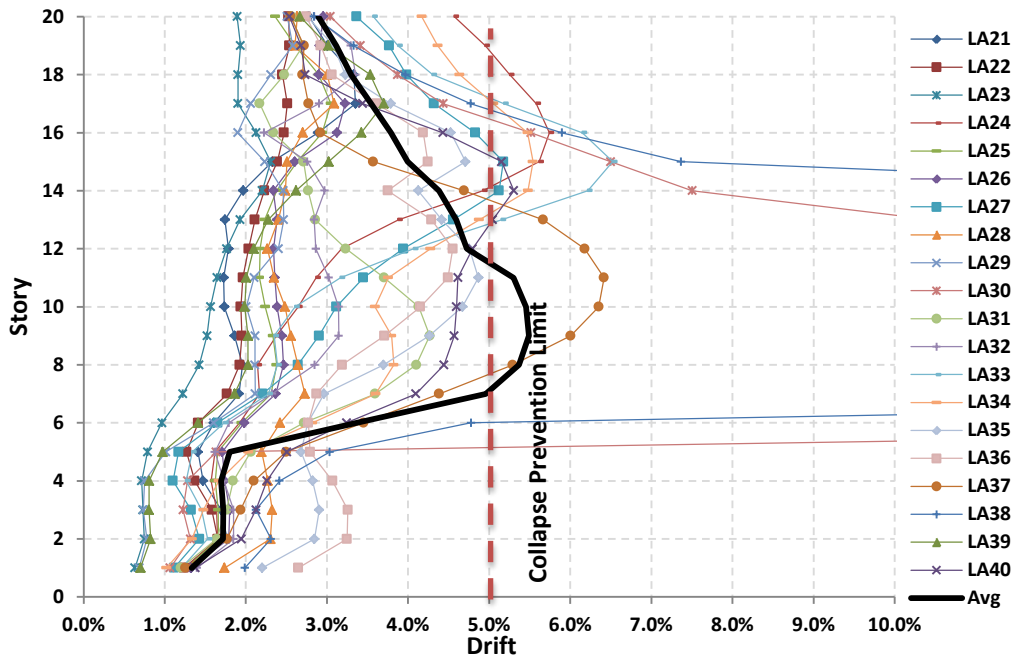
Figure 5.16 Story Drift Diagrams for HSAC20-2 Frame Subjected to L.A. MCE records
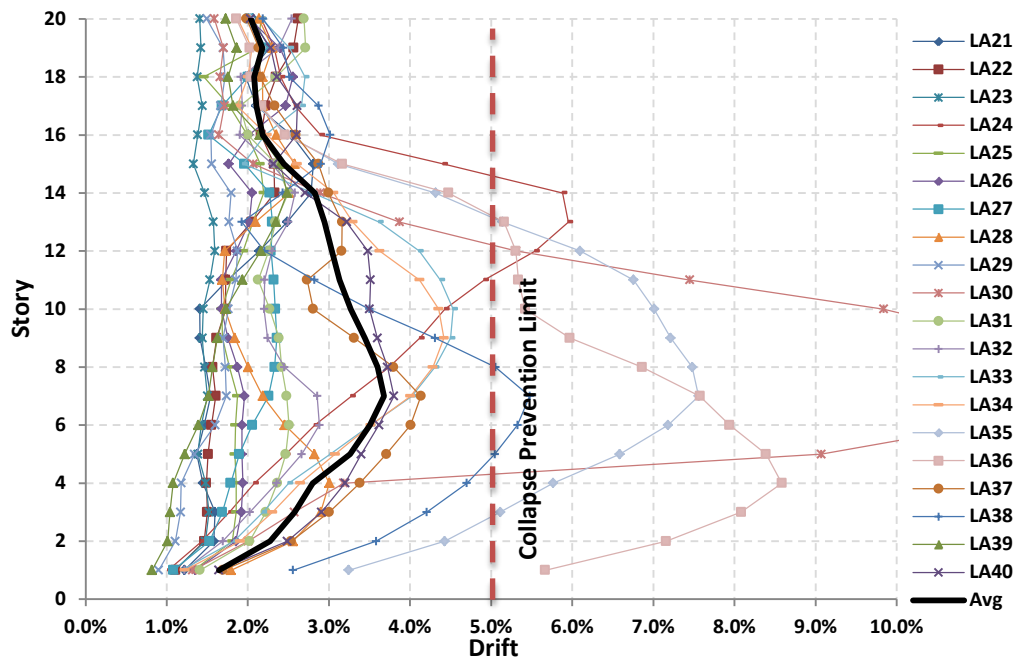
Figure 5.17 Story Drift Diagrams for HSAC20-3 Frame Subjected to L.A. MCE records
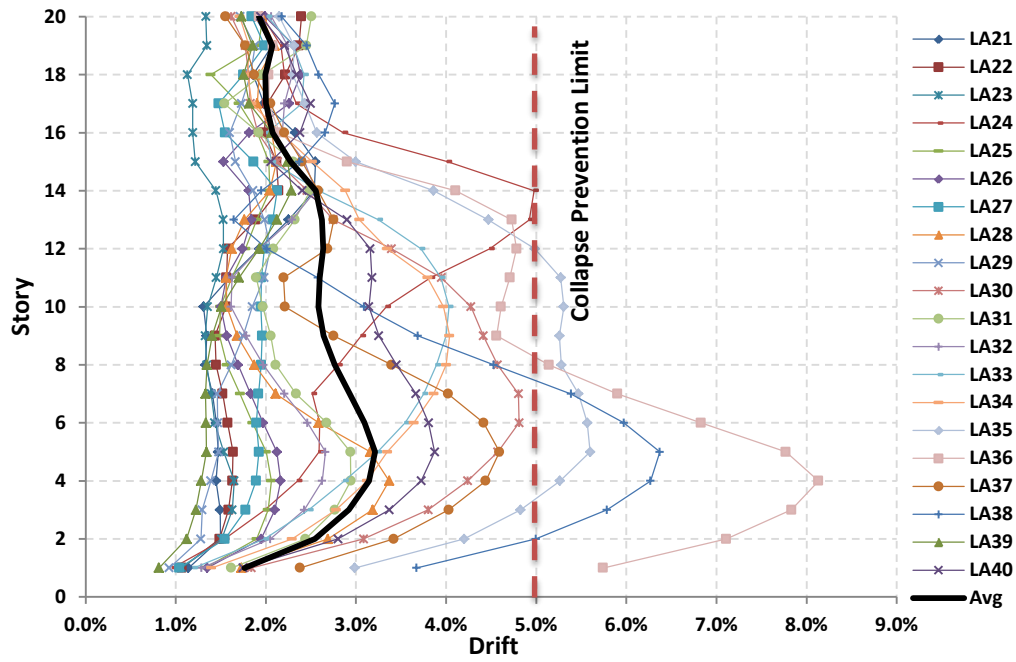
Figure 5.18 Story Drift Diagrams for HSAC20-4 Frame Subjected to L.A. MCE records
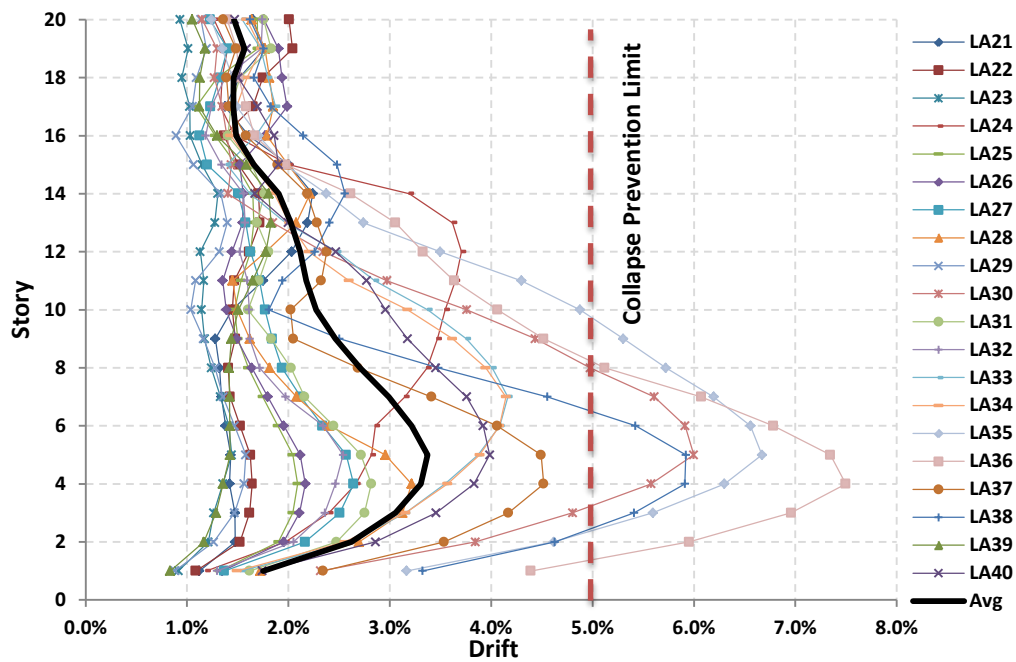
Figure 5.19 Story Drift Diagrams for HSAC20-5 Frame Subjected to the L.A. MCE Records
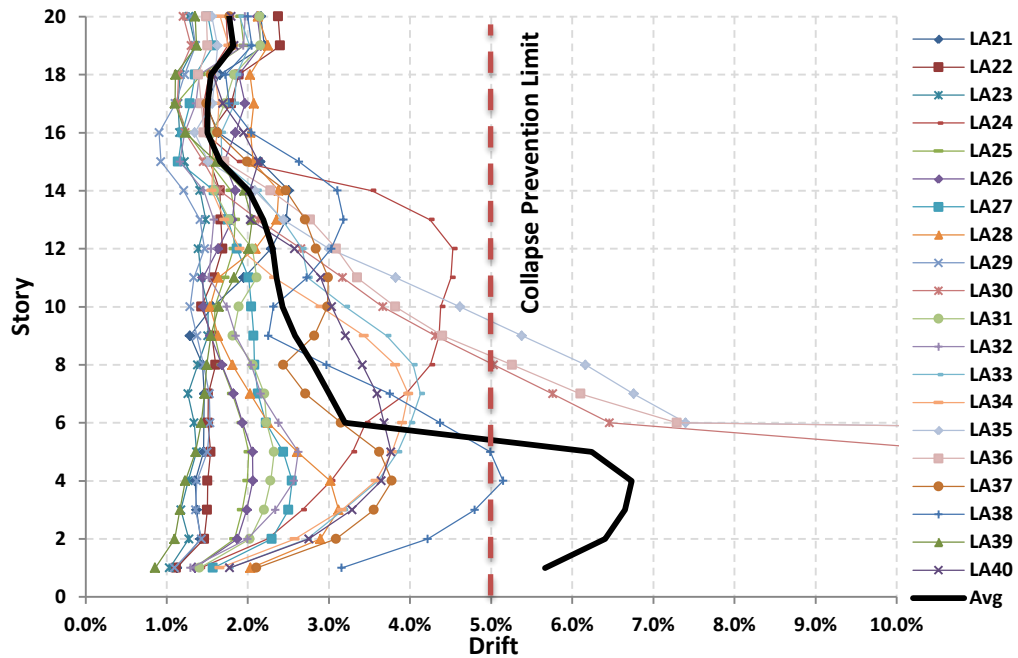
Figure 5.20 Story Drift Diagrams for Original Rigid SAC Frame Subjected to
the L.A. MCE Records

Figures 5.21 and 5.22 illustrate the average of drifts obtained from analyses of the five proposed hybrid frames and the original SAC rigid frame subjected to the DBE and MCE records, respectively. In the figures, each line shows an average of story drifts obtained from the analysis of a frame subjected to 20 ground motion records. Thus, each graph summarizes 120 nonlinear analysis drift results. Figure 5.21 shows that all proposed models meet the LS drift criteria except the HSAC20-1 model. Moreover, HSAC20-4 and HSAC20-5 models show smaller drift demands. In addition, the drift results from single earthquake records, shown in Figures 5.10 to 5.13, illustrate that HSAC20-4 and HSAC20-5 fail to meet LS drift criteria under three ground motions; while, the number of ground motions cause the model to fail the criteria for HSAC20-2 and HSAC20-3 frames are ten and four records, respectively.   Similarly, drift results of the proposed hybrid frames subjected to the MCE records confirms the effectiveness of HSAC20-4 and HSAC20-5 frames.
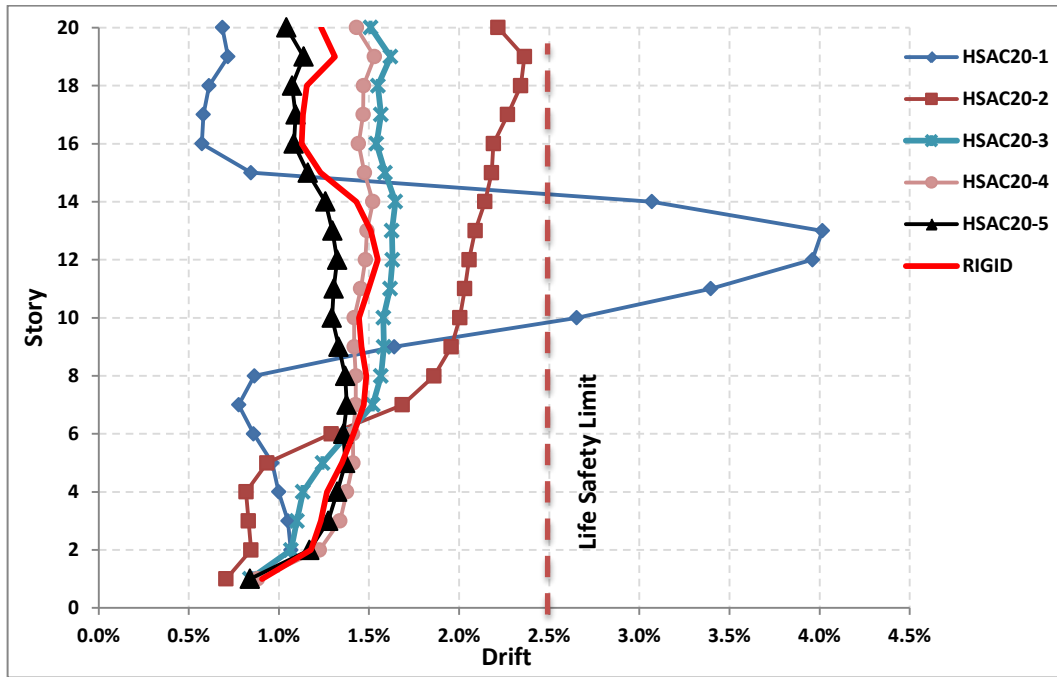
Figure 5.21 Average of Story Drift Diagrams for Various Models of 20-story Structure Subjected to L.A. DBE records
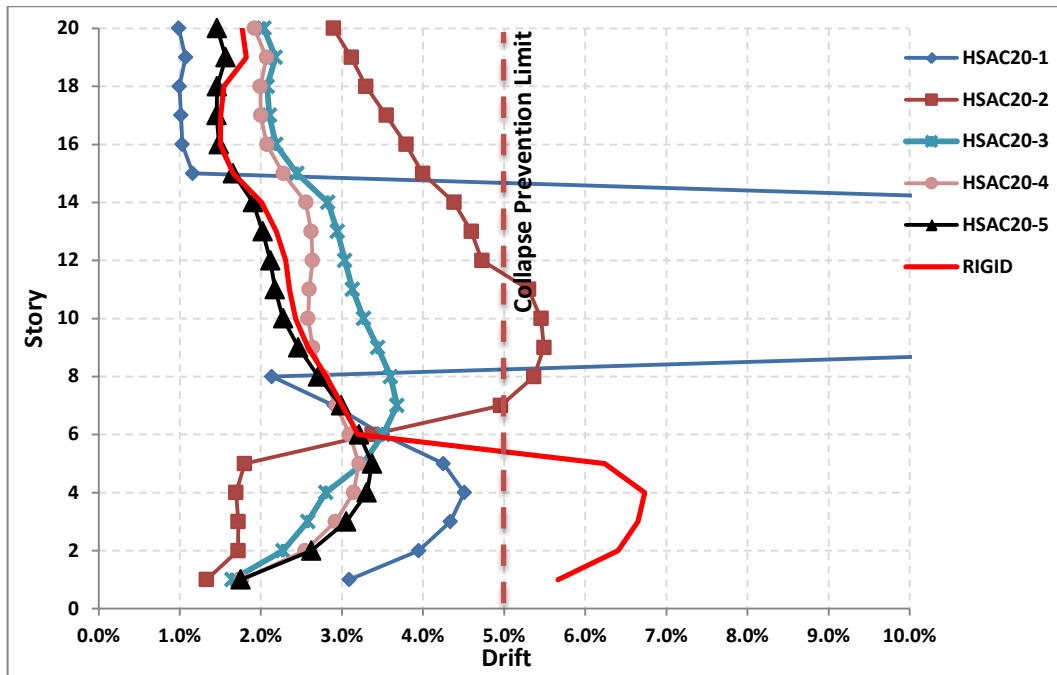
Figure 5.22 Average of Story Drift Diagrams for Various Models of 20-story Structure Subjected to L.A. MCE records

Although SACH20-3, SACH20-4, and SACH20-5 meet the performance drift criteria, the SACH20-3 fails to meet the criteria under five single records, while this number is four for the two later models. In addition, the amount of expected drift value is less in two later models.

These observations led to selecting patterns used in HSAC20-4 and HSAC20-5 models as the most effective patterns. These patterns, which were suggested based on the stability approach, will also be implemented on 3- and 9-story frames. Proposed hybrid models for the 3- and 9-story frames are shown in Figure 5.23. The suffix of 4 and 5 are considered for these models designations to be consistent with the 20-story hybrid frames designations.
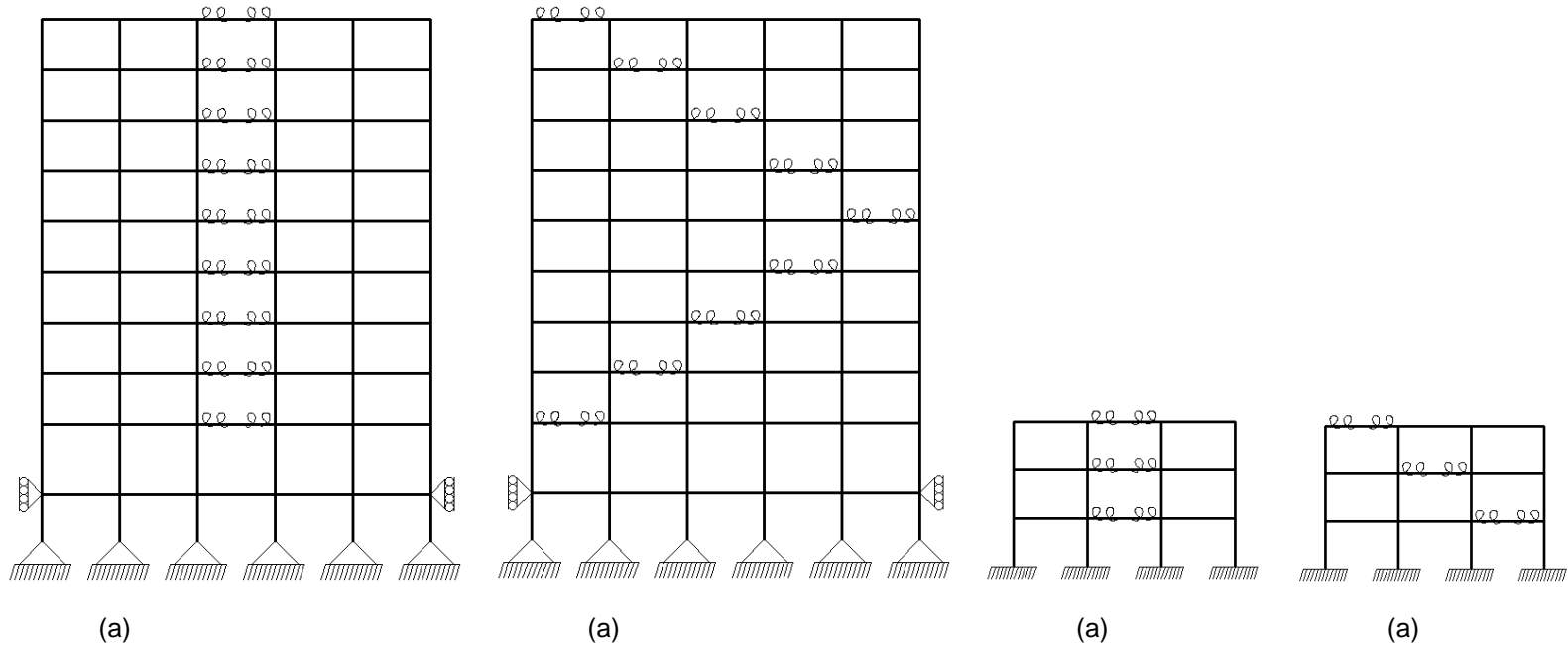
Figure 5.23 Hybrid Models for 3- and 9-story frames (a) HSAC9-4, (b) HSAC9-5,
(c) HSAC-3-4, and (d) HSAC3-5

5.4. Parametric Study on Connection Initial Stiffness

In this section, to determine the effective connection properties, a parametric study is performed on the initial stiffness of semi-rigid connections used in hybrid frames. Selected frames are subjected to the Los Angeles MCE level records and the average of results is presented for each frame.

If a beam member is considered as a compound member, which has been created from a beam column elastic member and semi-rigid connection components, the flexural rigidity of this compound is a function of the flexural rigidity of its components. The elastic beam-column member and the semi-rigid connection can be considered as two rotational springs. The compound's stiffness for this system of series springs can be obtained by:

$$K_{Compound} = \frac{1}{\frac{1}{K_{Beam}} + \frac{1}{K_{connection}}} = \frac{K_{Beam} * K_{connection}}{K_{Beam} + K_{connection}}$$

Equation: 5-1

Therefore, for a connection stiffness equal to infinity the stiffness of the compound is equal to the stiffness of the beam. On the other limit, for a connection stiffness equal to zero the compound's flexural stiffness equals to zero. Based on Equation 5-1, the connections initial stiffness is back calculated for a total component stiffness of 10% to 100% of the stiffness of the beam. For an elastic beam-column member subjected to double curvature bending the initial stiffness of the beam equals to 6EI/L. In this study, since the connection properties are assumed constant for all members, the section properties of the beam W21X50 is used for the back calculations. For the purpose of parametric study, the compound stiffness is varied between 10 to 100 percent of the beams' stiffness. Then, the frames are subjected to the MCE ground motions. Finally, the drift demands are compared for selection of the best connections' initial stiffness.

Average drift diagrams for HSAC20-4 and HSAC20-5 frames with various connection stiffness subjected to the LA MCE records are illustrated in Figures 5.24 and 5.26, respectively. These two graphs show that in both semi-rigid patterns used for the 20-story frame, there is a direct relation between connection stiffness and the maximum drift. Further study on the frames drift demands subjected to single earthquake records, showed that for ground motions with smaller acceleration intensity such as LA21, the more connection stiffness corresponds to the less drift demands as shown in Figure 5.26. However, when frames are subjected to a high intensity earthquake record such as LA30, the more connection stiffness causes the more drift demands as illustrated in Figure 5.27.

Average drift diagrams for HSAC9-4 and HSAC9-5 frames with various connection stiffness subjected to LA MCE records are shown in Figures 5.28 and 5.29, respectively. Although in both cases more connection stiffness corresponds to less amount of story drift, the difference in drift demands for frames with different connection rigidities are less than 6%. In addition, no failure has been seen in this analysis.

Average drift diagrams for HSAC3-4 and HSAC3-5 frames with various connection stiffness subjected to the LA MCE records are shown in Figures 5.28 and 5.29, respectively. In case of 3-story frames, the best frame performance occurs when the most connection rigidity is considered.

Based on the presented study, a connection with stiffness of 30% to 50% of the stiffness of the beam is selected for implementation in hybrid frames. The connections' hysteresis loops will be obtained from a nonlinear FEM analysis presented in Chapter 6 of this dissertation.
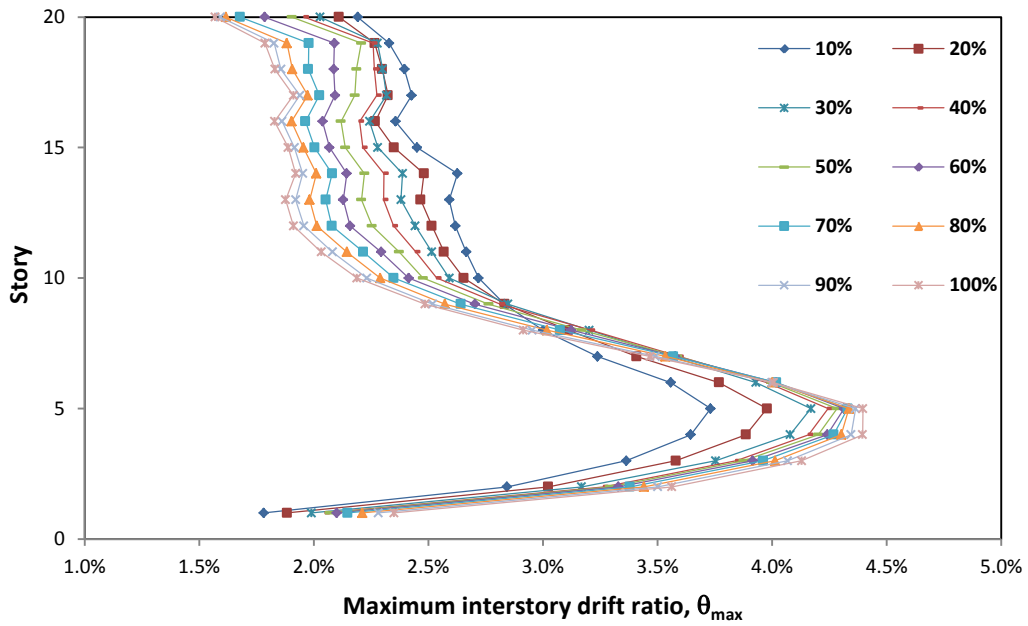
Figure 5.24 Average Story Drift Diagrams for HSAC20-4 with Various Connection Stiffness Subjected to the LA MCE Records
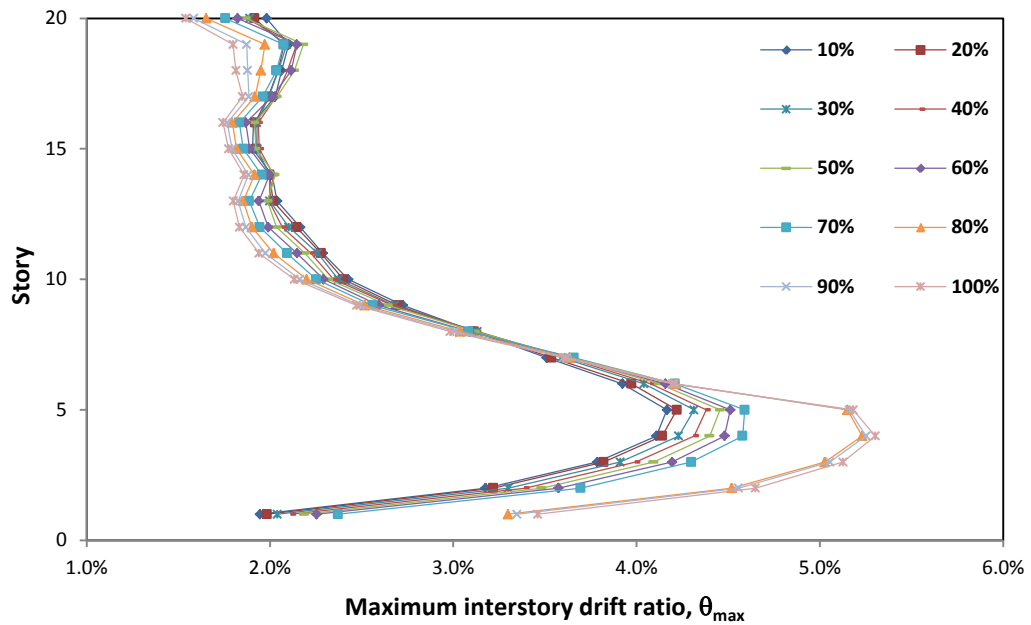
Figure 5.25 Average Story Drift Diagrams for HSAC20-5 with Various Connection Stiffness Subjected to the LA MCE Records
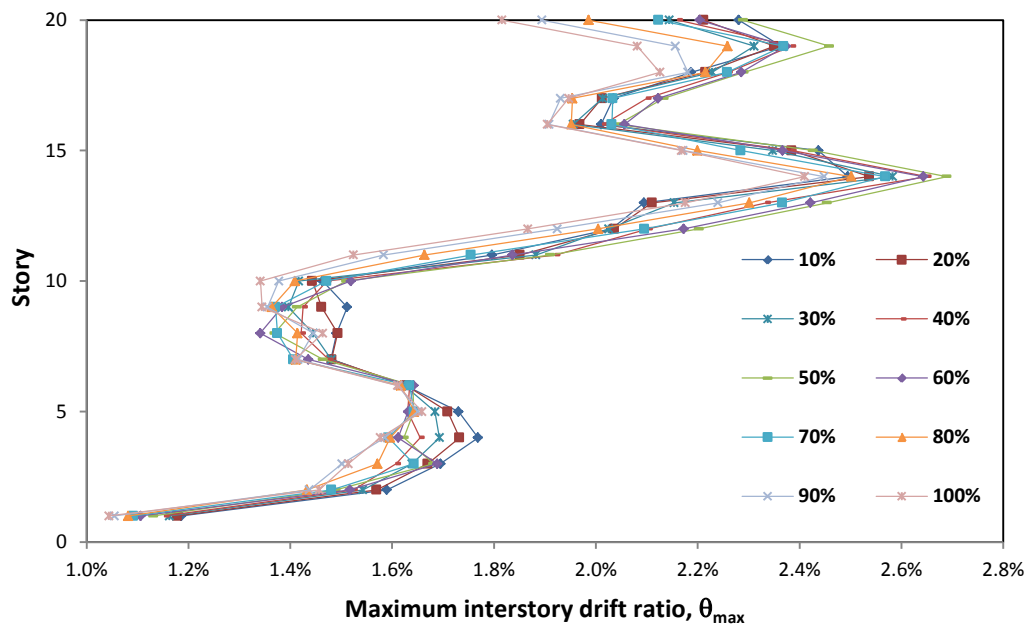
Figure 5.26 Story Drift Diagrams for HSAC20-5 with Various Connection Stiffness Subjected to the LA21 Record
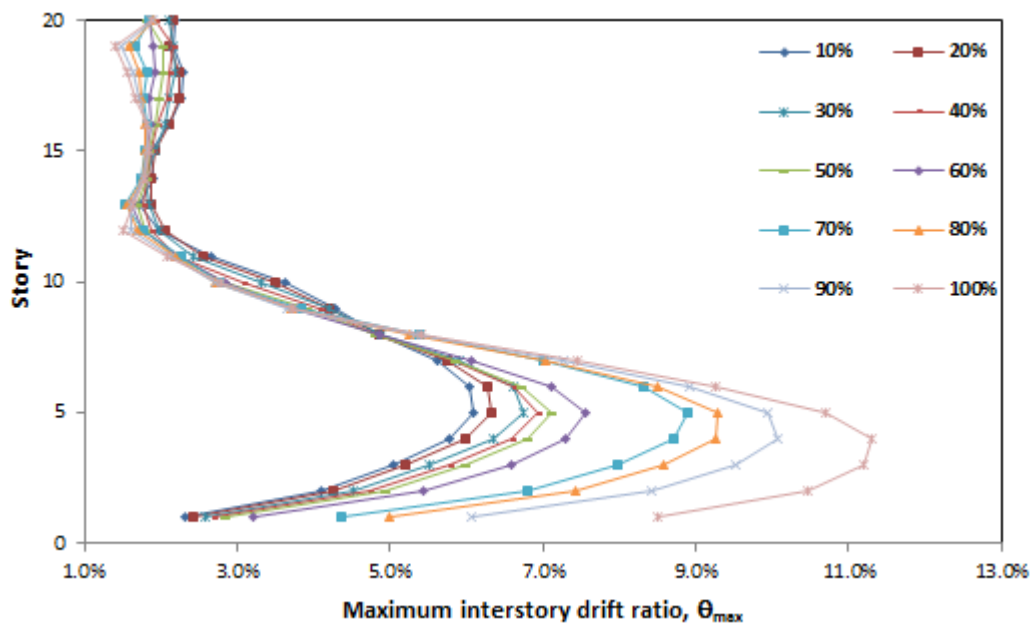
Figure 5.27 Story Drift Diagrams for HSAC20-5 with Various Connection Stiffness Subjected to the LA30 Record
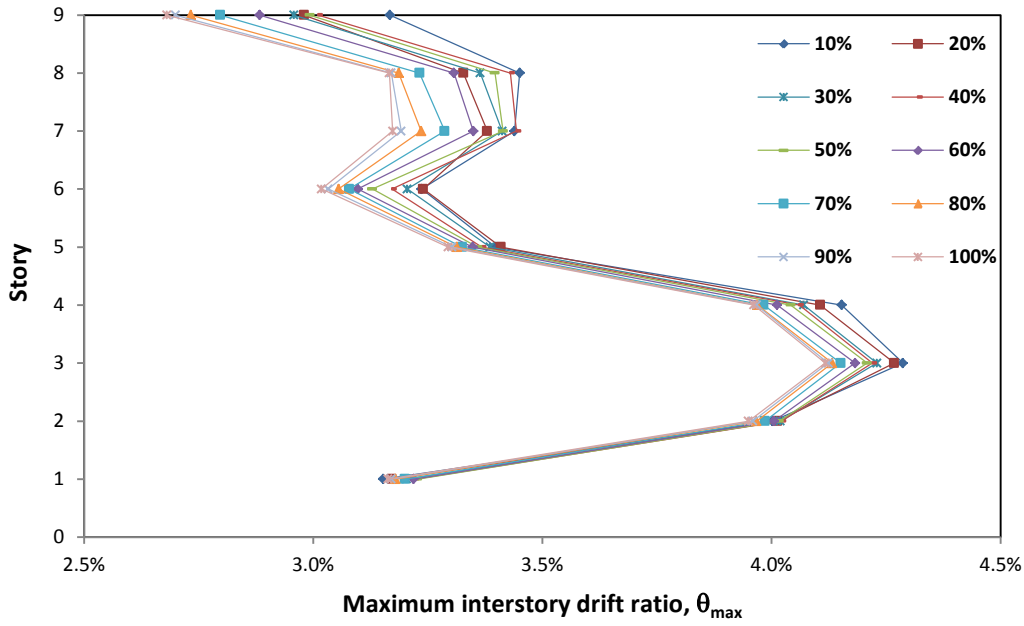
Figure 5.28 Average Story Drift Diagrams for HSAC9-4 with Various Connection Stiffness
Subjected to the LA MCE Records
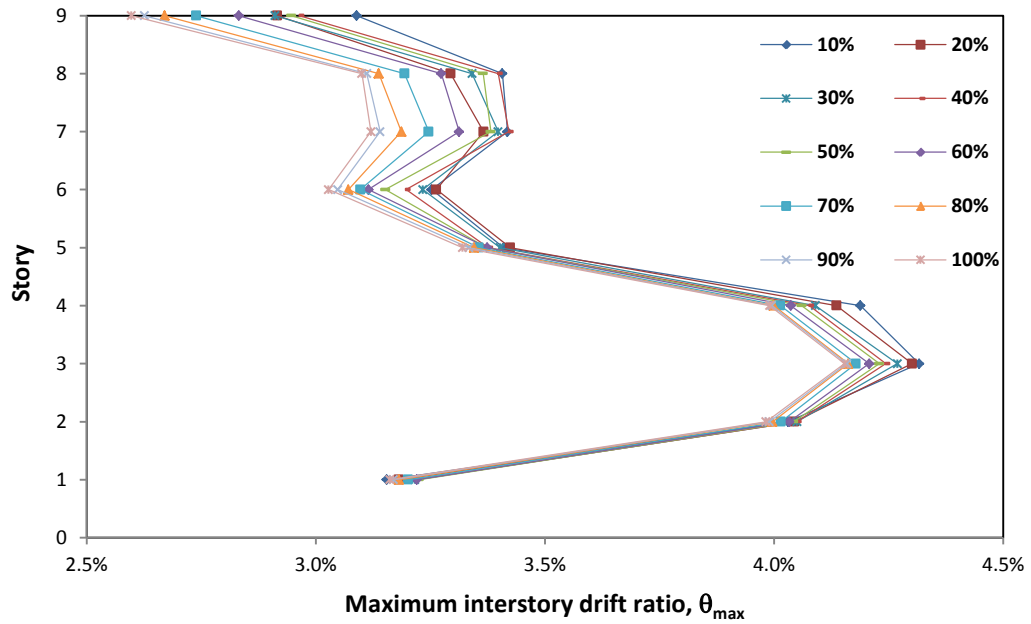
Figure 5.29 Average Story Drift Diagrams for HSAC9-5 with Various Connection Stiffness
Subjected to the LA MCE Records
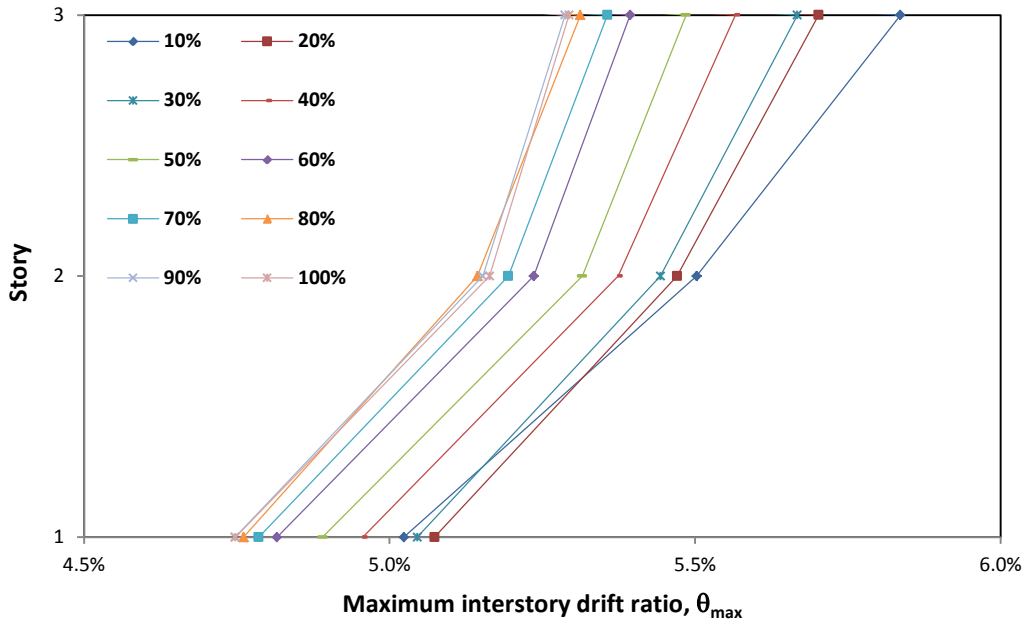
Figure 5.30 Average Story Drift Diagrams for HSAC3-4 with Various Connection Stiffness Subjected to the LA MCE Records
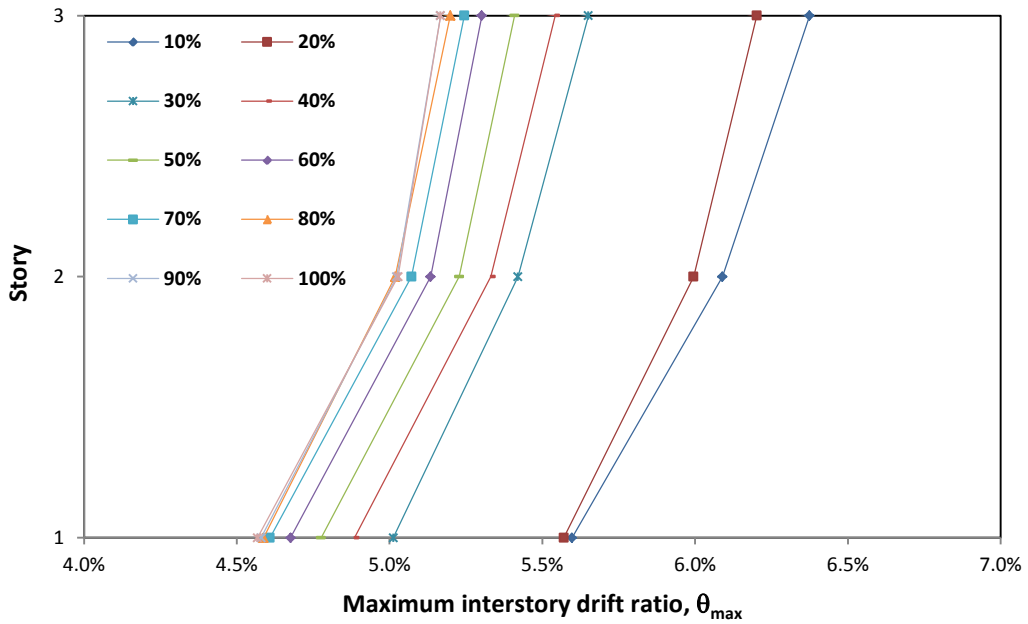
Figure 5.31 Average Story Drift Diagrams for HSAC3-5 with Various Connection Stiffness Subjected to the LA MCE Records

CHAPTER 6

SIMULATION OF CYCLIC PERFORMANCE OF STEEL CONNCETCTIONS USING THREE-DIMENSIONAL NONLINEAR FINITE ELEMENT METHOD

This Chapter is intended to introduce accurate computational benchmarks to predict the hysteresis behavior of beam-column steel connections by means of a 3D non-linear finite element analysis. In this study, element type, inelastic material behavior, bolt pre-tensioning, and contact properties between different components of connections are discussed. Incremental nonlinear analysis takes into account all three types of nonlinearities namely material, geometry, and contact properties in predicting moment-rotation hysteresis loops. The results obtained from the finite element analyses are validated by a series of full-scale structural tests performed by Abolmaali et al (2009). This study shows that cost efficient numerical analysis simulation is capable of replacing full-scale tests for steel connections. Finally, semi-rigid connections used in this study for different beam sizes are simulated. A bilinear curve is fitted to the moment-rotation hysteresis loop of each connection. These curves are then used in global modeling of the hybrid frames.

6.1. Selection of test cases for modeling verification

Five types of semi-rigid with slip critical connections were selected from experimental data conducted by Abolmaali et al (2003) .These connections include bolted/bolted double web angle; welded/bolted double web angle; top and seat angle; flush end-plate, and extended end-plate. The geometry of each connection is illustrated in Figures 6.1 to 6.5 and geometric values are presented in Table 6.1.

Table 6.1 Definitions and geometric values of connections. Units are in inches (mm)

Variable	Definition	Extended End-Plate	Top-and-Seat	Bolted/ Bolted Double Web Angle	Welded/ Bolted Double Web Angle	Flush End-Plate
b_p	end-plate width	10 (254)	-	-	-	6 (152)
d_p	end-plate depth	22-1/2 (572)	-	-	-	18 (457)
t_p	end-plate thickness	1/2 (13)	-	-	-	3/8 (22)
b_d	bolt diameter	7/8 (22)	7/8 (22)	3/4 (19)	3/4 (19)	3/4 (19)
N	Number of Bolts	-	-	5	4	-
ℓ_h	length of horizontal angle legs	-	6 (152)	5 (127)	5 (127)	-
ℓ_v	length of vertical angle leg	-	6 (152)	-	-	-
t	angle thickness	-	3/4 (19)	3/4 (19)	3/4 (19)	-
G	distance from the heel of the angle to the column bolt row	-	2-1/2(64)	-	-	-
p_f	flange pitch, the distance from top of the flange to first row of bolts	1-3/8 (35)	-	-	-	5/8 (41)
p_b	bolt pitch, the vertical distance between the centerline of bolts of connection	-	-	-	-	3 (76)
g_c	column bolt gauge	4-1/2 (114)	4 (102)	4-1/2 (114)	5-1/2 (140)	3 (76)
d	beam depth	16-5/16 (414)	16 (406)	24 (610)	24 (610)	-
b_f	column flange width	15-7/8 (401)	15-7/8 (401)	-	-	-
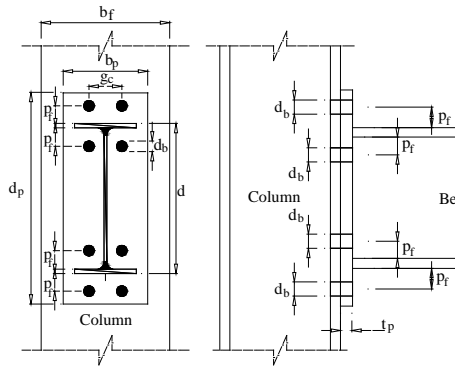
Figure 6.1 Configuration of extended end-plate connection test specimen
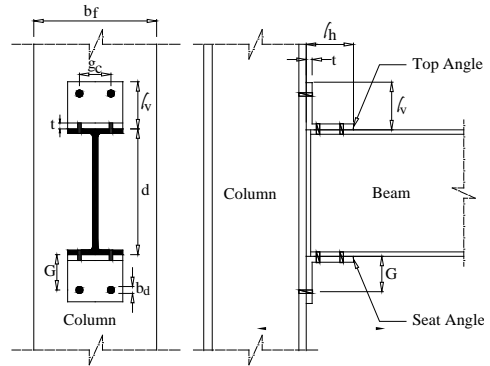
Figure 6.2 Configuration of Top-and-seat connection test specimen
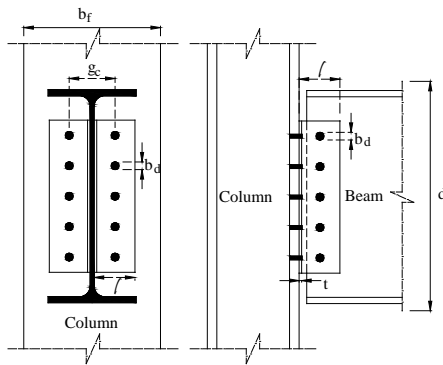
Figure 6.3 Configuration of Bolted/bolted double web angle connection test specimen
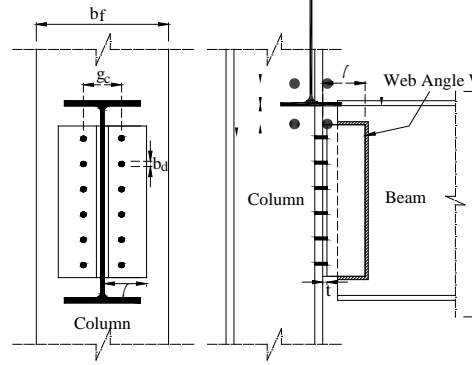
Figure 6.4 Configuration of Welded/bolted double web angle connection test specimen
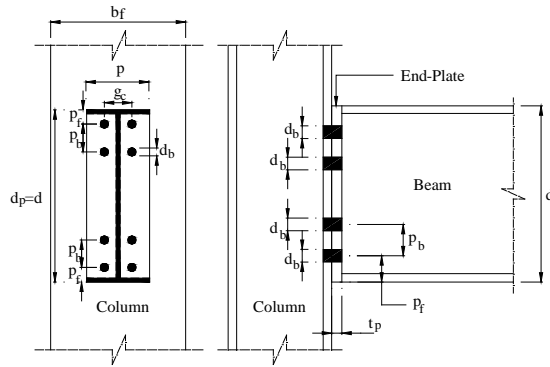
Figure 6.5 Configuration of Flush end-plate test specimen

<u>6.2. Test set up and instrumentation</u>

In this section, the test setup and instrumentation used by Abolmaali et al. are explained. The basic configuration of the test set up used for all types of connections is shown in Figure 6.6, which consisted of: (1) an actuator to apply the force; (2) a beam of a reaction frame to support the actuator; and (3) a column of a reaction frame to support the column in a typical test specimen. The entire reaction frame was bolted to the laboratory floor, and the column of the test specimen was connected to the column of the reaction frame. Lateral braces were provided at the beam end connected to the actuator swivel to prevent out-of-plane buckling of the test specimen.

The instrumentation consisted of two linear variable displacement transducers LVDTs acquire the relative connection rotation and two wire potentiometers to measure displacements at two separate points along the beam specimen span. In addition, a load cell and displacement transducers were installed in the actuator to measure the cyclic load applied to the beam-end and the actuator stroke (displacement), respectively.

The LVDTs were placed directly above and below the top and bottom beam flanges for the double web angle and the flush end-plate connections (Figures 6.6a and 6.6c). The locations of the DTs for the top and seat angle connection test specimens were directly above and below the outer edges of top and seat angle, respectively (Figure 6.6b). Finally, for the extended end-plate test specimens, the LVDTs were mounted in the column web to reach the centerlines of the top and bottom beam flanges by drilling two holes from back of the column flange (Figure 6.6d)

The relative displacements measured by the two LVDTs, divided by the vertical distance between their tips, was defined to be the local rotation of the connection. The global rotation of the connection was calculated by dividing the vertical displacement recorded by each wire potentiometer by the distance of the wire potentiometer from the face of the specimen column flange. Hence, the connection rotation at every load level was measured in three

independent ways. The moment applied to the connection was calculated by multiplying the force recorded by the actuator load cell by the distance from the center of the actuator to the face of the column.
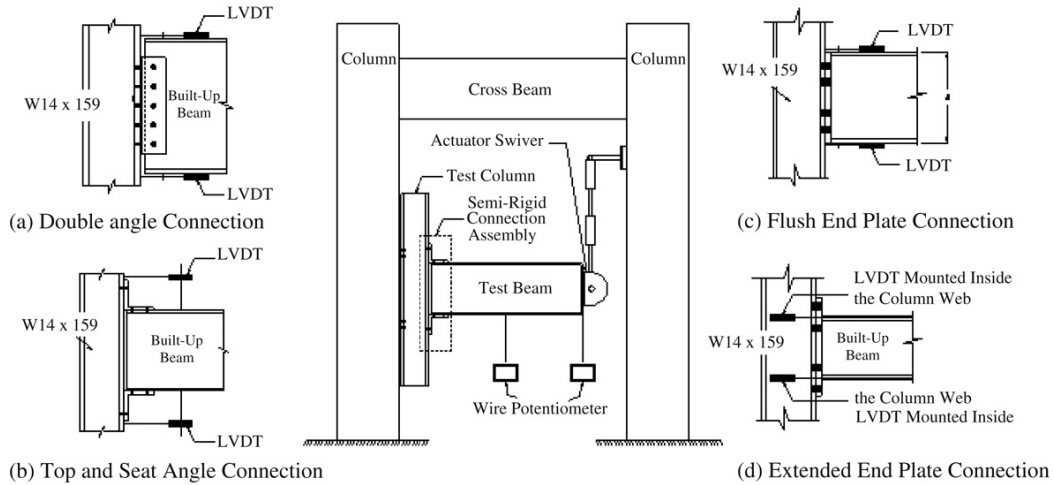
Figure 6.6 Typical configuration of the beam column connection test setup
(a) double angle connection, (b) top and seat connection,
(c) flush end plate connection, and (d) extended end plate connection

6.3. Finite element modeling

An accurate steel connection finite element model is a function of several parameters such as element types, mesh sizes, material properties, and contact models. It also depends on the techniques for applying the boundary conditions, external loading, and pre-tensioning forces in the bolts. In this section the appropriate parameters and techniques for a precise connection model is presented.

To validate the method, five nonlinear 3-D finite element models were developed to simulate the response of the beam-column connection under cyclic displacement control loading. The results obtained from the numerical analysis were compared with the results collected from the experimental testing to verify the accuracy of the numerical results. Elements types and mesh sizes are essential parameters for a precise simulation. In these connections, the steel plates were modeled using an 8-noded linear brick, reduced integration, and hourglass

control (bricks C3D8R). A 6-noded linear triangular prism (C3D6) was also used to model the bolts, bolt head, nuts, and the washers. Initially the models were seeded using 1/2 in (12 mm) spacing, and then the mesh was refined on critical locations to the desirable size (H-convergence). In the beam-column models, the size of the mesh was gradually increased up to 6 in (15.2 cm) at the regions with significantly low strain. The option "seed by number" provided in ABAQUS 6-12.1 was used for simplicity and consistency. The details of the sizes and location of the meshes of the bolts are presented in Table 6. 2.
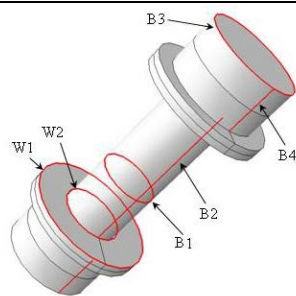
A typical meshed bolt is presented in Figure 6.7. The linear triangular prism element (C3D6) is used for both the bolt-head and the bolt-shank. The nut was modeled similar to the bolt-head and the extended length of the bolt was neglected. The nut, the bolt-head, and the bolt shank were considered as a single body. The bolt shank was modeled as a cylinder with a nominal diameter of the bolt. The washers were placed on both ends of the bolt (nut and bolt-head) to simulate experimental specimen. The length of the bolt was equal to the actual bolt length for each specimen.

Another key parameter is the number of layers of the mesh in the depth of the steel plates. Using less number of mesh layers may result in less accurate results; nevertheless, using more layers will increase the time of the computation. Based on the results of the study conducted by Bursi and Jaspart (1997, 1998), the number of the layers of mesh in the modeling of the steel bolted connections, significantly affects the accuracy of the numerical results. The models were meshed in one, two, and three layers and the results were compared with experimental values, which led to acceptable results in the case of two layers. In addition, the best results were obtained from the models with a superior order, 8-noded, with the reduced integration (Zienkiewics 1989).

Bolt pre-tensioning is the first step of the connection loading which might be applied by means of applying initial force or initial displacement. In this study, the pre-tensioning bolt-force was modeled by applying an initial displacement to two parallel surfaces in the bolt-shank,

103

using bolt-force with adjustments length function of the ABAQUS 6-12.1. The value of the initial displacement was adjusted by trial and error to achieve a sufficient pre-tensioning bolt-force specified by AISC design manual 2001. The bolts were pre-tensioned in the first step and the displacement control loads are applied to the specimen during the next steps.

Table 6.2 The mesh size distribution in the bolts

Element	Line Number	Number of Seeds	Schematic
Washer	W1	20	
	W2	15	
Bolt	B1	15	
	B2	10	
	B3	15	
	B4	4	
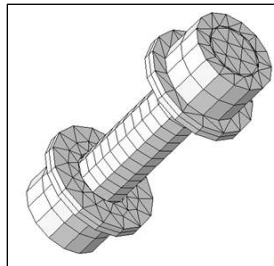
Figure 6.7 A typical bolt mesh

6.3.1. Loading and Material Modeling

Specimens were subjected to a cyclic displacement history in accordance with the FEMA 350 (2000) as shown in Figure 6.8. This was done by applying tip displacement to the beam.
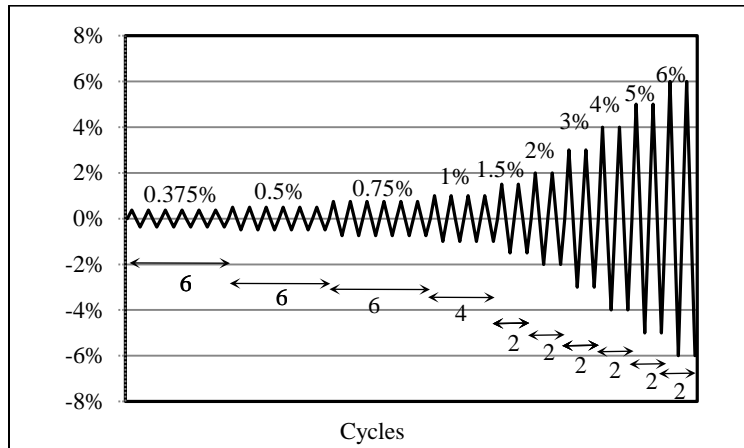
Figure 6.8 Cyclic loading history, FEMA 350

The combined hardening plasticity model was used in order to model the material behavior during the cyclic loading. The parameters suggested by Kiamanesh et al. (2010) and Ghobadi et al. (2008) for combined strain hardening of Grade-50 hot-rolled steel was selected in the analysis algorithm. Isotropic hardening was used to model the material properties of the high strength steel bolts with material constitutive law as shown in Figure 6.9.
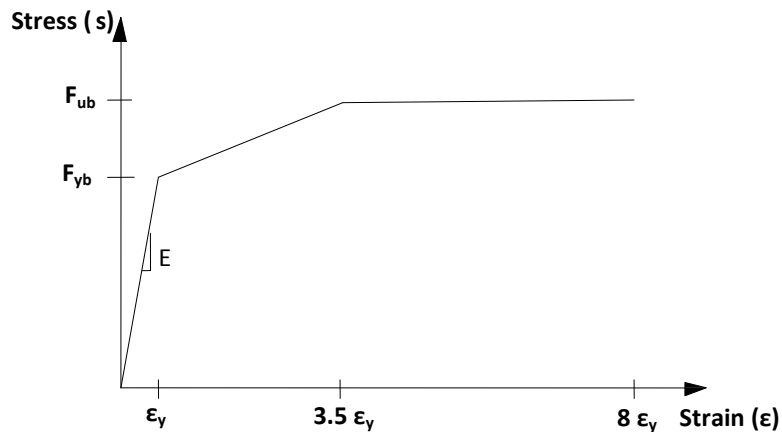
Figure 6.9 Stress-strain relationship for high strength bolts

The algorithm used for the combined hardening of the low-carbon material in ABAQUS was based on the study conducted by Doghri et al.(1988), which is capable of performing both kinematic and isotropic hardening. The kinematic hardening parameters C and

γ are defined as the initial hardening modulus and the rate at which the hardening modulus increases with increasing plastic strain, respectively.

The isotropic hardening behavior of the material is modeled with exponential law. The parameters Q∞ and b are defined as the maximum increase in the plastic range and the rate at which the maximum size is reached when plastic strain develops, respectively. The values of the combined strain hardening parameters used in this research are tabulated in Table 6.3.

A Young's modulus of $E=30 \times 10^3$ ksi (210 GPa) and a Poisson's ratio of $\nu=0.3$ were used to define the elastic response of the material with RyFy=55 ksi (385 MPa), where Ry=1.1 is the ratio of expected yield stress to specified the minimum yield stress Fy.

Table 6.3 Material Properties

Parameter	Value
C ksi (MPa)	2030 (14000)
γ	140
Q∞ ksi (MPa)	261 (1800)
b	0.26

6.3.2. Contact Modeling

The numerical results are highly sensitive to the contact properties between the components of the model. Contact algorithms should consider two physical constraints: 1) penetration of one surface into another is prohibited and 2) since the surfaces are not glued together, the normal traction on surfaces could only be compression; in other words, no tension between contact pairs is allowed. In ABAQUS, two contact pairs are called Master and Slave. The contact algorithm does not allow the Slave's nodes to penetrate in Master's surface.

The Lagrange multiplier method and penalty method are two widely used algorithms for modeling the contact phenomenon.

106

In the penalty method, a comparatively large number (known as penalty coefficients) is defined in the formulation of the total potential function that enforces the constraints to be satisfied. This number should be selected carefully because for very small values it does not guarantee the constraint to be satisfied (either penetration or tensile traction may occur) and for very large values, it causes ill conditioning of the system's equations and may cause the solution not to converge.

The Lagrange Multiplier Method does not require contact stiffness; instead it requires chattering control parameters by assuming that the contact status remains unchanged. If the contact status from the previous iteration is open and the current calculated penetration is smaller than the maximum allowable penetration, then contact remains open. Otherwise, the contact status switches to closed and the next iteration is processed. Lagrange multiplier method adds additional degrees of freedom to a FEM model and requires additional iterations to stabilize contact conditions. This will increase the computational cost and may even lead to solution divergence if many contact points are oscillating between sticking and sliding during iterations.

Augmentation iteration can be used within the penalty algorithm to reduce the magnitude of penetration. In this case, the algorithm is called Augmented Lagrange method. This method can be used only on hard contacts in which the pressure-overclosure relationship follows Figure 6.10.
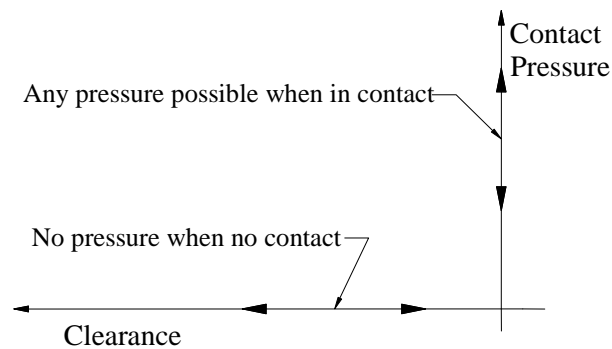
Figure 6.10 Hard contact pressure-overclosure relationship

Although Augmented Lagrange method increases the number of iterations, it makes the resolution easier by controlling the magnitude of penetration.

In bolted connections with slip critical bolts, the force and partial moments are transferred from beam to column by normal and frictional actions.

Small sliding surface-to-surface was considered for all the contacts. The welds were assumed to be rigid and modeled by tie-contact algorithm which constrains the transitional degrees of freedom between contact pairs. No rotational degrees of freedom are constrained in this algorithm. The frictional surfaces accompanied by tangential force were modeled by a tangential-contact algorithm. The surface contact between the end-plate and column was modeled by frictional contact using penalty stiffness with the penalty value of 0.2. The surfaces with normal force were modeled using the Augmented Lagrange Formulation. The tangential contact between the bolt-hole and the bolt shank was considered to be frictionless. Also, hard contact was used for the connection between bolt-head/nuts to the end-plate/column flange.

Master surfaces of the contacts pair represent the surface of column flange, bolt-head, bolt-shank, washer, whereas the slave surface is defined as the surface interfacing with the master surface. The master surface in general should have finer mesh.

<u>6.4. Results and discussion</u>

6.4.1. Extended End-Plate Connection

A typical 3-D finite element model of the extended end-plate connection is presented in Figure 6.11. A W16x67 hot-rolled cantilever beam was connected to a W14x159 column using an extended end-plate and eight high strength bolts. The cyclic displacement control load is applied to the tip of the beam.
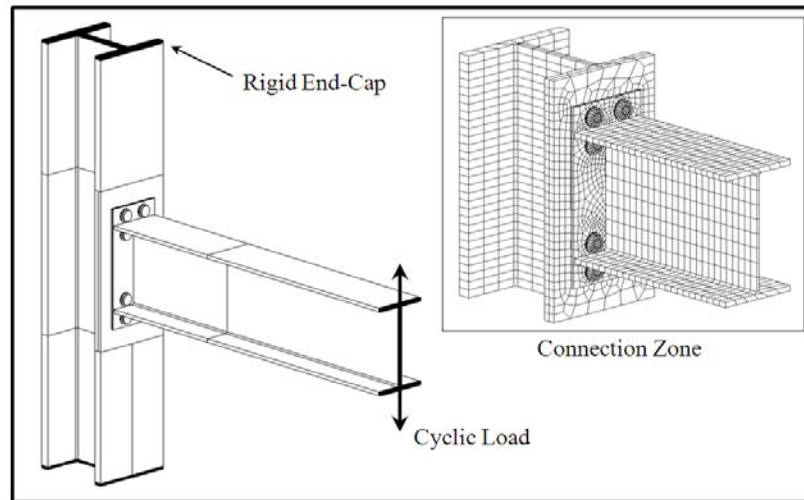
Figure 6.11 Extended end-plate finite element model and mesh properties

Figure 6.12 shows the comparison of the moment-rotation hysteresis obtained from finite element analysis with those from full-scale experimental tests. A close examination between the two plots shows that FEM is highly capable of predicting the connection response. Particularly, the numerical results closely follow the loading and unloading stiffness of the connection during each cycle. There is a 3.5% difference between the areas under the outer hysteresis loops of FEM and experiment.
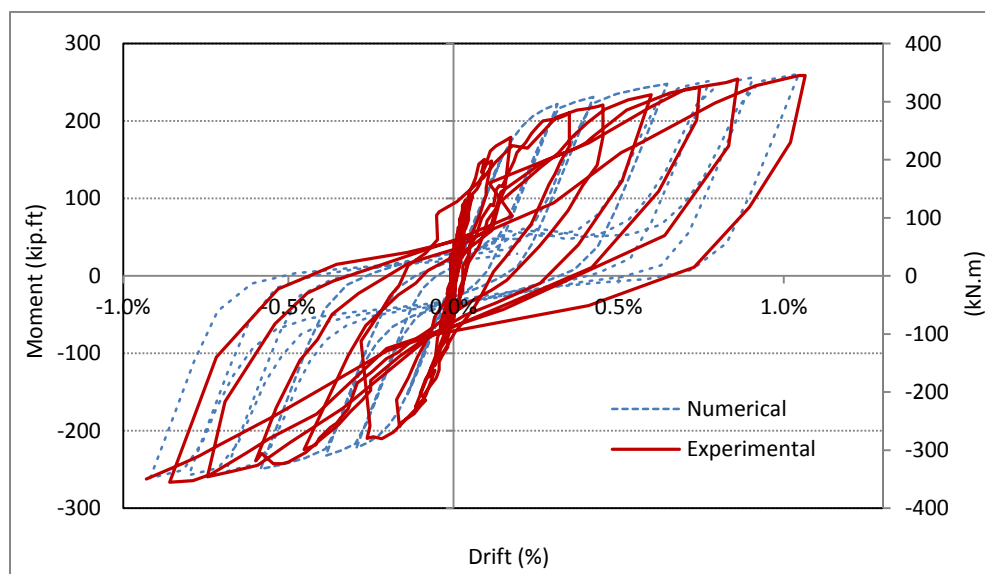
Figure 6.12 Comparison FEM and Experimental hysteresis for extended end-plate connections

Experimental data showed that the bolt-failure was the failure mode for this connection which is also confirmed in this study as shown in Figure 6.13.
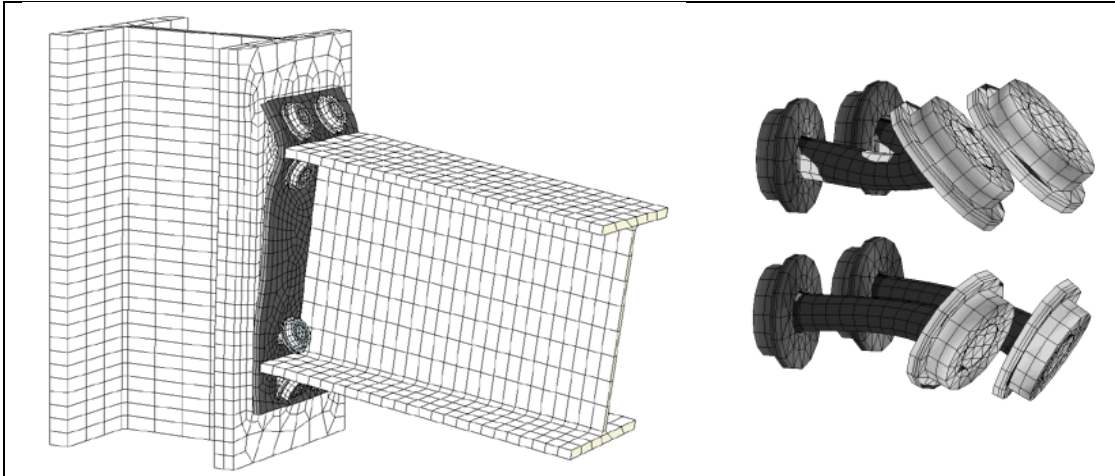
Figure 6.13 Failure of bolts in the Extended End-Plate Connection

6.4.2. Top-and-Seat Angle Connection

To model the behavior of the top-and-seat connection under cyclic loading, a hot-rolled W16x67 cantilever beam is connected to a hot-rolled W14x159 column using two 6x6x¾ angles. This finite element model is validated with the experimental results as shown in Figure 6.14. The hysteresis results illustrated in Figure 6.15 show the correlation between the moment-curvature curves obtained from experimental testing and finite element analysis. The FEM follows experimental hysteresis loops closely. The difference between areas under the outer loops of hysteresis loops obtained from experiment and FEM is 11.5 %.

The test specimens were designed such that the bolt and weld fracture were prevented. Thus, the failure was defined by excessive rotation whose value was typically 0.045 radians. Accordingly, no bolt failure is observed in the results from finite element analysis before the rotation of 0.04 radians is reached.
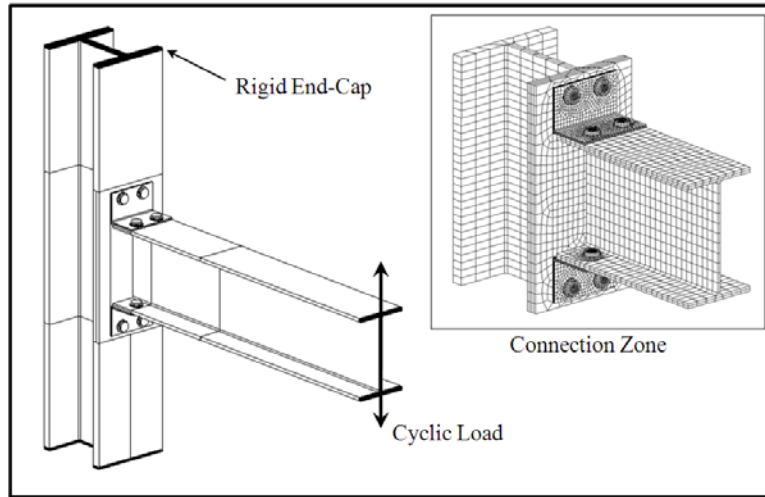
Figure 6.14 Top-and-seat angle connection finite element model, and mesh properties
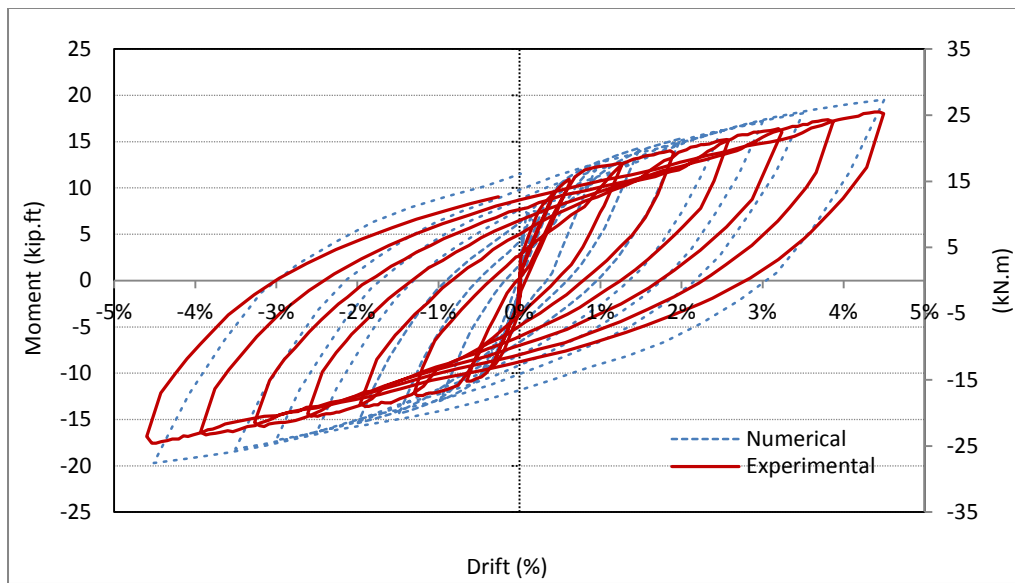
Figure 6.15 Comparison of FEM and Experimental hysteresis for Top-and-seat angle connection

6.4.3. Bolted/bolted double web angle connection

To model the behavior of the bolted/bolted double web angle connection under cyclic loading, a hot-rolled W24x104 cantilever beam is connected to a hot-rolled W14x159 column. This test specimen was bolted to both the beam web and the column flange using two 15 in

L5x5x¾ on both side of the web, as shown in Figure 6.16. This FEM is validated with the experimental results in Figure 6.17. The hysteresis results illustrated in Figure 6.17 shows a close correlation between the moment-curvature curves obtained from experimental testing and finite element analysis. The percentage difference between the hysteresis loops obtained from FEM and experimental is 16%.
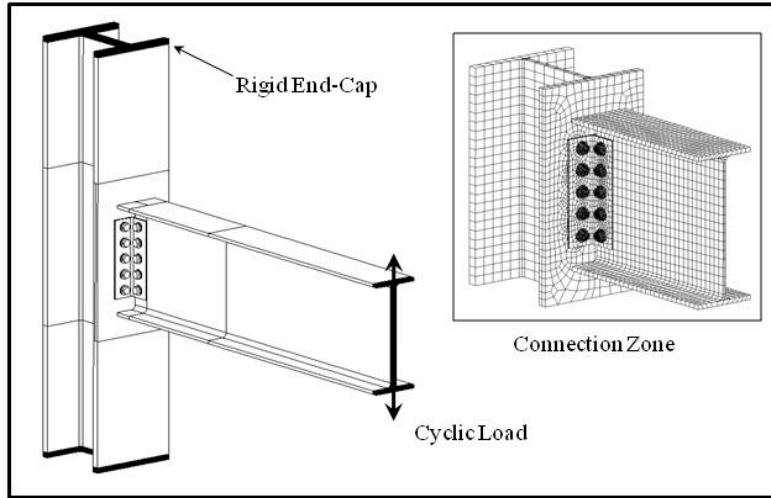
Figure 6.16 Bolted/bolted double web angle connection finite element model and mesh properties
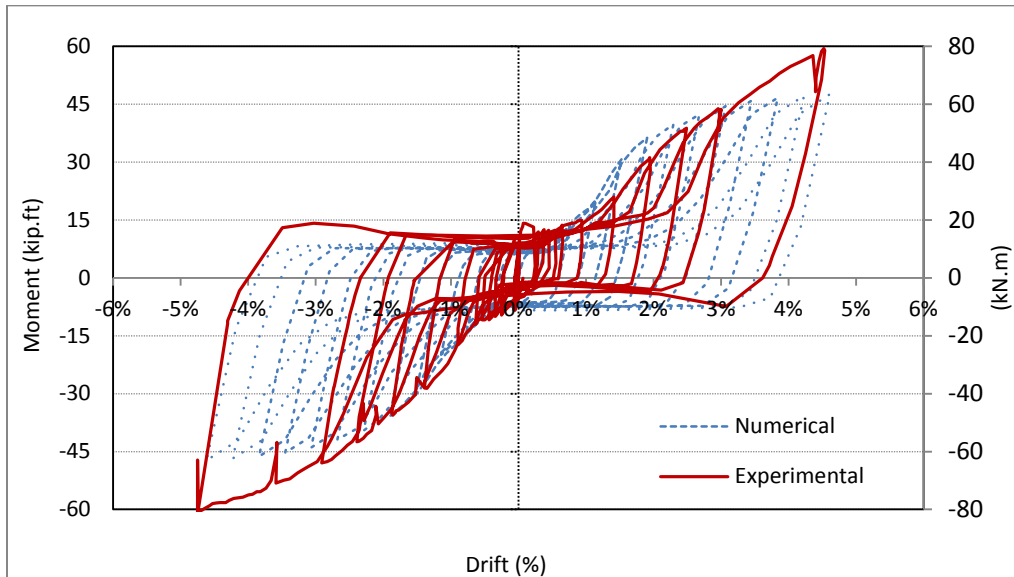
Figure 6.17 Comparison of FEM and Experimental hysteresis for Bolted/bolted double web angle connection

Abolmaali et al. (2003) discussed the formation of a flat region in the hysteresis loop of the bolted/bolted double web angle connections. This flat region is presented in Figure 6.17. This behavior is due to elongation of the beam web's bolt-holes (change in geometrical configuration of bolt holes from circular to oval shape), which causes the bolts to move freely in the bolt-holes during load reversal. The connection zone of the beam-web of this connection is presented in Figure 18, which shows that the bolt-holes undergo a large plastic deformation. This explains the sudden reduction of the stiffness in the connection during cyclic loading.
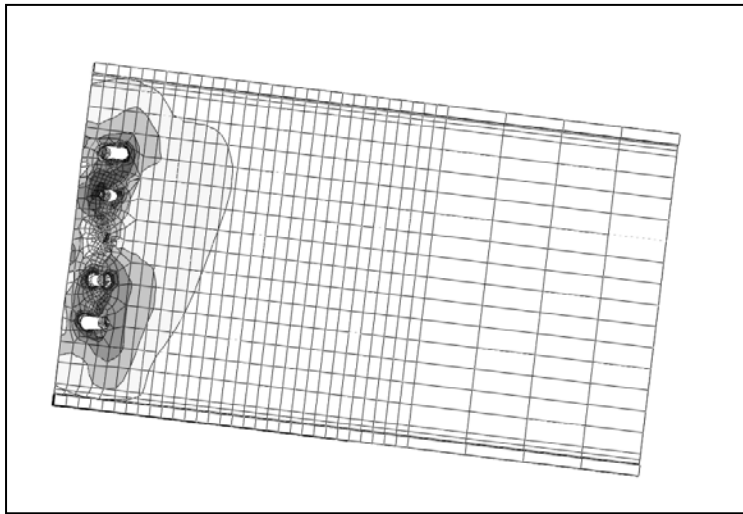
Figure 6.18 Deformation of the bolt-holes from round to oval due to excessive elongation in Bolted/bolted double web angle connection.

6.4.4. Welded-bolted double web angle connection

A 3-D finite element model of the welded-bolted double web angle connection is presented in Figure 6.19. A W24x104 hot-rolled cantilever beam is connected to a W14x159 column using two 15 in L5x5x¾ angle on both side of the web. The angles are welded to the beam-web and bolted to the column flange using eight ¾ in (19 mm) diameter high strength bolts.
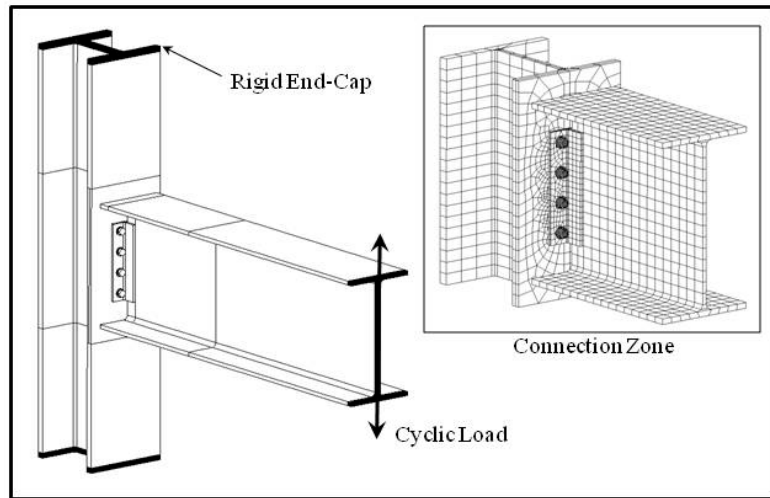
Figure 6.19 Welded-bolted double web angle finite element model

Figure 6.20 shows the comparison of the moment-rotation hysteresis loops obtained from the FEM with the experimental test. This figure also shows the close relationship between both hysteresis loops. The difference between the area under the outer loops of FEM and experimental is 9.3%.
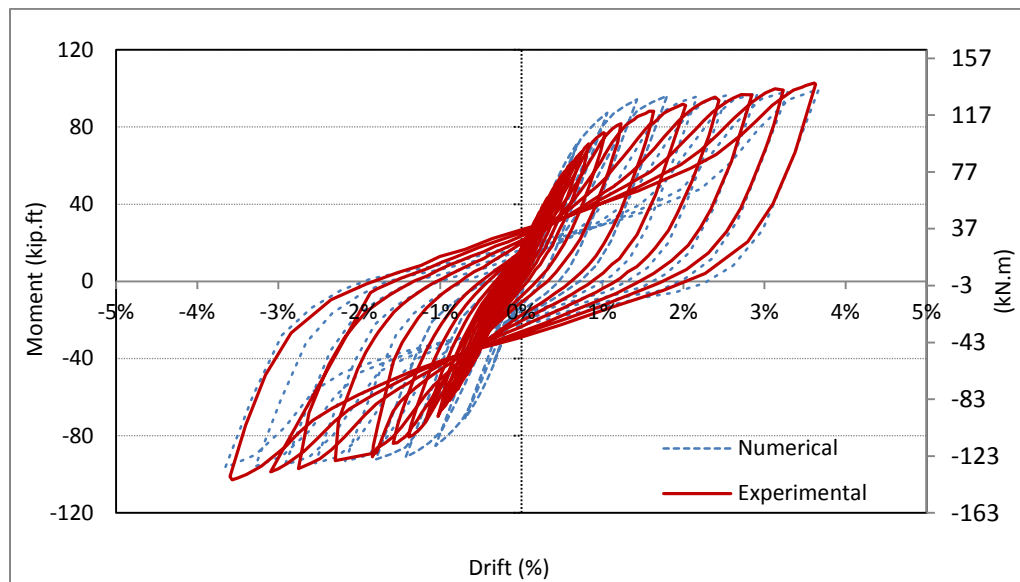
Figure 6.20 Comparison of FEM with Experimental hysteresis for welded-bolted double web angle connections

Further investigation conducted by Abolmaali et al. (2003) indicates that this model is failed due to excessive yielding of the angles. Same failure mode was observed during the finite element analysis as shown in Figure 6.21. During FEM analysis, the strains in bolts did not exceed the bolt ultimate strain until the experimental ultimate rotation was reached. This verifies that the FEM simulates the experimental behavior.
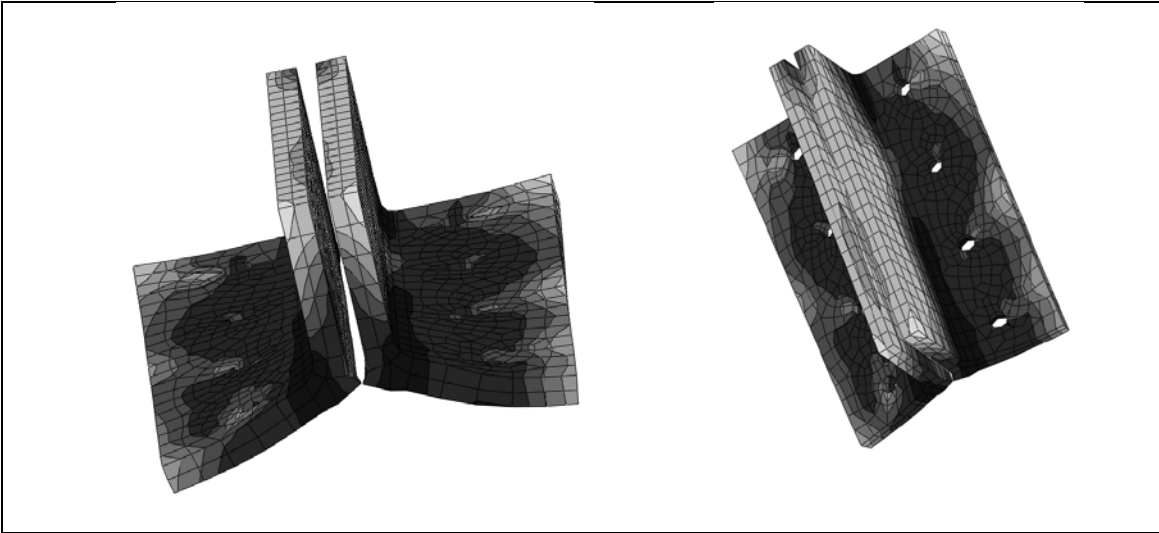
Figure 6.21: Failure of the angle due to excessive elongation in welded-bolted double web angle connection

6.4.5. Flush end-plate connections

A 3-D finite element model of the flush end-plate connection is presented in Figure 22. A W18x46 hot-rolled cantilever beam is connected to a W14x159 column using a 3/8 in. flush end-pate and eight ¾ in. high strength bolts.
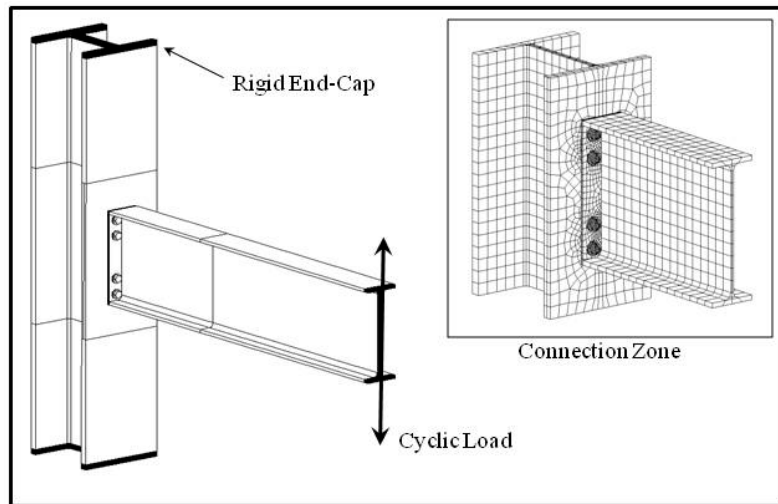
Figure 6.22 Flush end-plate connection finite element model and mesh properties

Figure 6.23 shows the results of the experiment test conducted on flush end-plate connection. In addition, the results of the applied moment versus the rotation of the end-plate of the same connection obtained from the numerical analysis are presented in this figure. A close examination of the results shows a satisfactory agreement between numerical and experimental results. The difference between outer areas of the hysteresis loops of the numerical and the experimental results is 5.6%.
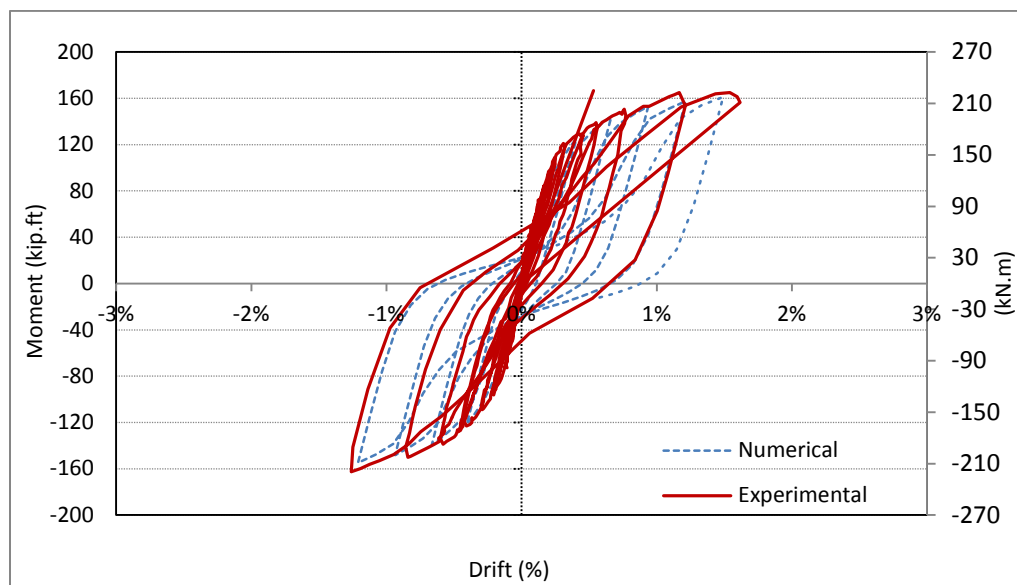
Figure 6.23 Comparison of FEM with Experimental hysteresis loops for extended end-plate connections

6.5. Conclusion for the simulation verification results

The results of this study showed excellent agreement between the moment-rotation hysteresis loops obtained from the FEM analysis and those obtained from experimental tests for all five types of semi-rigid connections. This includes the prediction of initial stiffness, unloading stiffness, and particularly the failure modes associated with each connection assembly. The energy dissipation characteristics of the connections were measured by the area under the outer loop of the moment-rotation hysteresis loops. The accuracy of the simulation capabilities presented here showed differences in the range of 3.5 and 16 percent when FEM and experimental results were compared for energy dissipation. The average difference was 9.2%.

In conclusion, results of this study confirmed that the moment-rotation hysteresis behavior of the steel connections might be well predicted by using an accurate 3D non-linear finite element analysis.

6.6. Behavior Semi-Rigid Connections Used in Hybrid Frame

In this section, semi-rigid connections for different beam sizes are selected based on the effective initial stiffness found in Chapter 5. The cyclic behavior of these connections is found using the nonlinear FEM tool. Then, a bilinear curve is fitted to the moment-rotation hysteresis loop of each connection. These curves will be used in global modeling of the hybrid frames.

For the purpose of selection of the type of semi-rigid connection, results of several experiments done by Abolmaali et al. and Chen et al. are studied. A schematic moment-rotation behavior for different types of bolted connections is also shown in Figure 6.24.

Based on the effective initial stiffness and ductility of the semi-rigid connections, top- and seat- angle with double web angle connections is found to be the best match for the purpose of this study.
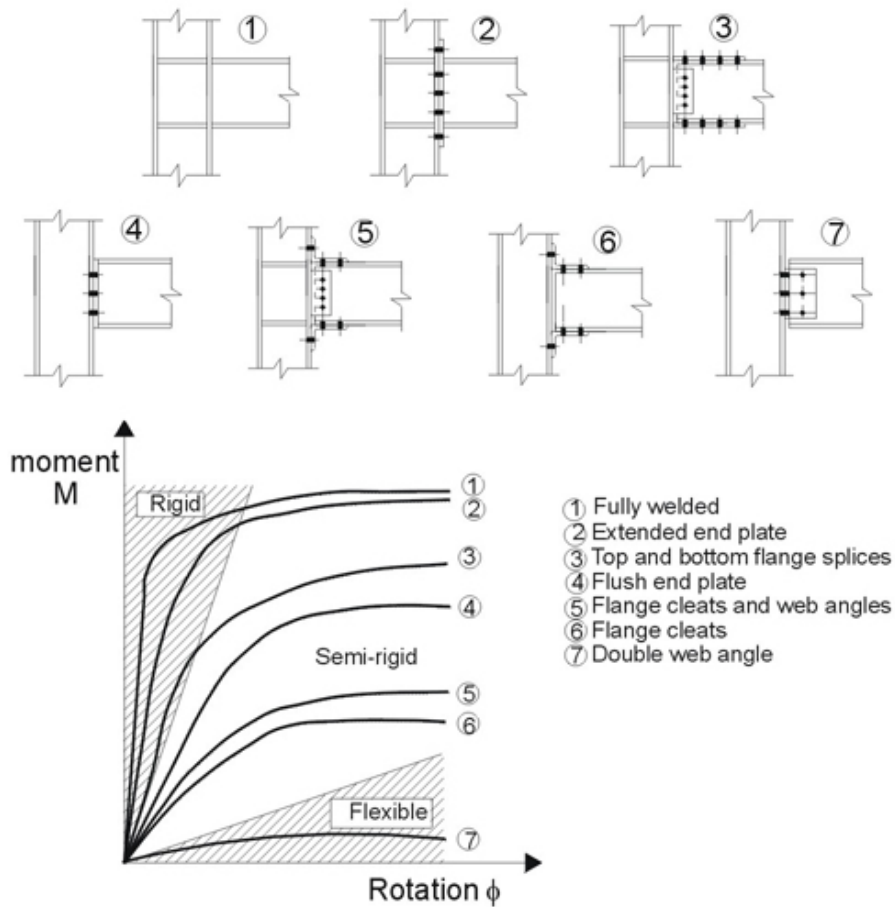
6.24 Moment-Rotation relationship for different semi-rigid connection types

The dimensions of the angles and bolts are initially selected from "the design tables for top-and seat-angle with double web-angle connections" prepared by Kim, Yosuk, and W-F. Chen (1998). To avoid pinching due to elongation of bolt-holes, as it was observed in the bolted-bolted double web angle connection experiment, the angles are welded to the beam's web and flanges. Then, the cyclic moment-rotation behavior of the connection for different beam sizes is obtained using nonlinear finite element analysis.

A typical sketch of the top- and seat- angle with double web angle connections selected for this study is shown in Figure 6.25. This connection is modeled for six different beam sections

of W21X50, W24X62, W27X84, W30X99, W33X141, and W36X150 that covers all the beam depths used in SAC frames.

A 3-D finite element model of the top- and seat- angle with double web angle connections is presented in Figure 6.26. A hot-rolled cantilever beam is connected to a W14x159 column using two 15 in L4x4x1/4 angle on both side of the web and two 8.3 in L4x4x1/4 on top and seat. The web angles are welded to the beam-web and bolted to the column flange using ten ¾ in (19 mm) diameter high strength bolts. The top- and seat- angles are also welded to the beam flange and bolted to the column flange using two ¾ in (19 mm) diameter high strength bolts.

Moment-rotation hysteresis loops for top- and seat- angle with double web angle obtained from the finite element analysis for the aforementioned six connections are shown in Figures 6.27 to 6.32. The connections properties are also summarized in Table 6-4. Finally, bolt forces for the connection for W21X50 beam section and the connection for W36X150 beam sections are presented in Figures 6.33 to 6.36. As show in these figures, bolts do not pass the yield force of 40 kip. The semi-rigid connection properties presented in Table 6-4 will be used on the hybrid frame models in Chapters 7, 8, and 9 of this dissertation.

Table 6.4 Semi-rigid connections properties

Beam Size	Θ_y	M_y (kip-in)	Θ_u	M_u (kip-in)	K_0	K_1
W21X50	0.003	1032	0.05	1750	344,000	15,277
W24X62	0.003	1203	0.05	2000	401,000	16,957
W27X84	0.003	1411	0.05	2250	470,333	17,851
W30X99	0.003	1584	0.05	2450	528,000	18,426
W33X141	0.003	1920	0.05	2900	640,000	20,851
W36X150	0.003	2080	0.05	3300	693,333	25,957
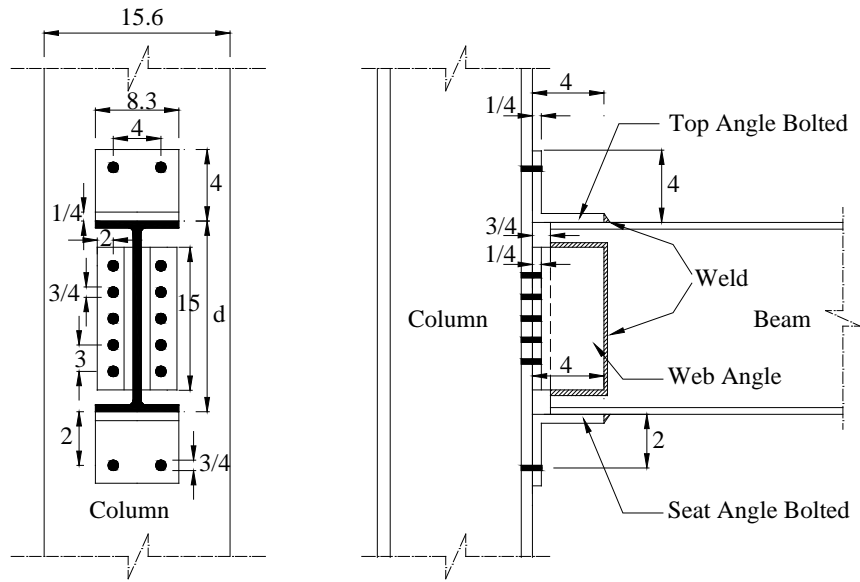
6.25 Typical sketch of top- and seat- angle with double web angle connections
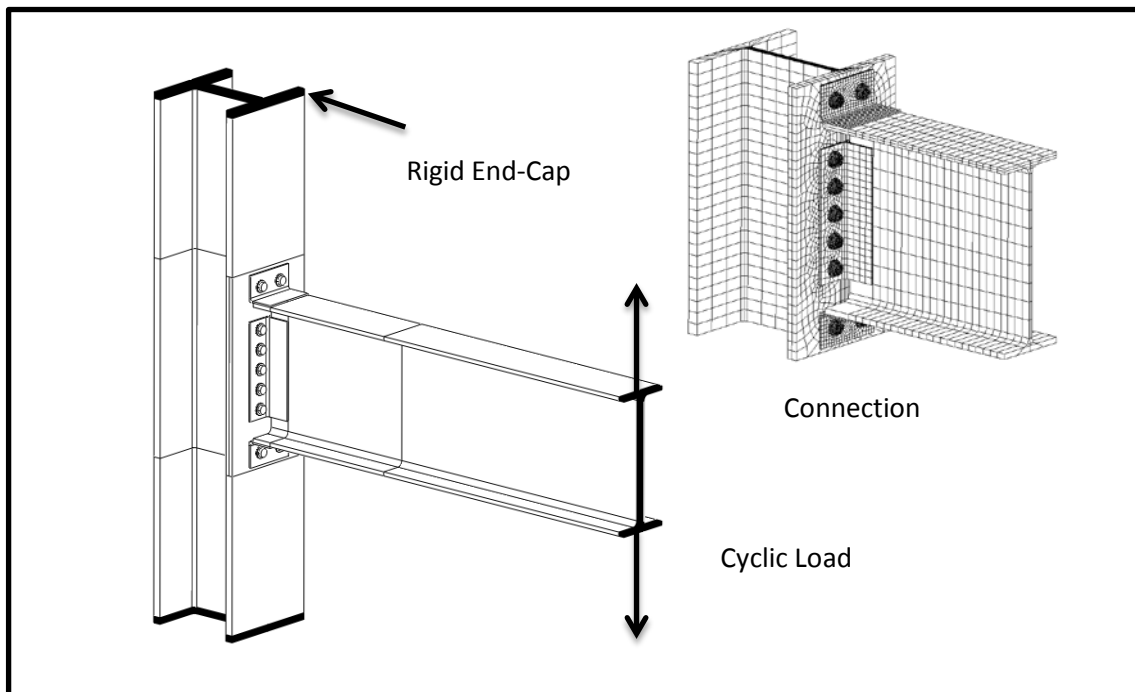
6.26 Top- and seat- angle with double web angle finite element model, and mesh properties
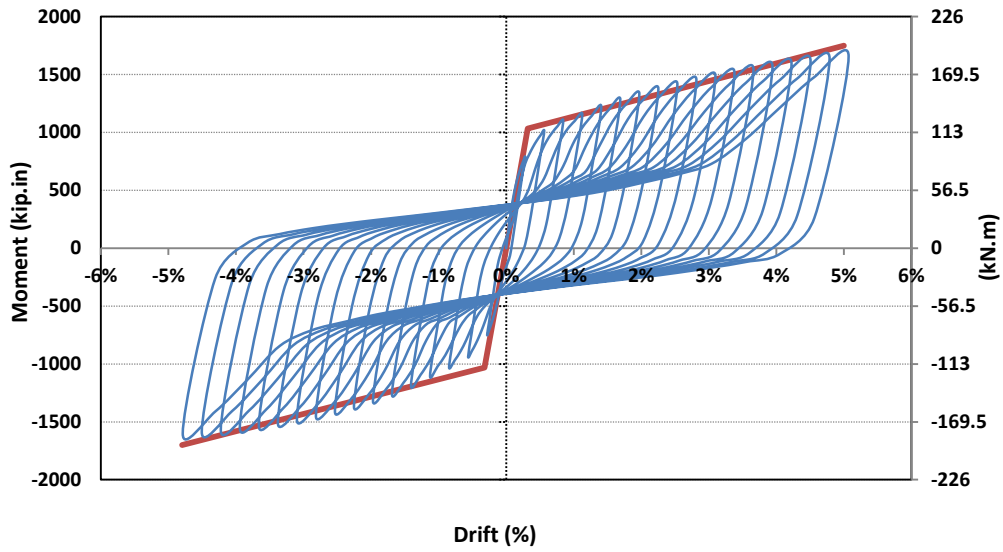
6.27 FEM hysteresis loops for top- and seat- angle with double web angle with W21X50
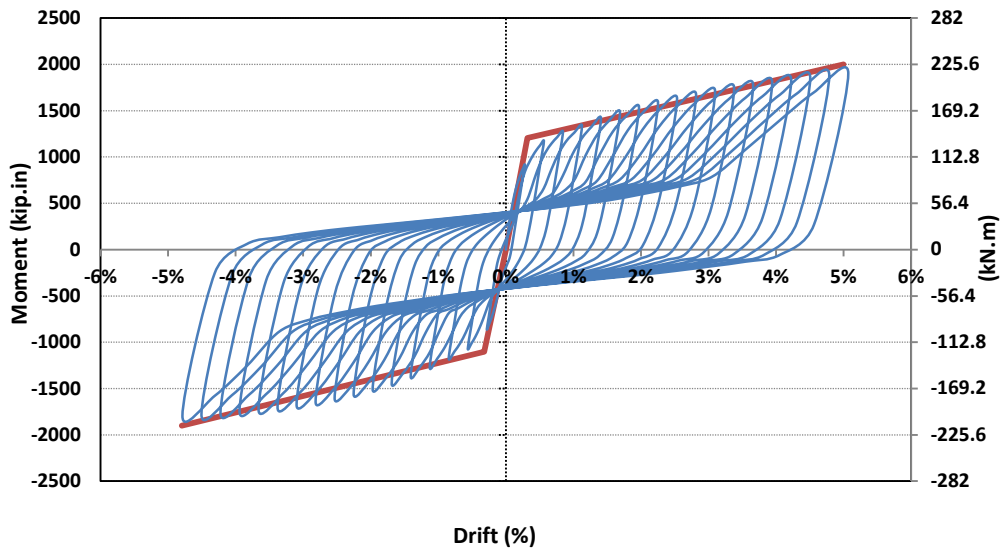
6.28 FEM hysteresis loops for top- and seat- angle with double web angle with W24X62

121
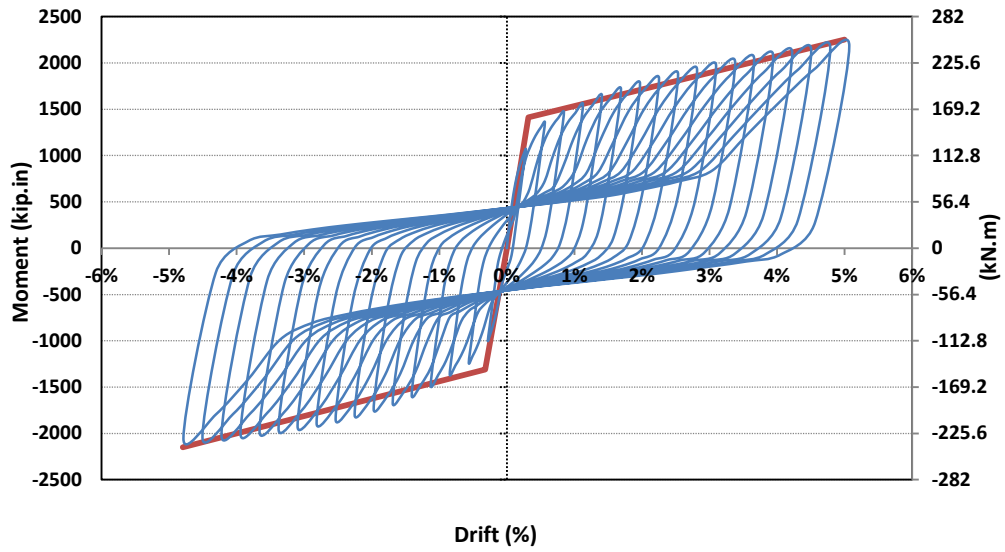
6.29 FEM hysteresis loops for top- and seat- angle with double web angle with W27X84
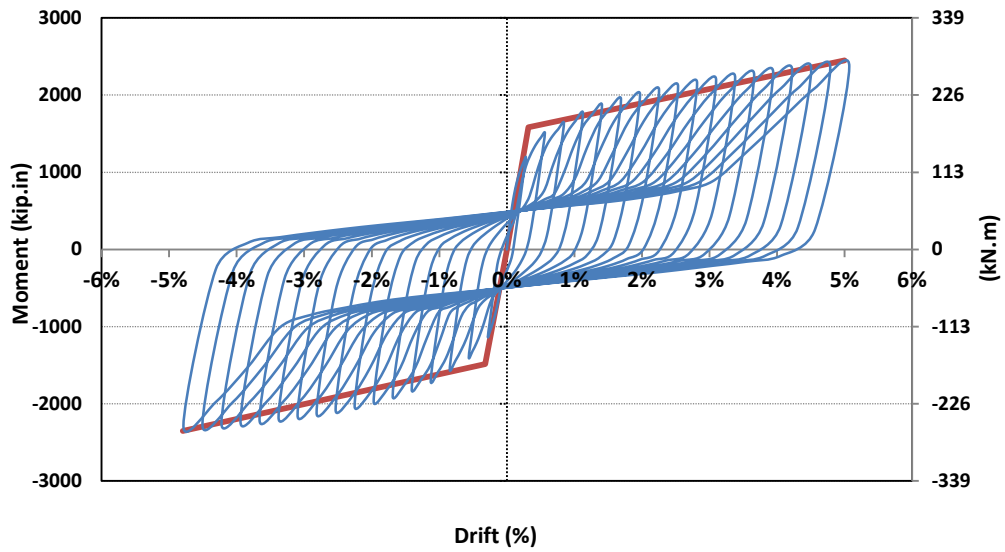
6.30 FEM hysteresis loops for top- and seat- angle with double web angle with W30X99
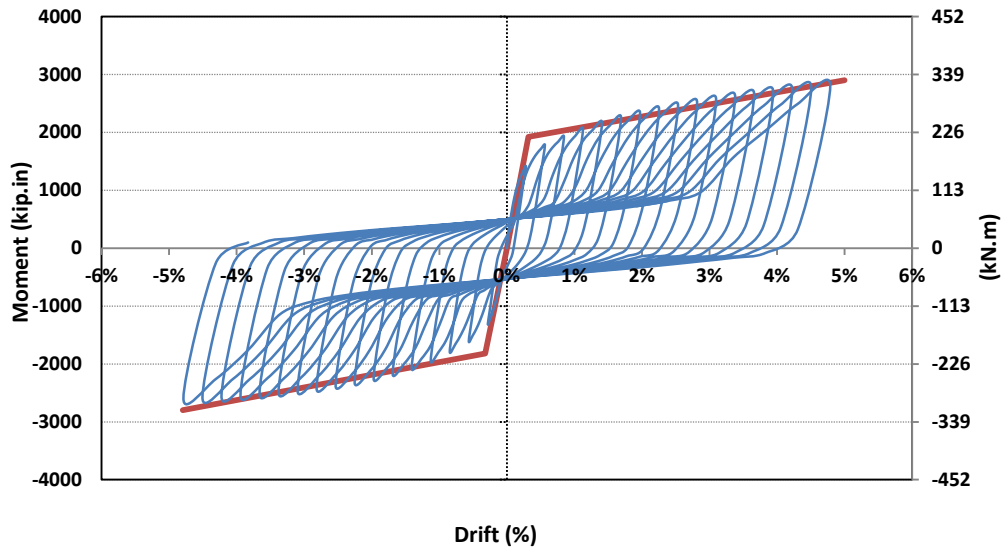
6.31 FEM hysteresis loops for top- and seat- angle with double web angle with W33X141
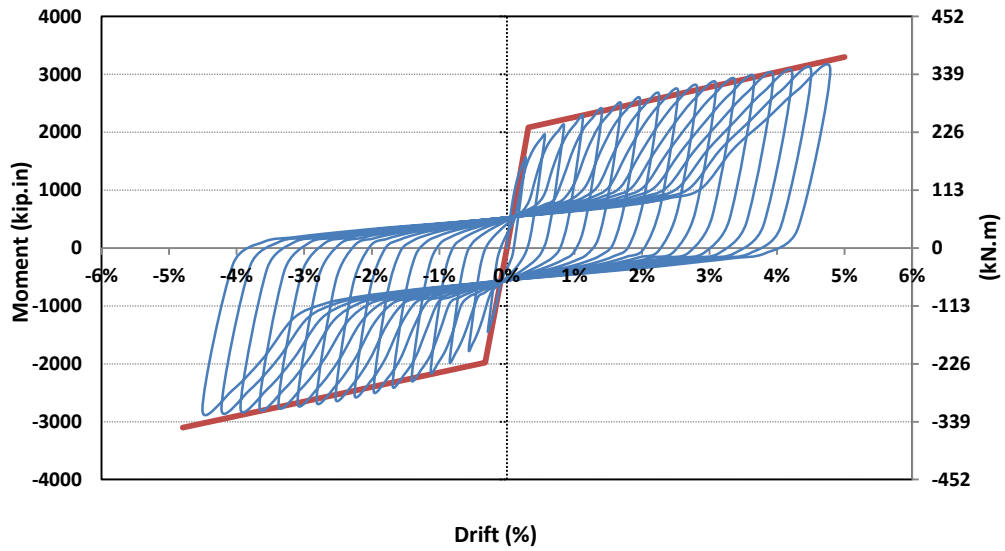
6.32 FEM hysteresis loops for top- and seat- angle with double web angle with W36X150
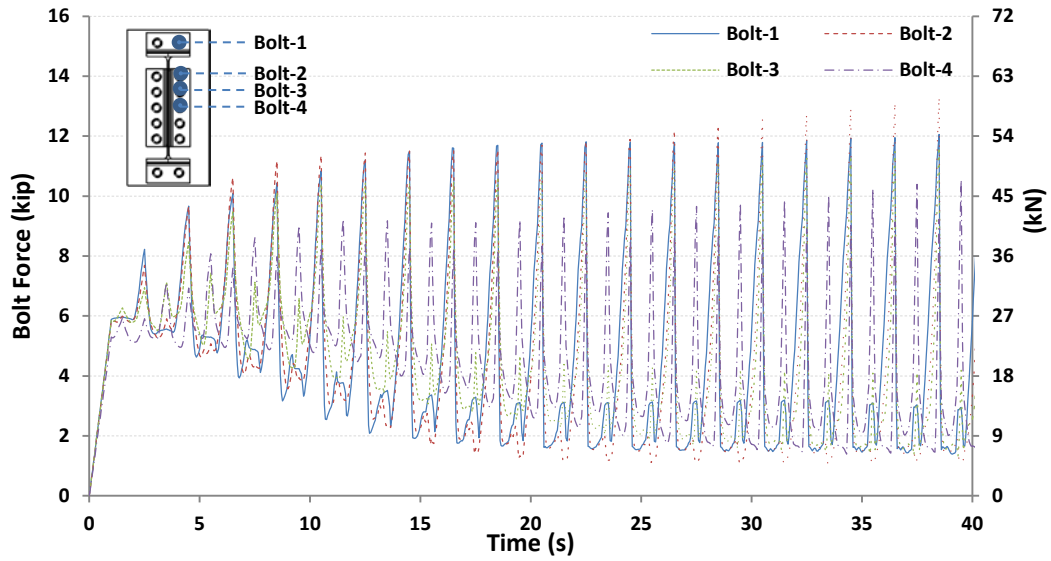
Figure 6.33 Variation of bolt forces versus loading time for the connection with W21X50 beam

(a)

(b)

(c)

(d)
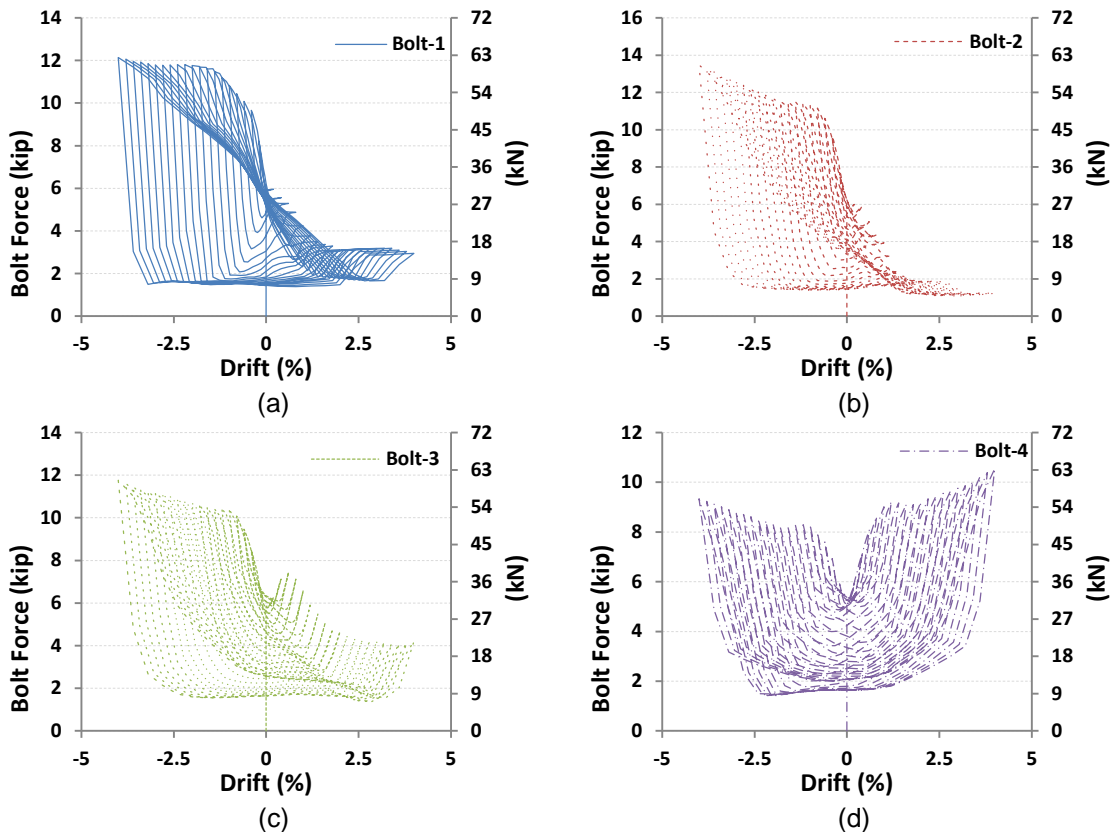
Figure 6.34 Bolt forces versus drift for the connection with W21X50 beam
(a) Bolt-1, (b) Bolt-2, (c) Bolt-3, and (d) Bolt-4
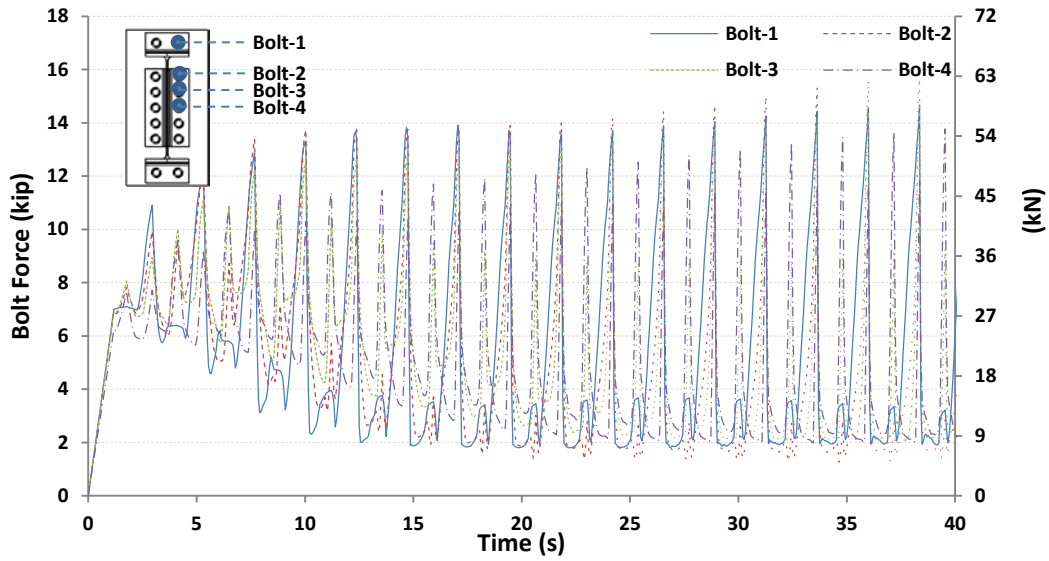
Figure 6.35 Variation of bolt forces versus loading time for the connection with W36X150 beam
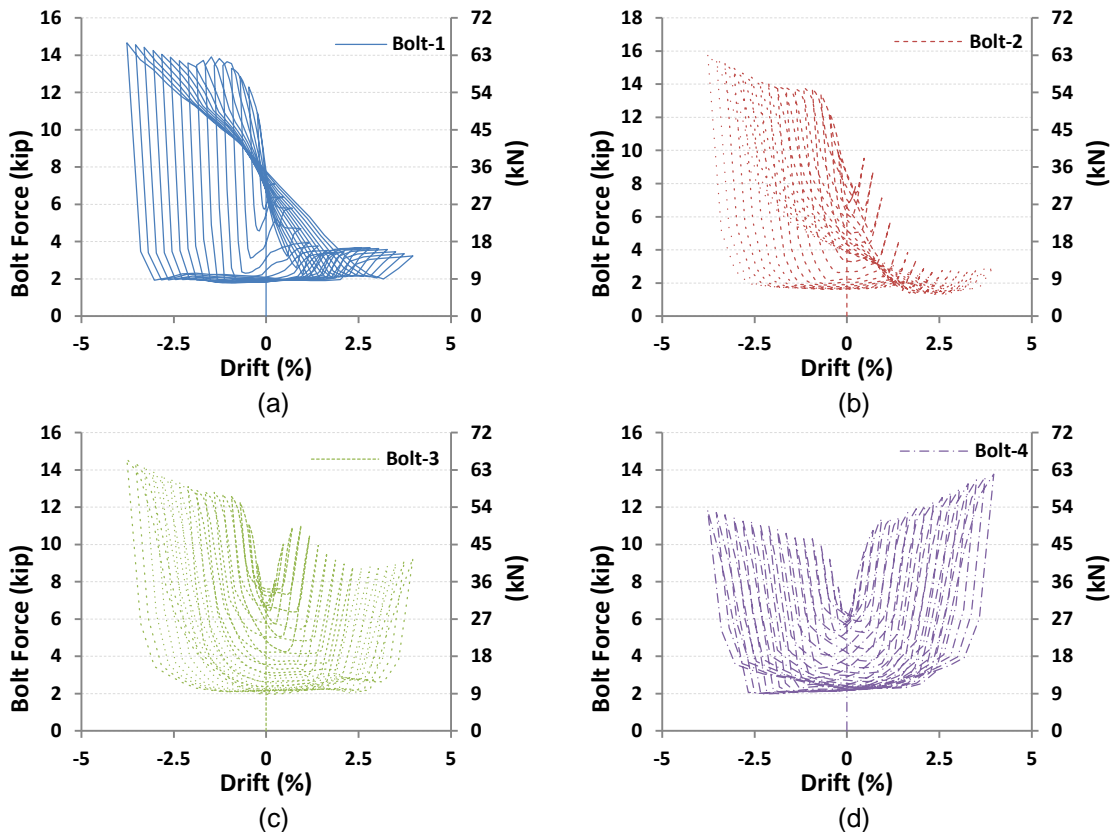
Figure 6.36 Bolt forces versus drift for the connection with W36X150 beam
(a) Bolt-1, (b) Bolt-2, (c) Bolt-3, and (d) Bolt-4

CHAPTER 7

LOCAL AND GLOBAL RESPONSES OF HYBRID FRAMES

This chapter focuses on the quantification of seismic demands at the structural and component levels for 3-, 9-, and 20-story rigid SAC frame structures located in Los Angeles site and their corresponding hybrid frames. The behavior and response of these structures is studied by subjecting the nonlinear analytical models of these structures to two sets of ground motions. Each set of ground motion consists of 20 records. These sets are representative of two different hazard levels of 10 percent probability of exceedance in 50 years (DBE) and 2 percent probability of exceedance in 50 years (MCE). The characteristics of the ground motions were presented in Chapter 4 of this dissertation in details. In addition, nonlinear static analysis (pushover analysis) is used to identify the strength, stiffness, and ductility of these frames. The semi-rigid connections, which were designed for different beam sizes in Chapter 6, are implemented in the hybrid frame models. Finally, the seismic demands of hybrid frames with the most effective semi-rigid connection patterns, as identified in Chapter 5, are compared with the seismic demands in their corresponding rigid frames.

7.1. Modal Properties

The modal characteristics of different structures are listed in Table 7.1. Since the seismic mass of structures of a particular number of stories remains constant in different models, a comparison of first mode periods reflects the differences in initial elastic stiffness of models. As the period of a structure increases, its initial elastic stiffness decreases. In hybrid frames, 20 to 33 percent of the rigid connections are replaced by the more flexible semi-rigid connection; thus, the first mode period of hybrid frames are expected to be greater than the first mode period of their corresponding rigid frames. Comparison of the tabulated first mode period of structures shows a difference of 6 to 13 percent between the period of hybrid frames and their corresponding rigid frames. The differences between the higher mode periods of the hybrid and rigid frame structures are less than 6 percent. The modal effective mass percentage is similar for different structures with the same number of stories.

Table 7.1 Modal Characteristics of Hybrid and SAC frame structures

Model Name	Period (s)			Modal Mass (Percentage)		
	First Mode	Second Mode	Third Mode	First Mode	Second Mode	Third Mode
SAC3-Rigid	1.104	0.3302	0.163	0.8134	0.1451	0.04125
HSAC3-4	1.18	0.3412	0.164	0.8064	0.151	0.0418
HSAC3-5	1.203	0.3453	0.164	0.8051	0.151	0.04386
SAC9-Rigid	2.344	0.8673	0.4982	0.819	0.1149	0.03854
HSAC9-4	2.49	0.9131	0.5203	0.8136	0.1166	0.04009
HSAC9-5	2.482	0.9128	0.5226	0.8166	0.1153	0.0385
SAC20-Rigid	3.911	1.353	0.7883	0.7871	0.1186	0.0373
HSAC20-4	4.445	1.486	0.8427	0.7717	0.1301	0.0386
HSAC20-5	4.172	1.441	0.838	0.787	0.1166	0.03725

<u>7.1.Nonlinear Static Response (Pushover)</u>

Nonlinear static (pushover) analysis is a seismic evaluation method in which a frame is pushed to a specified displacement level using a predetermined load pattern. The deformation and base-shear are calculated using an inelastic incremental static analysis. The load pattern approximately represents the inertial forces developed in location of substantial masses. In this study, pushover analysis is performed using the load pattern suggested in the NEHRP1994 document. The governing equation for the load pattern is

$$C_x = \frac{w_x h_x{}^k}{\sum_{i=1}^{n} w_i h_i{}^k}$$

Equation 7.1

in which C_x is the normalized load at the floor level of x, w_x and w_i are seismic weights at floor levels x and i respectively. h_x and . h_i are the height of the x and i stories from ground level, respectively. The coefficient k depends on the period of the frames and dictates the shape of the load pattern. For a frame with the first mode period of equal or less than 0.5, a coefficient of $k = 1$ is assumed, which results in a triangular pattern. On the other hand, for frames with the first mode period of more than 2.5, $k = 2$ is considered which results in a parabolic load distribution pattern. In this study, load patterns are calculated using a k value of 2, for all rigid and hybrid frames.

<u>7.2.Pushover Responses</u>

A global pushover curve visualizes the normalized base shear (base shear normalized by structural seismic weight, V/W) versus roof (global) drift angle (the roof displacement divided by the height of structure). The global pushover curves for 3-, 9-, and 20-story structures are shown in Figures 7.1, 7.2, and 7.3, respectively. The pushover curves for 3-story structures in Figure 7.1 shows there is a little difference in the response of HSAC3-4 and HSAC3-5 structures. The initial stiffness and maximum strength of the hybrid frames are less than those

128

of the rigid frame. The initial stiffness of HSAC3-4 and HSAC3-5 are 14 and 16 percent less than the stiffness of rigid frame, respectively. In addition, the maximum strength of the HSAC3-4 and HSAC3-5 frames is 15 and 17 percent less than the maximum strength of SAC rigid frame. The observed reductions in the initial stiffness and maximum strength of the hybrid frames were expected due to the fact that the hybrid frames used in this study are generated by substituting two rigid connections with two more flexible and less strength semi-rigid connections at each story level. The second observation was that two hybrid and the rigid 3-story models exhibit a negative post-yield stiffness in their pushover curves. Although, the material model for plastic hinges in beams and columns, panel zones, and semi-rigid connections includes a post-yield strain-hardening, the stiffness reduction due to p-delta effect governs; thus, the total post-yield stiffness is negative. The third observation is that the rigid model attains a negative post-yield stiffness at the global drift of 1.7 percent while the negative stiffness for hybrid frames starts at the global roof drift of 2.1 percent.

A very similar response is also observed for HSAC9-4 and HSAC9-5 models in Figure 7.2. The initial stiffness of HSAC9-4 and HSAC9-5 are 11 and 10 percent less than the stiffness of rigid frame, respectively. In addition, the maximum strength of the HSAC9-4 and HSAC9-5 frames is 11 and 12 percent less than the maximum strength of SAC rigid frame.

The initial stiffness of HSAC20-4 and HSAC20-5 frames is reduced by 25 and 12 percent if compared with the 20-stroy rigid frame, respectively. The maximum strength of these two models is also 15 and 14 percent less than the maximum strength of the rigid frame. The post yield negative stiffness in the 20-story rigid frame starts at global rood drift of 1.1 percent while the negative stiffness of hybrid frames starts at 1.3 percent.

In conclusion, the initial stiffness and maximum strength of the hybrid frames are between 11 to 25 percent less than the same responses in their corresponding rigid frames when they are subjected to a static load.
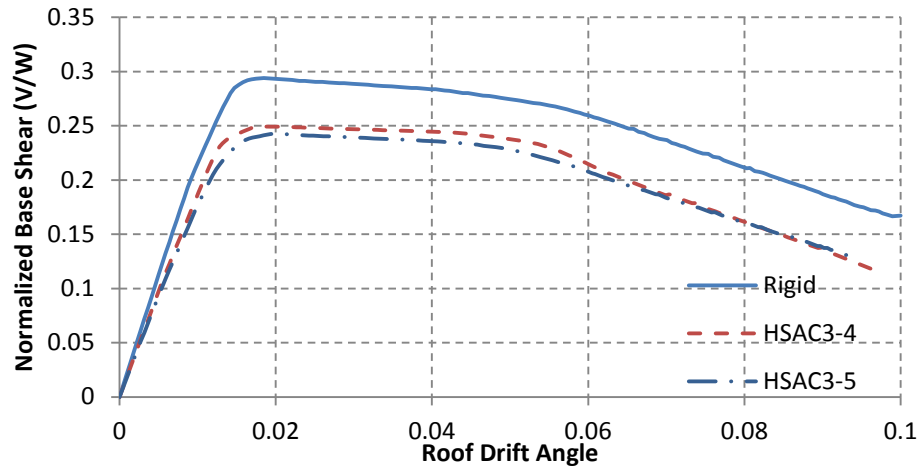
Figure 7.1 Global Pushover Curves for LA 3-story Structures
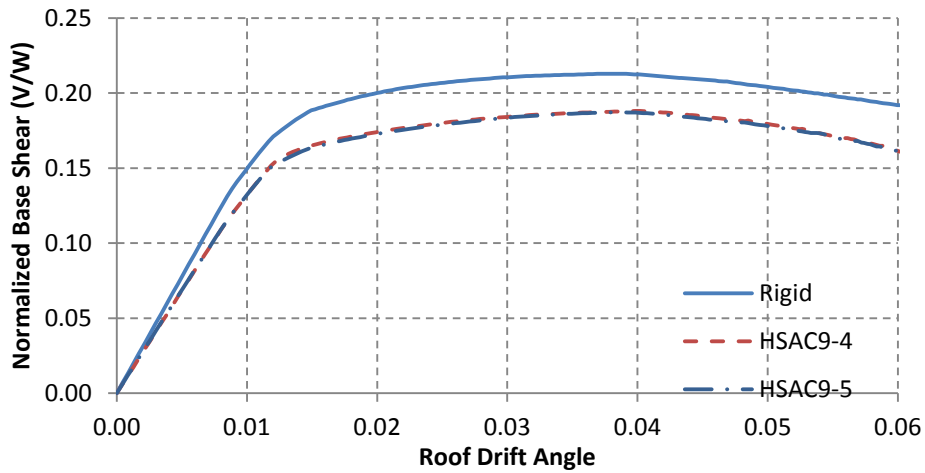
Figure 7.2 Global Pushover Curves for LA 9-story Structures
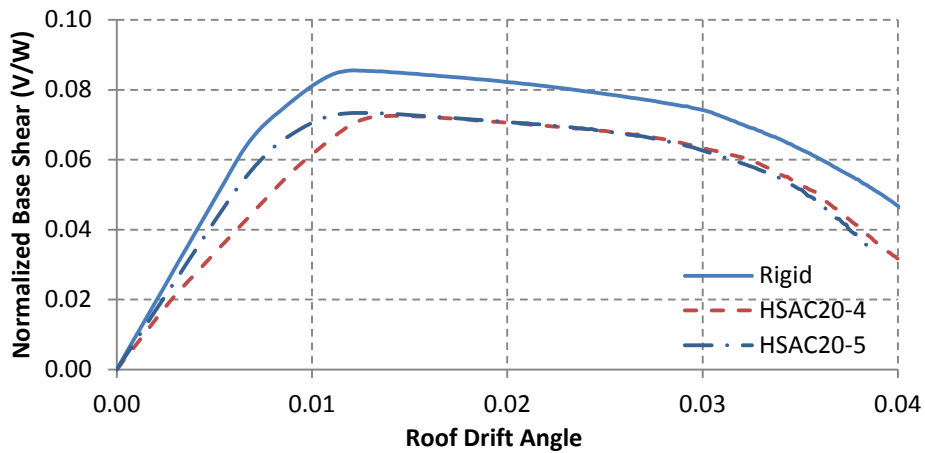
Figure 7.3 Global Pushover Curves for LA 20-story Structures

<u>7.3. Drifts</u>

The inter-story drift, which expressed in terms of lateral relative displacement of a story divided by the height of the story, is believed to be the best measurement for quantifying the seismic behavior of moment resisting frame structures. Not only the structural stability and overall performance of a frame can be related to the inter-story drift, but also it provides a good estimate on the structural members' forces and deformations. In addition, the performance of the non-structural members such as infill partitions and utility lines under seismic excitations is related to the inter-story drifts. In this study, the selected hybrid frames and their corresponding rigid frames are analyzed utilizing a nonlinear time history analysis. The story-drift angle demands are evaluated for two sets of ground motions (DBE and MCE). For each frame and each set of ground motions, the expected value (average) of inter-story drift is computed in all story levels. The frames are expected to maintain the life-safety (LS) and collapse-prevention (CP) performance level under the sets of DBE and MCE ground motions, respectively. The allowable inter-story drift limits for the LS and CP performance levels are 2.5 and 5 percent, respectively.

7.3.1. Drift Demands Results and Discussion

The maximum inter-story drift angle over the height of the SAC 20-story, HSAC20-4, HSAC20-5 buildings subjected to the set of DBE ground motions are illustrated in Figures 7.4 to 7.6 , respectively. Each figure shows the drift demand resulted from 20 different nonlinear time history analysis as well as the expected value of the maximum story-drifts. Figure 7.7 compares the expected values of the maximum story-drift angle demands for 20-story structures subjected to DBE set of ground motions. As shown in the figure, based on the average value of drift demands, all three structures satisfy the life-safety performance level, which equals to an inter-story drift of 2.5 percent, under DBE hazard level.

131
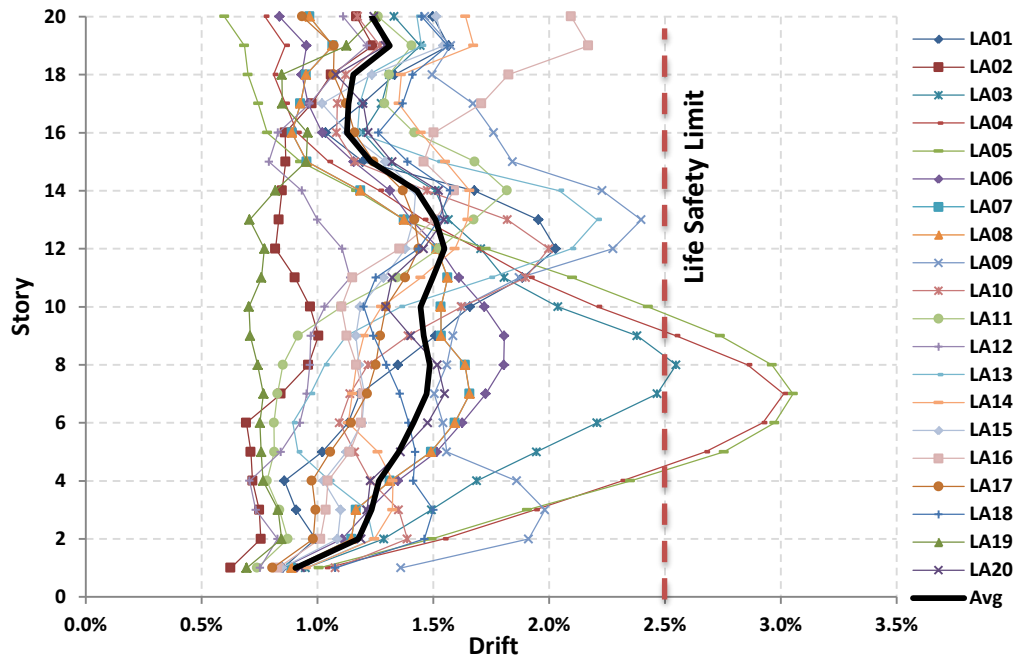
Figure 7.4 Maximum Story Drift Angle Demands for SAC 20-story Structure subjected to DBE set of Ground Motion
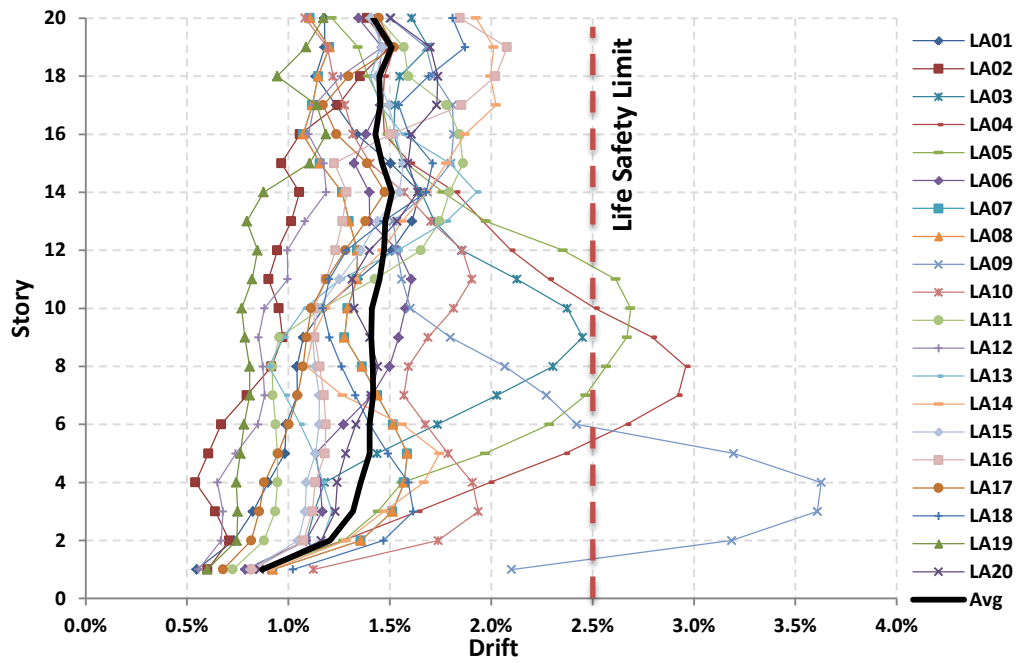
Figure 7.5 Maximum Story Drift Angle Demands for HSAC20-4 Structure subjected to DBE set of Ground Motion
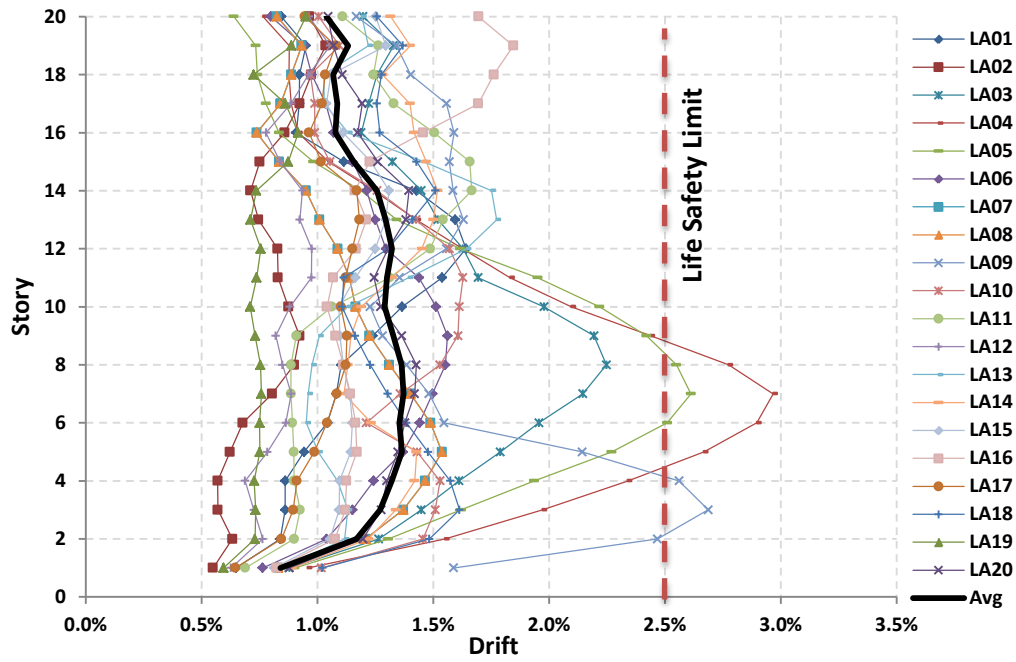
Figure 7.6 Maximum Story Drift Angle Demands for HSAC20-5 Structure subjected to DBE set of Ground Motion
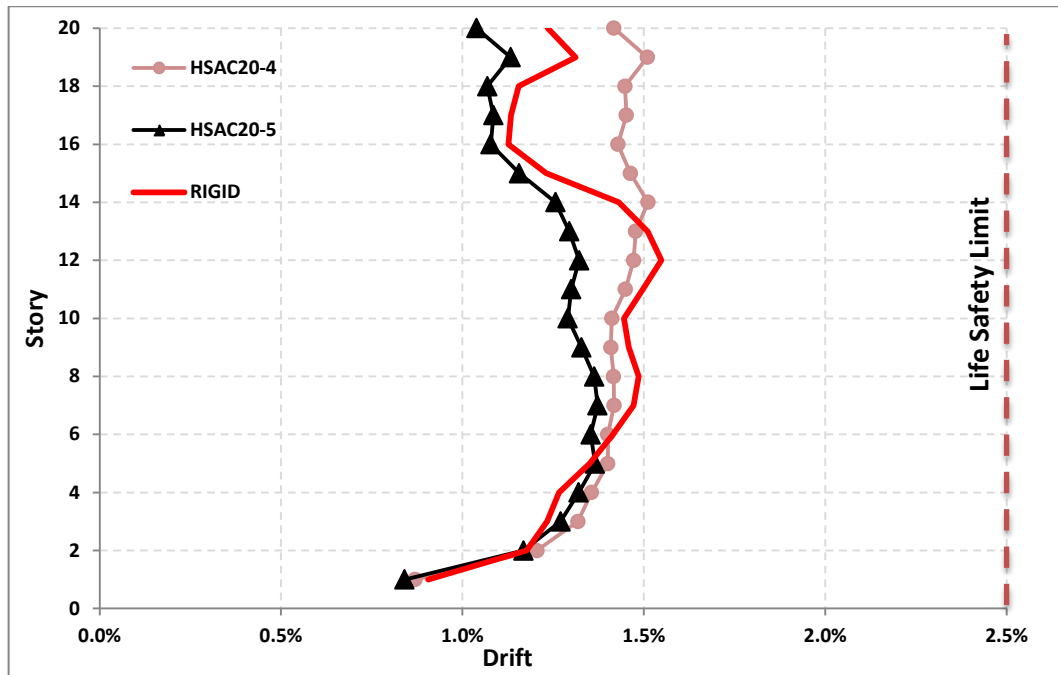
Figure 7.7 Expected Values of Maximum Story Drift Angle Demands for 20-story Structures Subjected to DBE set of Ground Motion

133

The maximum inter-story drift angle over the height of the SAC 20-story, HSAC20-4, HSAC20-5 buildings subjected to the set of MCE ground motions is illustrated in Figures 7.8 to 7.10 , respectively. Figure 7.11 summarizes the expected values of maximum story-drift angle demands for 20-story structures subjected to MCE set of ground motion. As shown in these figures, the average drift demands of hybrid frames satisfy the collapse-prevention (CP) performance limit while the original rigid sac frame fails to satisfy the criteria. In addition, as shown in Figure 7.8, the SAC 20-story frame model collapses under records LA30, LA35, and LA36. In this study, collapse is defined as formation of plastic hinges in all columns of two different stories of a frame. This phenomenon causes a large story drift (more than 10 percent) in a frame that makes it unstable. Although 20-story hybrid frames fail to pass the CP performance limit under a few earthquake records, collapse is not seen on any analyses cases. The maximum inter-story drift angle over the height of the 3- and 9-story frames under two sets of ground motions are illustrated in Figures 1 to 12 of Appendix A. The summary of average drift demands for 3- and 9-story frames is also presented in Figures 7.12 to 7.15.

As shown in Figures 7.12 and 7.13, the 9-story rigid SAC frame and its corresponding hybrid frames are all satisfy the LS and CP performance level under DBE and MCE sets of ground motions, respectively.

Figures 7.14 and 7.15 show the average drift demand over the height of 3-story frames subjected to DBE and MCE sets of ground motion, respectively. As shown in these figures, the original rigid SAC frame has a superior performance in compare with the corresponding hybrid frames. The expected values of drift demands for the rigid frame satisfy the LS and CP criteria under DBE and MCE ground motions, respectively; while, the hybrid frames are failed to satisfy criteria under both sets of ground motions.
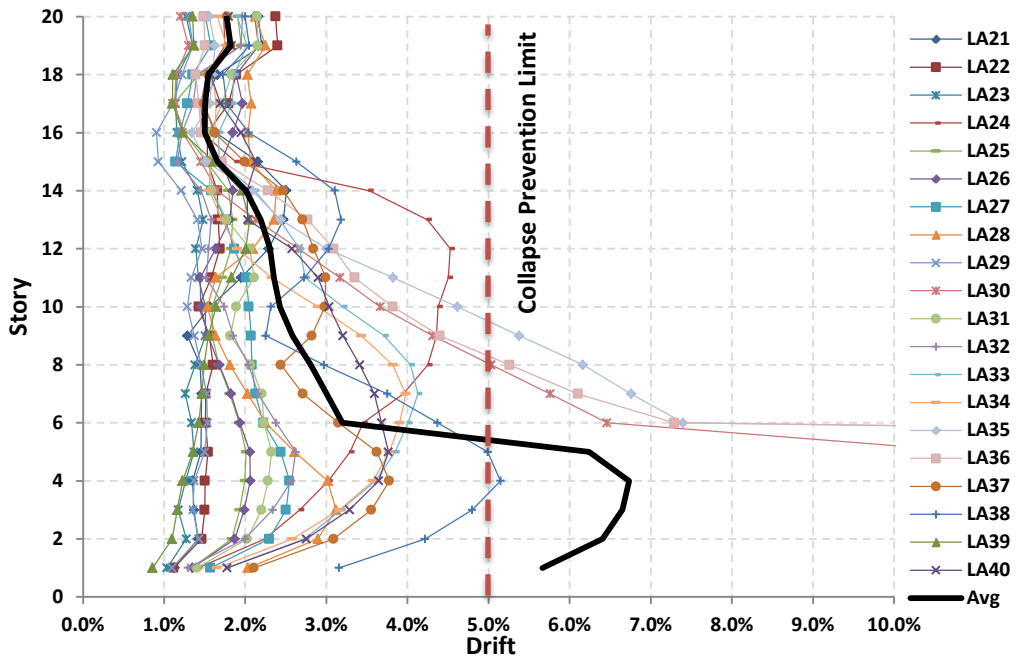
Figure 7.8 Maximum Story Drift Angle Demands for SAC 20-story Structure subjected to MCE set of Ground Motion
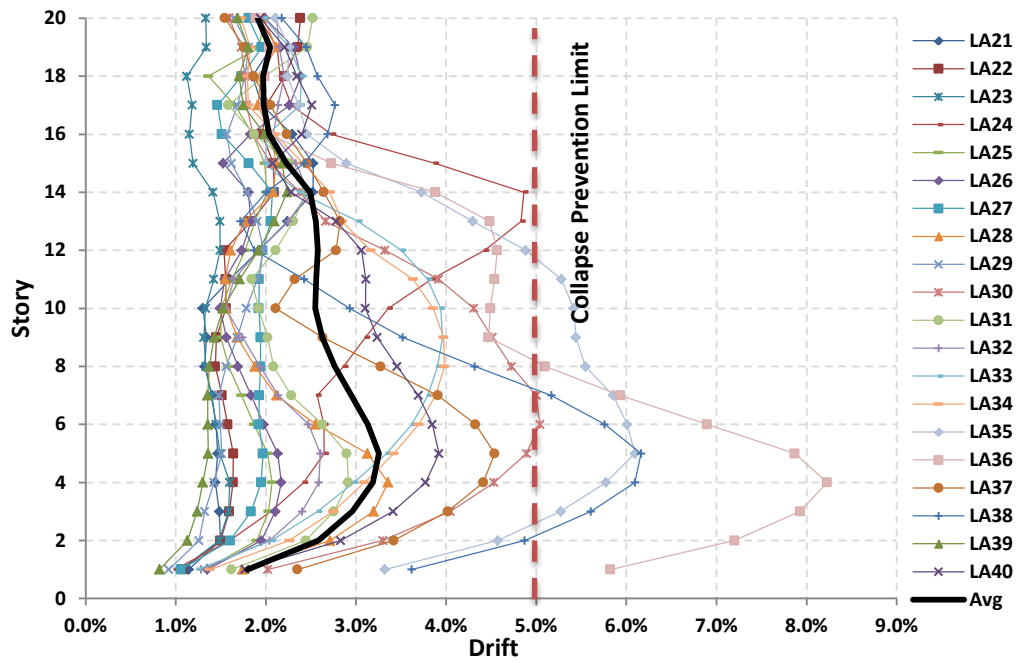
Figure 7.9 Maximum Story Drift Angle Demands for HSAC20-4 Structure subjected to MCE set of Ground Motion
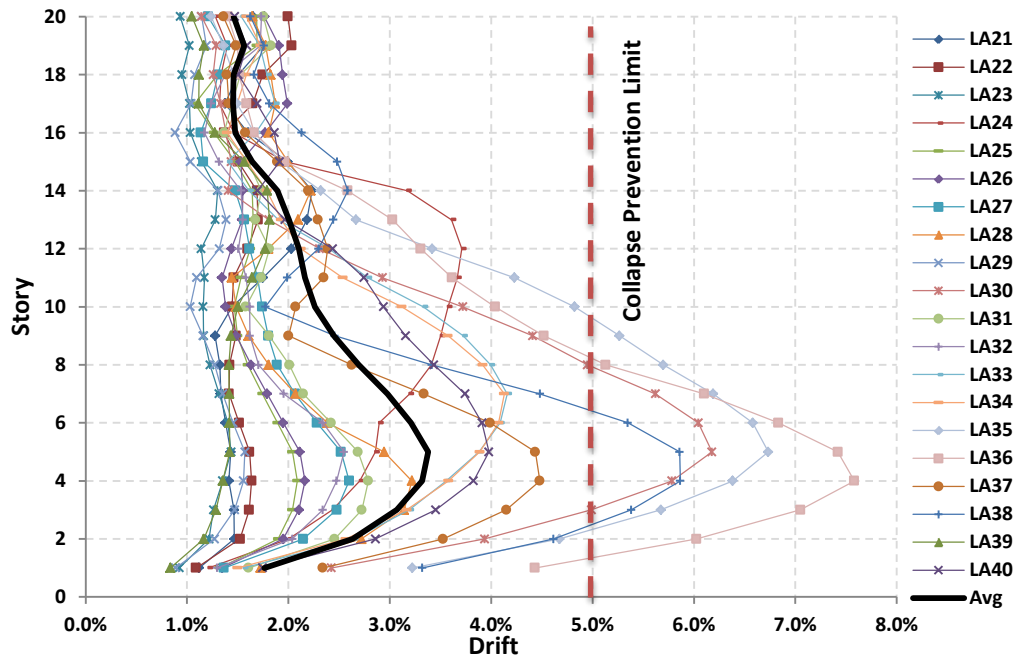
Figure 7.10 Maximum Story Drift Angle Demands for HSAC20-5 Structure subjected to MCE set of Ground Motion
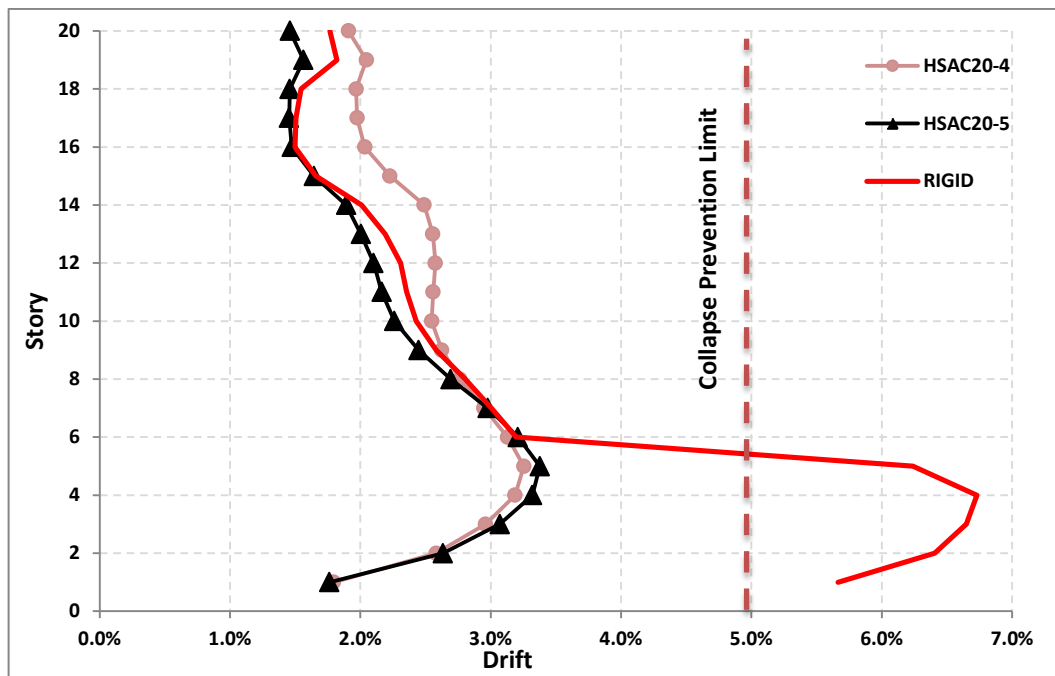
Figure 7.11 Expected Values of Maximum Story Drift Angle Demands for 20-story Structures Subjected to MCE set of Ground Motion
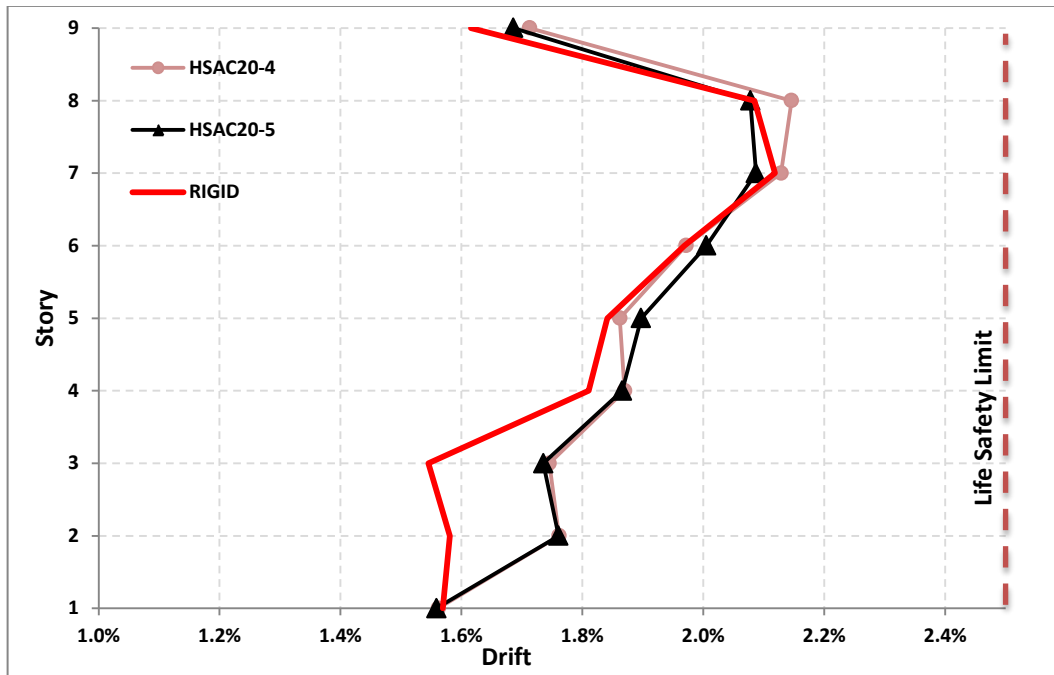
Figure 7.12 Expected Values of Maximum Story Drift Angle Demands for 9-story Structures Subjected to DBE set of Ground Motion
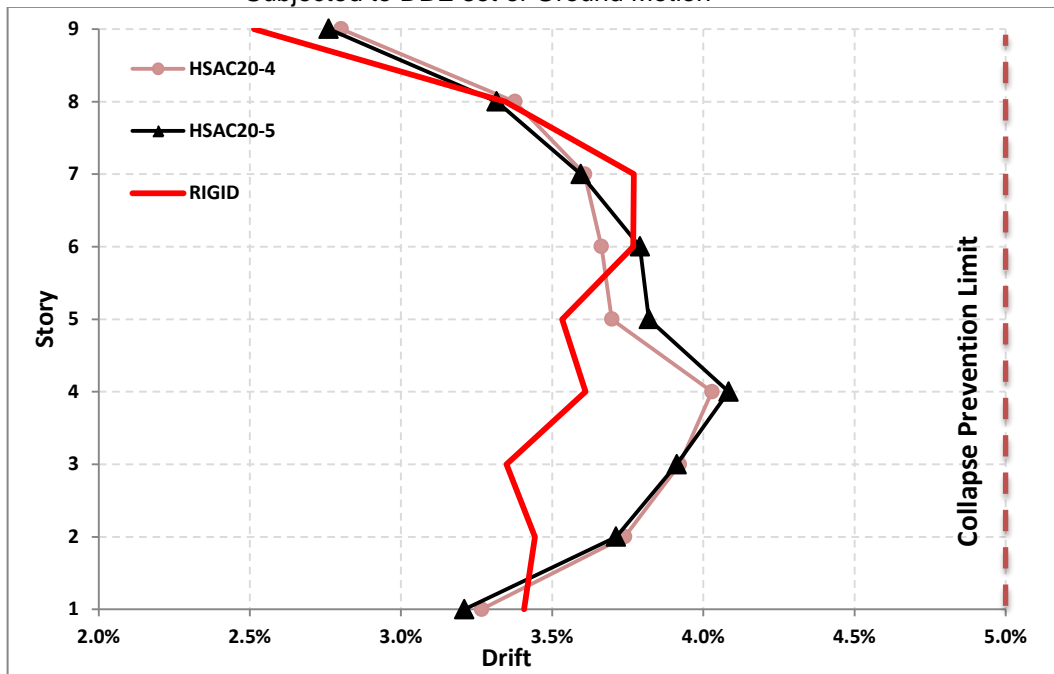
Figure 7.13 Expected Values of Maximum Story Drift Angle Demands for 9-story Structures Subjected to MCE set of Ground Motion
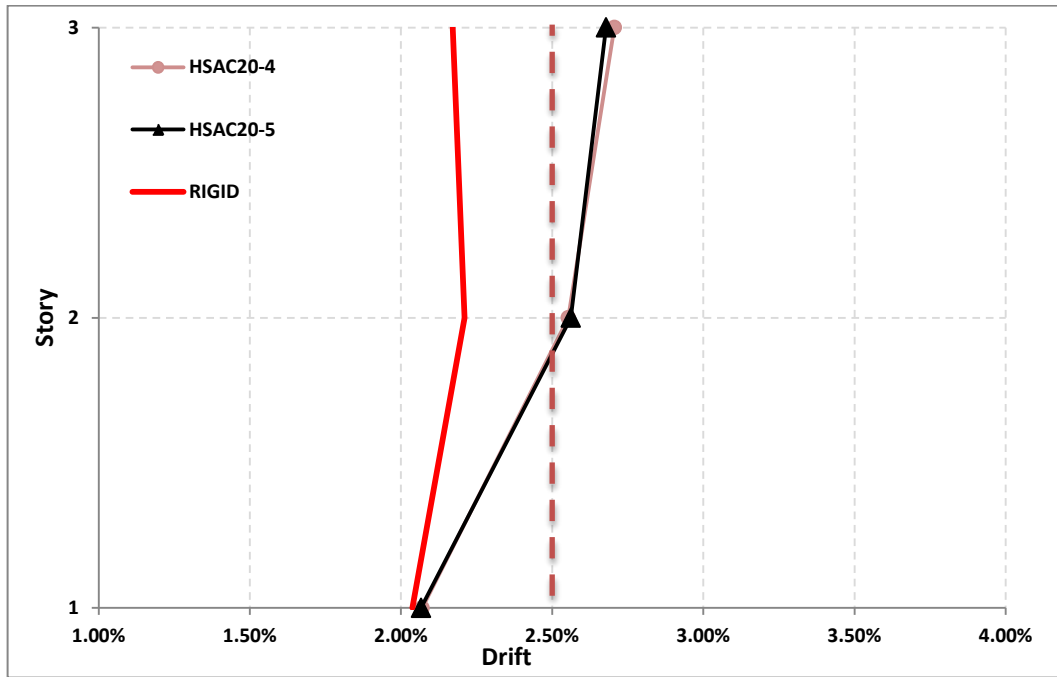
Figure 7.14 Expected Values of Maximum Story Drift Angle Demands for 3-story Structures Subjected to DBE set of Ground Motion
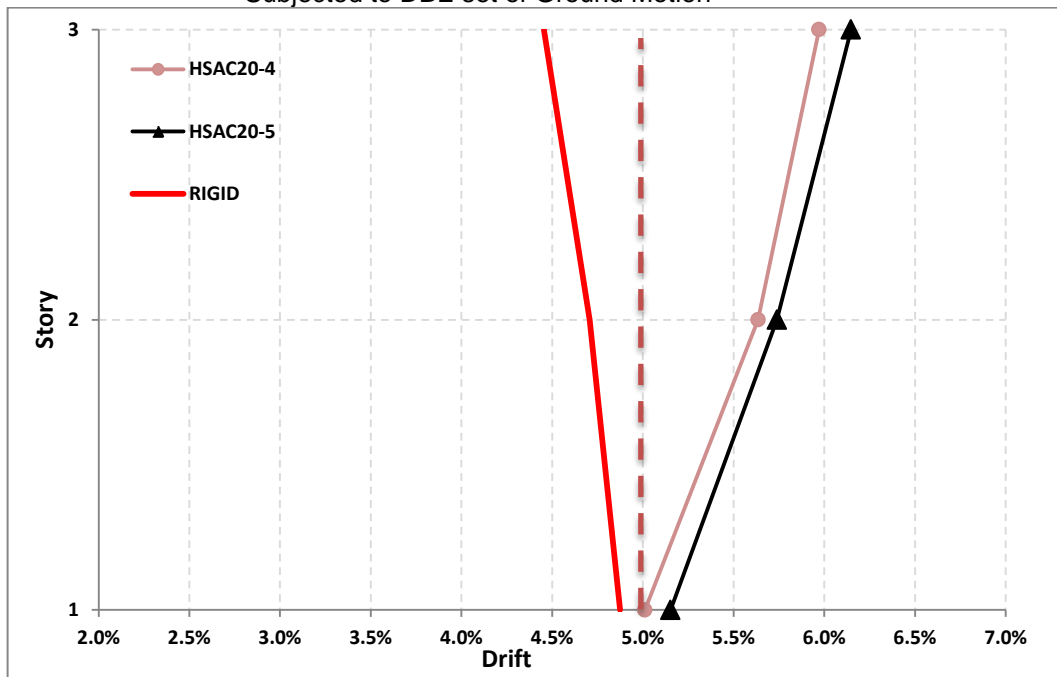
Figure 7.15 Expected Values of Maximum Story Drift Angle Demands for 3-story Structures Subjected to MCE set of Ground Motion

The MCE set of ground motions imposes high drift demands on the structures. This phenomenon is significantly observed in the 20-story frame due to the higher P-delta effects. The drift demands in lower stories (stories 1 to 6) are more than twice of the demands of higher stories of the 20-story frames. P-delta effects increase the moment demands in the frame members of the lower stories. Indeed, this effect causes the concentration of the plastic hinges in the lower stories of the SAC20-story frame, which results in more drift demands or collapse in the case of severe ground motions. Placement of the more flexible semi-rigid connections in hybrid frames, as shown in Chapter 5 of this dissertation, prevents the concentration of the plastic hinges in the lower stories. Furthermore, the semi-rigid connections transfer less moment to their adjacent column members; thus, they cause a delay in formation of plastic hinges in those columns.

Figures 7.12 and 7.13 show that the placement of the semi-rigid connections in the 9-story frame have a limited effects on the drift demands. However, using the hybrid frame is beneficial for the reduction of the members' force demands as will be shown in the next section.

Using semi-rigid connections in the 3-story frame downgrades the performance of the moment frame under seismic excitation as shown in Figures 7.14 and 7.15, which shows the maximum inter-story drift demands for the low-rise buildings are more affected by the strength and the initial stiffness of the frame rather than its ductility.

In general, the drift demands decrease as the frame height increases except in a few cases for the 20-story frames. The distribution of the drift demands over the height of the 3- and 9- stories are rather uniform. The drift distribution over the height of the 20-story frames is also rather uniform while they are subjected to the DBE ground motions; however, the drift demands are higher for lower stories when the frames are subjected to the MCE ground motions.

7.4. Members' Force Demands

The behavior of structures has so far been discussed based on the global demands values such as inter-story drifts and pushover curves. However, a frame structure is made of its members; thus, the behavior of members has a broad impact on the global behavior of the frames. In this section, member force demands in hybrid frames are compared with the same member force in their corresponding rigid frames.

The code criterion prevents formation of plastic hinges in columns by introducing the concept of strong column/weak beam. However, this criterion is violated in many cases due to the extensive moment demands on columns caused by P-delta effects in lower stories or by higher mode effects in upper stories. The plastic hinge formation in columns may also result in development of a story mechanism, which causes the collapse of a structure.

In general, lower member force demands increases the margin of safety against the collapse of structures.

7.4.1. Force demands

To compare the shear and bending moments of the hybrid versus the original rigid SAC frames, the ratios of the absolute value of maximum forces for the H-SAC were normalized with respect to the forces of the SAC frame. Thus, a ratio of unity indicates that the H-SAC forces are equal to the rigid SAC forces, and the ratio of less than unity implies a reduction in a given force for the hybrid frame (lower demand).

The beam's shear and moment ratios for the 3-, 9-, and 20-story rigid and hybrid frames subjected to two sets of ground motions are plotted in Figures 13 to 60 of Appendix A. in addition, the maximum, the minimum, and the average value of the beams moment and shear ratios are tabulated in Tables 7.2 and 7.3, respectively.

As shown in these figures, the average ratios of moment and shear in beams' of hybrid frames are less than unity. This means that the beam' force demands in hybrid frames on average is less than the beams' force demands in the corresponding rigid frames.

Looking at the average force-demand ratios in Tables 7.2 and 7.3 it can be seen that using hybrid frames reduces the force demands in beams by an average of between 15 to 30 percent. There is not a considerable difference between the demands ratio of two semi-rigid patterns, except in the 3-story hybrid frames in which patter 5 is showing a better performance with respect to the beams' demands.

The columns' shear and moment ratios for the 3-, 9-, and 20-story rigid and hybrid frames subjected to two sets of ground motions are plotted in Figures 61 to 108 of Appendix A. in addition, the maximum, the minimum, and the average value of the column moment and shear ratios are tabulated in Tables 7.3 and 7.4, respectively. Similar to the beams demands, the columns demands, with exception of the 3-story frames, also reduced between 5 to 15 percent.

In conclusion, the force demands in the beams and columns of the selected 3-, 9-, and 20-story hybrid frames are reduced up to 30 percent. Considering the fact that the structural members (beams and columns) sections in the hybrid frames are the same as those of the corresponding rigid frames, the observed reduction is noticeable.

Table 7.2 Average Hybrid / SAC Beams' Moment Response Ratio

Number of Stories	Model Name	Statistics	Under DBE Records	Under MCE Records
3-Story Frames	HSAC3-4	Average Min Max	0.852928 0.109214 1.33184	0.848482 0.113327 1.279051
	HSAC3-5	Average Min Max	0.714535 0.091195 1.333293	0.714431 0.096494 1.30124
9-Story Frames	HSAC9-4	Average Min Max	0.885143 0.041518 1.620771	0.855679 0.043508 1.443311
	HSAC9-5	Average Min Max	0.879655 0.069032 1.718118	0.858157 0.071671 1.492392
20-Story Frames	HSAC20-4	Average Min Max	0.87581 0.085019 2.024056	0.884292 0.087305 1.743018
	HSAC20-5	Average Min Max	0.83778 0.083955 1.598072	0.849292 0.086126 1.620467

Table 7.3 Average Hybrid / SAC Beams' Shear Response Ratio

Number of Stories	Model Name	Statistics	Under DBE Records	Under MCE Records
3-Story Frames	HSAC3-4	Average Min Max	0.851082 0.109235 1.209483	0.849580018 0.113327394 1.163425152
	HSAC3-5	Average Min Max	0.707344411 0.088126741 1.195338181	0.70956 0.091977 1.187796
9-Story Frames	HSAC9-4	Average Min Max	0.884962 0.041517 1.449971	0.854204 0.043509 1.335624
	HSAC9-5	Average Min Max	0.878221 0.068753 1.546303	0.857186 0.071661 1.352579
20-Story Frames	HSAC20-4	Average Min Max	0.872067 0.085021 1.957744	0.880398 0.087306 1.626262
	HSAC20-5	Average Min Max	0.835916 0.084134 1.384076	0.848436 0.08632 1.3617

Table 7.4 Average Hybrid / SAC Columns' Moment Response Ratio

Number of Stories	Model Name	Statistics	Under DBE Records	Under MCE Records
3-Story Frames	HSAC3-4	Average Min Max	0.998095 0.724739 1.397793	1.011482 0.678047 1.402851
	HSAC3-5	Average Min Max	0.966758 0.43678 1.487752	0.995878 0.410165 1.585858
9-Story Frames	HSAC9-4	Average Min Max	0.922671 0.132746 1.980153	0.936048 0.011988 1.999354
	HSAC9-5	Average Min Max	0.925433 0.064352 1.978066	0.946694 0.010614 1.962316
20-Story Frames	HSAC20-4	Average Min Max	0.924373 0.172548 3.998256	0.942267 0.071488 3.910291
	HSAC20-5	Average Min Max	0.861947 0.117791 3.982799	0.905082 0.1733 4.070266

Table 7.5 Average Hybrid / SAC Columns' Shear Response Ratio

Number of Stories	Model Name	Statistics	Under DBE Records	Under MCE Records
3-Story Frames	HSAC3-4	Average Min Max	0.9373 0.672397 1.417518	0.951282 0.648837 1.519133
	HSAC3-5	Average Min Max	0.889678 0.492155 1.595357	0.915025 0.550015 1.584794
9-Story Frames	HSAC9-4	Average Min Max	0.90265 0.520342 1.380348	0.893615 0.513829 1.214773
	HSAC9-5	Average Min Max	0.906691 0.40137 1.466093	0.910624 0.388715 1.298332
20-Story Frames	HSAC20-4	Average Min Max	0.89811 0.455418 1.85421	0.924687482 0.513241885 1.584691834
	HSAC20-5	Average Min Max	0.850091 0.34596 1.330094	0.888059 0.342912 1.545806

CHAPTER 8

INCREMENTAL MODAL ANALYSIS

Developed here is a new modal analysis procedure for assessment of structures during a seismic loading. The incremental mode shapes from the Eigen vector solution is used to find the Eigen stiffness corresponding to each mode shape. This in turn determines the locations of the collapse for the regions in frame along its height where the slope of Eigen vectors approaches zero. To prevent collapse, which is defined by the plastic hinge formation of all columns in two different stories, semi-rigid connection locations could be identified on trial bases.

In this chapter, first the conventional modal analysis procedure and incremental modal analysis will be comprehensively explained. Then, the results of the nonlinear incremental modal analysis on the rigid and hybrid frames will be discussed.

<u>8.1 Modal Analysis Procedure for Linear Systems:</u>

The differential equations governing the response of a multistory frame subjecting to a lateral ground motion of $\ddot{u}_g$ are as follows:

$$\mathbf{m\ddot{u} + c\dot{u} + ku = -m\iota\ddot{u}_g} \tag{1}$$

where "$\mathbf{u}$" is the vector of lateral relative displacements of the story levels with respect to the ground. "$\mathbf{m}$", "$\mathbf{c}$", and "$\mathbf{k}$" are the mass matrix, the classical damping matrix, and the frame lateral stiffness matrix, respectively. The mass matrix is a diagonal matrix. The $\mathbf{m}_{jj}$ element of the mass matrix equals to the lumped mass at the jth floor of the frame. The classical damping matrix accounts for the energy-dissipating mechanisms and would be constructed using Rayleigh Damping method (Chopra 2012). The lateral stiffness matrix, $\mathbf{k}$, would be constructed by assembling stiffness matrices of the frame elements into a global stiffness matrix (Chopra 2012).

The influence vector "ι" is an N x 1 vector. All elements of the influence vector are equal to unity.

The right hand side term of the equation (1) can also be expressed as the earthquake effective force.

$$\mathbf{p}_{\text{eff}}(\mathbf{t}) = -\mathbf{m\iota\ddot{u}_g} \tag{2}$$

This effective force is obtained by multiplication of the time independent spatial distribution vector over the frame height, $\mathbf{s} = \mathbf{m\iota}$, by the scalar time variant function of $\ddot{u}_g(t)$, the ground acceleration.

The force distribution may also be expressed as the summation of the modal inertia force distribution, $\mathbf{s_n}$, as shown in equation 3.

$$\mathbf{m\iota} = \sum_{n=1}^{N} \mathbf{s_n} = \sum_{n=1}^{N} \Gamma_n \, \mathbf{m\phi_n} \tag{3}$$

Where

$$\Gamma_n = \frac{L_n}{M_n} \qquad\qquad L_n = \phi_n^T m \iota \qquad\qquad M_n = \phi_n^T m \phi_n \qquad\qquad (4)$$

The vector ϕ_n is the nth natural mode of the frame. The earthquake effective force may also be expressed as the summation of the modal effective forces as

$$p_{eff}(t) = \sum_{n=1}^{N} p_{eff,n}(t) = \sum_{n=1}^{N} -s_n \ddot{u}_g(t) \qquad\qquad (5)$$

Where $p_{eff,n}$ and s_n are the contribution of the nth mode in the total earthquake effective force and the modal inertia, respectively.

When the response of the frame is solely resulted from the effective force of the nth mode, the displacement can be obtained by

$$u_n(t) = \phi_n q_n(t) \qquad\qquad (6)$$

Where $q_n(t)$ is obtained by solving the equation of motion for a Single Degree of Freedom (SDF) system using equation 6.

$$\ddot{q}_n + 2\zeta_n \omega_n \dot{q}_n + \omega_n^2 q_n = -\Gamma_n \ddot{u}_g(t) \qquad\qquad (7)$$

In which, ζ_n and ω_n are the damping ratio and natural frequency of the nth mode of the Multi Degree of Freedom (MDF) frame system, respectively. Damping ratio can be selected from the values that Newmark and Hall (1982) recommended for different type and conditions of structures under different levels of the earthquake. The solution to Equation 7 will result in:

$$q_n(t) = \Gamma_n D_n(t) \qquad\qquad (8)$$

Where $D_n(t)$ is the solution to the differential equation governing the response of a SDF with vibration properties, the damping ratio, and natural frequency of the nth mode of the MDF frame subjected to a ground motion of $\ddot{u}_g$.

$$\ddot{D}_n + 2\zeta_n \omega_n \dot{D}_n + \omega_n^2 D_n = -\ddot{u}_g(t) \qquad\qquad (9)$$

Substituting $\mathbf{q_n(t)}$ from equation 8 into equation 6, the displacement of the frame solely resulted from the effective force of the nth mode is:

$$\mathbf{u_n(t) = \Gamma_n \phi_n D_n(t)}$$

(10)

In general, any response of a MDF system, such as inter-story drift angle or member forces, can be expressed as:

$$\mathbf{r_n(t) = r_n^{st} A_n(t)}$$

(11)

Where $\mathbf{r_n^{st}}$ is the response of the frame to the static force of $\mathbf{s_n}$, and

$$\mathbf{A_n(t) = \omega_n^2 D_n(t)}$$

(12)

 is the pseudo-acceleration of a SDF system with the vibration properties, natural frequency and damping ratio, of the nth mode of the frame.

Finally, the result of a MDF system to the total effective force of the earthquake is obtained by summation of the responses due to effective force of each mode shape.

$$\mathbf{u(t) = \sum_{n=1}^{N} u_n(t) = \sum_{n=1}^{N} \Gamma_n \phi_n D_n(t)}$$

(13)

$$\mathbf{r(t) = \sum_{n=1}^{N} r_n(t) = \sum_{n=1}^{N} r_n^{st} A_n(t)}$$

(14)

Total displacement and other responses can be calculated using equations 13 and 14.

8.2 Natural Vibration Frequencies and Modes of un-damped system

The differential equation governing the free vibration of a MDF system without damping is

$$\mathbf{m\ddot{u} + ku = 0}$$
(15)

This equation represents a system of N homogeneous differential equations. N equals the number of Degree of Freedoms (DOFs) of the MDF system. For frames with rigid diaphragms, N is equal to the number of frame's stories. m and k are the systems' mass and stiffness matrix, respectively.

The free vibration of a MDF system under one of its natural vibration modes is described as:

$$u_n(t) = \phi_n q_n(t) \tag{16}$$

Where ϕ_n is a vector with N elements corresponding to the deflected shape of the MDF system. ϕ_n does not varies by the time. $q_n(t)$ for a MDF frame system can be described by a harmonic function of :

$$q_n(t) = A_n \cos \omega_n t + B_n \sin \omega_n t \tag{17}$$

A_n and B_n can be determined using initial conditions of the motion and the boundary conditions of the frame. Substituting $q_n(t)$ from Equation 17 into Equation 16, the equation of the free vibration is:

$$u_n(t) = \phi_n(A_n \cos \omega_n t + B_n \sin \omega_n t) \tag{18}$$

Substituting displacement from Equation 18 into the differential equation of the motion of the system, Equation 15, gives:

$$[-\omega_n^2 m\phi_n + k\phi_n]q_n(t) = 0 \tag{19}$$

The solution to the Equation 19 will satisfy the differential equation of motion. To satisfy this equation either $q_n(t)$ or the term $[-\omega_n^2 m\phi_n + k\phi_n]$ should be equal to zero. The assumption of $q_n(t) = 0$, will result in the trivial solution of the $u_n(t) = 0$. Which means the system will not vibrate. On the other hand, equating the second term to zero gives:

$$k\phi_n = \omega_n^2 m\phi_n \tag{20}$$

This equation is called the matrix eigenvalue problem. Stiffness matrix k and mass matrix m are known. The nth mode shape ϕ_n and the natural circular frequency of the nth mode ω_n are the unknowns of the equation. The Equation 20 can also be rewritten as:

$$[k - \omega_n^2 m]\phi_n = 0 \tag{21}$$

The N homogeneous equations derived from Equation 20 have the trivial solution of $\phi_n = 0$ which is not corresponding to the vibrational behavior of the MDF system. This system

of N homogeneous equation has a non-trivial solution if the determinant of the matrix of coefficient equals zero.

$$\det[\mathbf{k} - \omega_n^2 \mathbf{m}] = 0 \tag{22}$$

Expansion of the Equation 22 will result in a polynomial of order N in ω_n^2 which known as the characteristic equation. Since both m and k matrices are symmetry and positive definite, solving the Equation 22 will result in N positive roots for ω_n^2 so called eigenvalues. The square roots of the natural frequencies of the system are known as natural frequency of the system. Next, the eigenvectors $\boldsymbol{\phi}_n$ corresponding to the eigenvalues will be obtained. This eigenvectors are known as natural modes of vibration.

The natural mode shapes of vibration can be assembled into a matrix $\boldsymbol{\Phi}$ called the modal matrix.

$$\boldsymbol{\Phi} = \begin{bmatrix} \boldsymbol{\phi}_{jn} \end{bmatrix} = \begin{bmatrix} \boldsymbol{\phi}_{11} & \boldsymbol{\phi}_{12} & \cdots & \boldsymbol{\phi}_{1N} \\ \boldsymbol{\phi}_{21} & \boldsymbol{\phi}_{22} & \cdots & \boldsymbol{\phi}_{2N} \\ \vdots & \vdots & \ddots & \vdots \\ \boldsymbol{\phi}_{N1} & \boldsymbol{\phi}_{N2} & \cdots & \boldsymbol{\phi}_{NN} \end{bmatrix} \tag{23}$$

The eigenvalues may also be assembled in a diagonal matrix of $\boldsymbol{\Omega}^2$ called the spectral matrix.

$$\boldsymbol{\Omega}^2 = \begin{bmatrix} \omega_1^2 & 0 & 0 & 0 \\ 0 & \omega_2^2 & 0 & 0 \\ 0 & 0 & \ddots & 0 \\ 0 & 0 & 0 & \omega_N^2 \end{bmatrix} \tag{24}$$

Therefore, a compact presentation of the equation relating eigenvalues and eigenvectors can be written as:

$$\mathbf{k}\boldsymbol{\Phi} = \mathbf{m}\boldsymbol{\Phi}\boldsymbol{\Omega}^2 \tag{25}$$

The most important properties of the mode shapes is the orthogonally of the mode shapes in elastic systems which makes the governing equations of motion uncoupled.

If a vector $\boldsymbol{\phi}_n$ is a natural mode shape of a MDF system, any scale factor of this vector in turn is the same mode shape and essentially satisfies the Equation 21. To make the mode shapes standardize, a scale factor will regularly multiplied to the vector. In this study, the mode

149

shapes are normalized with respect to the mass m. In this case, the scale factor should satisfy the following equation.

$$\mathbf{\Phi}^T \mathbf{m} \mathbf{\Phi} = \mathbf{I} \tag{26}$$

The natural modes in this case are called the mass orthonormal set.

For a set of mass orthonormal natural modes, if both sides of Equation 25 pre-multiplied by $\mathbf{\Phi}^T$ the Eigen-stiffness matrix will be define as:

$$K = \mathbf{\Phi}^T \mathbf{k} \mathbf{\Phi} = \mathbf{\Omega}^2 \tag{26}$$

Where, K is a positive definite matrix with elements $K_n = \omega_n^2$.

8.3 Nonlinear Incremental Modal Analysis Procedure

In this section, the procedure for the Nonlinear Incremental Modal Analysis (NIMA) is established. NIMA is a combination of the Nonlinear Response History Analysis (NRHA) and the Modal Analysis (MA). In contrast to linear systems, the force-deformation curves of frame members are nonlinear. The unloading and reloading force-deformation curves are not the same as the initial force-deformation curve. Thus, the stiffness of each frame component is a function of displacement. The stiffness of members could vary depending on the state of deformation and the state of loading or unloading. As described in Chapter 4, the load-deformation curves for different frame components, such as beams, columns, and connections, are obtained by experiments.

The differential equation governing the response of a nonlinear MDF system subjecting to a lateral ground acceleration record $\ddot{u}_g$ is as follow.

$$\mathbf{m}\ddot{\mathbf{u}} + \mathbf{c}\dot{\mathbf{u}} + \mathbf{f}_s(\mathbf{u}) = -\mathbf{m}\mathbf{\iota}\ddot{u}_g(t) \tag{27}$$

Where the mass matrix (**m**), damping matrix (**c**), and the influence vector (**ι**) are as previously defined for the linear MDF systems. As described, the stiffness of frame's members will not remain constant during earthquake loading. Therefore, the force term $'\mathbf{ku}'$ in differential

equation for linear MDF systems, which is calculated by the multiplication of the constant stiffness matrix by lateral displacements vector of the floors relative to the ground, is replaced with the path-dependent inelastic force term $f_s(u)$. Equation 27 represents a system of N nonlinear differential equation for N lateral floor displacements $\mathbf{u_i}$. Obtaining the response of this nonlinear system requires an incremental numerical solution. The total stiffness matrix should be updated in each time increment from the elements stiffness matrices corresponding to the present state of deformation. The geometric nonlinearity effects, known as P-Δ effects, should also be considered in the updated stiffness matrix formulation. The constant average acceleration method with Newton-Raphson iteration is used to solve the nonlinear system of equations. The time intervals should be selected small enough to ensure the numerical solution converges. The described procedure is the procedure of the NRHA.

The NIMA analysis is conducted by performing an additional step of the modal analysis as described in section 8.1 in each time increment of the NRHA. Although the mass and damping matrices are constant during a NRHA, variation in the stiffness matrix will result in dissimilar eigenvalues and eigenvectors. Essentially, the vibration properties including the natural periods and mode shapes of a structure will vary during a NRHA.

8.4 Results and discussion

The 3-, 9-, and 20-story SAC and their corresponding hybrid frames' are evaluated using NIMA in this study. A tcl code is developed under Opensees software to perform the NIMA on the nine selected frames. Since modal analysis is performed in each time increment of the analysis, the NIMA analysis is resulted in thousands of output files depending on the number of time increments in a given earthquake. Then a C# code is developed to organize the outputs data and filter out the similarities. In this study, the NIMA analysis is performed for all nine selected frames under the set of MCE ground motions.

The results of the NIMA analysis for 20-Story original SAC and SAC20H-5 frames are presented and discussed intensively in this chapter. Other frames' results are shown in Appendix B.
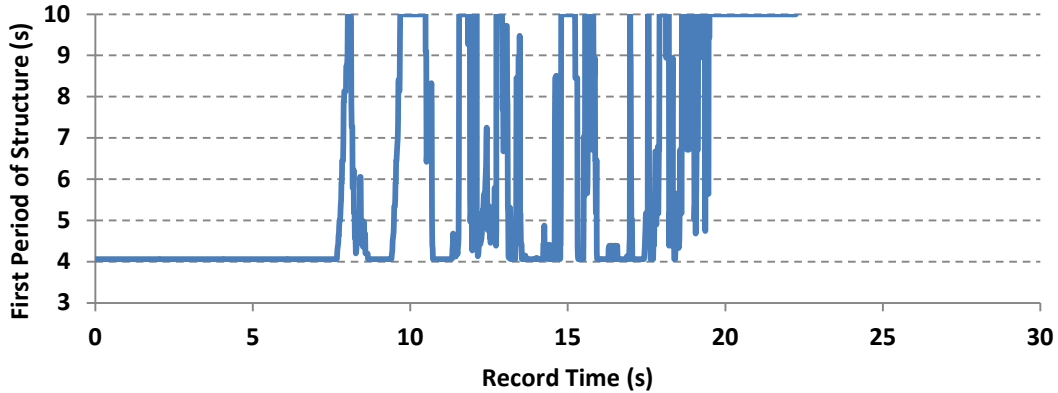
Figure 8.1 The first period of 20-Story SAC frame during LA36 ground motion

Figure 8.1 shows the variation of the first period of the 20-Story SAC frame during LA36 ground motion. The first period of the frame does not remain constant during the earthquake as shown in this figure. As mentioned in chapter 4 of this dissertation, the stiffness of the frame components (Beams, columns, and panel zones) is a function of displacement. A typical moment-rotation curve for plastic hinges is shown in Figure 8.2. The initial stiffness matrix of the frame is assembled when all the frame components are in the initial tangent stiffness state. As the frame is subjected to the earthquake, some of the frame's components might exceed the yield limit; therefore, the component stiffness and correspondingly the total stiffness of the frame vary. However, the components' stiffness may return to their initial elastic stiffness on the unloading path. If all of the frame components are in their initial elastic state, the total stiffness of the system equals to the initial stiffness of the system and consequently the period of the structure will be the same as its initial period. As shown in Figure 8.2, the frame components have less stiffness when they pass the yield limit. Thus, the total stiffness of the system is less than the initial stiffness if some members yield. In turn, the structure is softer and

152

has a longer natural period. In Figure 8.1, regions with first period higher than initial period correspond to states of structural nonlinearity. Larger periods correspond to more nonlinearity.
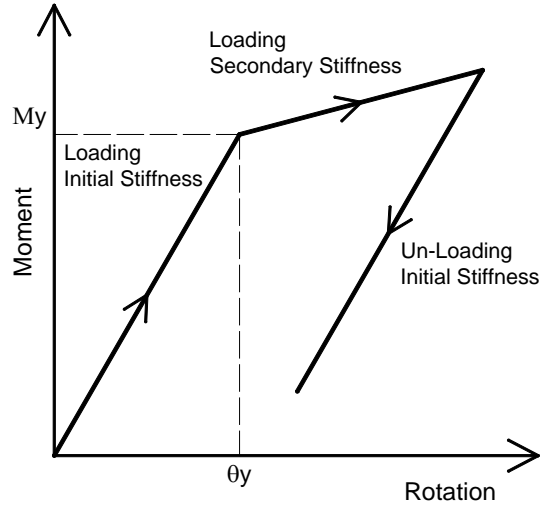
Figure 8.2 Typical Components Moment-Rotation Behavior

Figure 8.3 shows the acceleration versus time graph for LA36 ground motion. The LA36 ground motion is chosen for this study because it is strong enough to push the 20-story SAC frame to the collapse state. As shown in this figure, this record contains several strong pulses between the times period of 7 to 16 seconds. These pulses push the structural members in the nonlinear state. Thus, after each pulse, members experience a residual displacement and the frame will not return to its original un-deformed shape. P-delta effect also magnifies the force demands on the deformed frame. Ground motion pulses along with P-delta effect may bring a frame to the collapse state. Figure 8.4, illustrates the first mode Eigen stiffness for 20-story SAC frame during LA36 ground motion. As an alternative to the first period of structure, the Eigen stiffness of the first mode is also investigated. Since the mode shapes are mass normalized, the Eigen stiffness is equal to ω_n^2, as explained in Equation 26. Therefore, the modal stiffness is in an inverse relation with the period of structure.
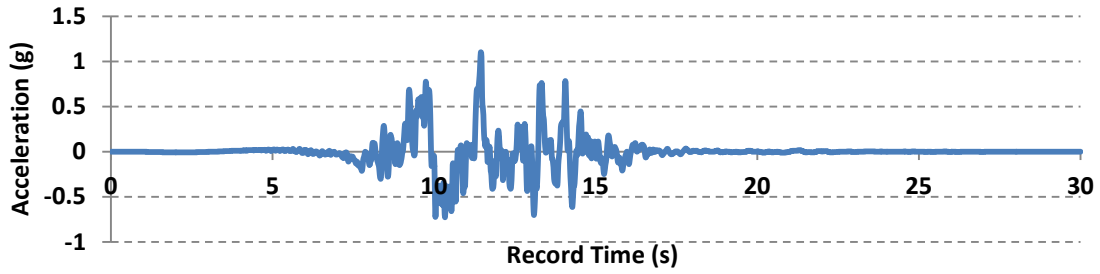
Figure 8.3 the acceleration versus time graph for LA36 ground motion
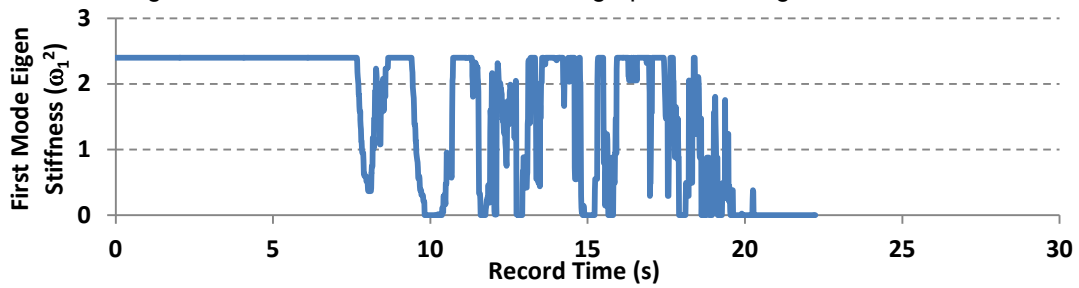
Figure 8.4 the first mode Eigen stiffness versus time graph for 20-story SAC frame under LA36 ground motion
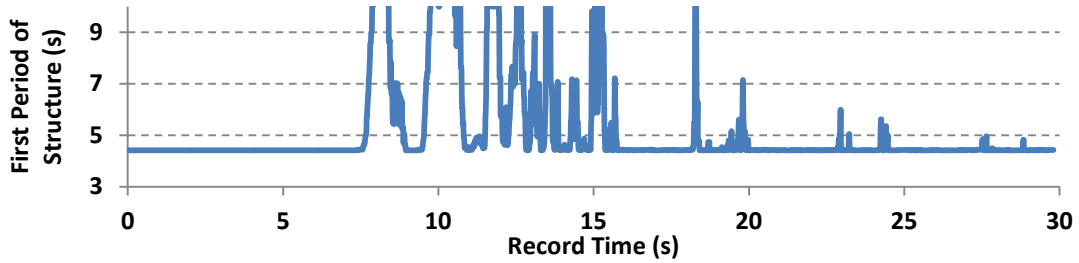
Figure 8.5 The first period of HSAC20-5 frame during LA36 ground motion
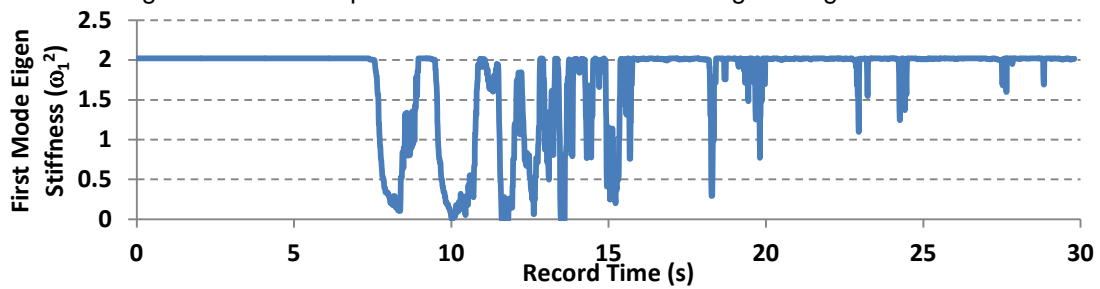
Figure 8.6 the first mode Eigen stiffness versus time graph for HSAC20-5 frame under LA36 ground motion

As the Eigen stiffness of a frame approaches zero, the period of the frame approaches infinity.

The Eigen stiffness reaches zero several times between record times of 9 to 20 seconds, as shown in Figure 8.4. In turn, the frame experiences high nonlinearity due to the ground motions strong impulses. However, the frame might be resurrected after an impulse and gained back its initial stiffness. However, as explained before, the residual displacements in a frame after an impulse, makes it more vulnerable against next impulses. The Eigen stiffness after 21 second reaches zero and remains constant, which implies that the frame is collapsed.

On the other hand, Figures 8.5 and 8.6 show the first period and the first mode Eigen stiffness for the HSAC20-5 frame during LA36 ground motion, respectively. Although, the Eigen stiffness reaches zero a few times in the time window of 10 to 14 seconds, the structure withstands the whole 30 period of the ground motion.

The comparison of the first mode Eigen stiffness of SAC 20-Story frame vs. HSAC20-5 frame during LA36 ground motion is shown in Figure 8.7. Although the initial first mode Eigen stiffness of the SAC frame is more than the initial Eigen stiffness of the HSAC20-5 frame, the SAC frame's stiffness goes below the HSAC20-5 frame's stiffness several times during earthquake and especially after the earthquake.
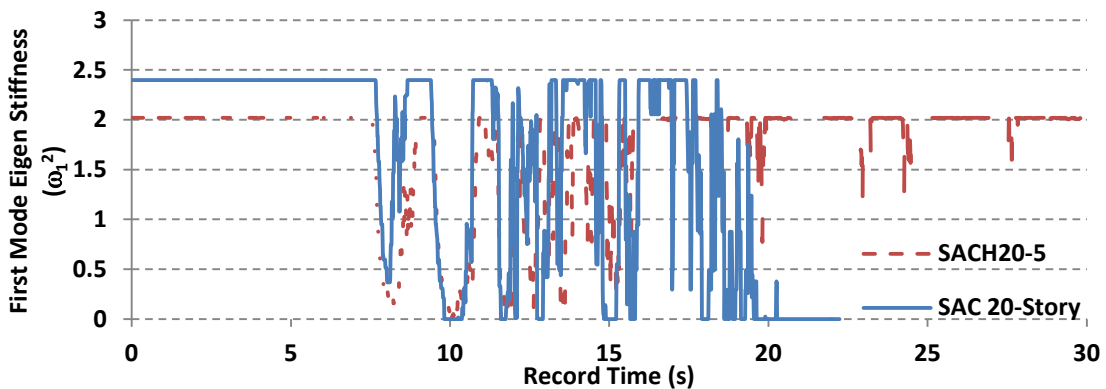
Figure 8.7 Comparison of the first mode Eigen stiffness of SAC 20-Story frame vs. HSAC20-5 frame during LA36 ground motion

For a better understanding of the behavior of these frames, the incremental modal shape and deformed shape of these frames during the LA36 ground motion is investigated. Figures 8.8 to 8.10 show the modal and deformed shape of the SAC 20-story frame in selected time steps during earthquake. In modal shape figures, the bold-line shows the modal shape at the selected time, and narrow lines show the mode shape history of the past selected times. Moreover, the initial elastic mode shape is shown by a bold dashed-line. The time steps are selected from the local peak values in the first mode period graph. The initial mode shape of the frame is almost linear as shown in Figure 8.8 (t = 0s). As the first pulse hits the fames, several beams in the lower five stories of the frame yield. Since the lower stories loose stiffness, they tend to deform more than upper stories. Thus, the parabolic mode shape at t = 8 s is a result of the yielding of the beams in lower stories. The same conclusion can be made from the mode-shape at t=9.8 s. The excitation of the higher modes causes the middle stories' beams to yield. For example looking at the mode shape at t=10.4 s implies that the lower stories have gained back their initial stiffness, and stories 6 to 9 are in their secondary stiffness. The frame loses and gains back the stiffness several times during the ground motion, however, after the time of t=15 s, due to intensive yielding of the lower stories' members, especially columns, the frames tends to deform similar to the mode shape of the frame at t=15s. Finally, the extensive deformation of lower stories results in the collapse of the structure at t=21s.

Figures 8.11 and 8.12 show the modal and deformed shape of the HSAC20-5 frame in selected time steps during the LA36 record. The zigzag line on the deformed shape figures shows the locations of the semi-rigid connections. Looking at the mode shapes of the HSAC20-5 frame structure, it is observed that a better distribution of nonlinearity along the frame height, avoids the concentration of the plastic hinges in a few lower stories and prevents collapse in this frame.
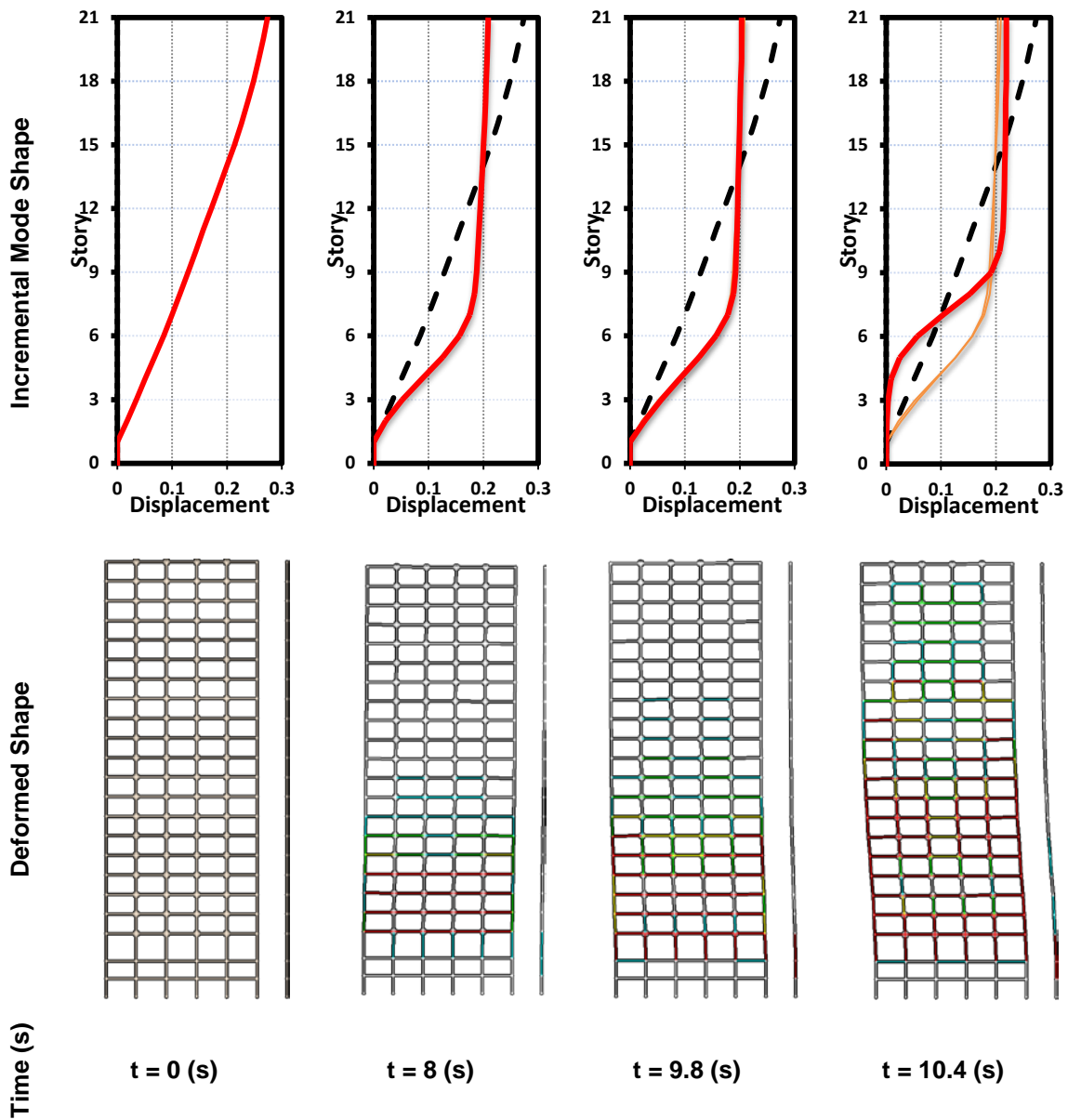
Figure 8.8 Selected incremental modes shapes and deformed shapes of the SAC 20-story frame during LA36 ground motion between 0 to 10.4 seconds
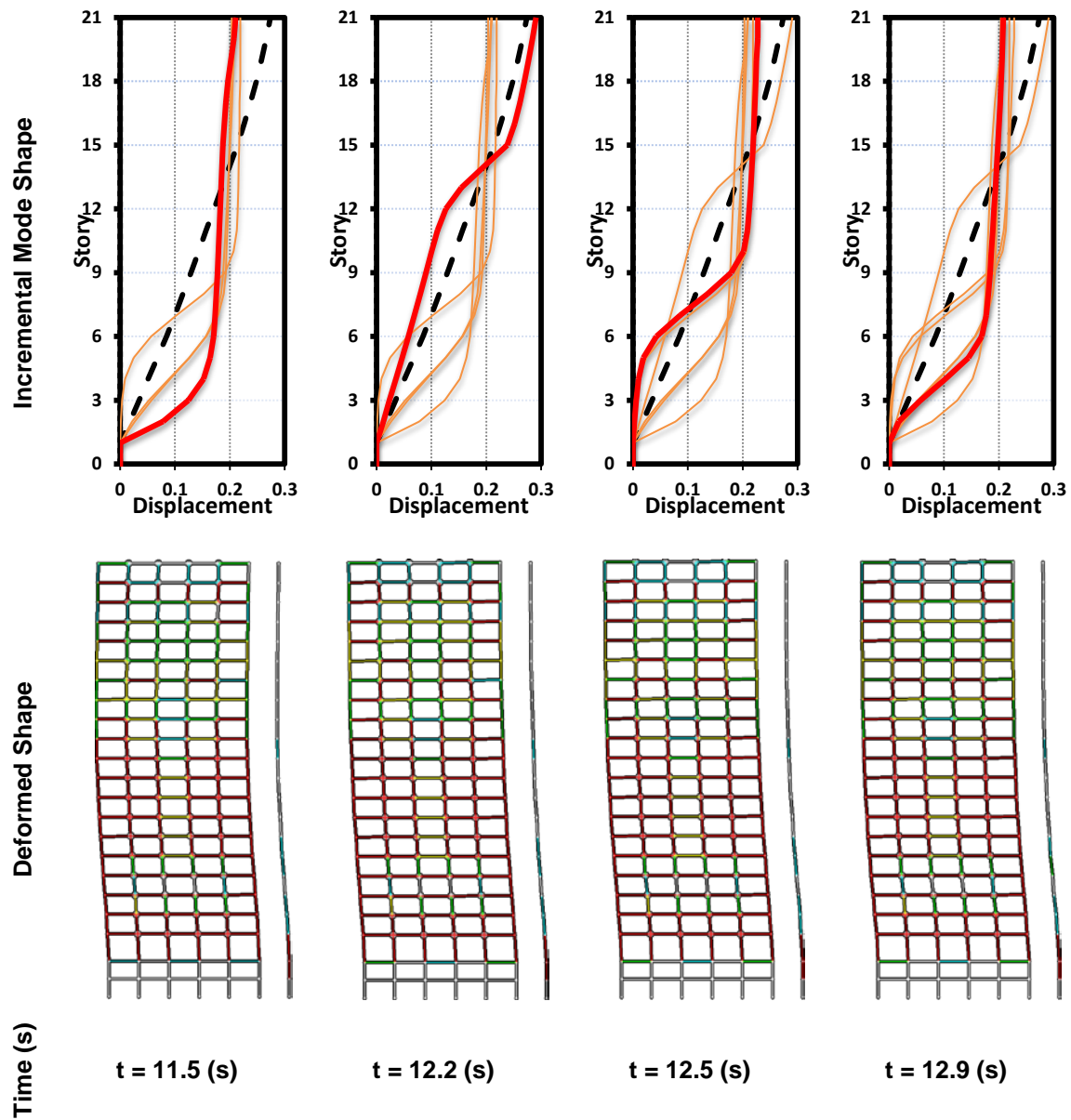
Figure 8.9 Selected incremental modes shapes and deformed shapes of the SAC 20-story frame during LA36 ground motion between 10.4 to 13 seconds
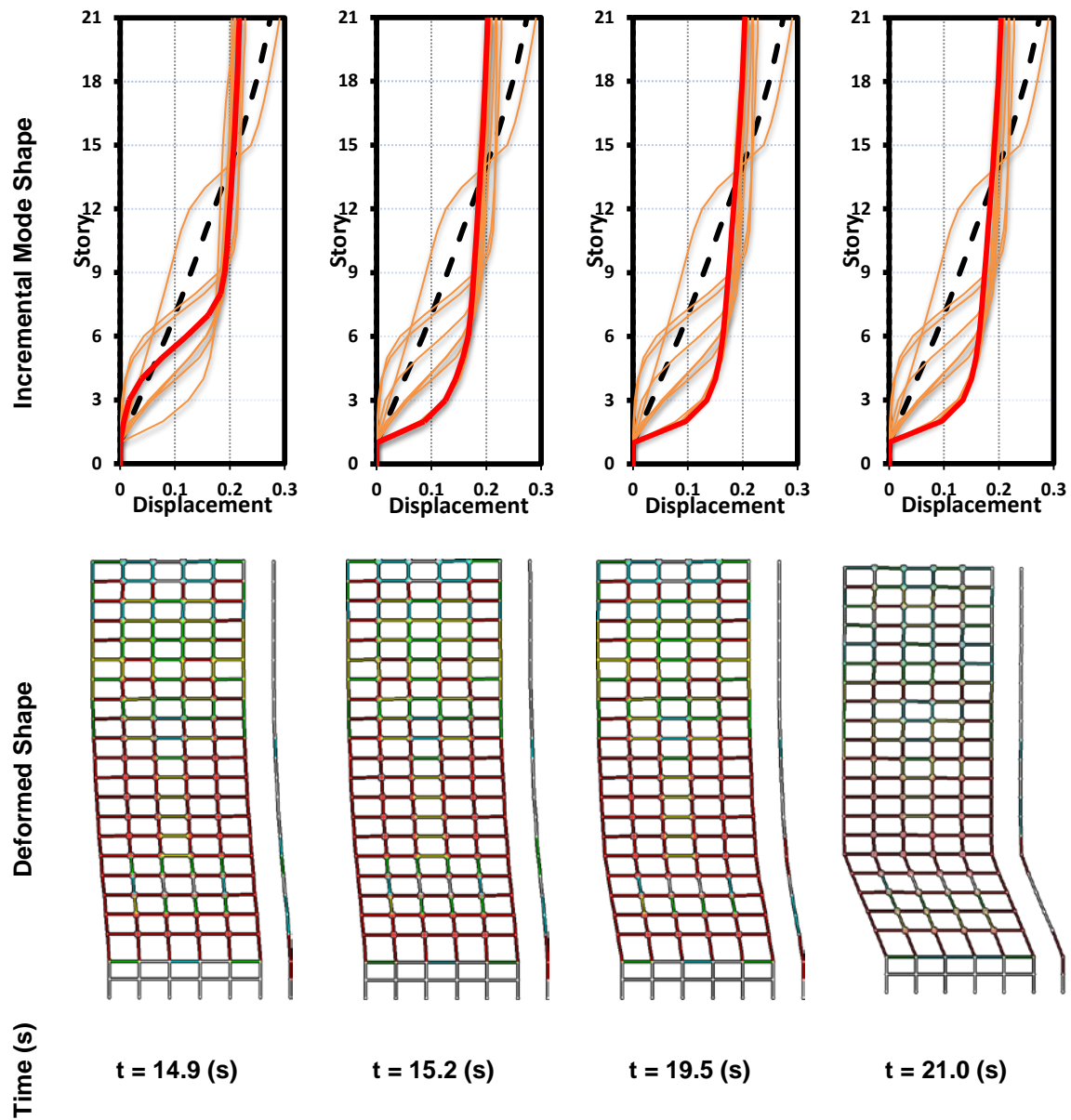
Figure 8.10 Selected incremental modes shapes and deformed shapes of the SAC 20-story frame during LA36 ground motion between 13 to 21 seconds
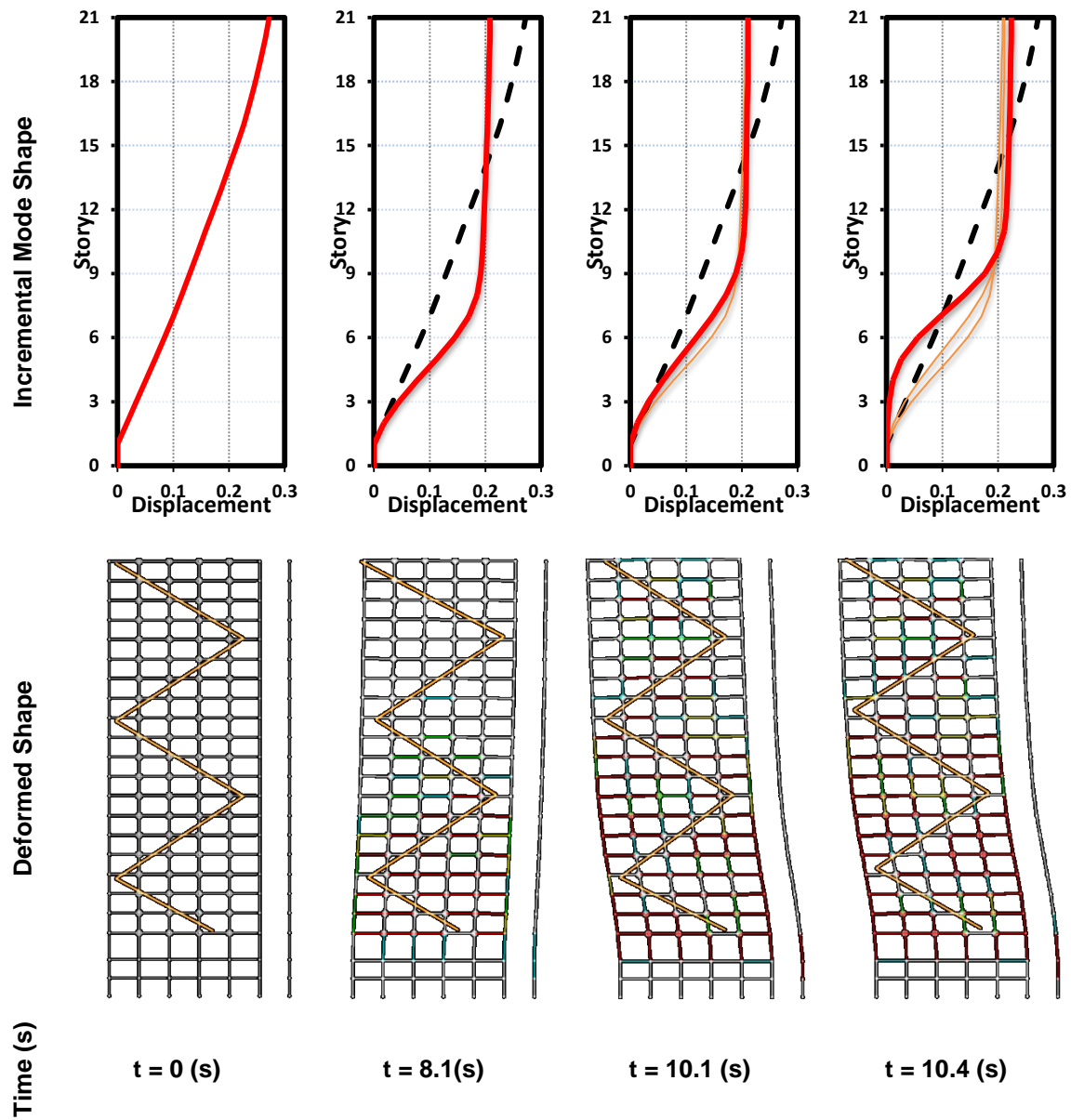
Figure 8.11 Selected incremental modes shapes and deformed shapes of the HSAC20-4 frame during LA36 ground motion between 0 to 10.4 seconds
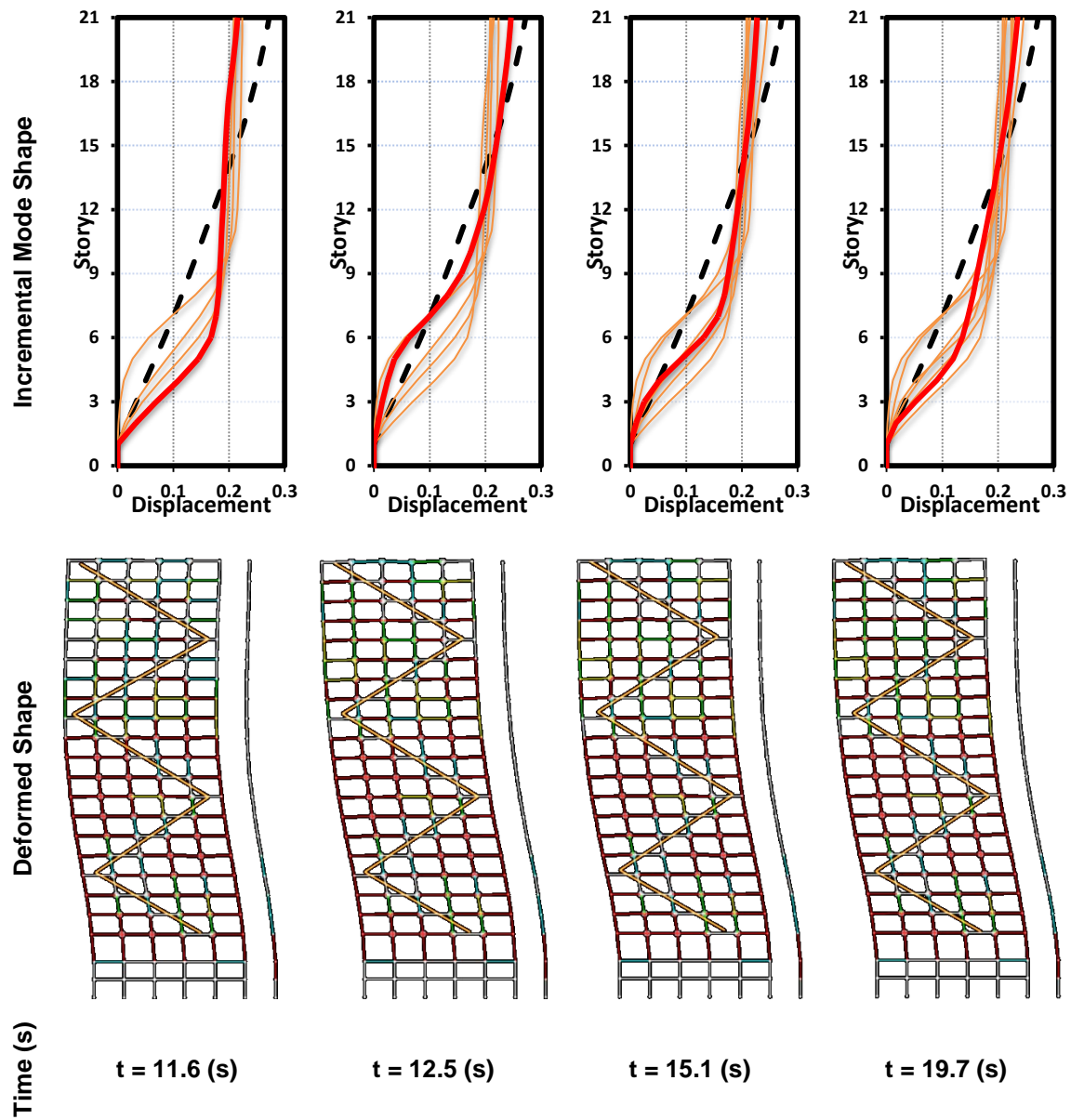
Figure 8.12 Selected incremental modes shapes and deformed shapes of the HSAC20-4 frame during LA36 ground motion between 10.4 to 30 seconds

(a)   (b)
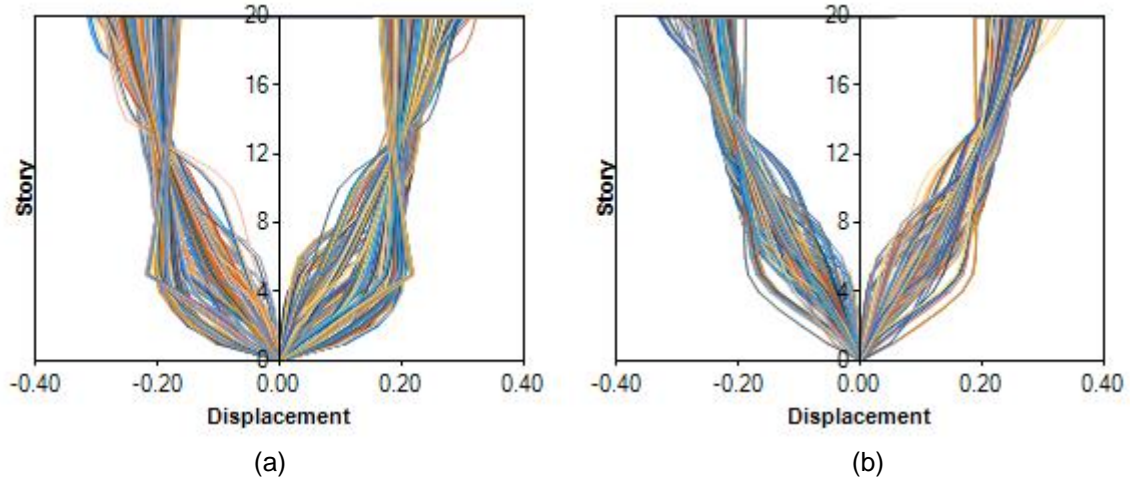
Figure 8.13 Comparison the incremental mode shapes of the
a) SAC 20-story and b) HSAC20-5 frames during LA36 ground motion

Figure 8.13 shows all the different mode shapes for the SAC 20-story and HSAC20-5 frames during LA36 ground motion. Comparison of the outer envelope of the mode shapes in these figures reveals that in the case of SAC 20-story the slope of the mode shapes envelope for lower stories approaches zero. In turn, this is the place that collapse takes place as shown in Figure 8.10 t=21 s. On the other hand, the envelope of the mode shapes of HSAC20-5 frame does not exhibit a flat region. However, the smallest slope corresponds to the lower stories where the maximum nonlinearity occurs. This pattern is also repeated when these two frames are subjected to LA30 and LA35 records in which the SAC rigid frame collapse while the corresponding hybrid frames do not collapse.

In order to verify this observation with other records, NIMA was performed on the SAC 20-story under LA23 record. This record is not strong enough to bring the frame to the collapse state. The record was analyzed twice. Once without scale factor and the second time with scale factor of 3.1 in which the frame is collapsed. The incremental modal results of these analyses are shown in Figure 8.14.

(a)   (b)
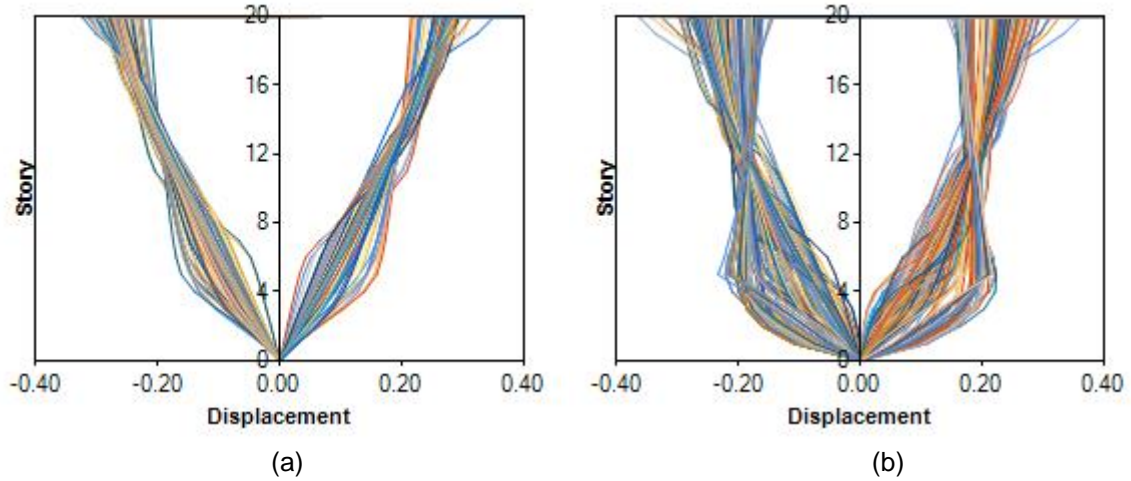
Figure 8.14. Comparison the incremental mode shapes of the SAC 20-story frame under LA21 ground motion with a) Scale Factor of 1, b) Scale Factor of 3.1

As shown in this figure, the same results are obtained from these analyses.

Finally, the NIMA analysis procedure is explained in this chapter comprehensively. The analysis turns to show the most possible failure modes and the place where failure occurs. More results of NIMA analysis can be found in Appendix B.

CHAPTER 9

RELIABILITY ANALYSIS

This chapter focuses on evaluating and quantifying the collapse performance of the Los Angeles SAC 3-, 9-, and 20-story rigid frames and their corresponding hybrid frames by application of the FEMA P695 reliability analysis methodology. An Incremental Dynamic Analysis (IDA) is performed on the comprehensive nonlinear models of the three rigid and their six corresponding hybrid frames. The IDA is performed by applying the 20 records of the set of MCE, 2 percent probability of exceedance in 50 years, ground motions as introduced in Chapter 4 of this dissertation. Finally, the collapse performance of the frames is quantified and compared by computing the Collapse Margin Ratio (CMR) value.

9.1 IDA overview

Incremental Dynamic Analysis (IDA), also known as Dynamic Push Over (DPO), is an analysis method developed by Vamvatsikos and Cornell (2002) which aims at determining the global capacity of structures. In this method, structures are subjected to one or more ground motions, each scaled to multiple level of intensity measure (IM). An IM is a non-negative parameter such as Peak Ground Acceleration (PGA) or Spectral Acceleration (Sa) , which represents the ground motion's intensity. Then, the structure is analyzed under each scaled ground motion utilizing a nonlinear dynamic analysis and the damage measure (DM) of interest is recorded. A DM is a measurable response of a structure such as ductility, global drift, or inter-story drift that is an output of the nonlinear dynamic analysis under the prescribed seismic loading. The smallest scale factor is selected to ensure an elastic response of the structure, then the scale factor increases until the collapse limit state is reached. The scale factor

increment should be small enough to capture the collapse point. Finally, a graph of DM data versus IM data is plotted which is also known as IDA curves.

In this sturdy, the 5% damped first mode spectral acceleration (Sa (T1, 5%)) and the inter-story drift angle (θ_{max}) are selected as the IM and DM parameters, respectively. Figure 9.1 shows two typical IDA curves. Each point on the IDA curves corresponds to the maximum inter-story drift resulted from a nonlinear dynamic analysis subjected to one ground motion record that is scaled to one intensity level.
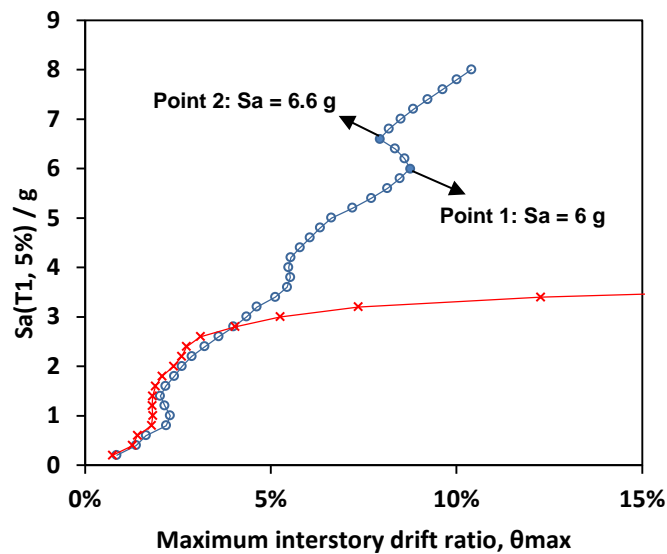
Figure 9.1 Typical IDA curves

The drift capacity of a frame for a particular ground motion is defined as the lowest value of the following criteria:

a) The point where the slope of the IDA curve falls below 20 percent of the initial slope of the curve

b) The upper-bond inter-story drifts capacity of 10 percent.

An interesting phenomenon in the IDA curve is that in some cases a higher intensity level is resulted in lower DM response. An example of this phenomenon is observed by comparison of Point 1 and Point 2 as shown in Figure 9.1. As an accelerogram is scaled up, the weak pulses in the applied ground motion record may become strong enough to cause

yielding in some structural members. This in fact, changes the dynamic properties of the structure such as stiffness and the first mode period. Consequently, the response of the structure under the subsequent strong cycles is changed. An extreme case of this phenomenon is that a structure is collapsed under lower intensities of the ground motion while it resists against the same ground motion with higher intensity. This phenomenon is addressed as "structural resurrection" by Vamvatsikos and Cornell (2002).

The IDA curves will be used to determine the capacity of the SAC rigid and hybrid frames under MCE ground motions.

9.2. Collapse Fragility Curves

A fragility function for collapse limit-state expresses the probability of exceeding the limit state under a given ground motion with certain level of intensity. A fragility function is be expressed by the equation 9.1.

$$F(x) = P[S_a \geq S_{a,c} | S_a = x] = P[S_{a,c} \leq x] \qquad 9.1$$

In which, $F(x)$ is the value of the fragility function, S_a is the spectral acceleration, $S_{a,c}$ is the capacity of the structure, and x is the spectral acceleration demand. By assuming that the spectral acceleration demand (x) is independent of the spectral acceleration capacity of the system $(S_{a,c})$, the probability can be expressed as the probability that $S_{a,c}$ is less than or equal to x.

The fragility function is produced by using collapse data from IDA results through a cumulative distribution function (CDF) that expresses the probability of collapse as a function of ground motion intensity (Ibarra et al., 2002). For this purpose, a lognormal distribution is fitted to the collapse data obtained from IDA results.

For a given structure and a given set of ground motions, the fragility curve is developed by following the procedure described below.

a) Calculate the spectral acceleration intensity that causes collapse for each ground motion using IDA results.

b) Sort spectral acceleration corresponding to collapse points from smallest to largest

c) Estimate $P[S_{a,c} \leq x]$ with (i-0.5)/N in which the "I" is the ith number in the sorted range of ground motions and N is the total number of ground motions.

d) Plot the points of the probability of collapse versus the spectral acceleration causes that collapse

e) Fit a lognormal probability distribution to the calculated points using Equations 9.2 to 9.4.

Logarithmic Mean of Spectral Acceleration	$$\mu_{LnSa} = \frac{1}{N}\sum_{i=1}^{N} Ln(Sa_i)$$	9.2
Logarithmic Standard Deviation of Spectral Acceleration	$$\sigma_{LnSa} = \sqrt{\frac{1}{N-1}\sum_{i=1}^{N}[Ln(Sa_i) - \mu_{LnSa}]^2}$$	9.3
Probability density function	$$f(x; \mu, \sigma) = \frac{1}{x\sigma\sqrt{2\pi}}e^{-\frac{(\ln x - \mu)^2}{2\sigma^2}}, \quad x > 0$$	9.4

In this study, the cumulative probability distribution function is calculated using the function presented in Equation 9.5 in Microsoft EXCEL.

Cumulative distribution function	$$LOGNORM.DIST(Sa_i, \mu_{LnSa}, \sigma_{LnSa}, true)$$	9.5

Figure 9.2 shows a typical fragility curve. In this figure, each point on the graph corresponds to a cumulative probability of collapse obtained from Step (d) of the above-mentioned procedure. The solid line in this figure also illustrates the lognormal CDF curve fitted to these points.
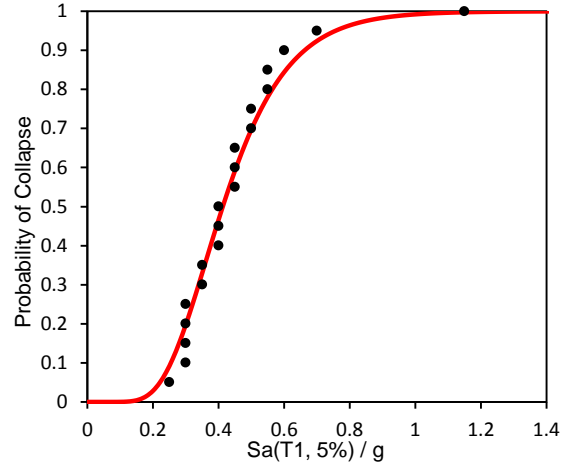
Figure 9.2 A typical Fragility Curve

9.3 Collapse Margin Ratio

While for a structure, the IDA is performed and the fragility curve is developed, the median collapse intensity, S_{CT}, should be identified. The lowest intensity at which one-half of the records cause collapse is the median collapse intensity, S_{CT} (FEMA 2009). In turn, this value is the spectral acceleration corresponding to the 50 percent probability of collapse in the fragility curve. The S_{CT} value is a representative of the capacity of the structure.

On the other hand, the MCE intensity, S_{MT}, which is defined as the median 5%-damped spectral acceleration of the MCE ground motions at the fundamental period of the structure, is a representative of the plausible demands applied to a structure.

To quantify the collapse performance of steel frames, FEMA P695 introduces the collapse margin ratio, CMR, which is the ratio of the S_{CT} to the S_{MT}, as shown in Equation 9.6.

Collapse Margin Ratio $$CMR = \frac{S_{CT}}{S_{MT}}$$ 9.6

Indeed a larger CMR corresponds to a less probability of collapse.

Figure 9.3 shows an example of how the collapse margin ratio is calculated for a frame. Assuming a frame has a fundamental period of 4.2 seconds, first, the S_{MT} is determined from the 5% damped median acceleration spectrum of MCE ground motions. The S_{MT} equals to 0.25 g as shown in Figure 9.3a. Then the median collapse capacity is obtained from the frame's fragility curve. The S_{CT} corresponds to a 50 percent probability of collapse and equals to 0.51 g as shown in Figure 9.3 b. Consequently, the collapse marginal ratio for this frame equals to the ratio S_{CT} to S_{MT}, which is 2.04.

(a)   (b)
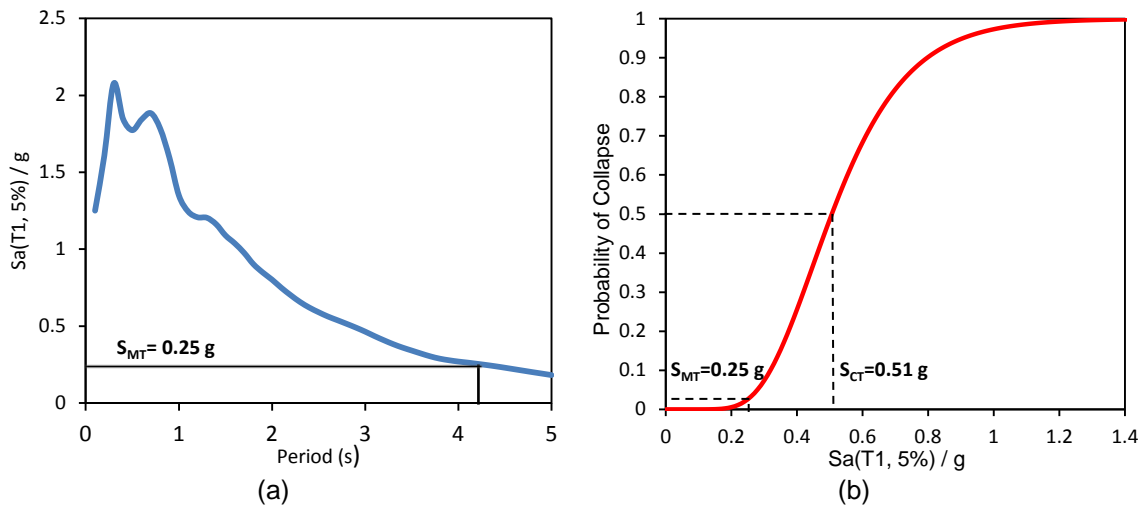
9.3 A typical CMR graphical calculation (a) Median Acceleration Spectrum of MCE records with 5 % damping (b) Collapse fragility curve

9.4 Results and Conclusion

In order to quantify the performance of the SAC rigid and hybrid frames used in this study, the collapse margin ratio for different frames is calculated. The MCE ground motions, which were produced by Sommerville et al. (1999) for SAC buildings located in Los Angeles site, are used as the input records for the incremental dynamic analysis. The IDA curves and their corresponding fragility curves for different 3- , 9-, and 20-story frames are shown in Figures 9.4 to 9.6, respectively. Hollow circles in the IDA curves correspond to the collapse points in these graphs. Moreover, each black dot in the fragility curve corresponds to a cumulative probability of collapse obtained from the IDA curves.

The collapse margin ratio for different SAC rigid and hybrid frames is shown in Table 9.1. A larger CMR corresponds to a better performance. Comparing the CMR values for the 3-story frames, the rigid frame has the best performance against collapse. As the number of stories increases, the performance of the hybrid frames improves. The performance of the 9-story frames is approximately 10% better than the performance of the rigid frame. The hybrid frames have a superior performance in the case of 20-story frames. As shown in Table 9.1, the performance of the hybrid frames is between 20 to 33 percent better than the performance of the rigid frame.

Moreover, the pattern of semi-rigid does not made a huge difference in CMR of the 3- and 9-story buildings; while, it has a considerable, approximately 13%, difference for the 20-story frame.

Table 9.1 Collapse Margin Ratio for different frame models

	Structure Type	CMR
3 Story	Rigid	1.44
	HSAC3-4	1.25
	HSAC3-5	1.23
9 Story	Rigid	1.51
	HSAC9-4	1.64
	HSAC9-5	1.67
20 Story	Rigid	1.48
	HSAC20-4	1.80
	HSAC20-5	1.99
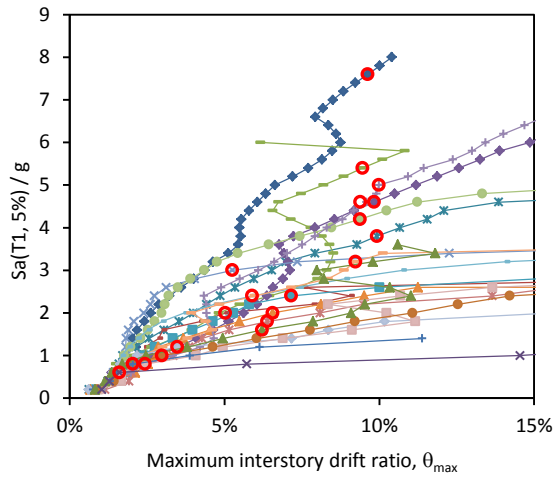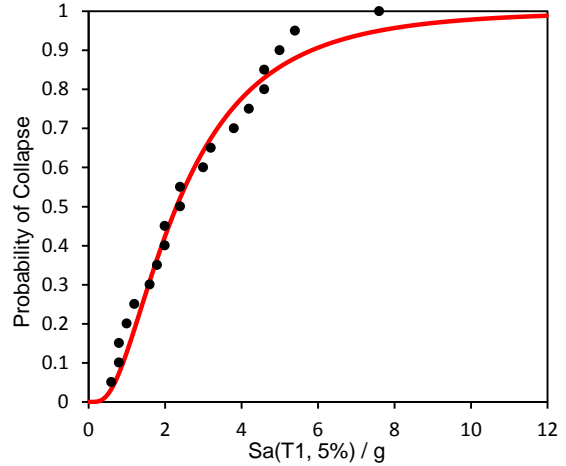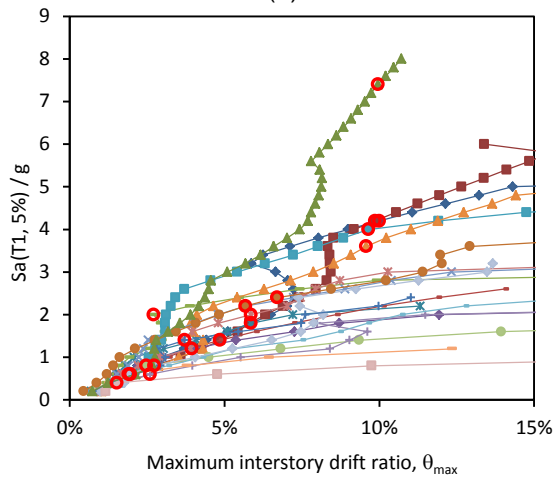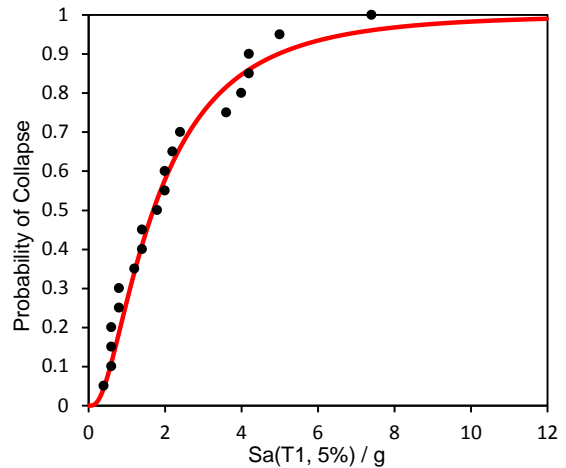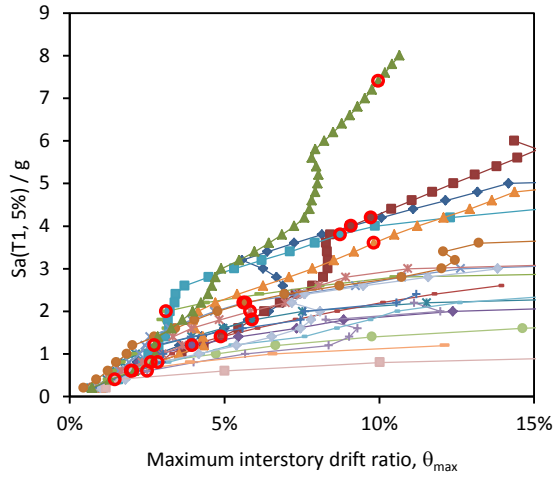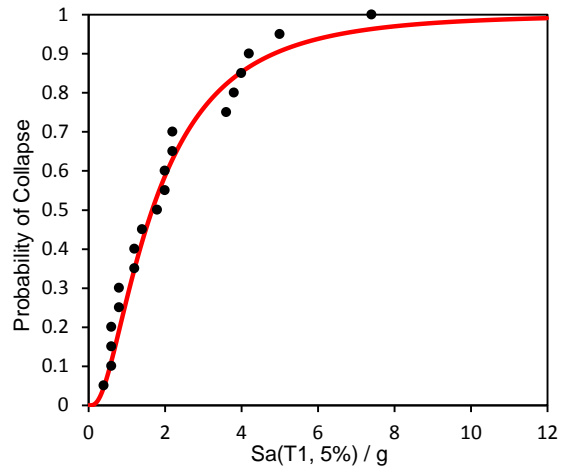
Figure 9.4 IDA curves for models (a) 3-story rigid, (b) HSAC3-4, (c) HSAC3-5, and fragility curves for models (d) 3-story rigid, (e) HSAC3-4, and (f) HSAC3-5
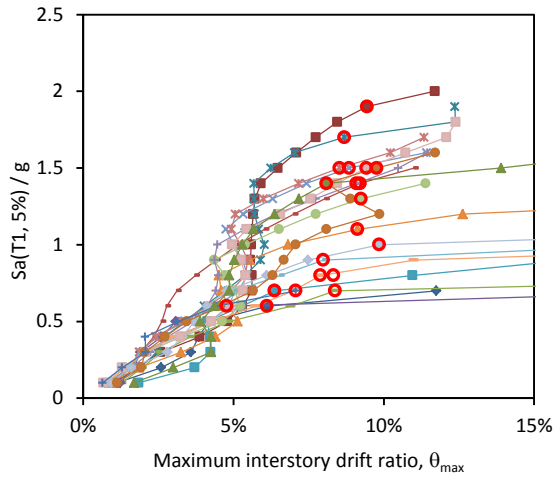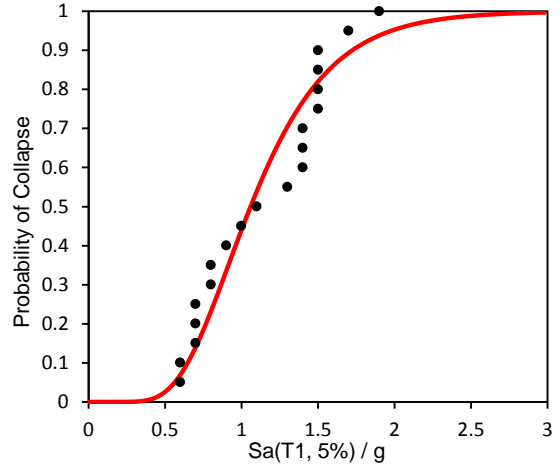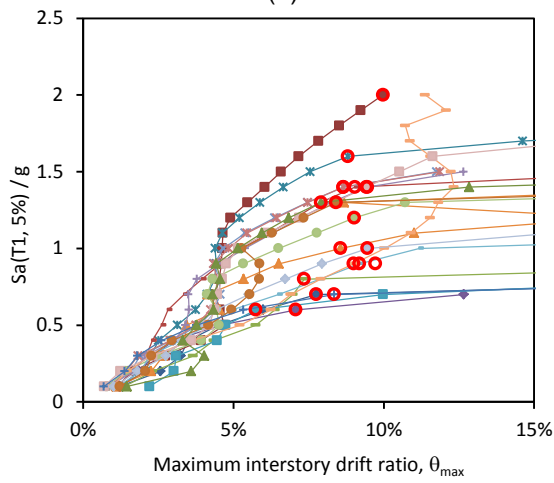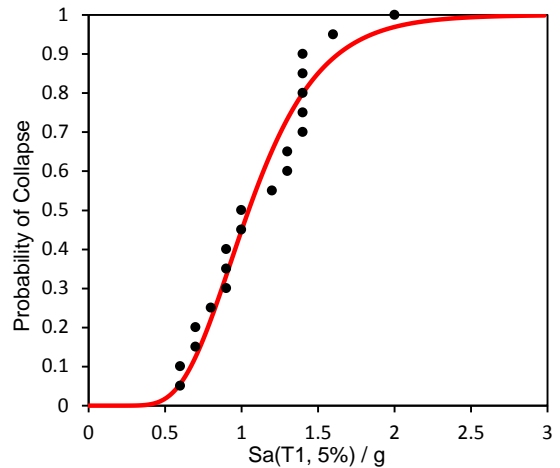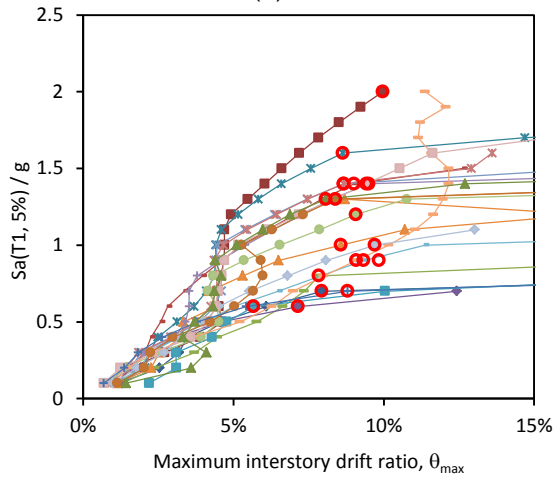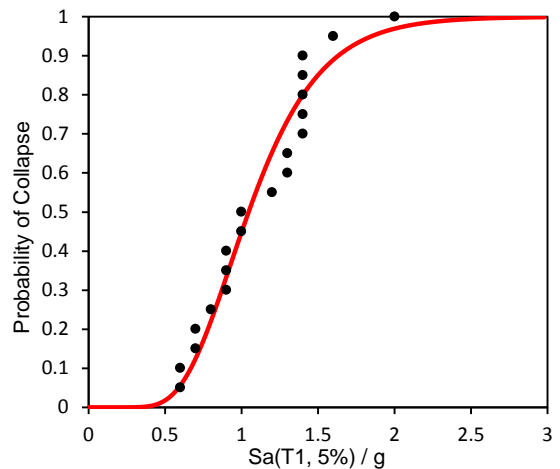
Figure 9.5 IDA curves for models (a) 9-story rigid, (b) HSAC9-4, (c) HSAC9-5, and fragility curves for models (d) 9-story rigid, (e) HSAC9-4, and (f) HSAC9-5
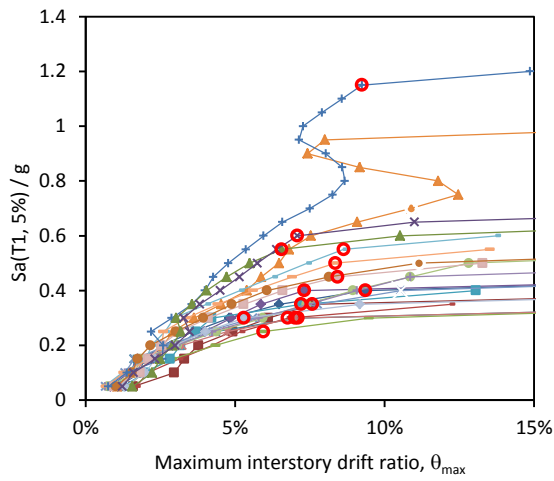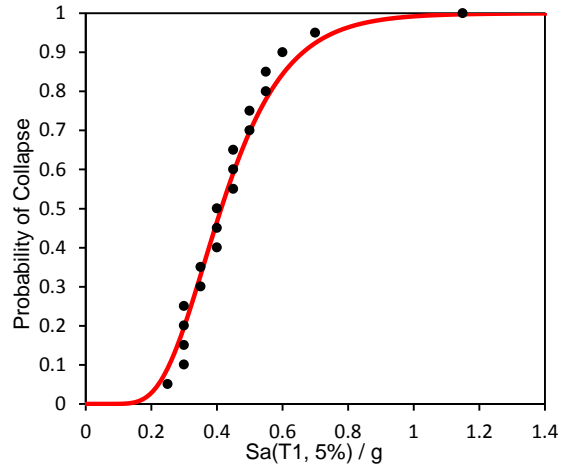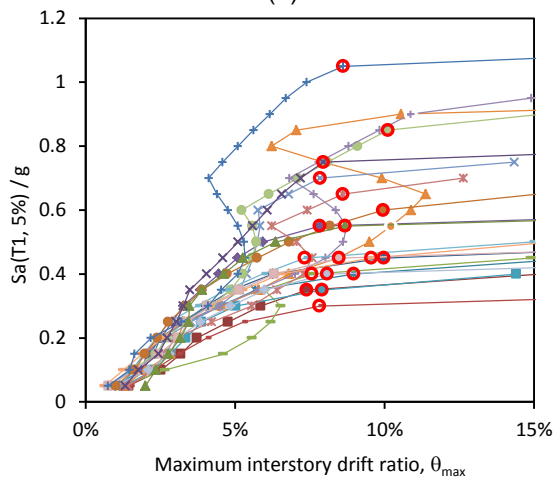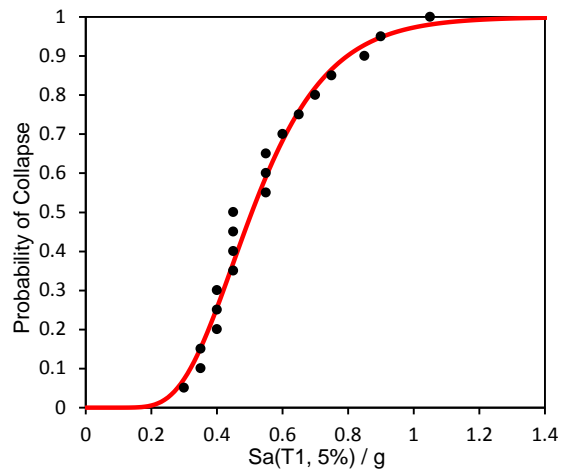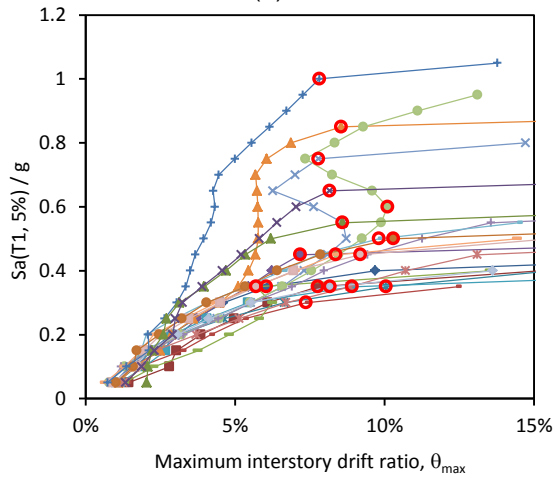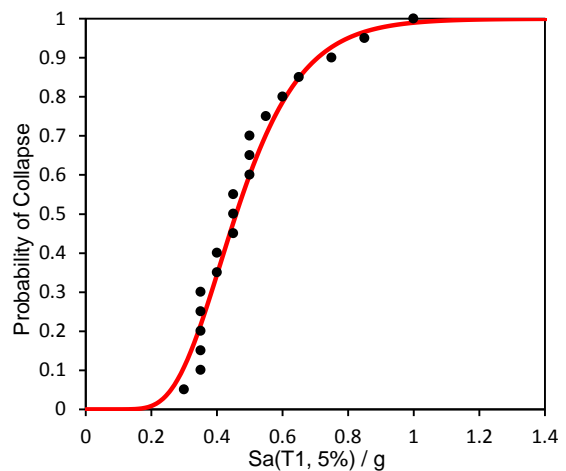
Figure 9.6 IDA curves for models (a) 20-story rigid, (b) HSAC20-4, (c) HSAC20-5, and fragility curves for models (d) 20-story rigid, (e) HSAC20-4, and (f) HSAC20-5

CHAPTER 10

SUMMARY AND CONCLUSIONS

10.1 Summary

A new lateral resistant system called hybrid frame, which is a combination of semi-rigid and fully rigid connections in steel frame, is introduced to improve the performance of moment resistant steel frames subjected to seismic excitations. The SAC frames for Los Angeles site are used as benchmark cases for this study. Hybrid frames are designed by replacing selected fully-rigid connections with semi-rigid connections in the SAC frame.

The concept of the hybrid frame is initially tested on the 9- and 20-story SAC frames using a linear elastic time history analysis. The linear analysis results showed that the force demands in hybrid frame members is significantly less than the force demands in corresponding rigid frames. This concept is then implemented and evaluated in the 3-, 9-, and 20-story frames utilizing a comprehensive nonlinear model with the state-of-the-art modeling techniques.

Effects of semi-rigid connections on local and global responses of the hybrid frames under static and seismic loading were explored. Three different approaches on selection of the semi-rigid connections were adopted. Five different patterns of semi-rigid connections were applied for the 20-story frame using the presented hypotheses and two of the most effective patterns are selected. The effective patterns on this basis were then applied to the 3- and 9-story frames. The optimized connection stiffness was identified by performing a sensitivity study on the initial stiffness of semi-rigid connections.

Accurate computational benchmarks to predict the hysteresis behavior of beam-column steel connections by means of a 3D non-linear finite element analysis were introduced. The element types, inelastic material behavior, bolt pre-tensioning, and contact properties between different components of connections for an accurate modeling were discussed. Incremental

nonlinear finite element analysis took into account all three types of nonlinearities including material, geometry, and contact properties in predicting moment-rotation hysteresis loops. The results obtained from the finite element analyses were validated by a series of full-scale structural tests performed by Abolmaali et al. (2003). This study showed that cost efficient numerical analysis simulation is capable of replacing full-scale tests for steel connections. The semi-rigid connections used in this study for different beam sizes were simulated. A multi-linear curve was fitted to the moment-rotation hysteresis loop of each connection. These curves were then used in global modeling of the hybrid frames.

The seismic demands at the structural and component levels for 3-, 9-, and 20-story rigid SAC frame structures located in Los Angeles site and their corresponding hybrid frames were then quantified. The behavior and response of these structures were studied by subjecting the nonlinear analytical models of these structures to two sets of ground motions. Each set of ground motion consisted of 20 records. These sets were representative of two different hazard levels of 10 percent probability of exceedance in 50 years (DBE) and 2 percent probability of exceedance in 50 years (MCE). In addition, nonlinear static analysis (pushover analysis) was used to identify the strength, stiffness, and ductility of these frames. The semi-rigid connections, which were designed for different beam sizes were implemented in the hybrid frame models. The seismic demands of hybrid frames with the most effective semi-rigid connection patterns were compared with the seismic demands in their corresponding rigid frames.

To evaluate the structures during a seismic loading and potential cause of collapse, a new modal analysis procedure was undertaken. The mode shapes from the Eigen vector solution was used to find the Eigen stiffness corresponding to each mode shape during each time step increment. This in turn determined the locations of the collapse for the regions in frame along with its height where the slope of Eigen vectors approached zero.

Finally, the collapse performance of the Los Angeles SAC 3-, 9-, and 20-story rigid frames and their corresponding hybrid frames were evaluated by application of the FEMA P695

175

reliability analysis methodology. An Incremental Dynamic Analysis (IDA) was performed on the comprehensive nonlinear models of the three rigid and their six corresponding hybrid frames. The IDA was performed by applying the 20 records of the set of MCE ground motions. Then, the collapse performance of the frames was quantified and compared by computing the Collapse Margin Ratio (CMR) value.

10.2. Conclusion Remarks

- The force demands in the beams and columns of the selected 3-, 9-, and 20-story hybrid frames are reduced up to 30 percent. Considering the fact that the structural members (beams and columns) sections in the hybrid frames are the same as those of the corresponding rigid frames, the observed reduction is due to the replacement of rigid connections with semi-rigid connections.

- A flat region in the first mode shape obtained from the nonlinear incremental modal analysis, NIMA, is directly related to the cause of collapse at a given analysis increment.

- The pattern of semi-rigid connection does not make a significant difference in CMR of the 3- and 9-story buildings while it has approximately 13% difference on the 20-story frame which is significant.

- Comparing the collapse margin ration, CMR, values for the 3-story frames (low rise), the rigid frame has the best performance against collapse. As the number of stories increases, the performance of the hybrid frames improves. The seismic performance of the 9-story frames is improved by approximately 10% compared with the performance of the rigid frame. 20-story frames, hybrid frames have a superior performance compared with frames with all rigid connections. The performance of the high-rise hybrid frames is enhance by 20 to 33 percent.

- Results of this study also confirmed that the moment-rotation hysteresis behavior of the steel connections might be quite well predicted by using an accurate 3D non-linear finite element analysis.

10.3 Suggested Future Studies

Some aspects of the research work presented herein needs to be further studied.

Some suggestions for future studies on these topics are:

- Further investigation on the identification of the optimum semi-rigid pattern in hybrid frames is needed. For this purpose, the location of the semi-rigid connections can be identified by using a constrained optimization method mathematical formulation.

- Since the most effective pattern, proposed Z-shape pattern, identified in this study is not symmetry; it might produce torsion in a 3D frame. Thus, evaluation of this concept on a 3D nonlinear model is suggested.

APPENDIX A

DRIFT AND FORCE DEMANDS

Drift demands
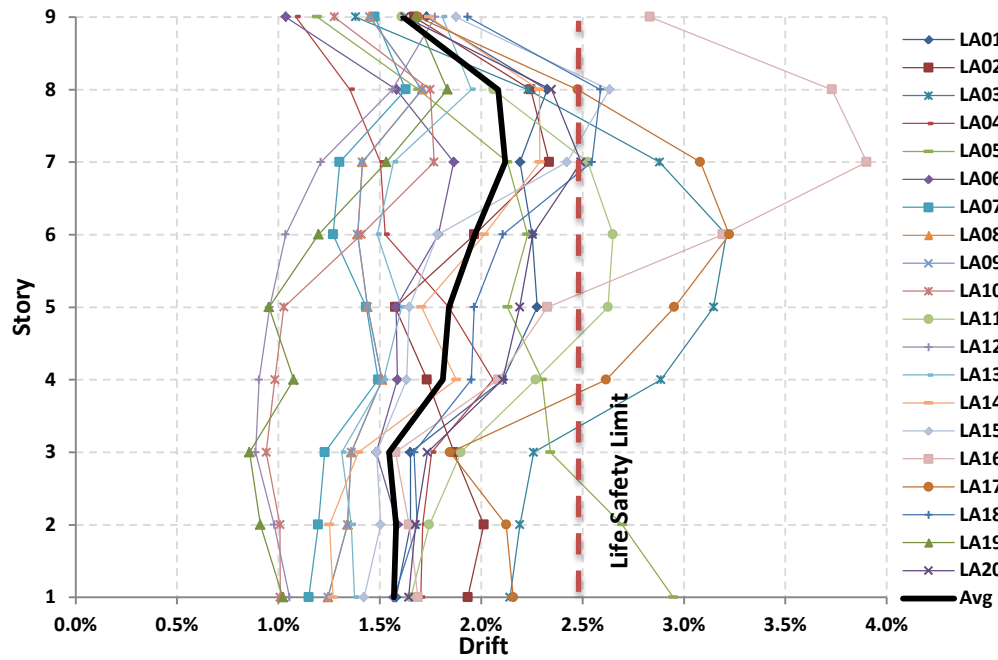
Figure 1 Maximum Story Drift Angle Demands for SAC 9-story Structure subjected to DBE set of Ground Motion
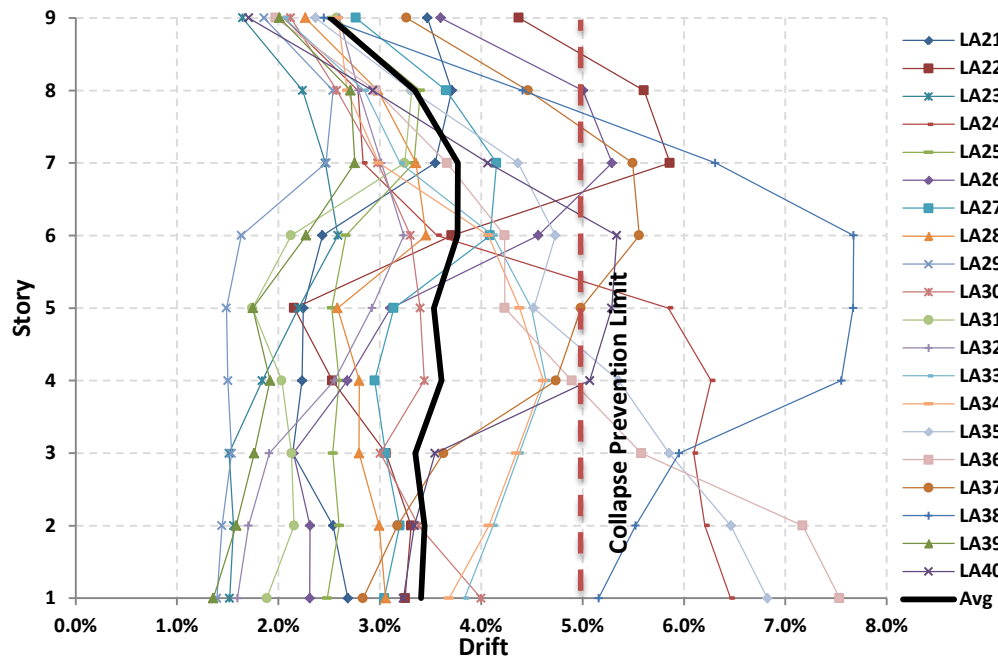
Figure 2 Maximum Story Drift Angle Demands for SAC 9-story Structure subjected to MCE set of Ground Motion
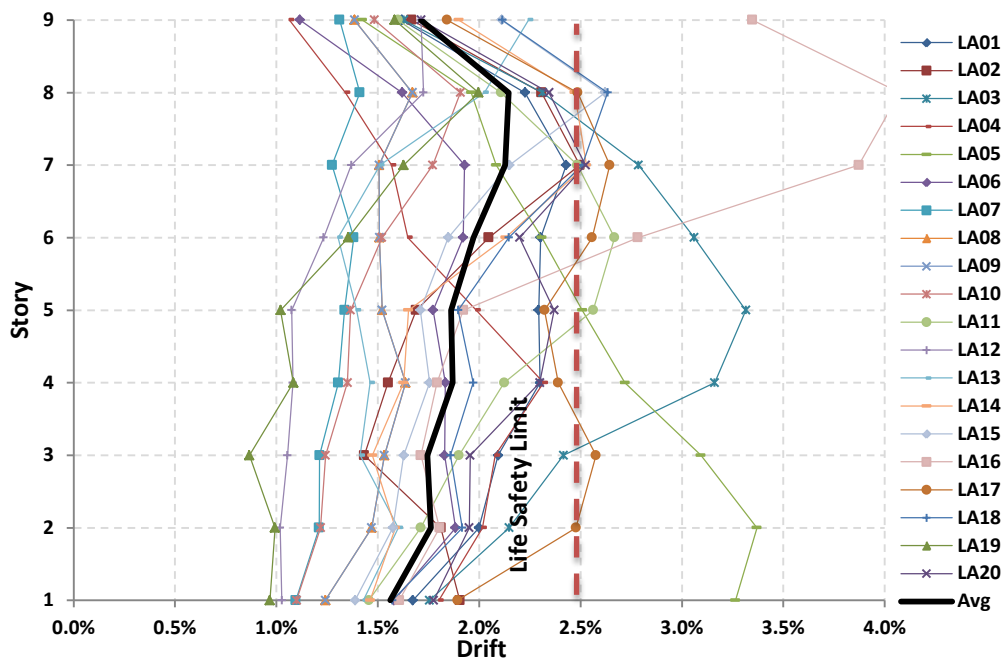
Figure 3. Maximum Story Drift Angle Demands for HSAC9-4 Structure subjected to DBE set of Ground Motion
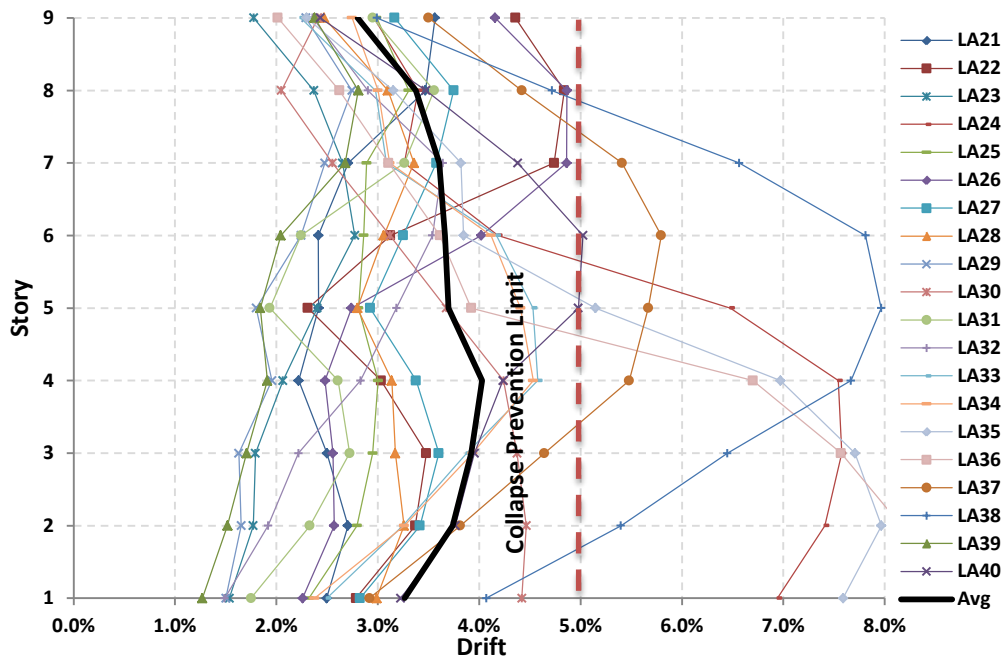
Figure 4. Maximum Story Drift Angle Demands for HSAC9-4 Structure subjected to MCE set of Ground Motion
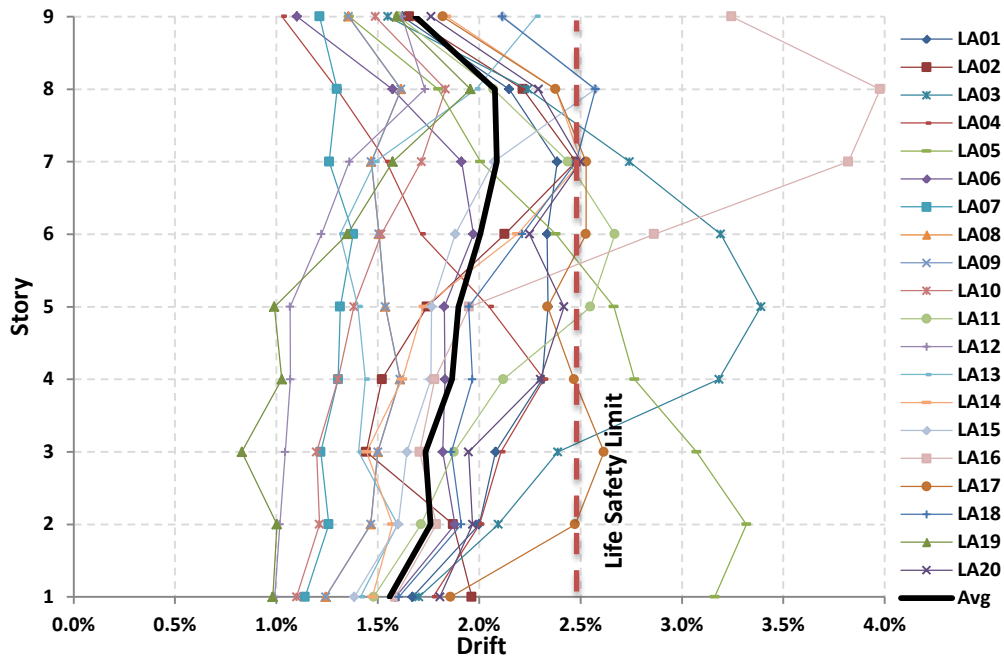
Figure 5. Maximum Story Drift Angle Demands for HSAC9-5 Structure subjected to DBE set of Ground Motion
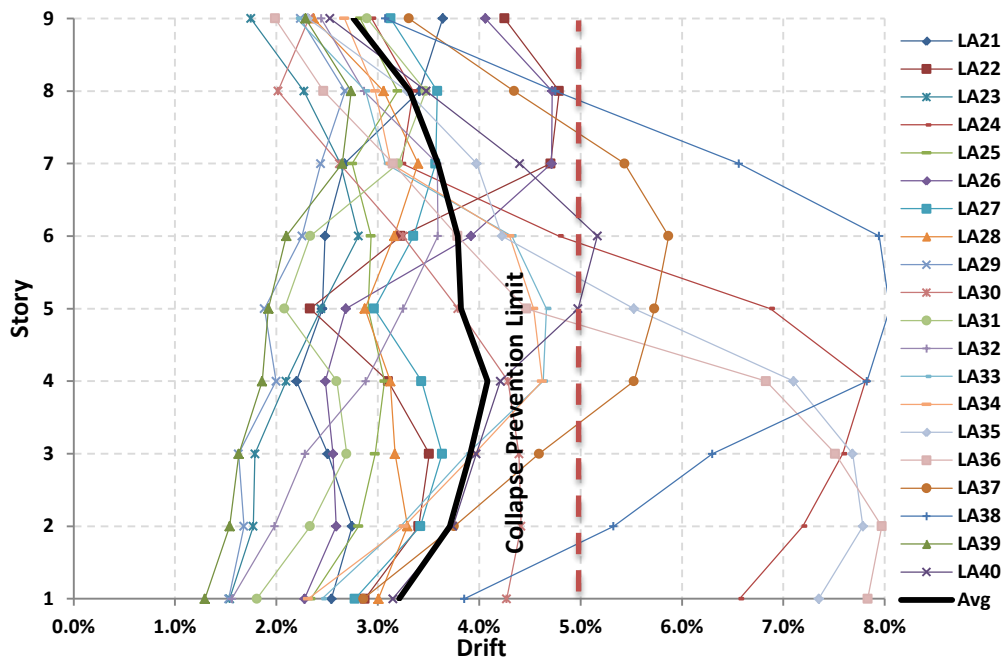
Figure 6. Maximum Story Drift Angle Demands for HSAC9-5 Structure subjected to MCE set of Ground Motion
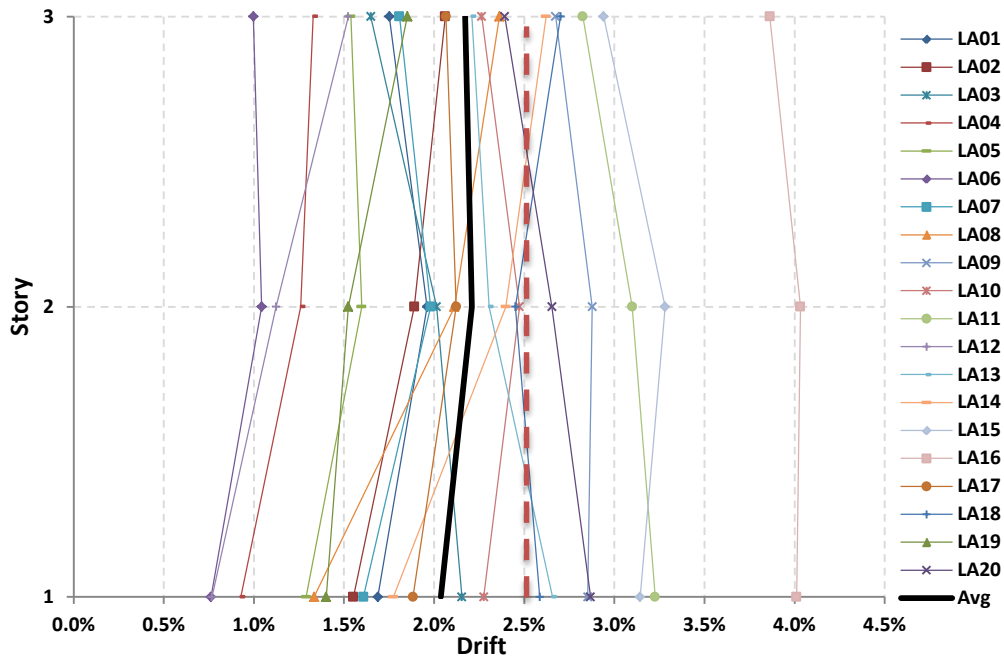
Figure 7. Maximum Story Drift Angle Demands for SAC 3-story Structure subjected to DBE set of Ground Motion
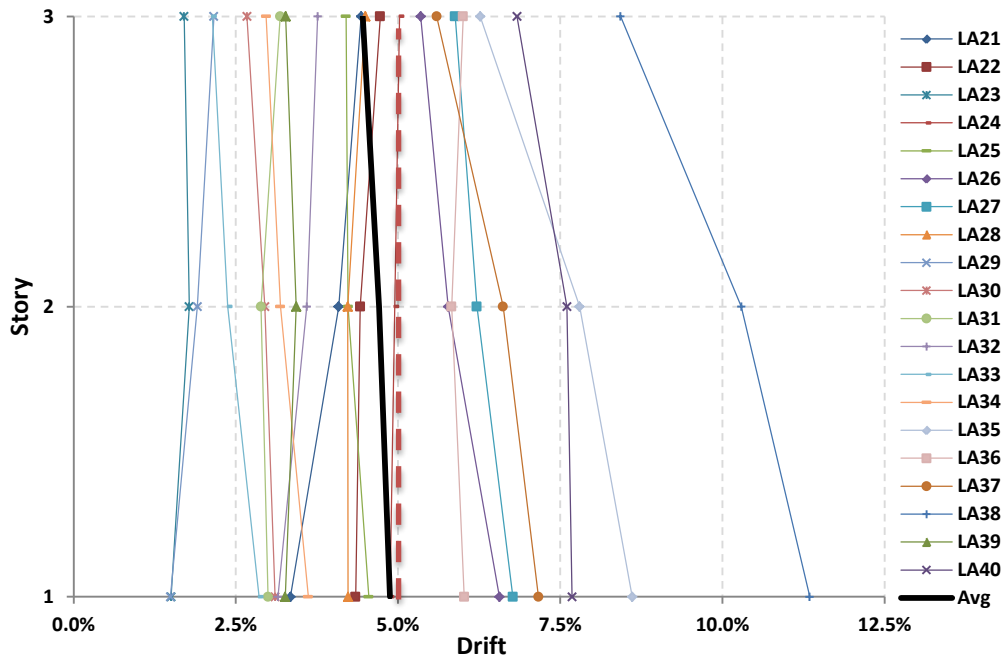
Figure 8. Maximum Story Drift Angle Demands for SAC 3-story Structure subjected to MCE set of Ground Motion

182
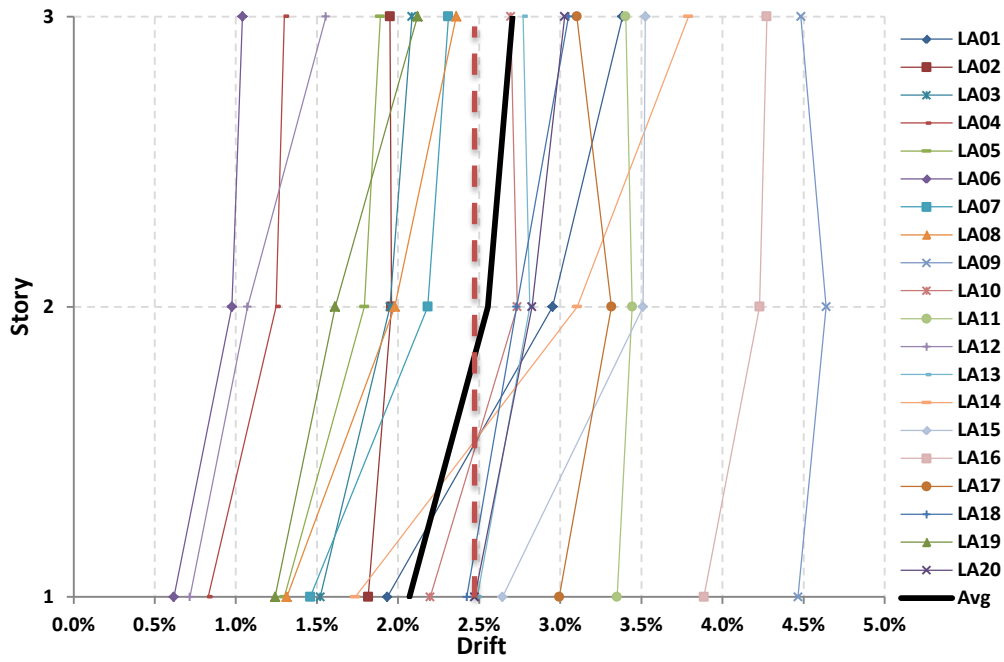
Figure 9. Maximum Story Drift Angle Demands for HSAC3-4 Structure subjected to DBE set of Ground Motion
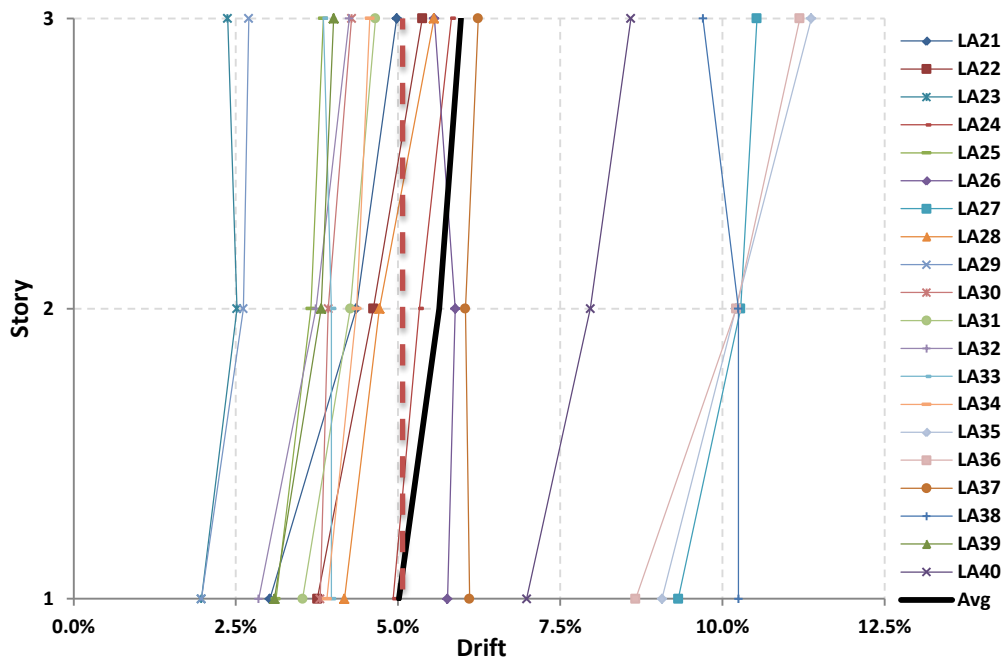
Figure 10. Maximum Story Drift Angle Demands for HSAC3-4 Structure subjected to MCE set of Ground Motion
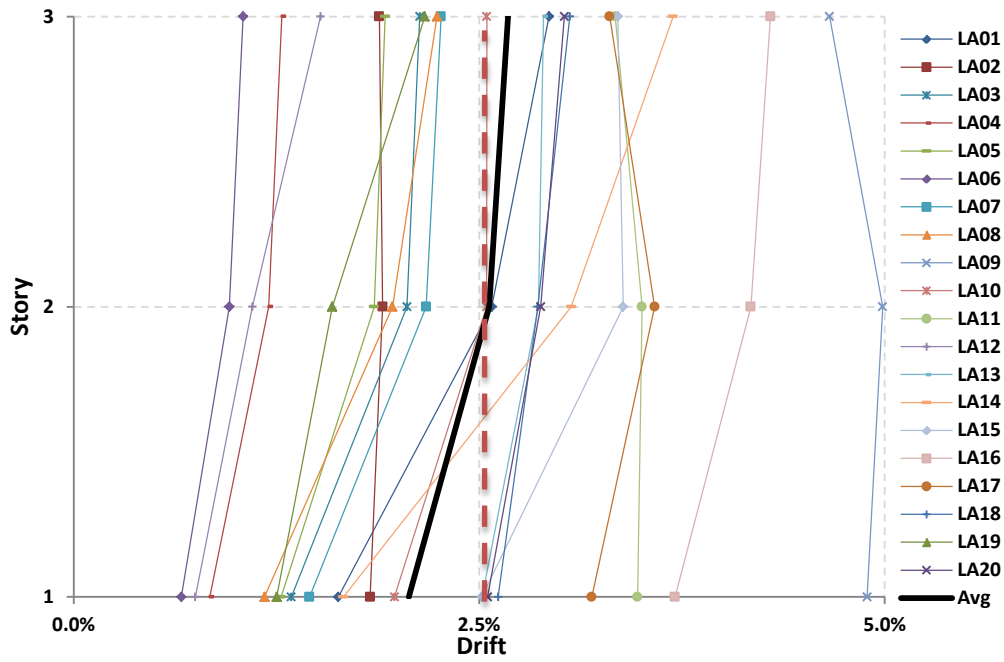
Figure 11. Maximum Story Drift Angle Demands for HSAC3-5 Structure subjected to DBE set of Ground Motion
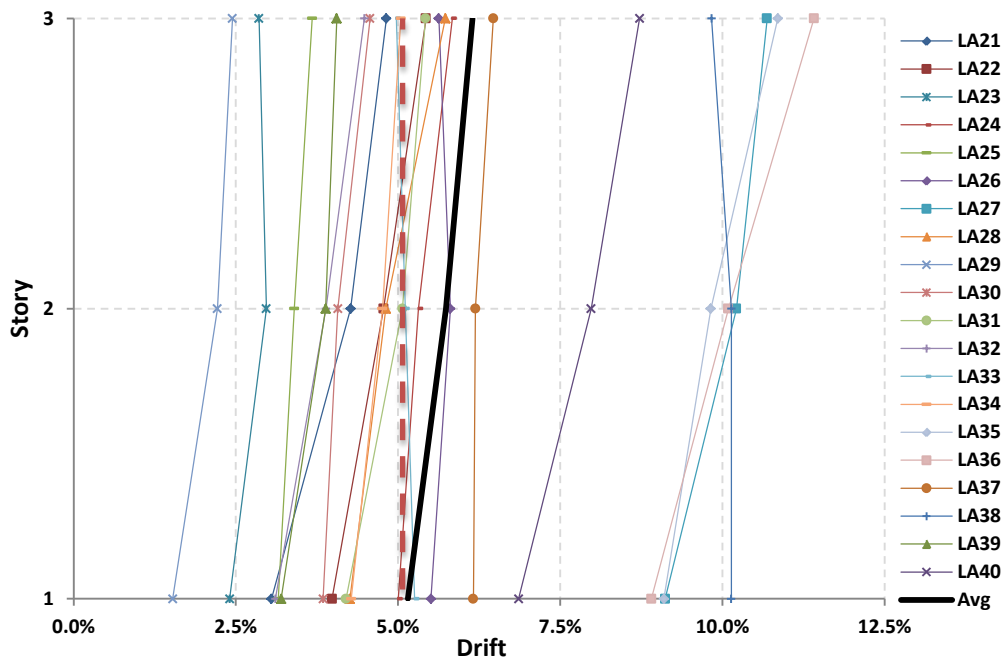
Figure 12. Maximum Story Drift Angle Demands for HSAC3-5 Structure subjected to MCE set of Ground Motion

<u>Beams Responses</u>

Moment
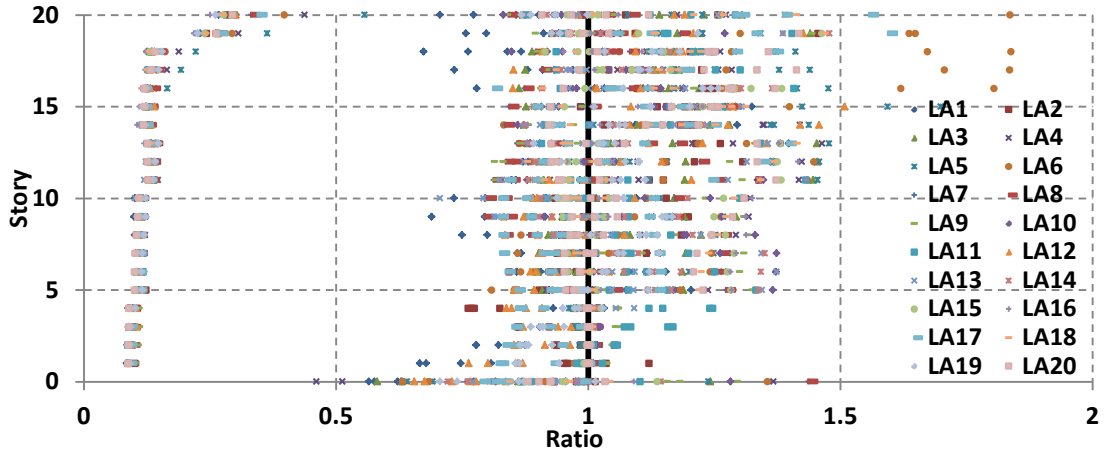
Figure 13 the ratios of the moment in beams for the 20-Story HSAC20-4/SAC subjected to DBE
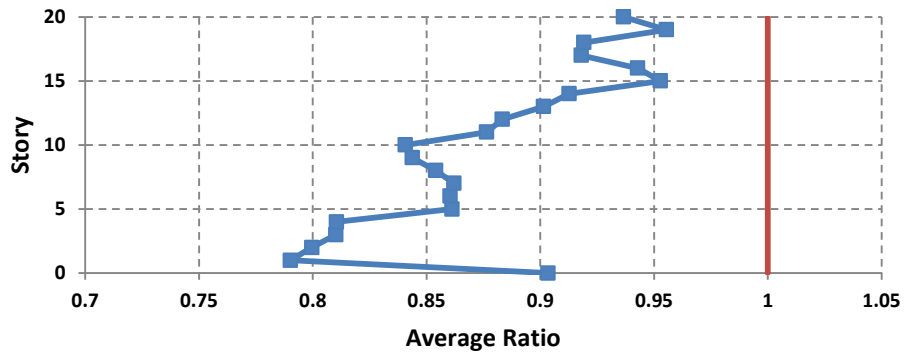
Figure 14 the average ratios of the moment in beams of each story for the 20-Story HSAC20-4/SAC subjected to DBE
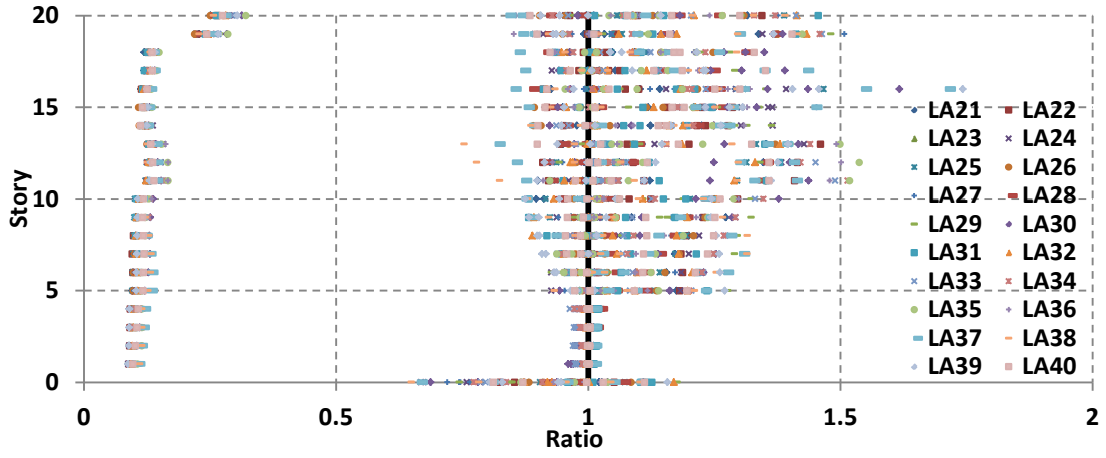
Figure 15 the ratios of the moment in beams for the 20-Story HSAC20-4/SAC subjected to MCE
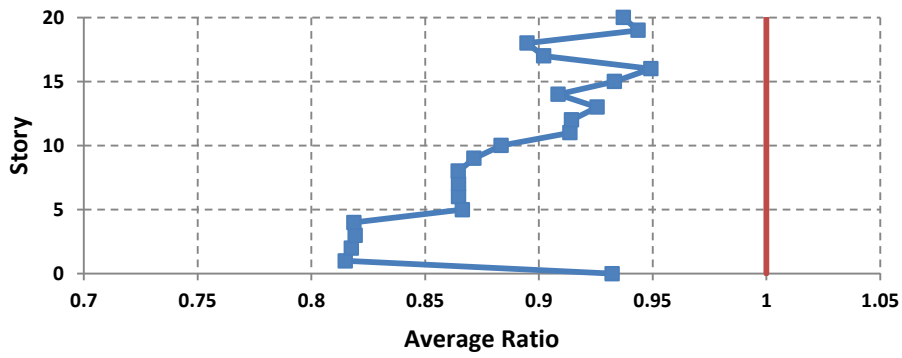
Figure 16 the average ratios of the moment in beams of each story for the 20-Story HSAC20-4/SAC subjected to MCE
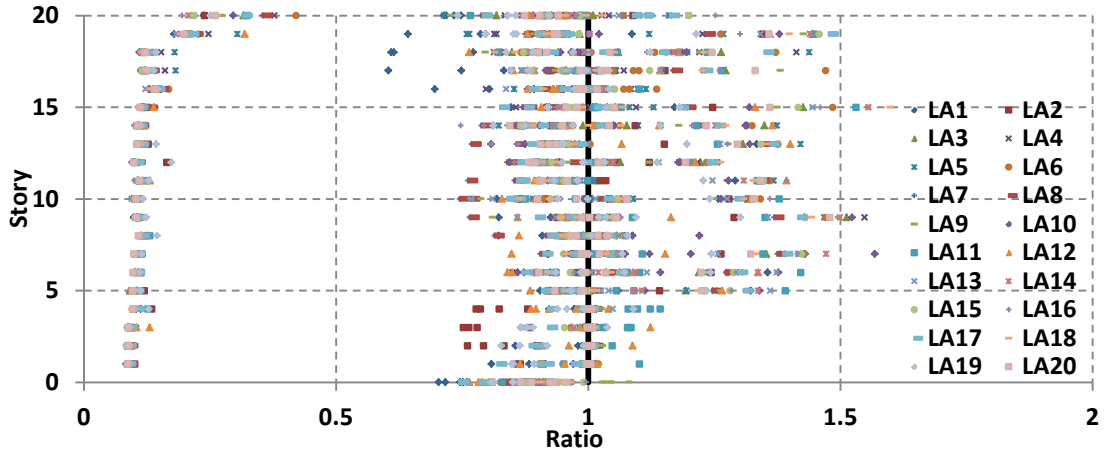
Figure 17 the ratios of the moment in beams for the 20-Story HSAC20-5/SAC subjected to DBE
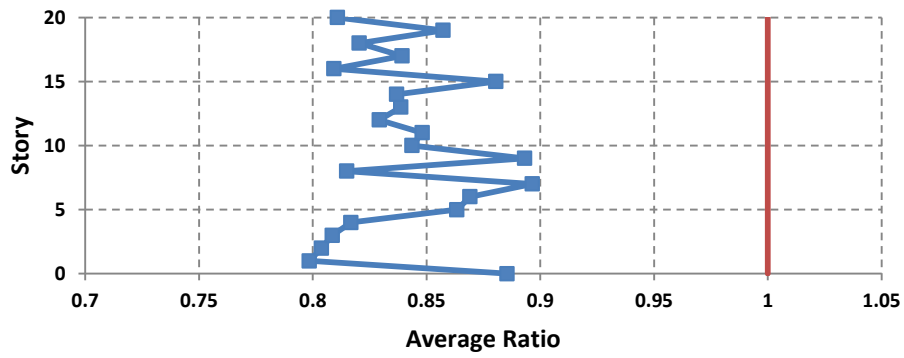
Figure 18 the average ratios of the moment in beams of each story for the 20-Story HSAC20-5/SAC subjected to DBE

187
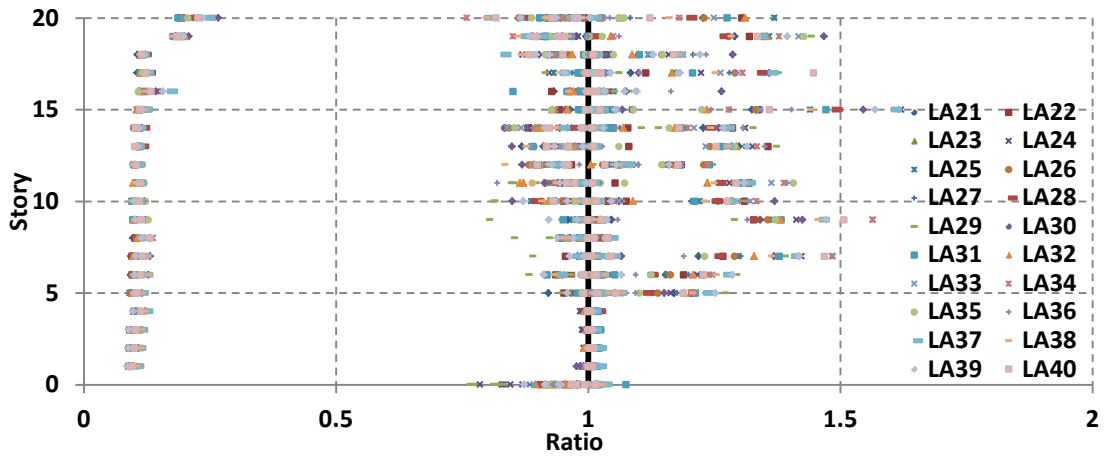
Figure 19 the ratios of the moment in beams for the 20-Story HSAC20-5/SAC subjected to MCE
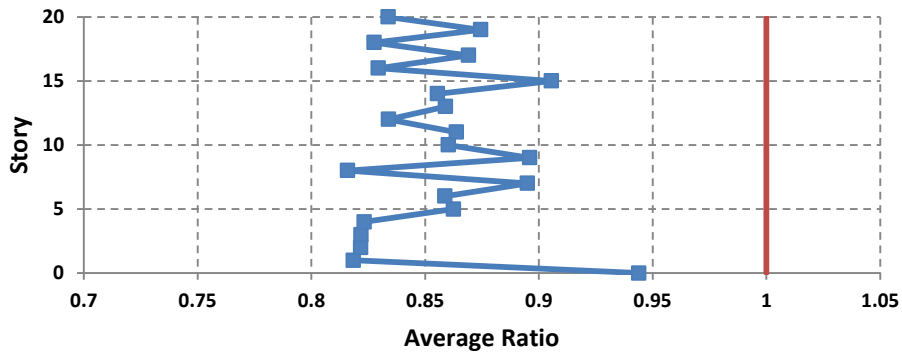
Figure 20 the average ratios of the moment in beams of each story for the 20-Story HSAC20-5/SAC subjected to MCE
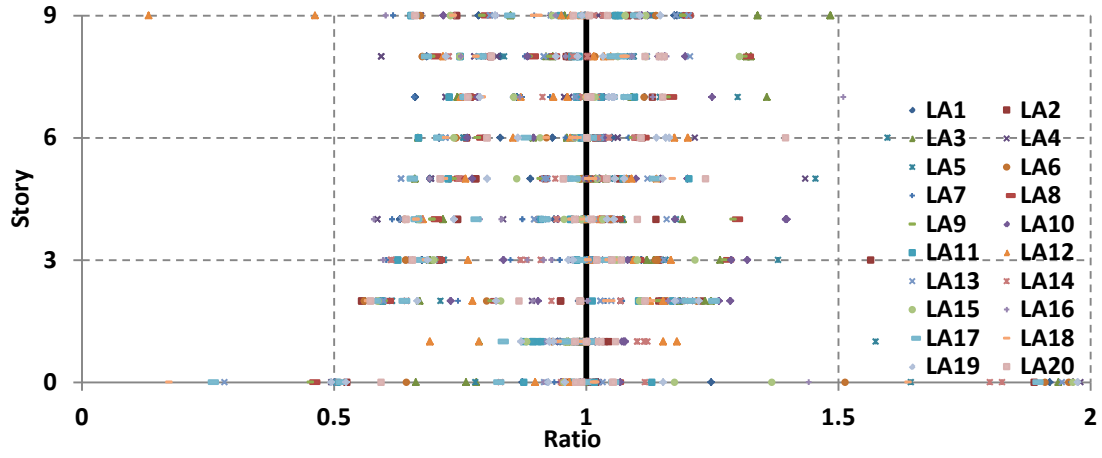
Figure 21 the ratios of the moment in beams for the 9-Story HSAC9-4/SAC subjected to DBE
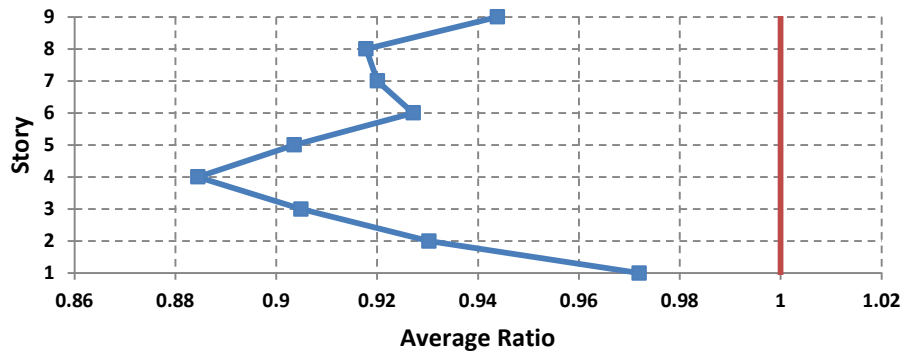
Figure 22 the average ratios of the moment in beams of each story for the 9-Story HSAC9-4/SAC subjected to DBE
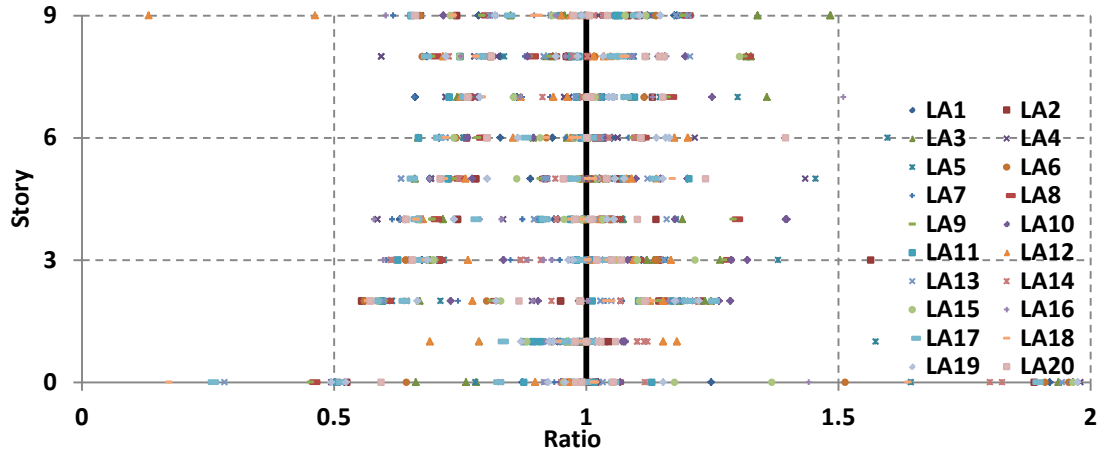
Figure 23 the ratios of the moment in beams for the 9-Story HSAC9-4/SAC subjected to MCE
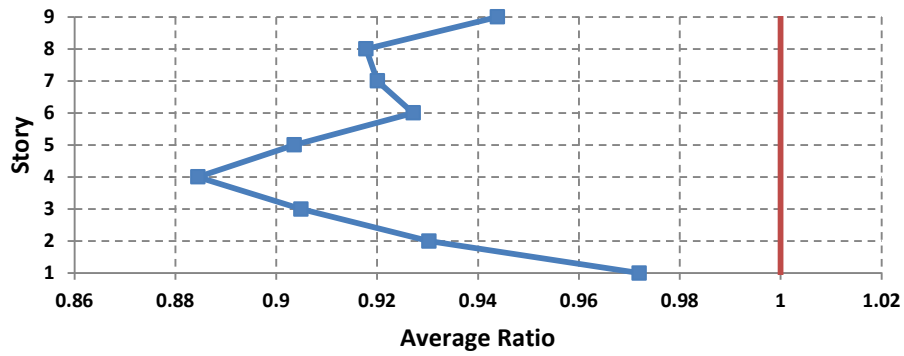
Figure 24 the average ratios of the moment in beams of each story for the 9-Story HSAC9-4/SAC subjected to MCE
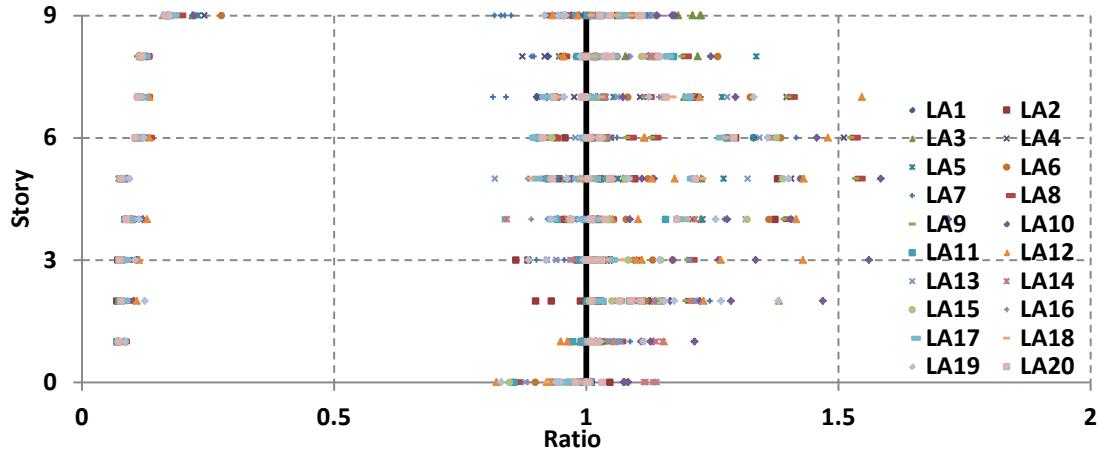
Figure 25 the ratios of the moment in beams for the 9-Story HSAC9-5/SAC subjected to DBE
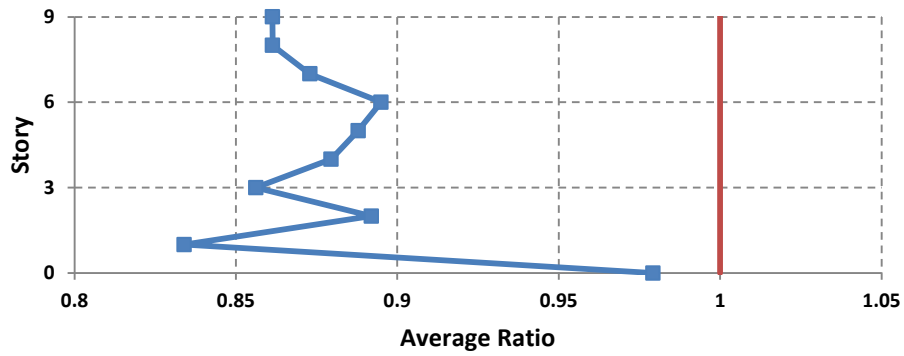
Figure 26 the average ratios of the moment in beams of each story for the 9-Story HSAC9-5/SAC subjected to DBE

191
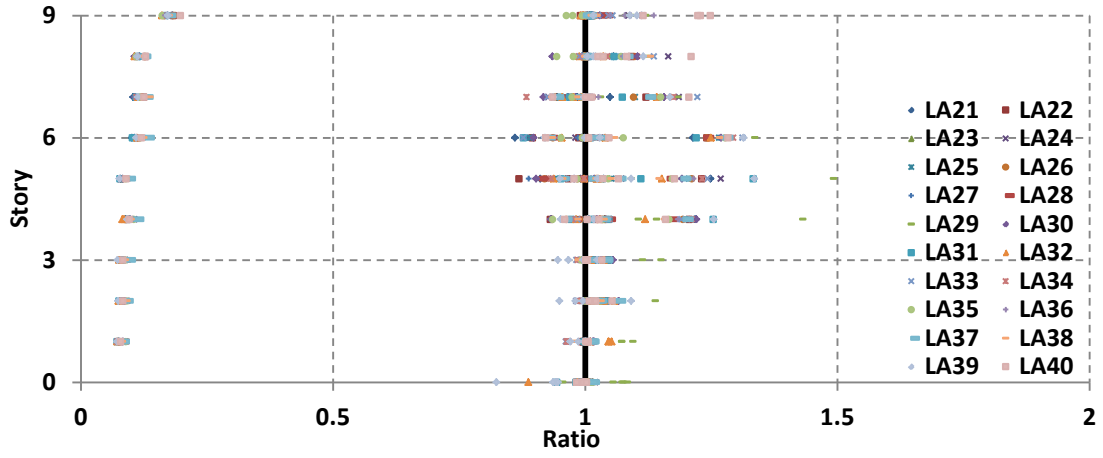
Figure 27 the ratios of the moment in beams for the 9-Story HSAC9-5/SAC subjected to MCE
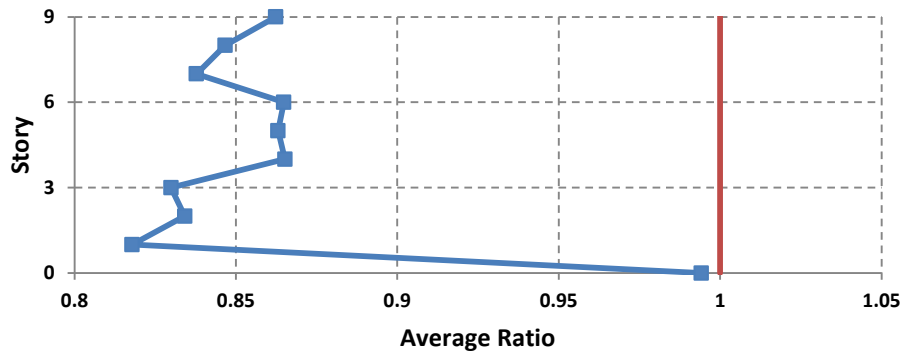
Figure 28 the average ratios of the moment in beams of each story for the 9-Story HSAC9-5/SAC subjected to MCE
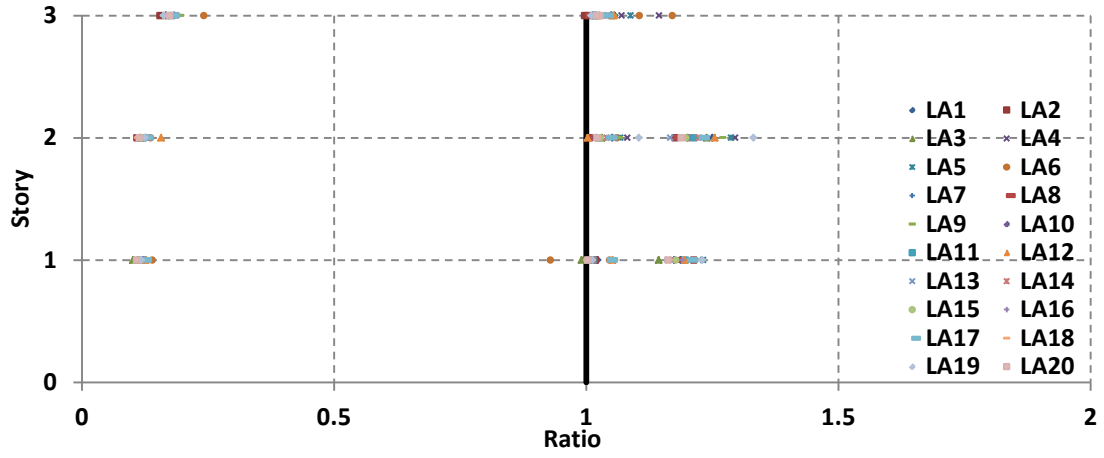
Figure 29 the ratios of the moment in beams for the 3-Story HSAC3-4/SAC subjected to DBE
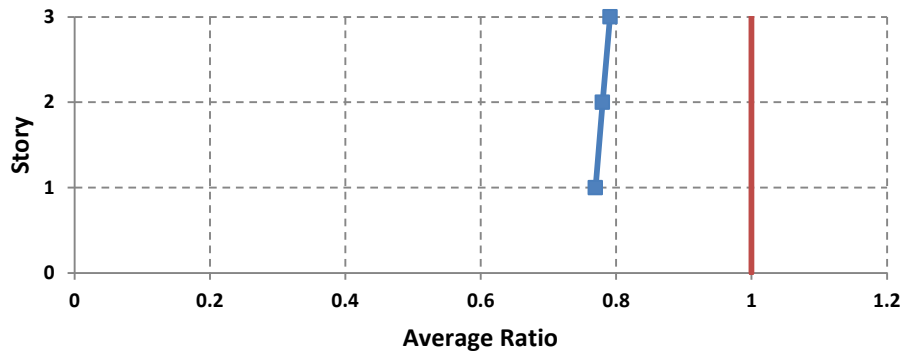
Figure 30 the average ratios of the moment in beams of each story for the 3-Story HSAC9-4/SAC subjected to DBE
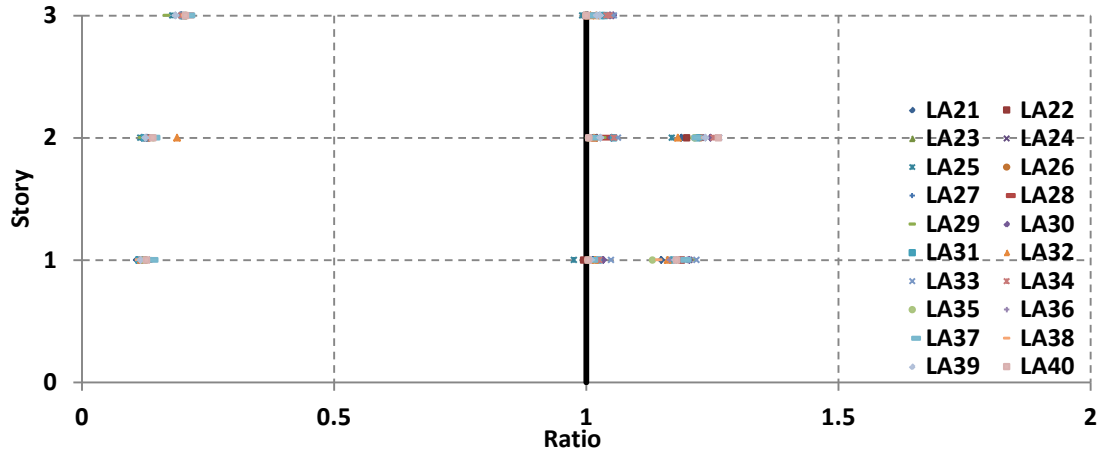
Figure 31 the ratios of the moment in beams for the 3-Story HSAC3-4/SAC subjected to MCE
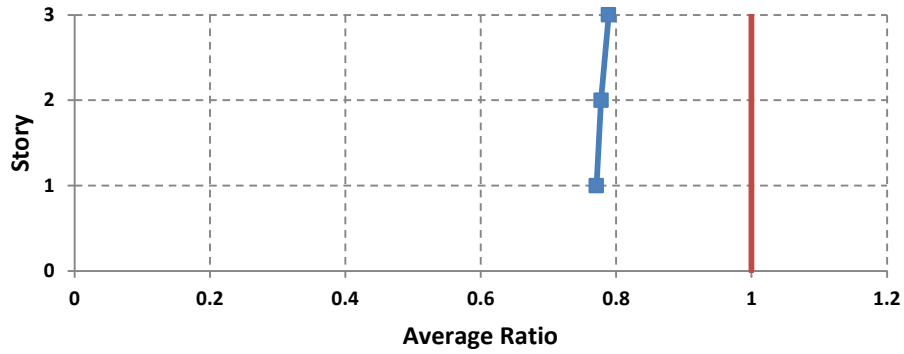
Figure 32 the average ratios of the moment in beams of each story for the 3-Story HSAC3-4/SAC subjected to MCE
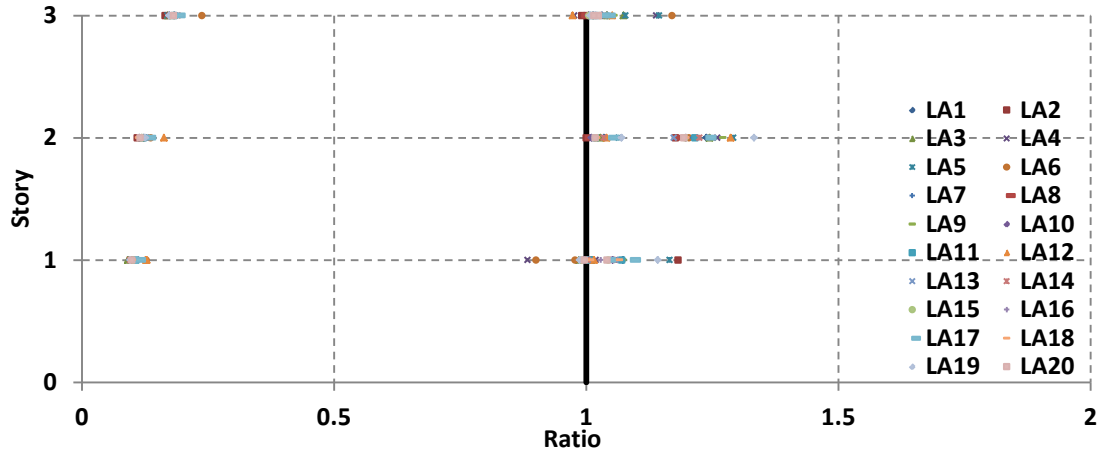
Figure 33 the ratios of the moment in beams for the 9-Story HSAC9-5/SAC subjected to DBE
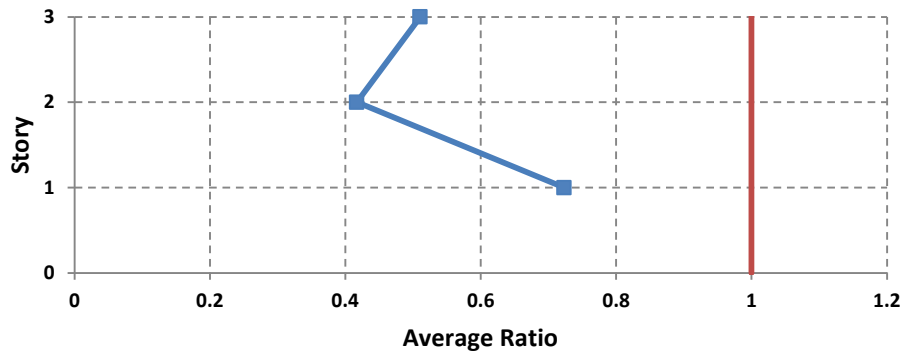
Figure 34 the average ratios of the moment in beams of each story for the 9-Story HSAC9-5/SAC subjected to DBE
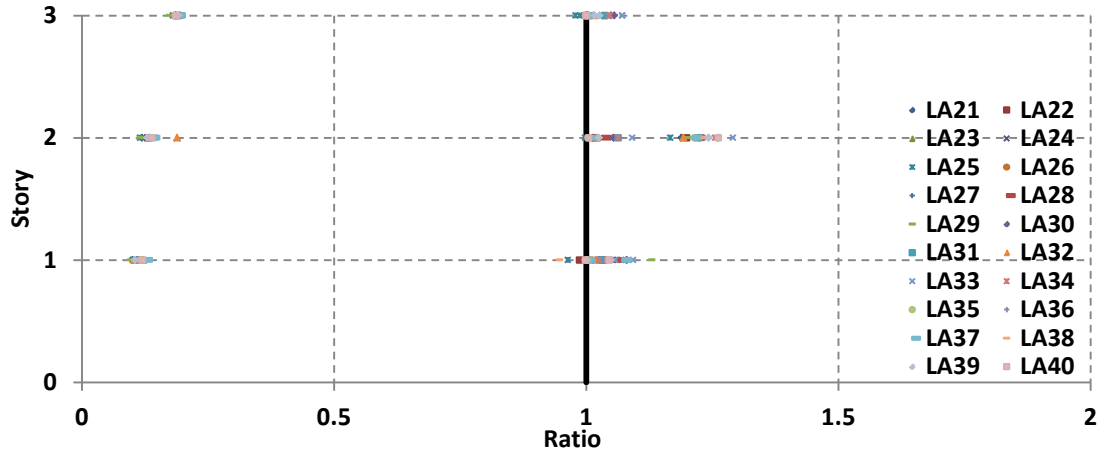
Figure 35 the ratios of the moment in beams for the 9-Story HSAC9-5/SAC subjected to MCE
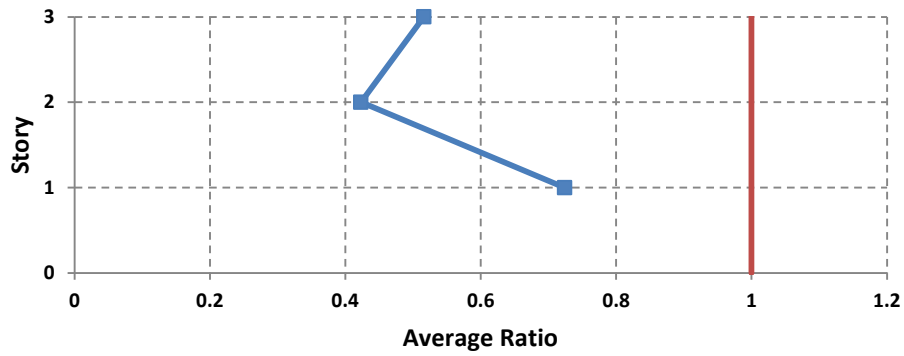
Figure 36 the average ratios of the moment in beams of each story for the 9-Story HSAC9-5/SAC subjected to MCE
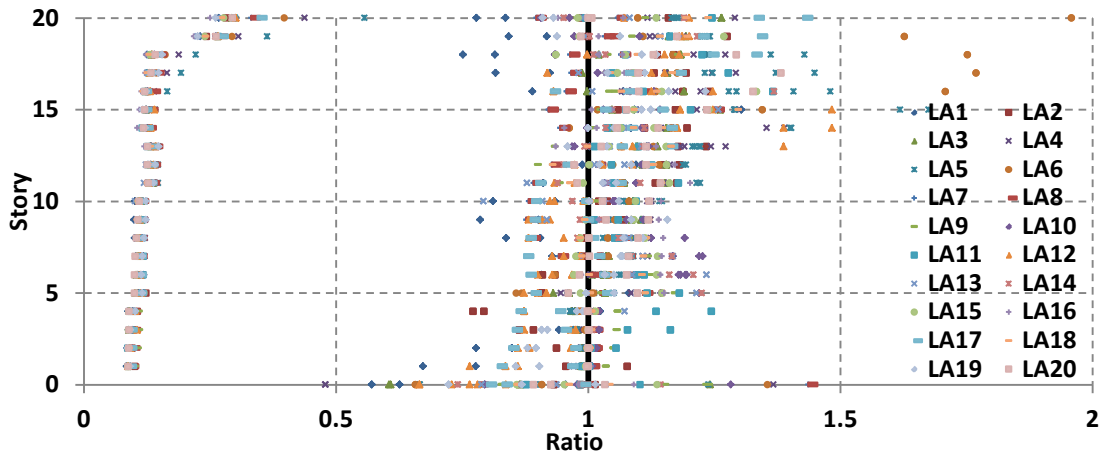
Shear

Figure 37 the ratios of the shear in beams for the 20-Story HSAC20-4/SAC subjected to DBE
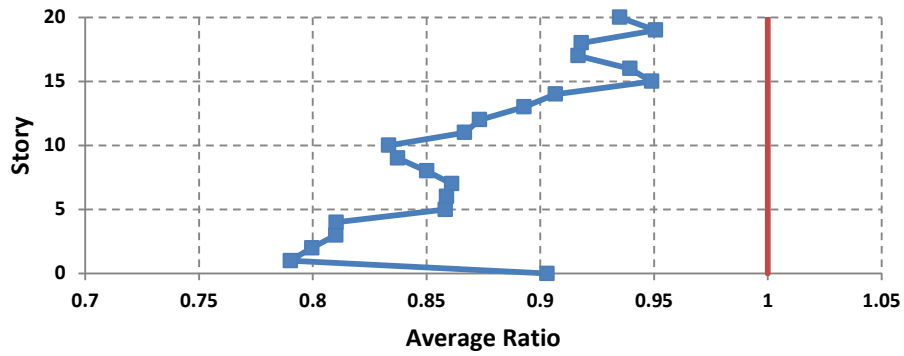
Figure 38 the average ratios of the shear in beams of each story for the 20-Story HSAC20-4/SAC subjected to DBE
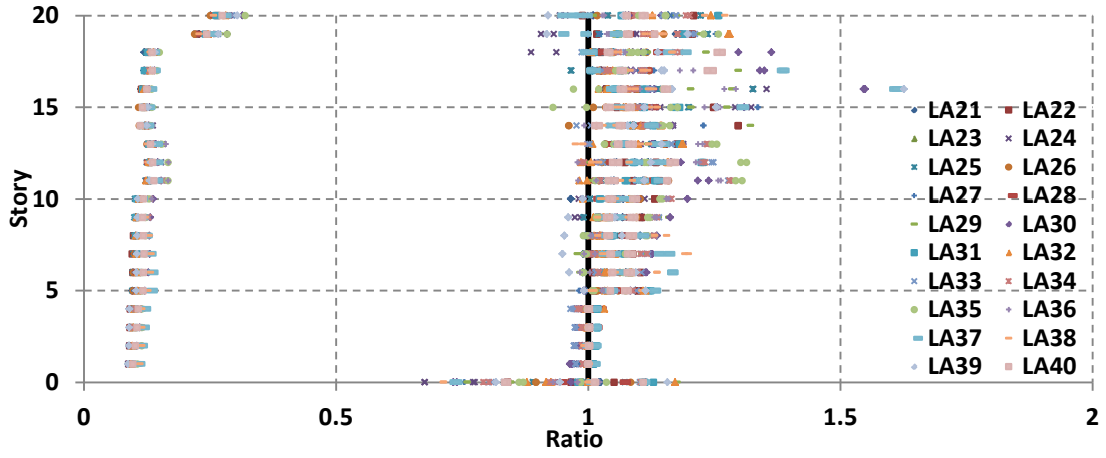
Figure 39 the ratios of the shear in beams for the 20-Story HSAC20-4/SAC subjected to MCE
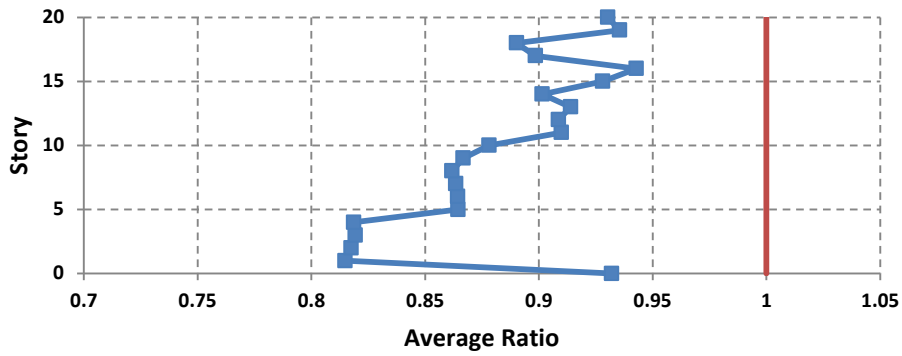
Figure 40 the average ratios of the shear in beams of each story for the 20-Story HSAC20-4/SAC subjected to MCE
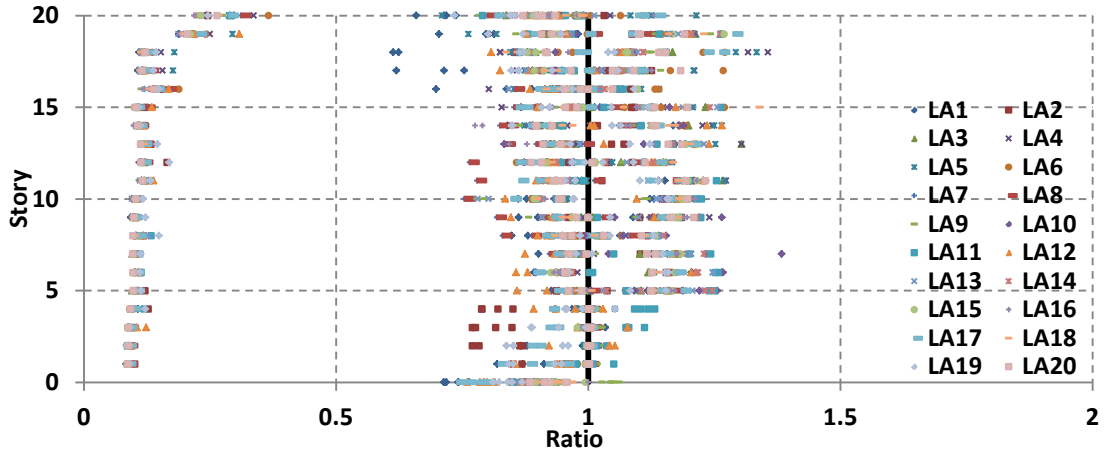
Figure 41 the ratios of the shear in beams for the 20-Story HSAC20-5/SAC subjected to DBE
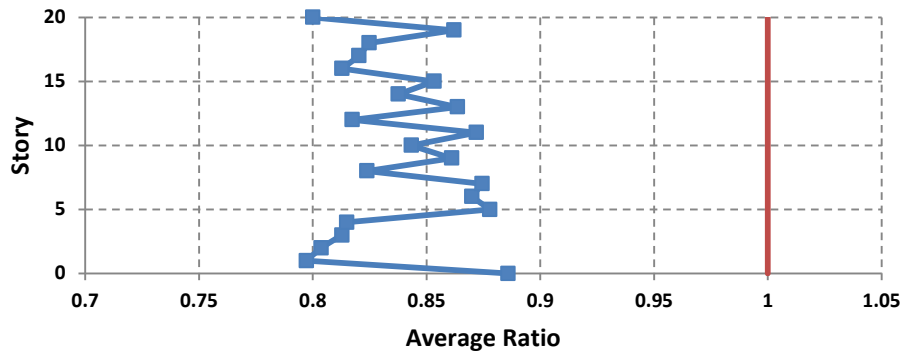
Figure 42 the average ratios of the shear in beams of each story for the 20-Story HSAC20-5/SAC subjected to DBE
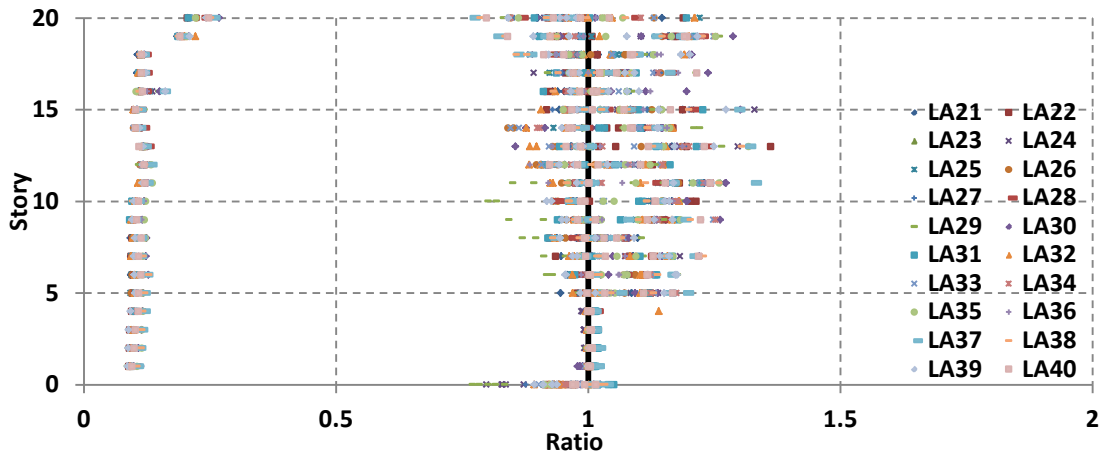
Figure 43 the ratios of the shear in beams for the 20-Story HSAC20-5/SAC subjected to MCE
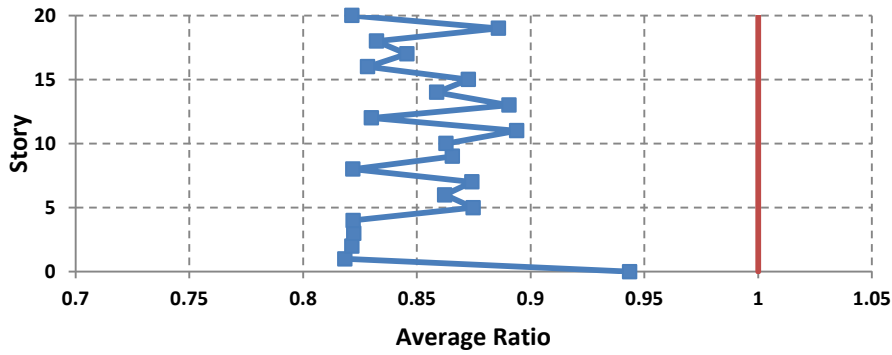
Figure 44 the average ratios of the shear in beams of each story for the 20-Story HSAC20-5/SAC subjected to MCE
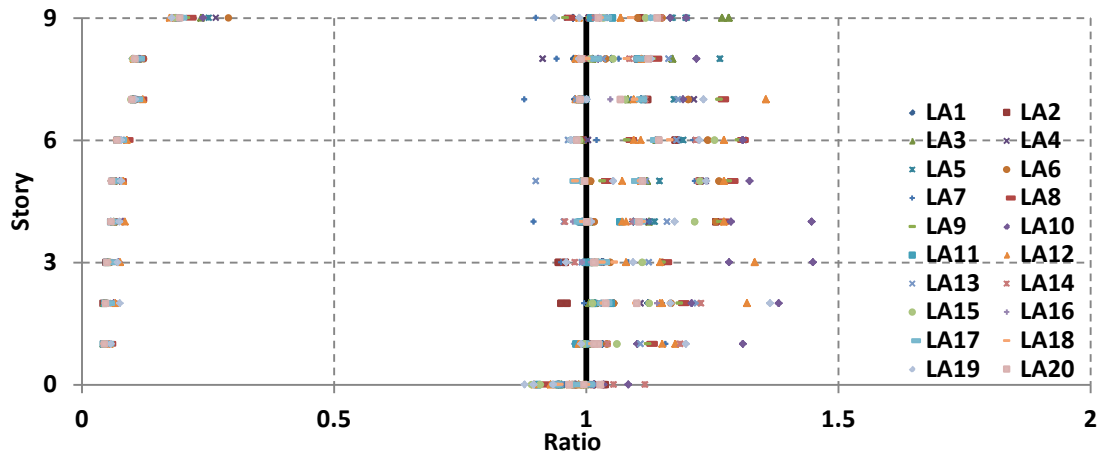
Figure 45 the ratios of the shear in beams for the 9-Story HSAC9-4/SAC subjected to DBE
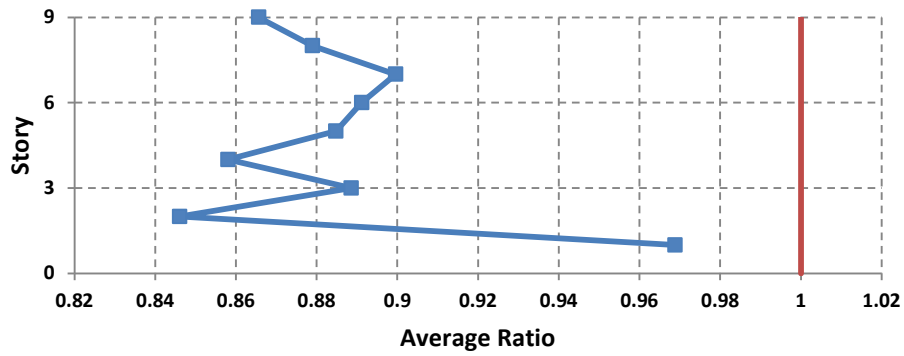
Figure 46 the average ratios of the shear in beams of each story for the 9-Story HSAC9-4/SAC subjected to DBE
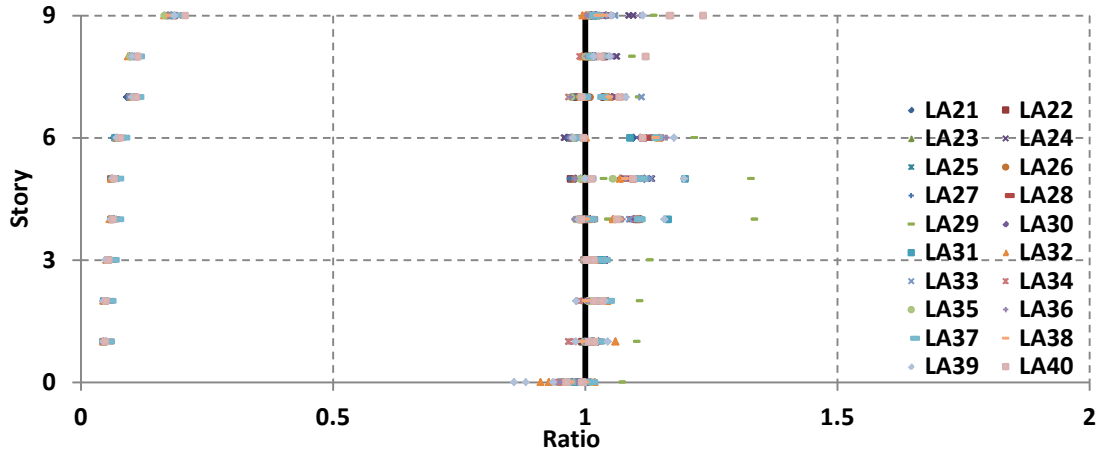
Figure 47 the ratios of the shear in beams for the 9-Story HSAC9-4/SAC subjected to MCE
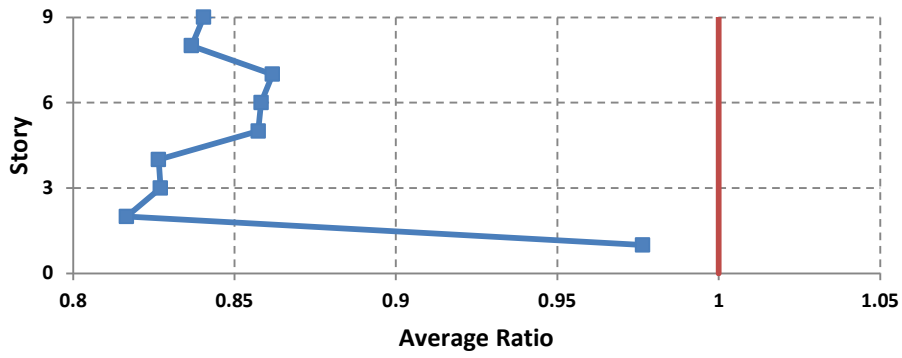
Figure 48 the average ratios of the shear in beams of each story for the 9-Story HSAC9-4/SAC subjected to MCE
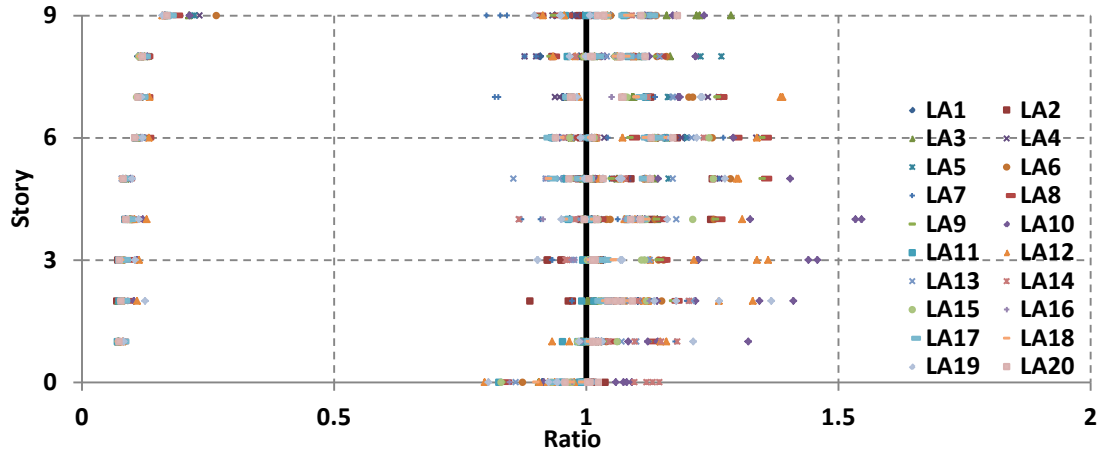
Figure 49 the ratios of the shear in beams for the 9-Story HSAC9-5/SAC subjected to DBE
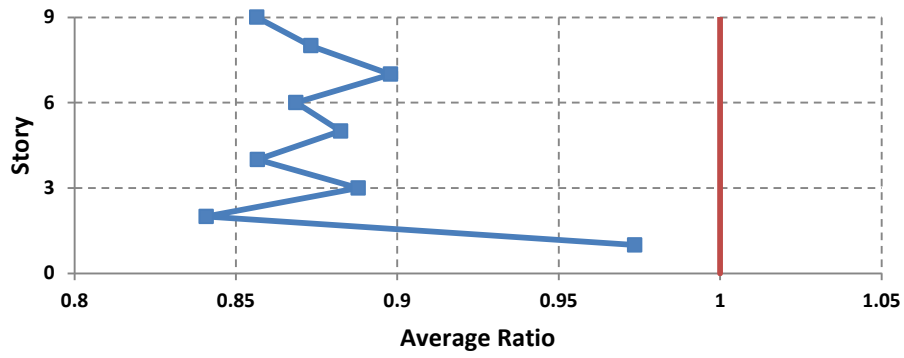
Figure 50 the average ratios of the shear in beams of each story for the 9-Story HSAC9-5/SAC subjected to DBE
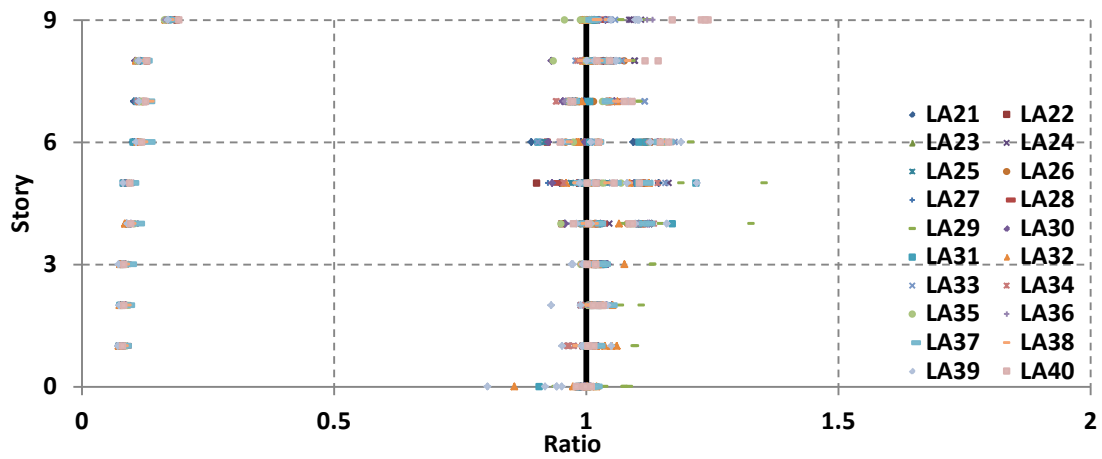
Figure 51 the ratios of the shear in beams for the 9-Story HSAC9-5/SAC subjected to MCE
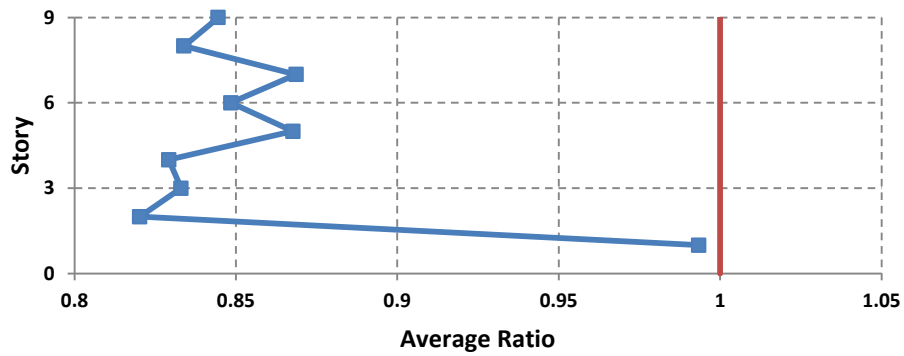
Figure 52 the average ratios of the shear in beams of each story for the 9-Story HSAC9-5/SAC subjected to MCE
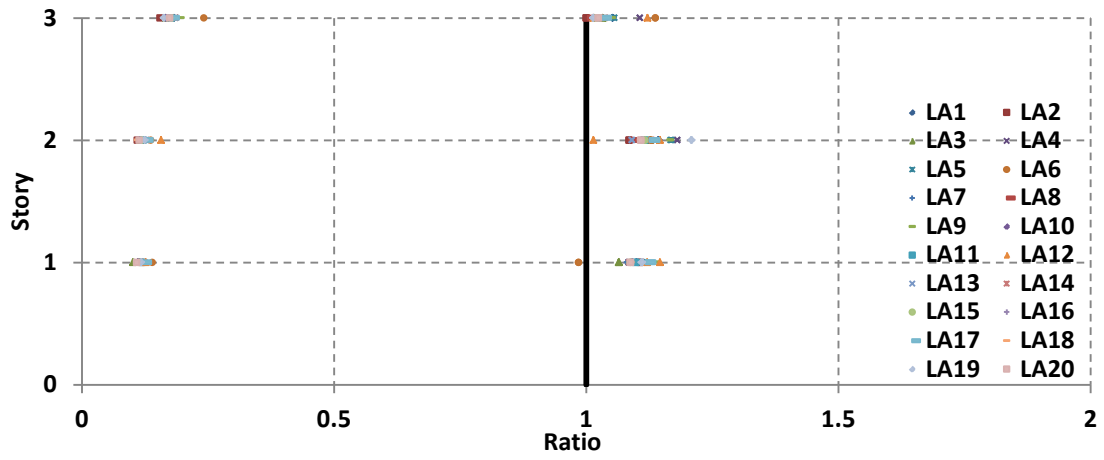
Figure 53 the ratios of the shear in beams for the 3-Story HSAC3-4/SAC subjected to DBE
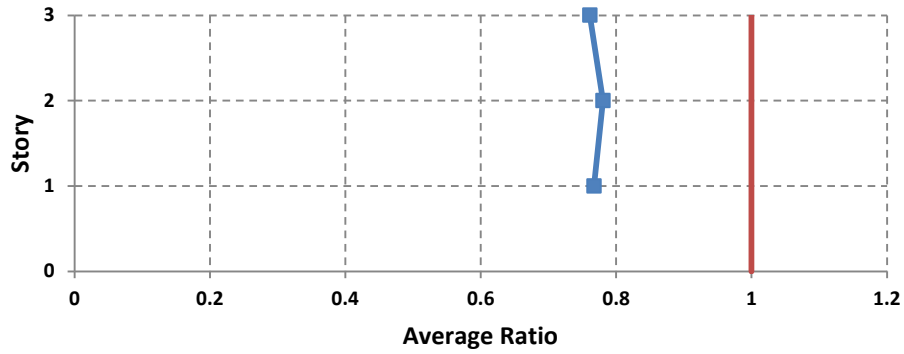
Figure 54 the average ratios of the shear in beams of each story for the 3-Story HSAC3-4/SAC subjected to DBE
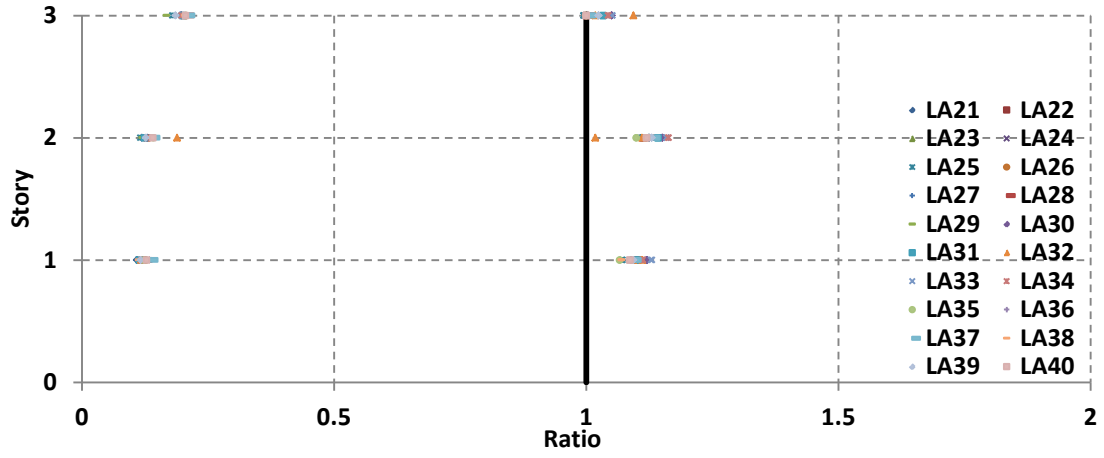
Figure 55 the ratios of the shear in beams for the 20-Story HSAC20-4/SAC subjected to MCE
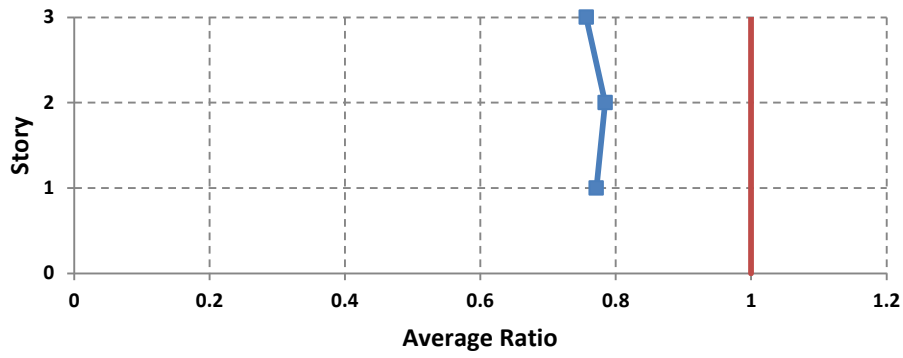
Figure 56 the average ratios of the shear in beams of each story for the 20-Story HSAC20-4/SAC subjected to MCE
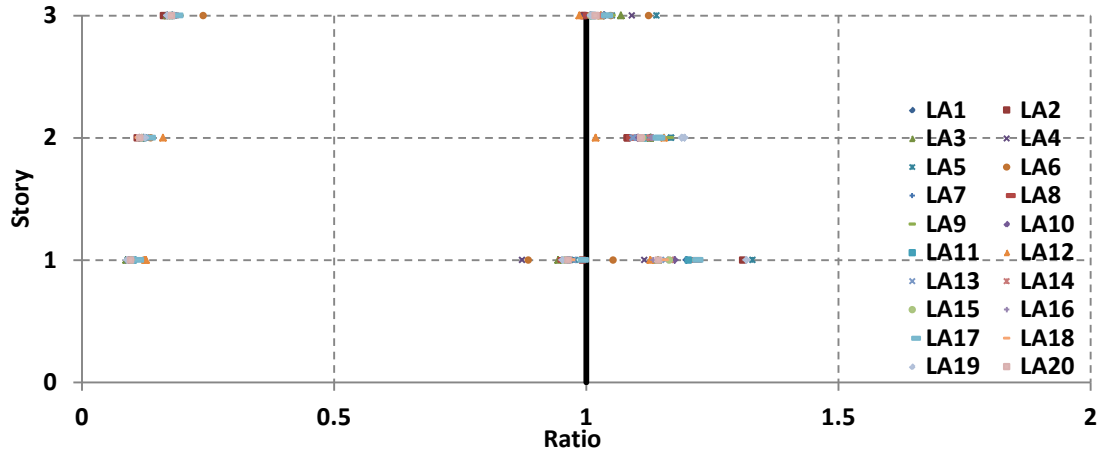
Figure 57 the ratios of the shear in beams for the 3-Story HSAC3-5/SAC subjected to DBE
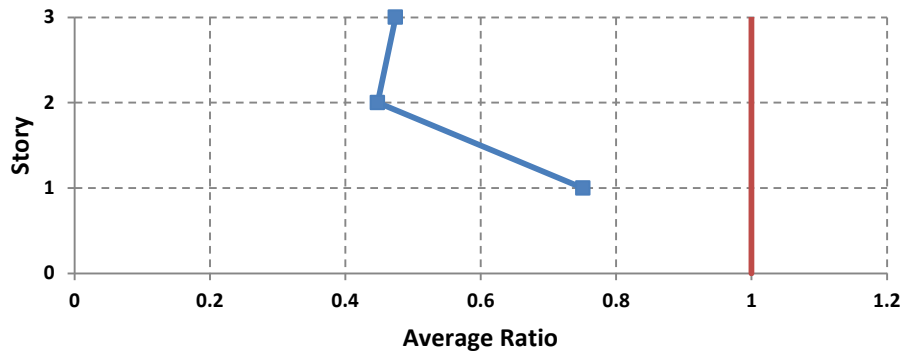
Figure 58 the average ratios of the shear in beams of each story for the 3-Story HSAC3-5/SAC subjected to DBE
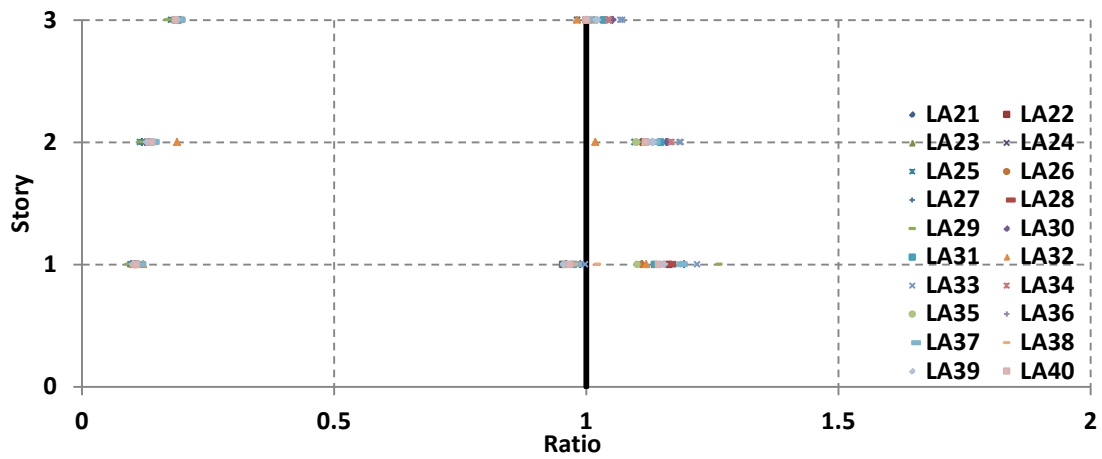
Figure 59 the ratios of the shear in beams for the 20-Story HSAC20-5/SAC subjected to MCE
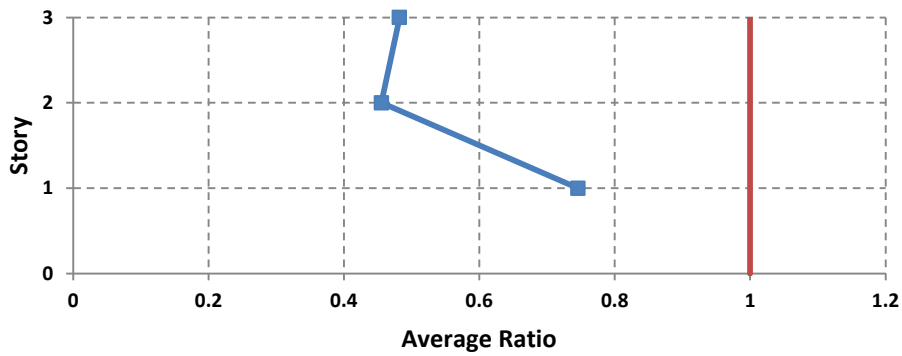
Figure 60 the average ratios of the shear in beams of each story for the 20-Story HSAC20-5/SAC subjected to MCE
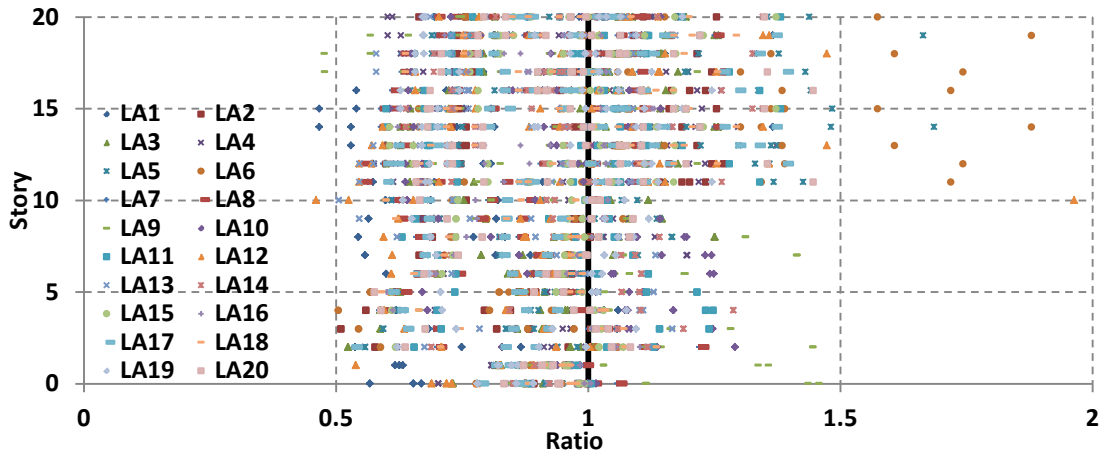
Moment

Figure 61 the ratios of the moment in columns for the 20-Story HSAC20-4/SAC subjected to DBE
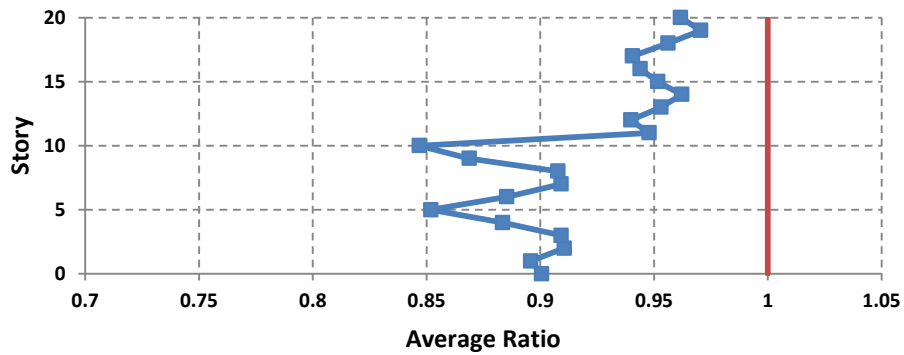
Figure 62 the average ratios of the moment in columns of each story for the 20-Story HSAC20-4/SAC subjected to DBE
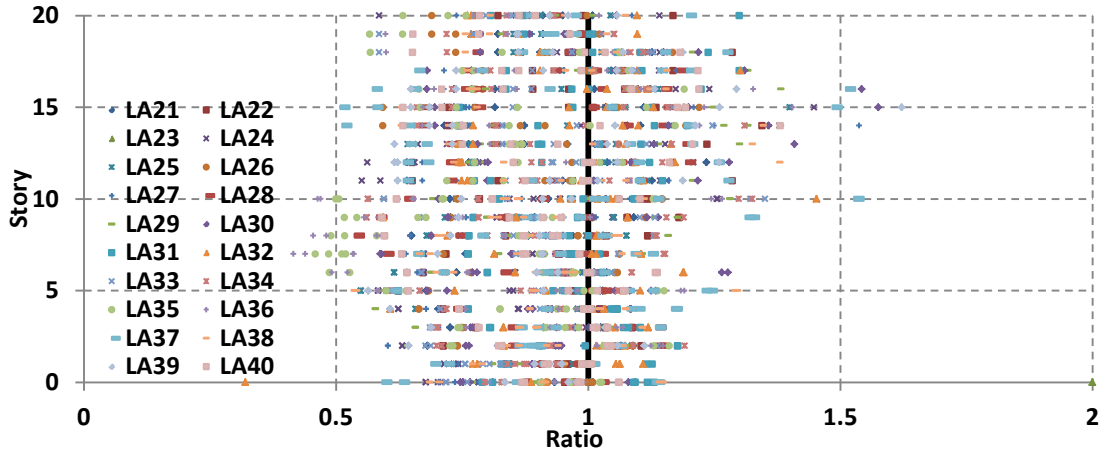
Figure 63 the ratios of the moment in columns for the 20-Story HSAC20-4/SAC subjected to MCE
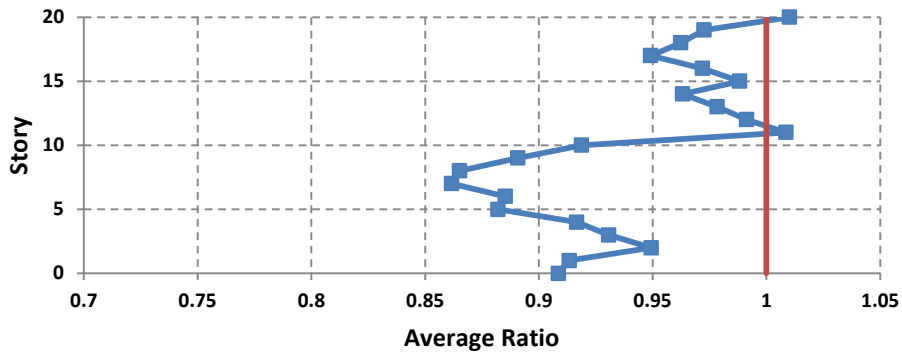
Figure 64 the average ratios of the moment in columns of each story for the 20-Story HSAC20-4/SAC subjected to MCE
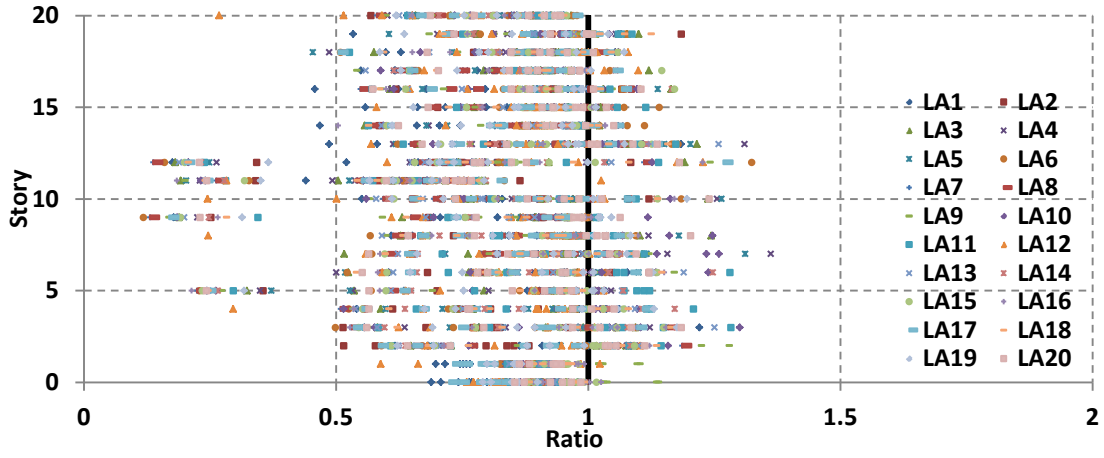
Figure 65 the ratios of the moment in columns for the 20-Story HSAC20-5/SAC subjected to DBE
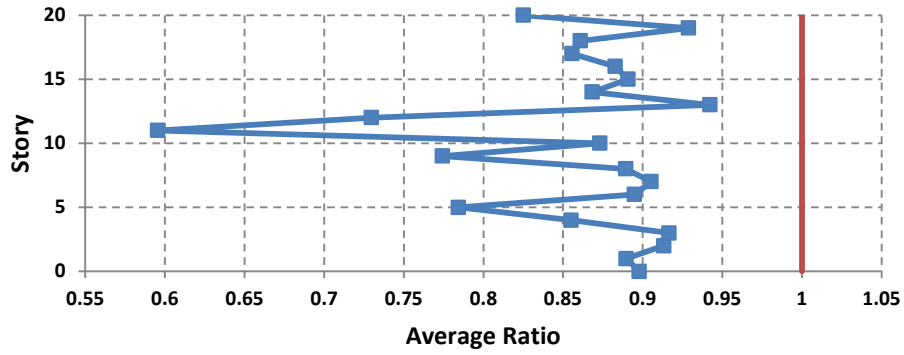
Figure 66 the average ratios of the moment in columns of each story for the 20-Story HSAC20-5/SAC subjected to DBE
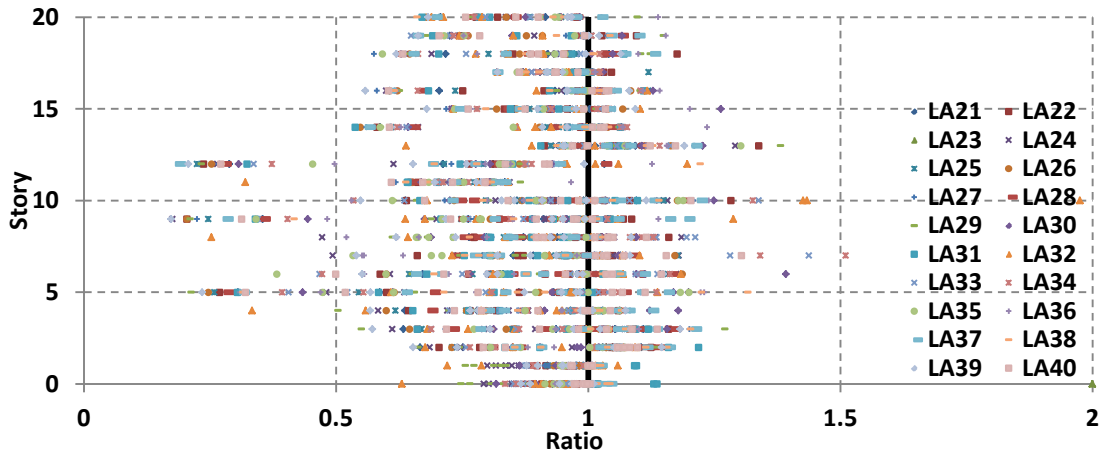
Figure 67 the ratios of the moment in columns for the 20-Story HSAC20-5/SAC subjected to MCE
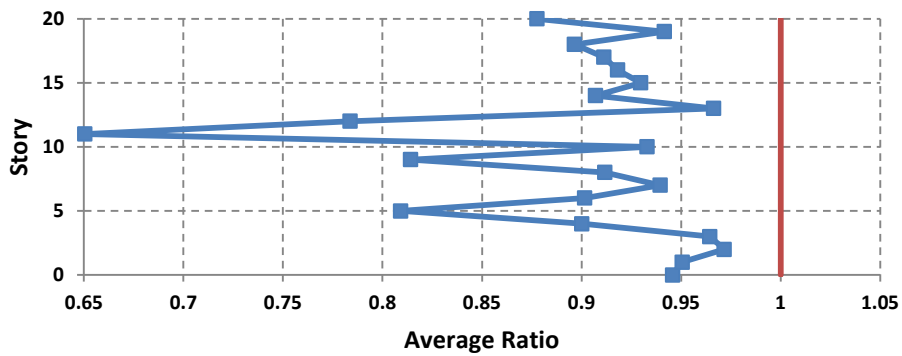
Figure 68 the average ratios of the moment in columns of each story for the 20-Story HSAC20-5/SAC subjected to MCE

Figure 69 the ratios of the moment in columns for the 9-Story HSAC9-4/SAC subjected to DBE

Figure 70 the average ratios of the moment in columns of each story for the 9-Story HSAC9-4/SAC subjected to DBE
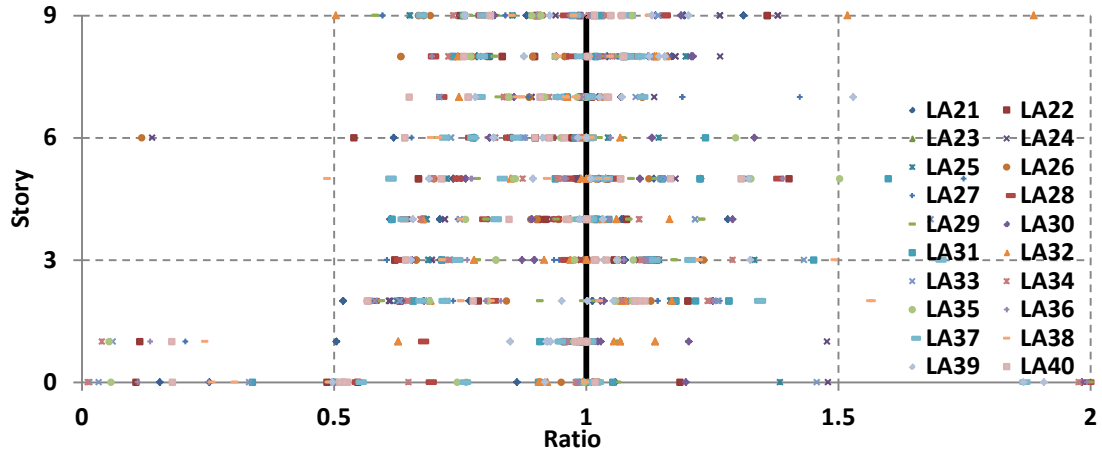
Figure 71 the ratios of the moment in columns for the 9-Story HSAC9-4/SAC subjected to MCE
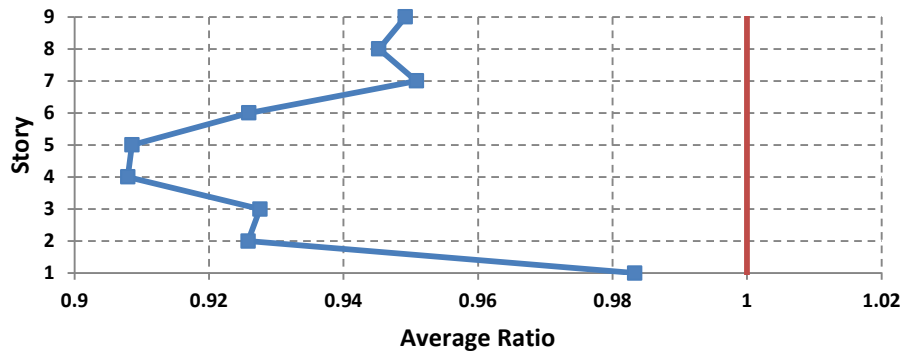
Figure 72 the average ratios of the moment in columns of each story for the 9-Story HSAC9-4/SAC subjected to MCE
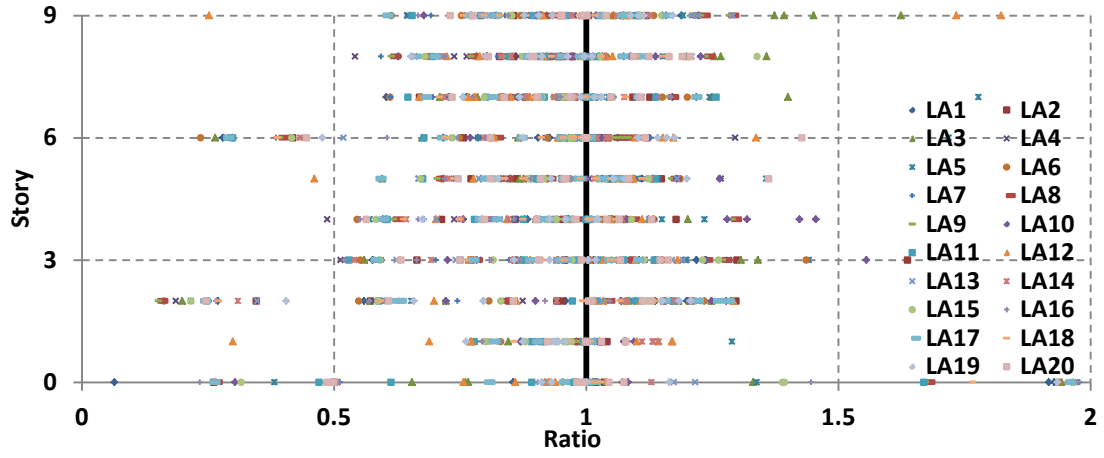
Figure 73 the ratios of the moment in columns for the 9-Story HSAC9-5/SAC subjected to DBE
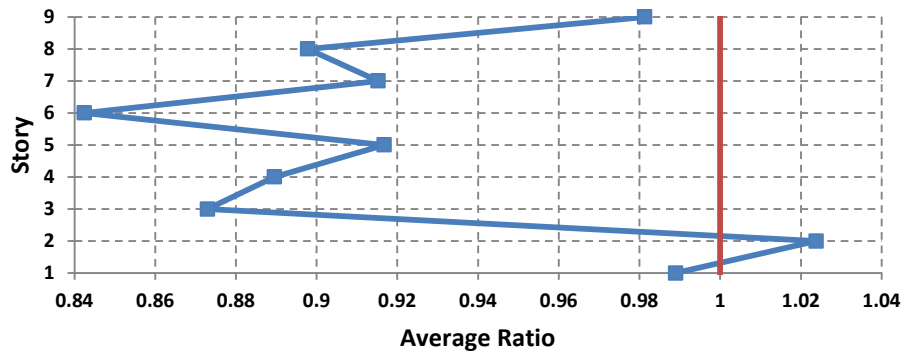
Figure 74 the average ratios of the moment in columns of each story for the 9-Story HSAC9-5/SAC subjected to DBE
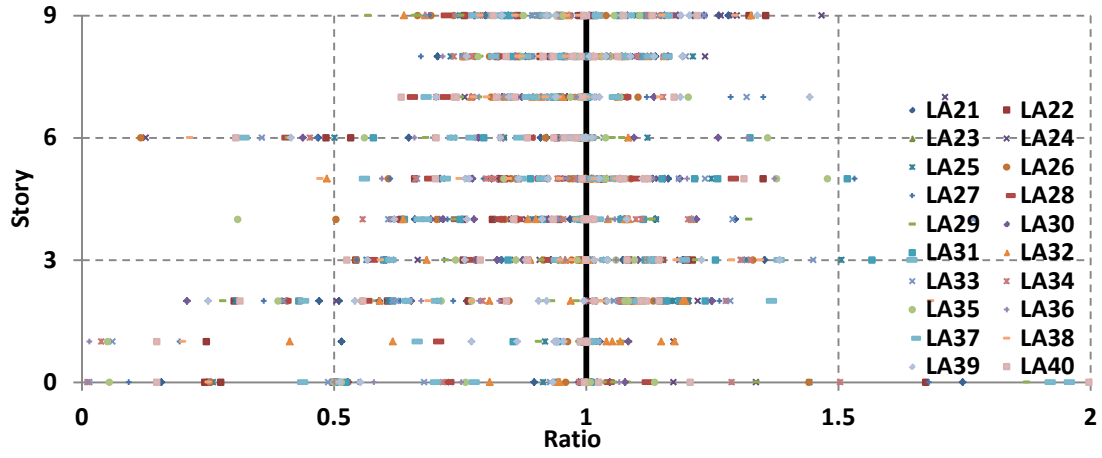
Figure 75 the ratios of the moment in columns for the 9-Story HSAC9-5/SAC subjected to MCE
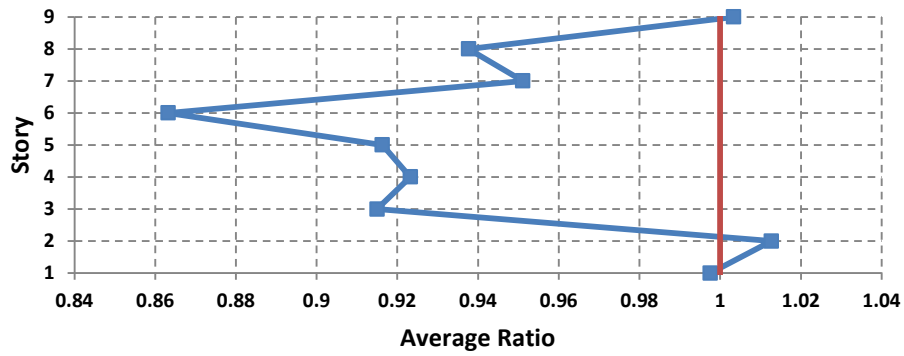
Figure 76 the average ratios of the moment in columns of each story for the 9-Story HSAC9-5/SAC subjected to MCE
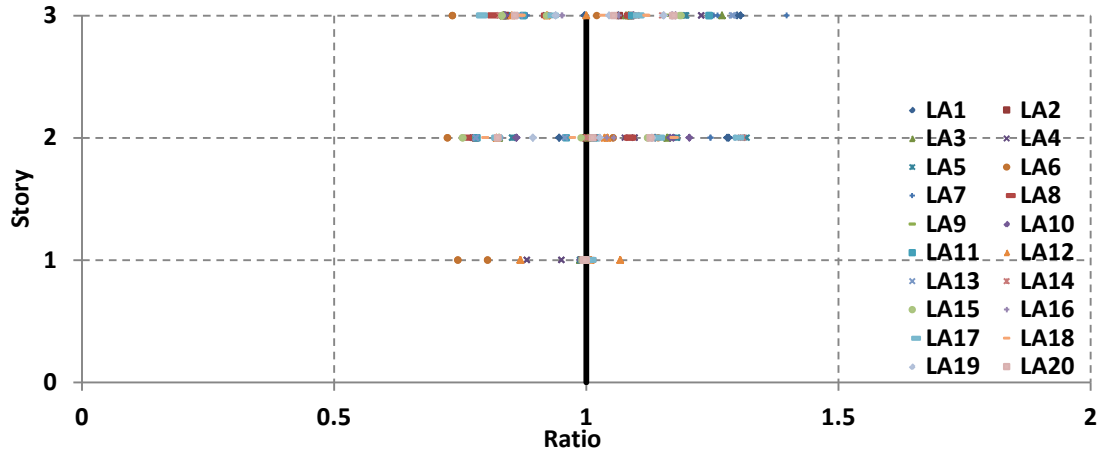
Figure 77 the ratios of the moment in columns for the 3-Story HSAC3-4/SAC subjected to DBE
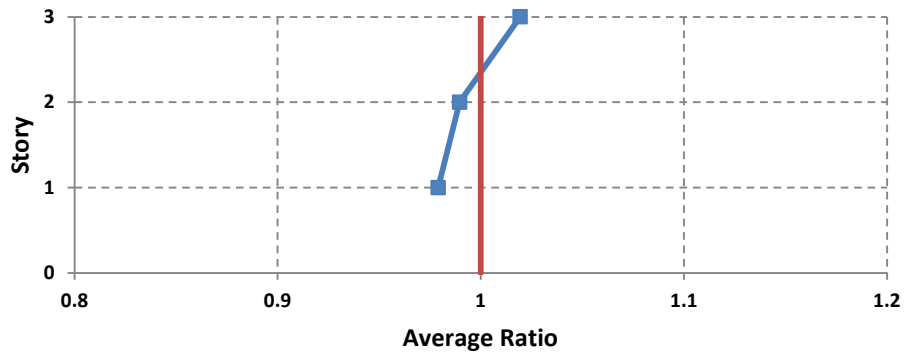
Figure 78 the average ratios of the columns in beams of each story for the 3-Story HSAC9-4/SAC subjected to DBE
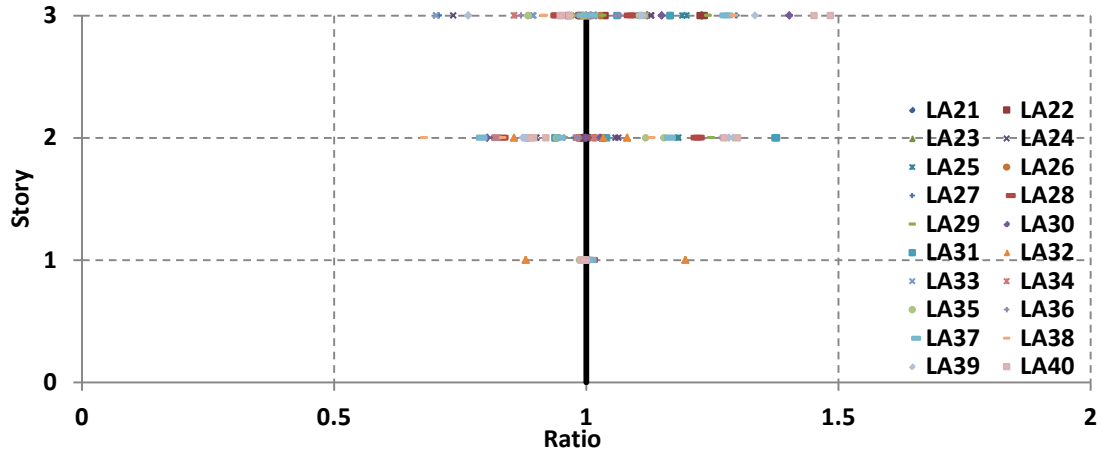
Figure 79 the ratios of the moment in columns for the 3-Story HSAC3-4/SAC subjected to MCE
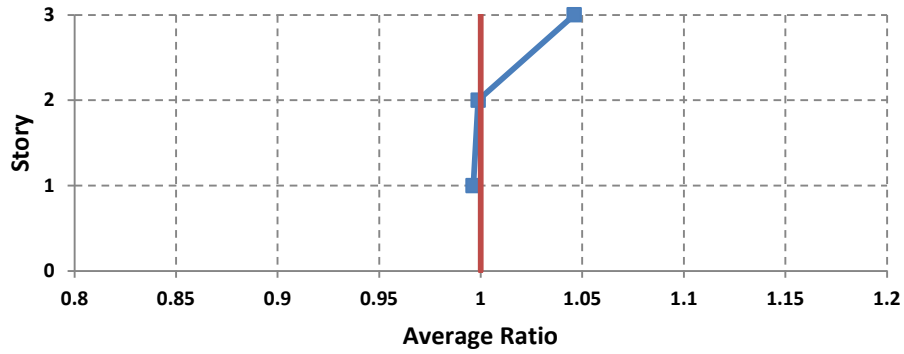
Figure 80 the average ratios of the moment in columns of each story for the 3-Story HSAC3-4/SAC subjected to MCE
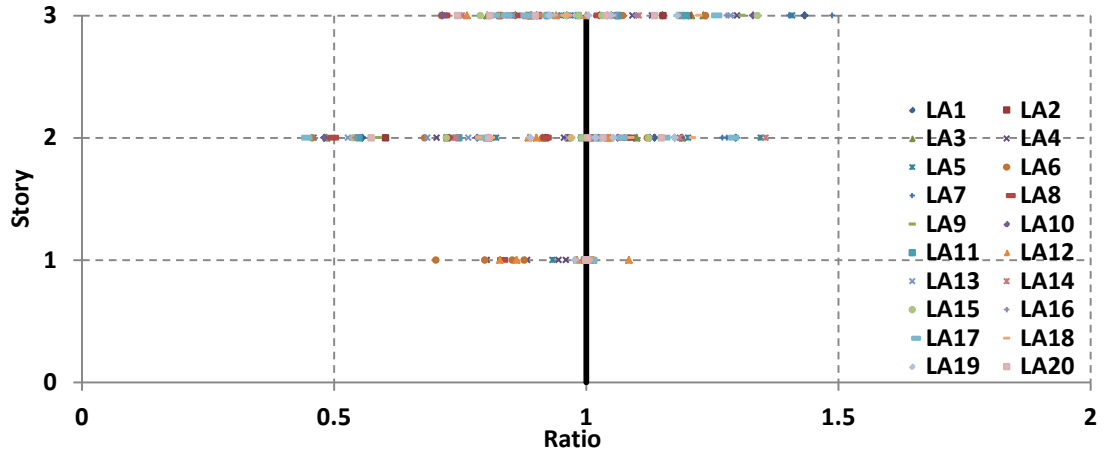
Figure 81 the ratios of the moment in columns for the 9-Story HSAC9-5/SAC subjected to DBE
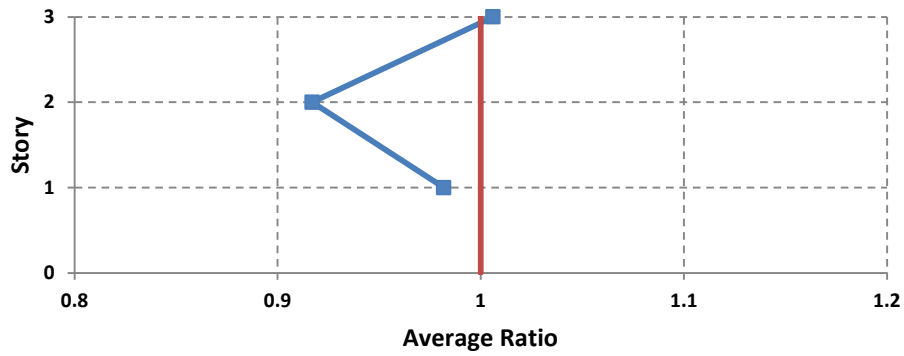
Figure 82 the average ratios of the moment in columns of each story for the 9-Story HSAC9-5/SAC subjected to DBE
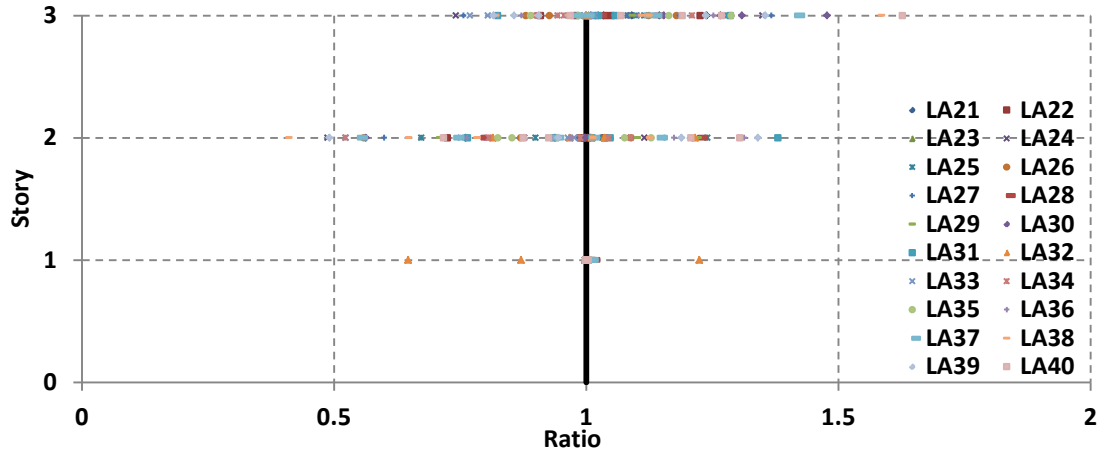
Figure 83 the ratios of the moment in columns for the 9-Story HSAC9-5/SAC subjected to MCE
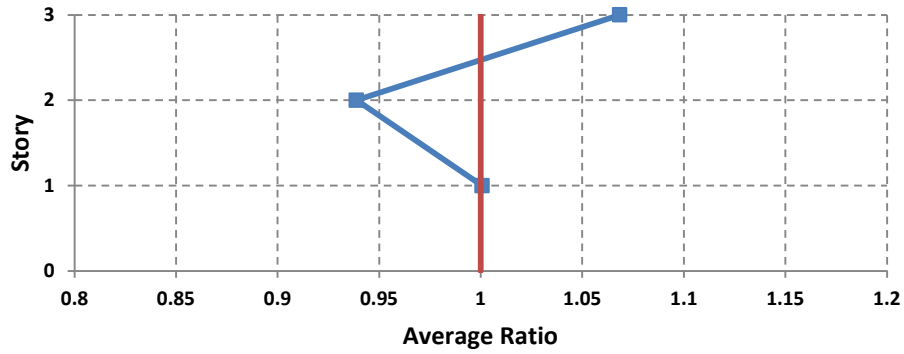
Figure 84 the average ratios of the moment in columns of each story for the 9-Story HSAC9-5/SAC subjected to MCE
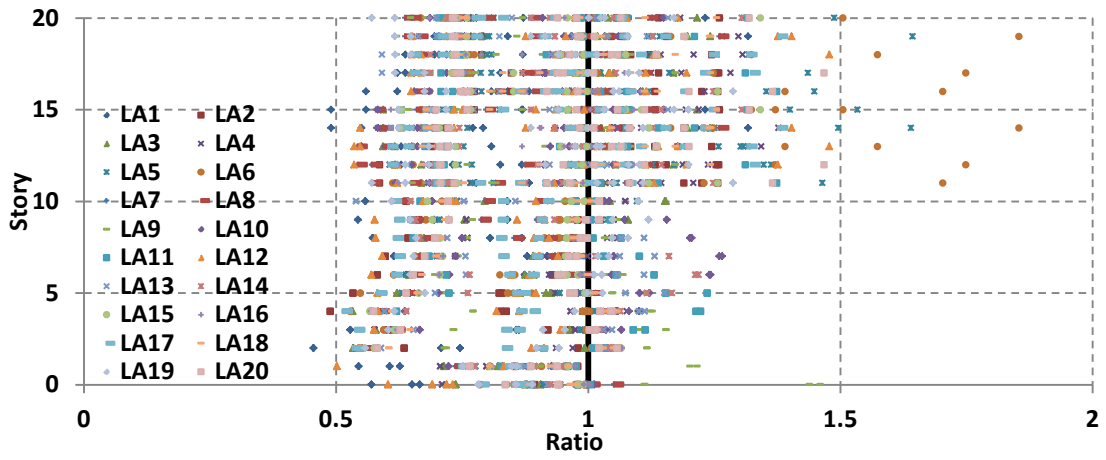
Shear

Figure 85 the ratios of the shear in columns for the 20-Story HSAC20-4/SAC subjected to DBE
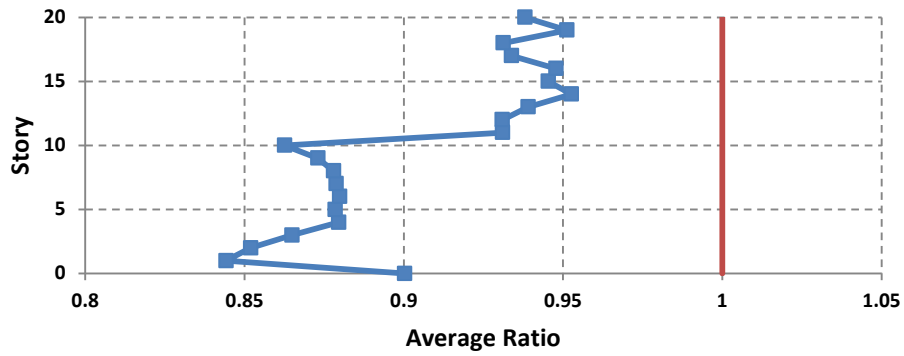
Figure 86 the average ratios of the shear in columns of each story for the 20-Story HSAC20-4/SAC subjected to DBE
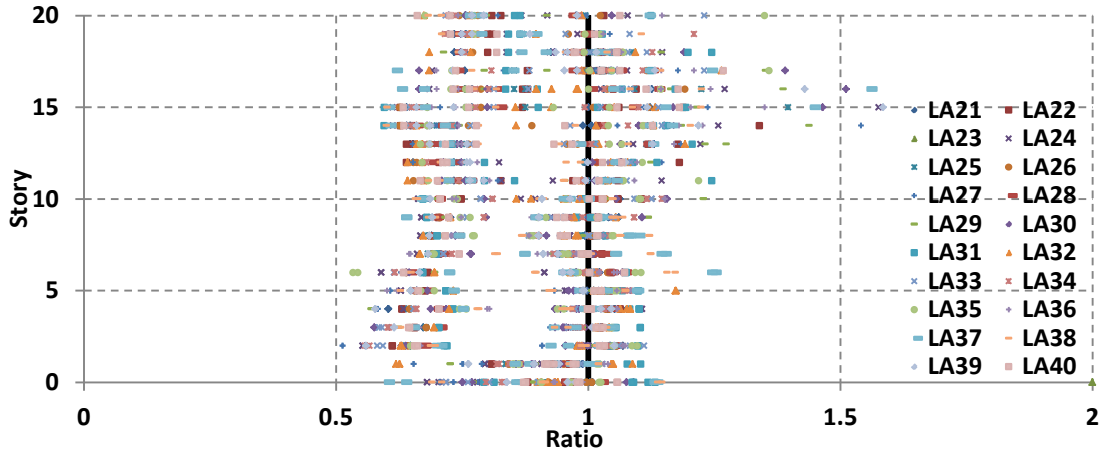
Figure 87 the ratios of the shear in columns for the 20-Story HSAC20-4/SAC subjected to MCE
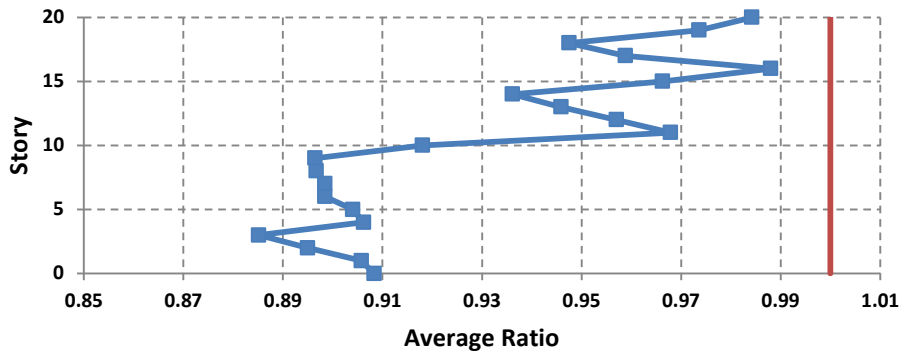
Figure 88 the average ratios of the columns in beams of each story for the 20-Story HSAC20-4/SAC subjected to MCE
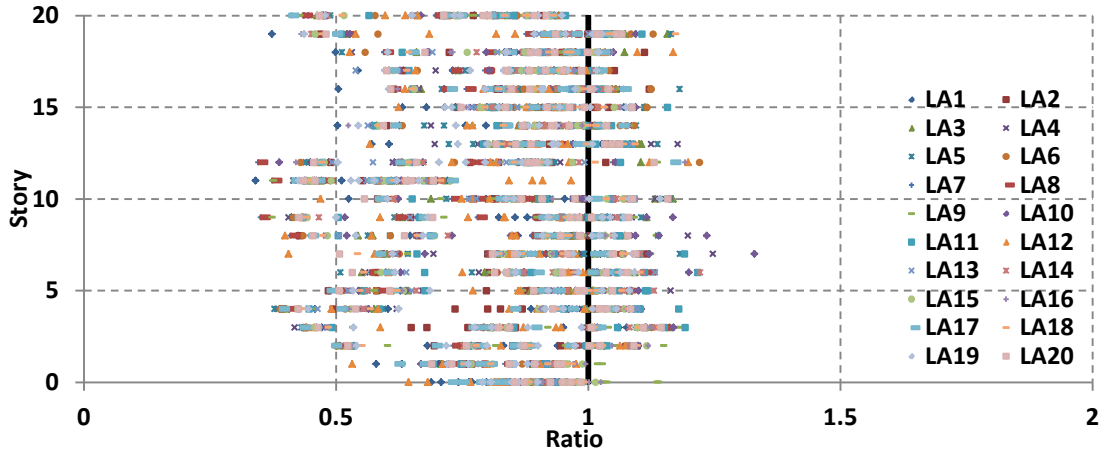
Figure 89 the ratios of the shear in columns for the 20-Story HSAC20-5/SAC subjected to DBE
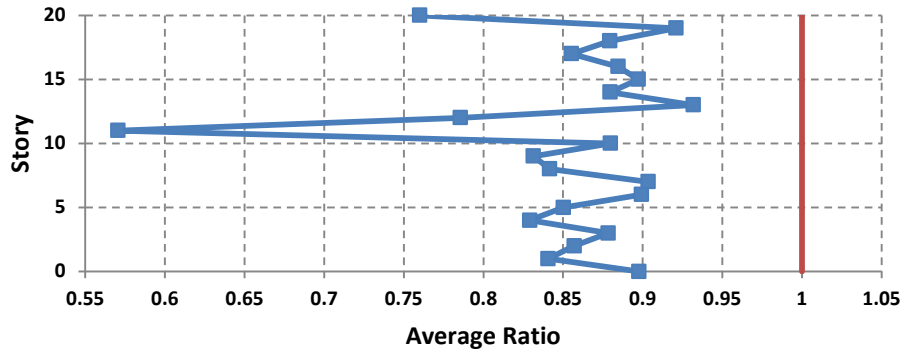
Figure 90 the average ratios of the columns in beams of each story for the 20-Story HSAC20-5/SAC subjected to DBE
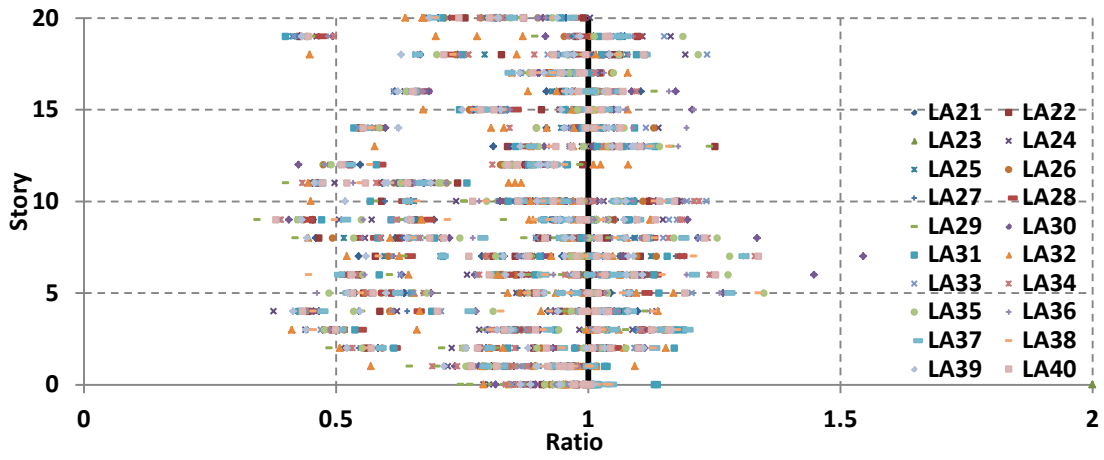
Figure 91 the ratios of the shear in columns for the 20-Story HSAC20-5/SAC subjected to MCE
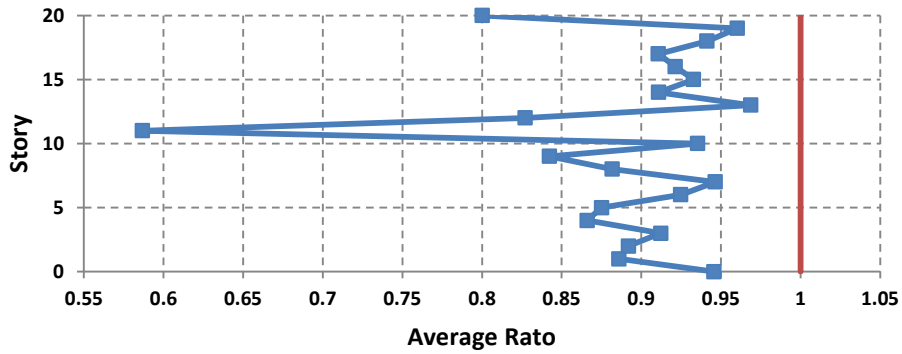
Figure 92 the average ratios of the shear in columns of each story for the 20-Story HSAC20-5/SAC subjected to MCE
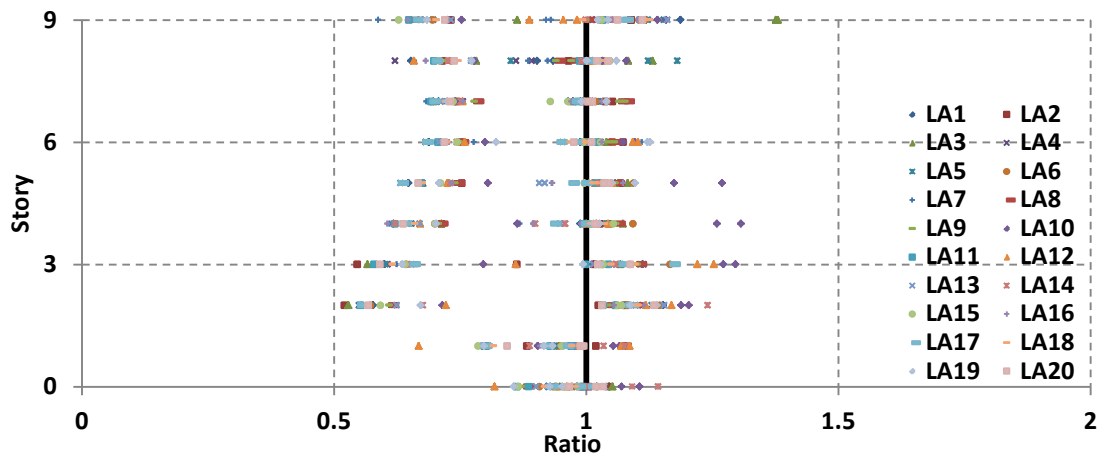
Figure 93 the ratios of the shear in columns for the 9-Story HSAC9-4/SAC subjected to DBE
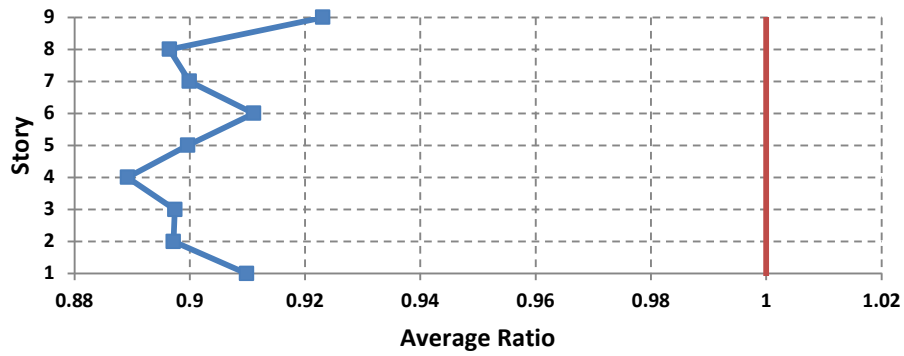
Figure 94 the average ratios of the columns in beams of each story for the 9-Story HSAC9-4/SAC subjected to DBE
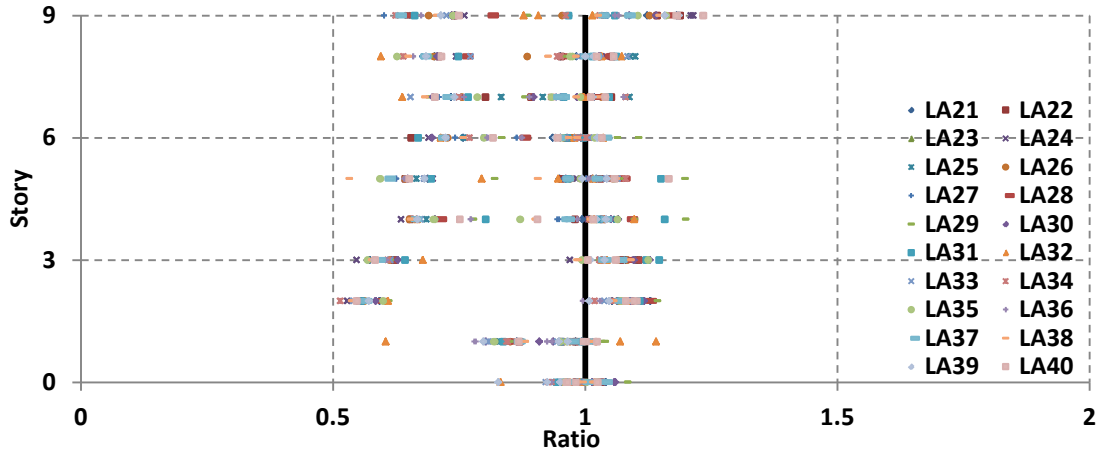
Figure 95 the ratios of the shear in columns for the 9-Story HSAC9-4/SAC subjected to MCE
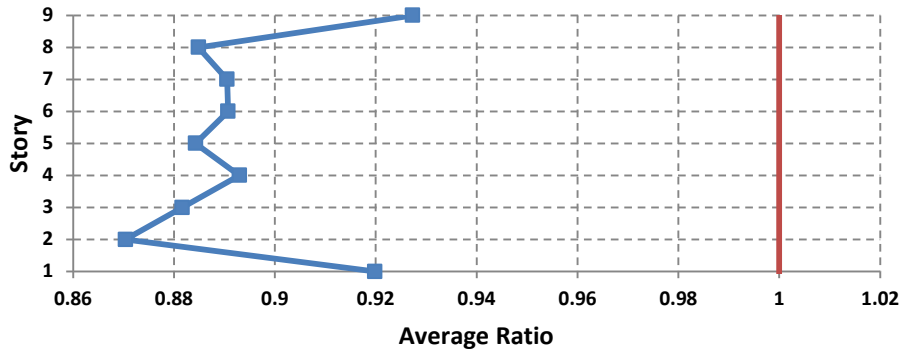
Figure 96 the average ratios of the shear in columns of each story for the 9-Story HSAC9-4/SAC subjected to MCE
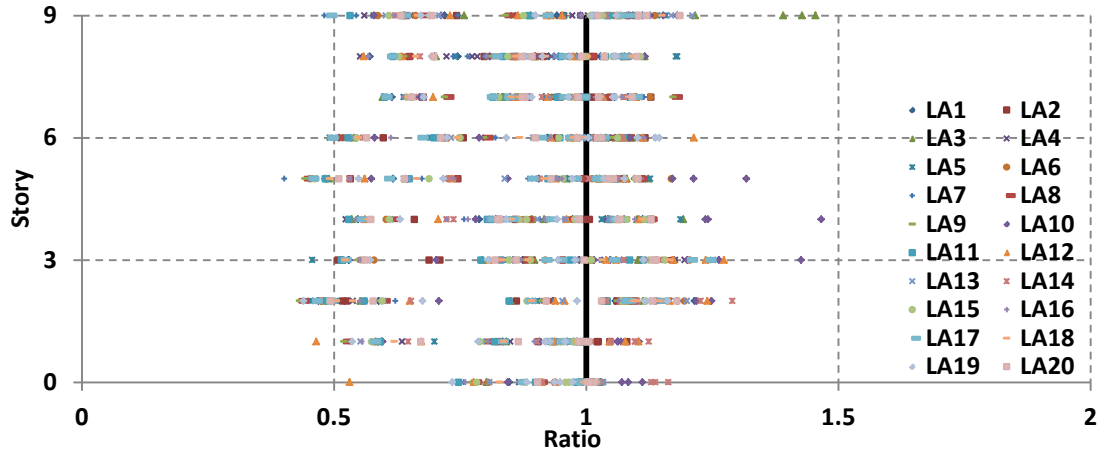
Figure 97 the ratios of the shear in columns for the 9-Story HSAC9-5/SAC subjected to DBE
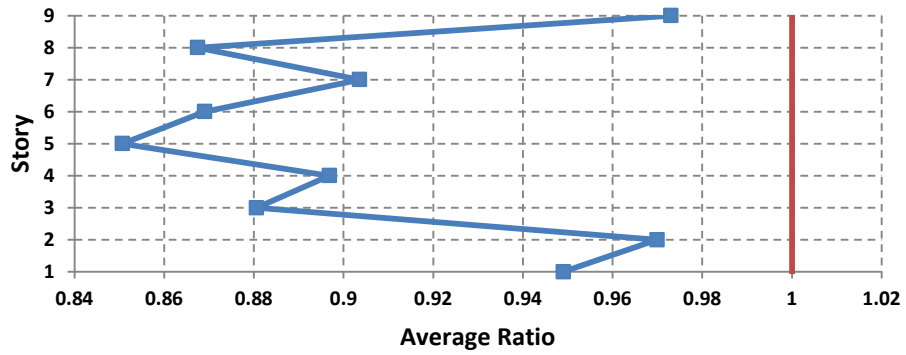
Figure 98 the average ratios of the shear in columns of each story for the 9-Story HSAC9-5/SAC subjected to DBE
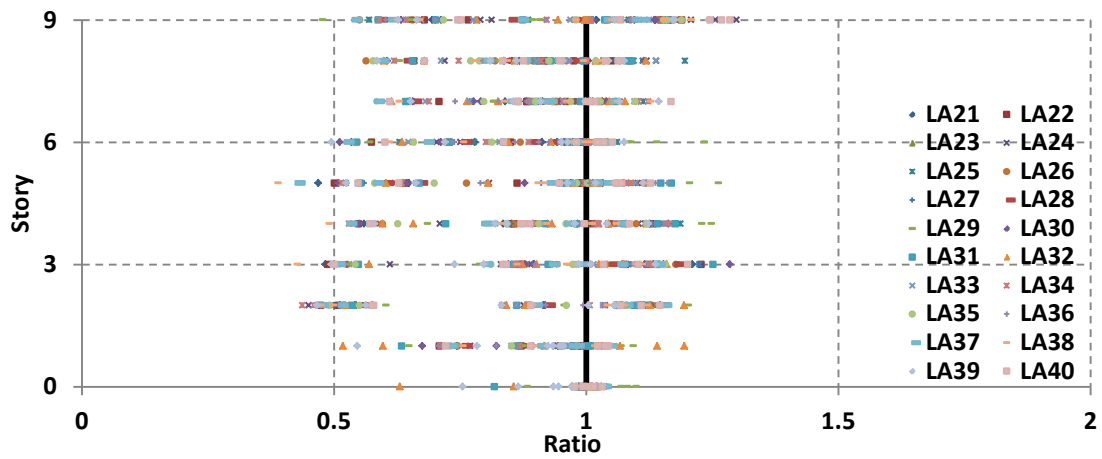
Figure 99 the ratios of the shear in columns for the 9-Story HSAC9-5/SAC subjected to MCE
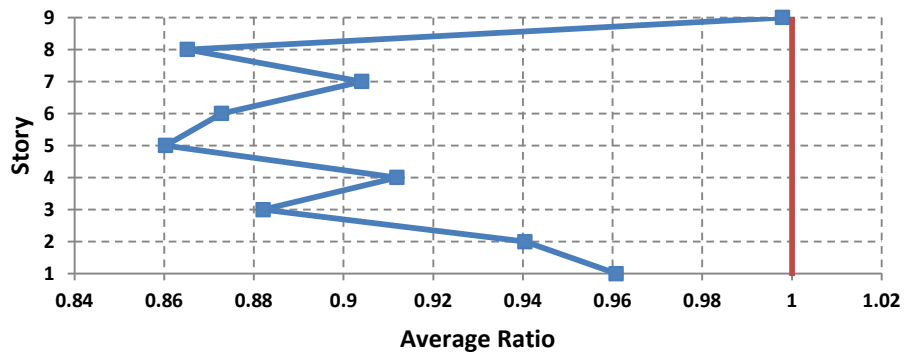
Figure 100 the average ratios of the columns in beams of each story for the 9-Story HSAC9-5/SAC subjected to MCE
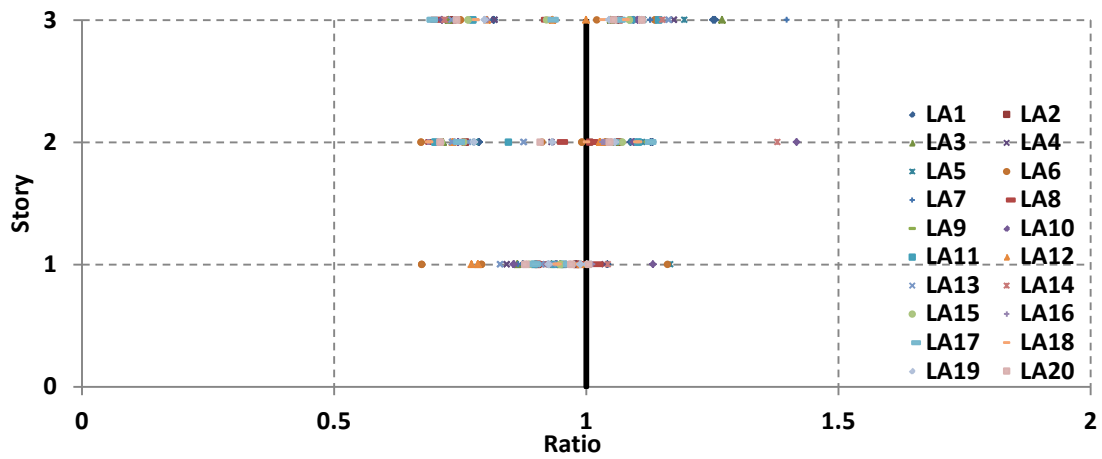
Figure 101 the ratios of the shear in columns for the 3-Story HSAC3-4/SAC subjected to DBE
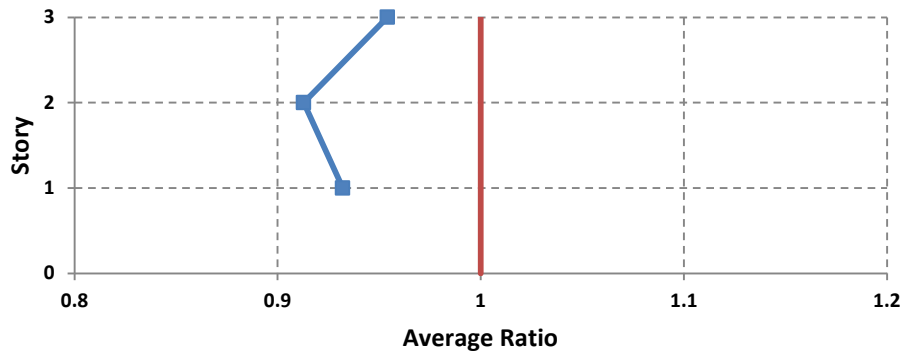
Figure 102 the average ratios of the shear in columns of each story for the 3-Story HSAC3-4/SAC subjected to DBE
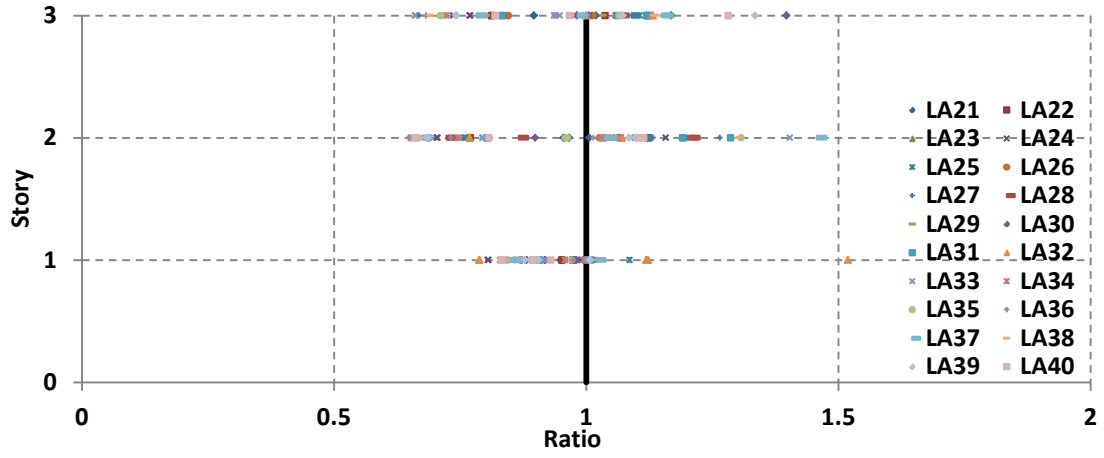
Figure 103 the ratios of the shear in columns for the 20-Story HSAC20-4/SAC subjected to MCE
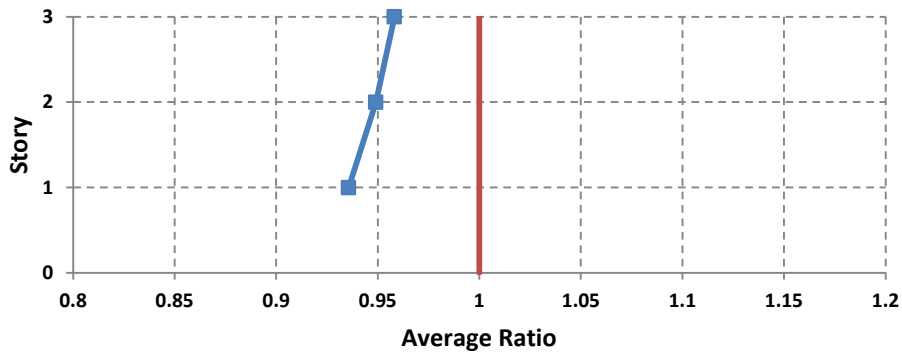
Figure 104 the average ratios of the shear in columns of each story for the 20-Story HSAC20-4/SAC subjected to MCE
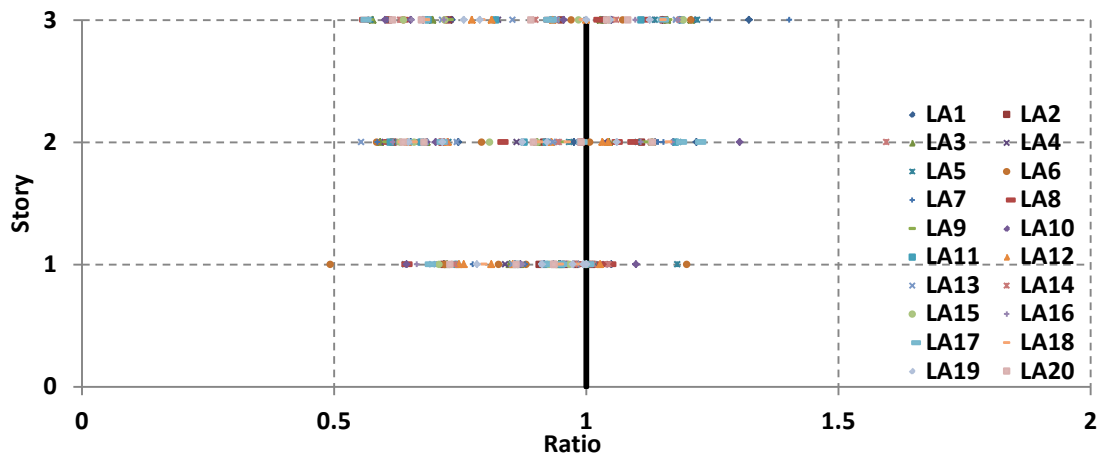
Figure 105 the ratios of the shear in columns for the 3-Story HSAC3-5/SAC subjected to DBE
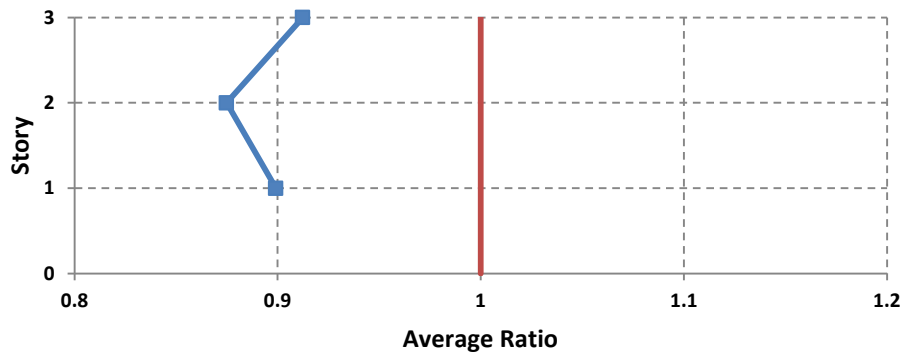
Figure 106 the average ratios of the shear in columns of each story for the 3-Story HSAC3-5/SAC subjected to DBE
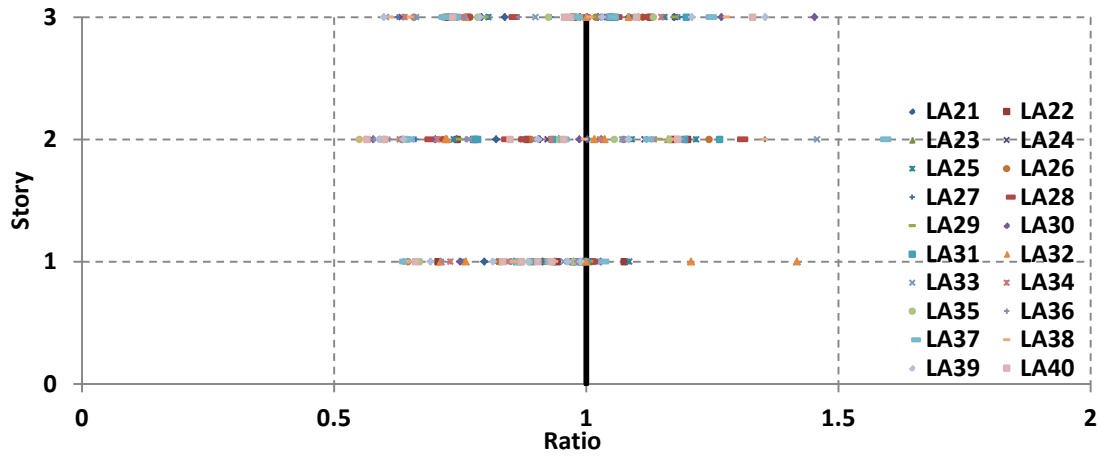
Figure 107 the ratios of the shear in columns for the 20-Story HSAC20-5/SAC subjected to MCE
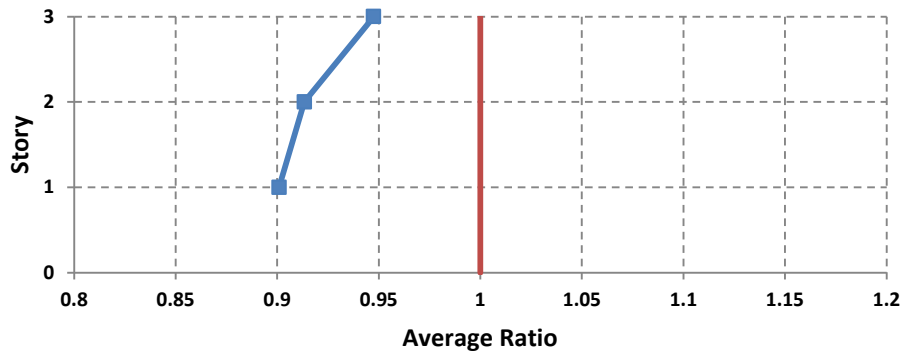
Figure 108 the average ratios of the shear in columns of each story for the 20-Story HSAC20-5/SAC subjected to MCE

APPENDIX B

INCREMENTAL MODAL SHAPES

(a) Incremental Mode Shapes for LA21

(b) Incremental Mode Shapes for LA22

(c) Incremental Mode Shapes for LA23

(d) Incremental Mode Shapes for LA24

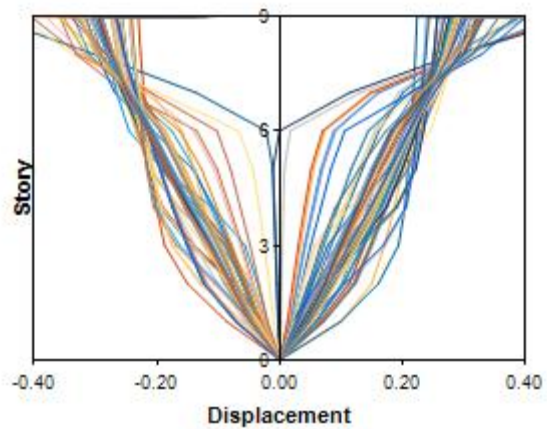(e) Incremental Mode Shapes for LA25

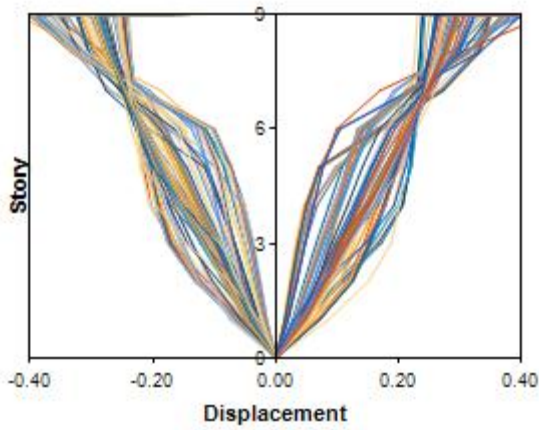(f) Incremental Mode Shapes for LA26
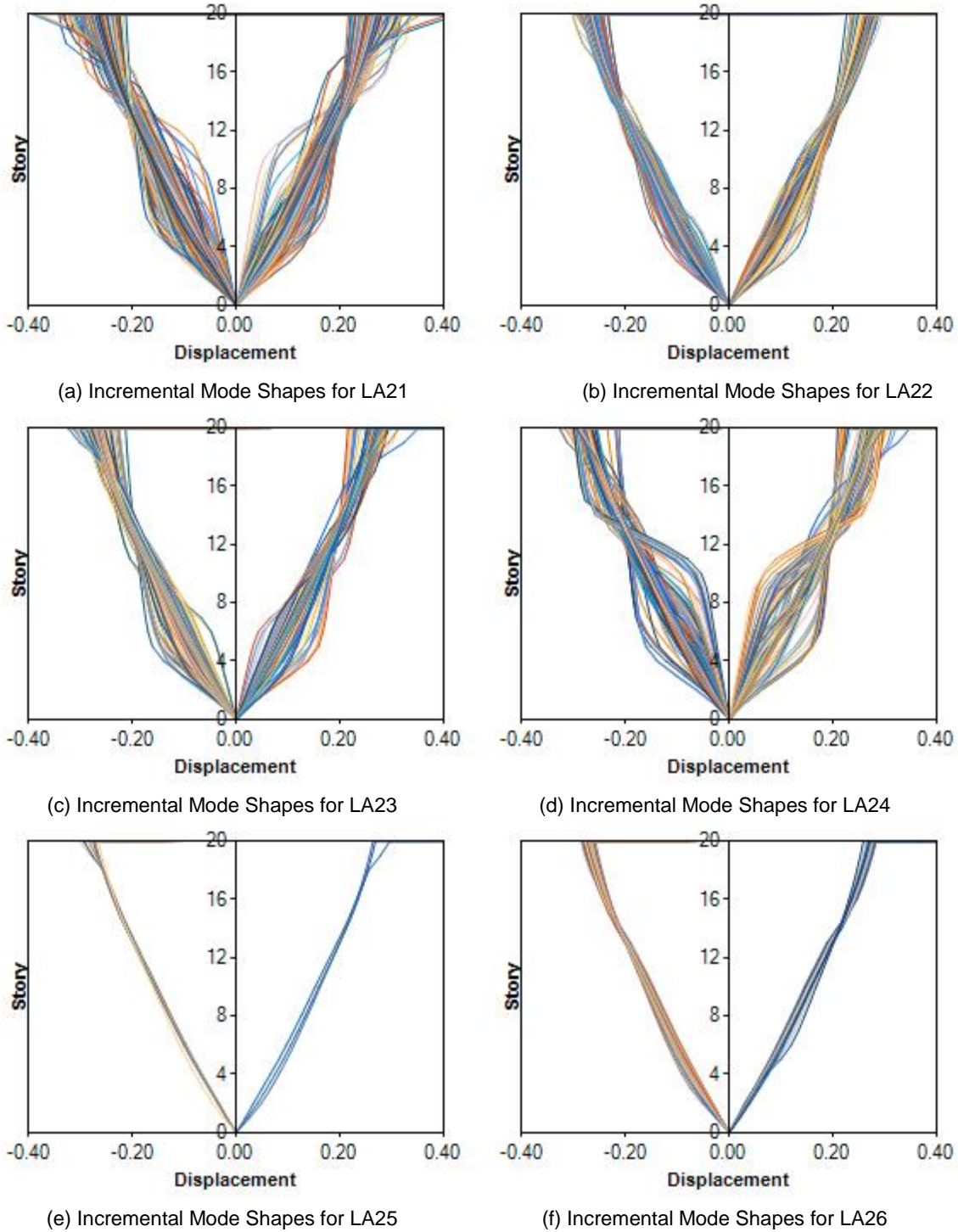
Figure 1. Incremental First Mode shapes of the SAC 20-Story Rigid Frame under LA21 to LA26

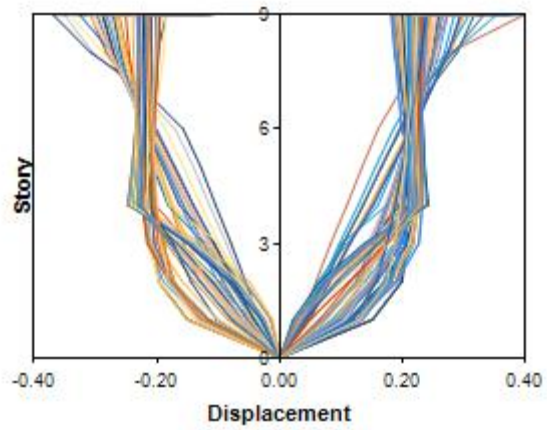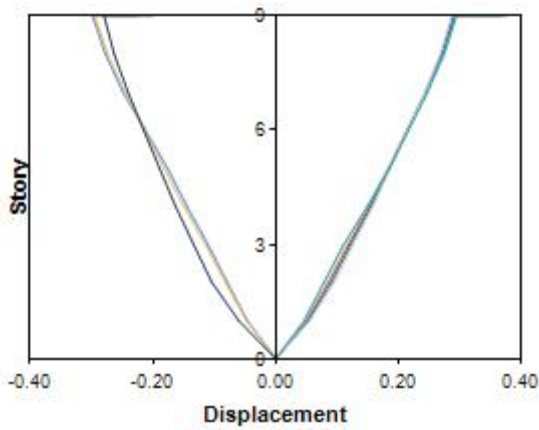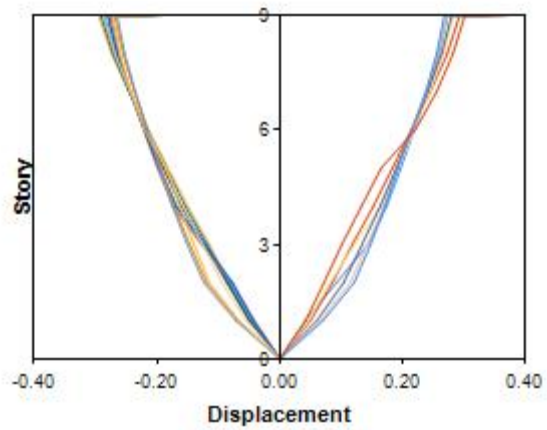(a) Incremental Mode Shapes for LA27

(b) Incremental Mode Shapes for LA28

(c) Incremental Mode Shapes for LA29

(d) Incremental Mode Shapes for LA30

(e) Incremental Mode Shapes for LA31

(f) Incremental Mode Shapes for LA32
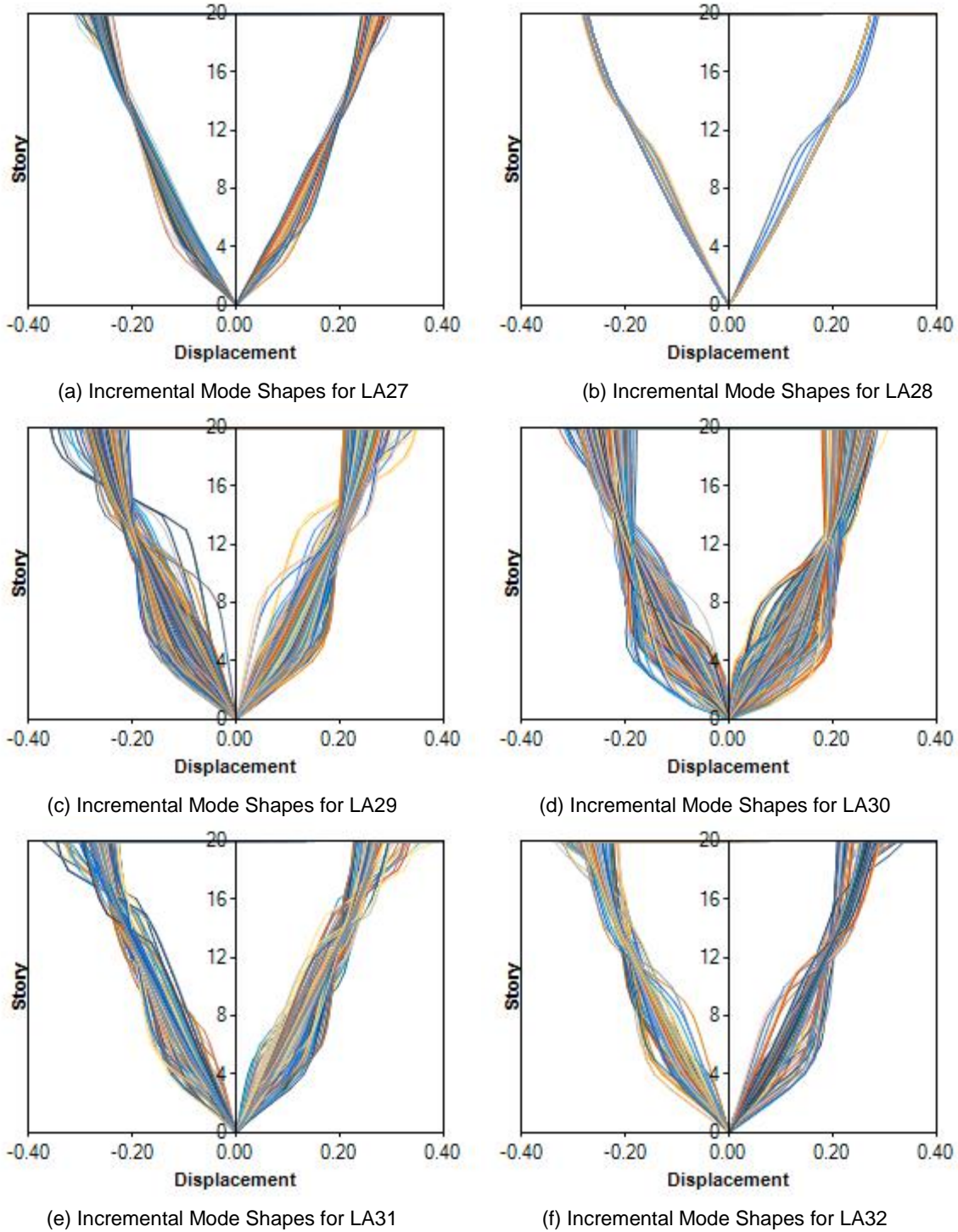
Figure 2. Incremental First Mode shapes of the SAC 20-Story Rigid Frame under LA27 to LA32
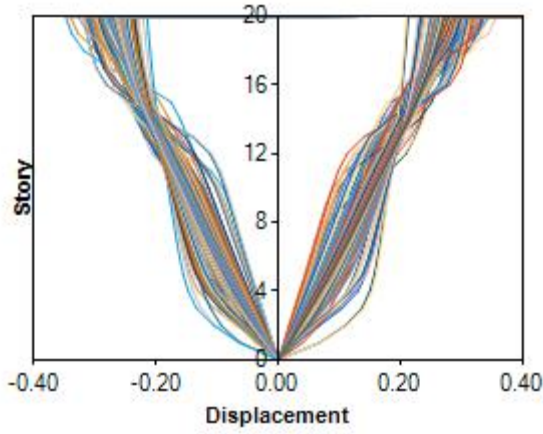
(a) Incremental Mode Shapes for LA33
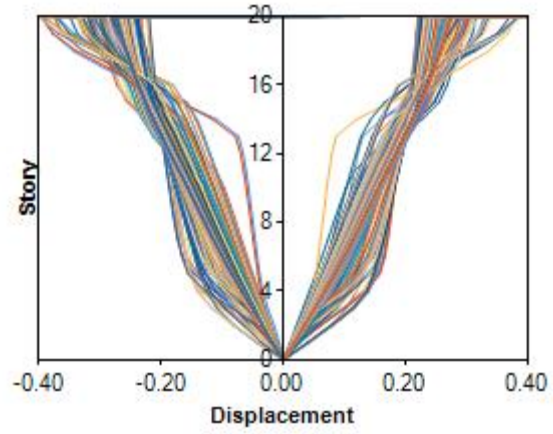
(b) Incremental Mode Shapes for LA34
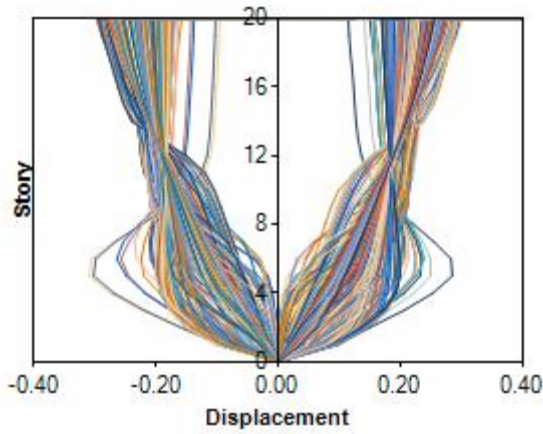
(c) Incremental Mode Shapes for LA35
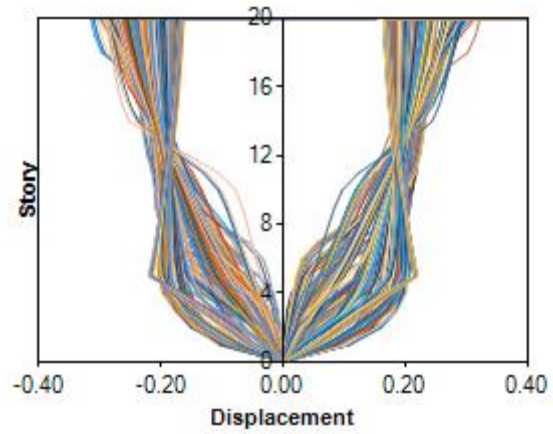
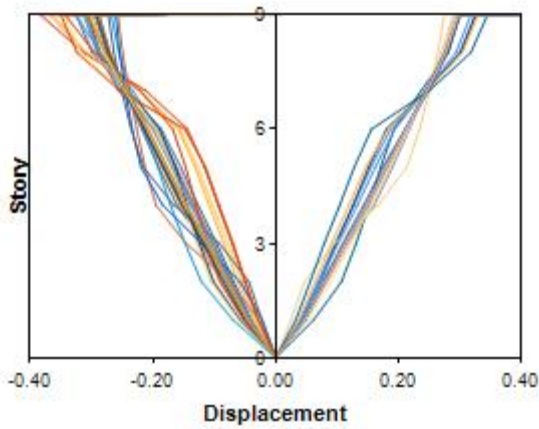(d) Incremental Mode Shapes for LA36
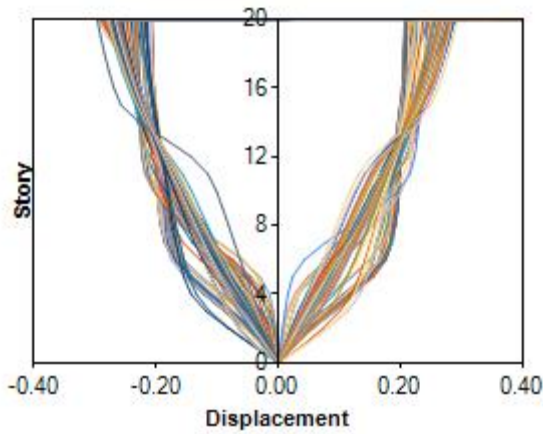
(e) Incremental Mode Shapes for LA37
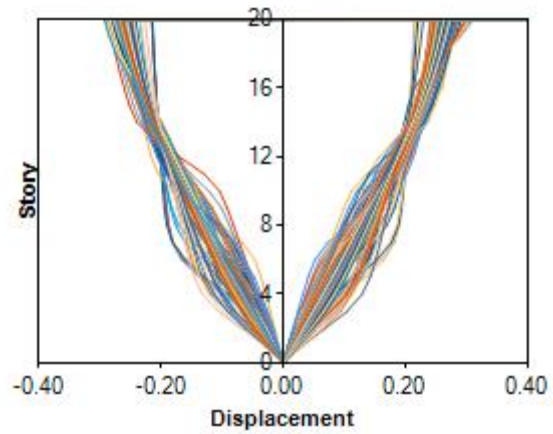
(f) Incremental Mode Shapes for LA38

Figure 3. Incremental First Mode shapes of the SAC 20-Story Rigid Frame under LA33 to LA38

236
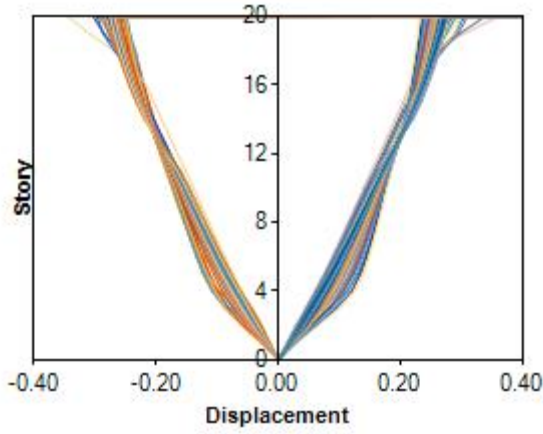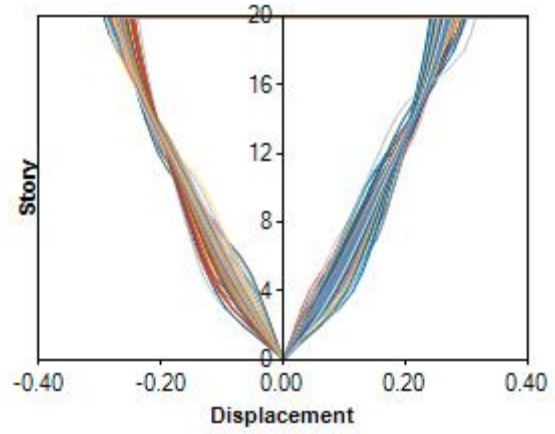
(a) Incremental Mode Shapes for LA39   (b) Incremental Mode Shapes for LA40

Figure 4. Incremental First Mode shapes of the SAC 20-Story Rigid Frame under LA39 to LA40

(a) Incremental Mode Shapes for LA21

(b) Incremental Mode Shapes for LA22

(c) Incremental Mode Shapes for LA23

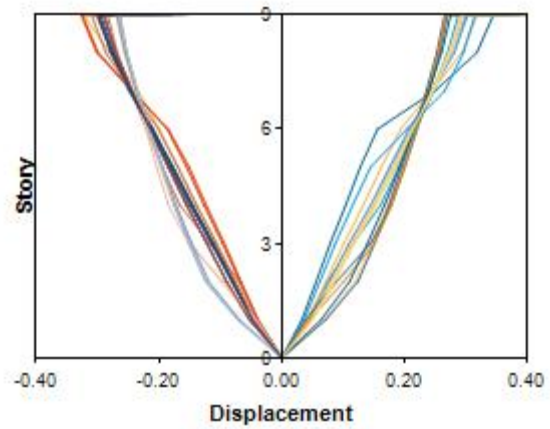(d) Incremental Mode Shapes for LA24

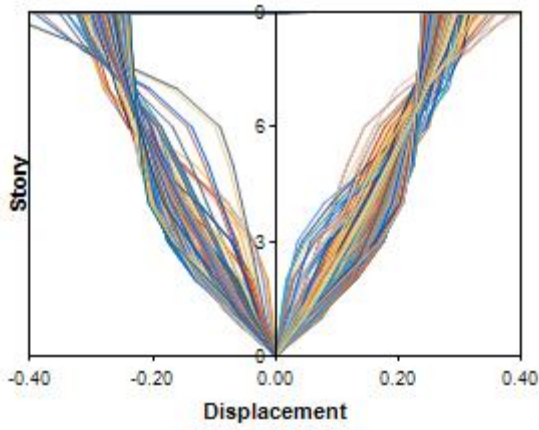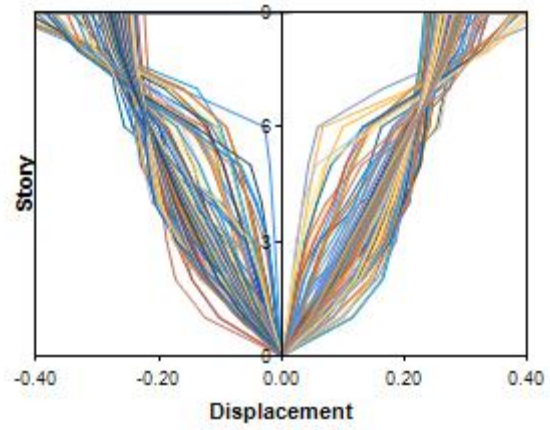(e) Incremental Mode Shapes for LA25

(f) Incremental Mode Shapes for LA26
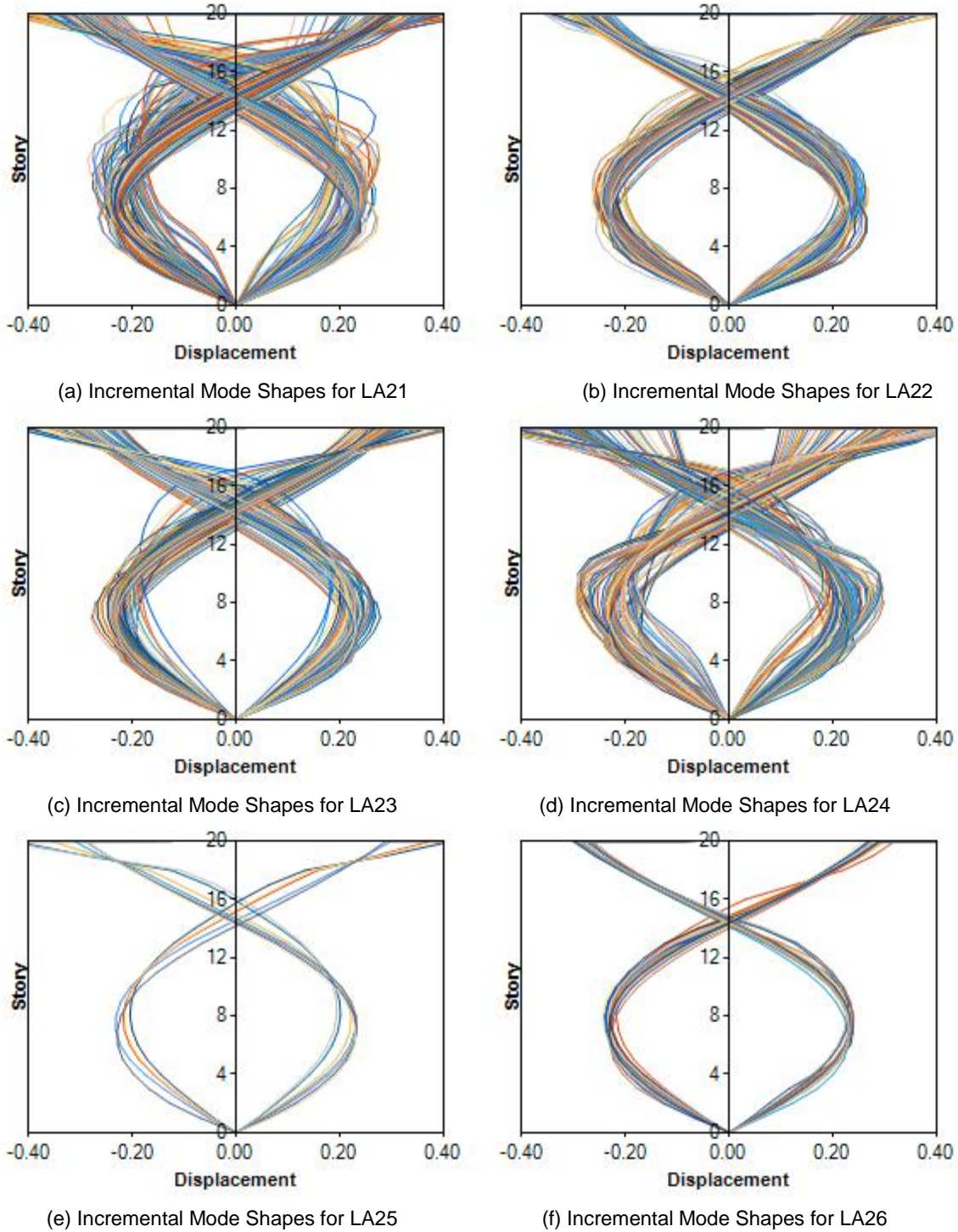
Figure 5. Incremental Second Mode shapes of the SAC 20-Story Rigid Frame under LA21 to LA26
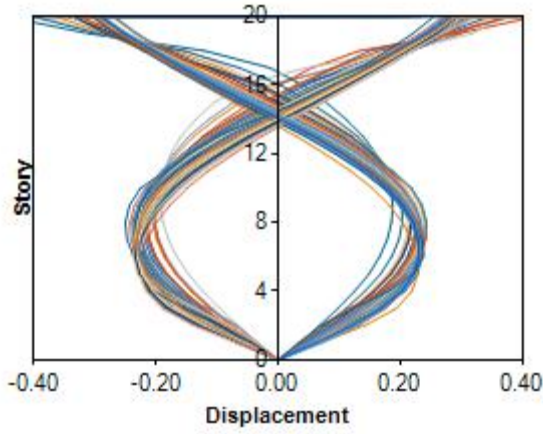
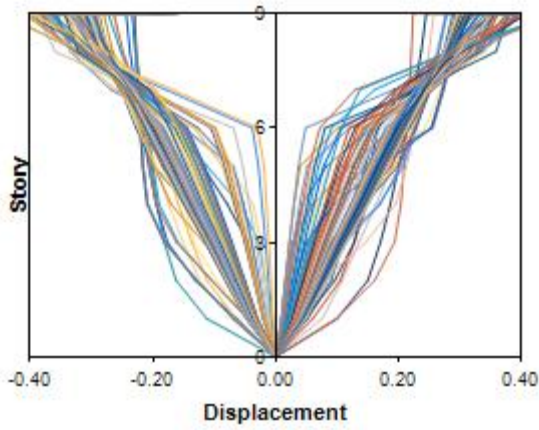(a) Incremental Mode Shapes for LA27
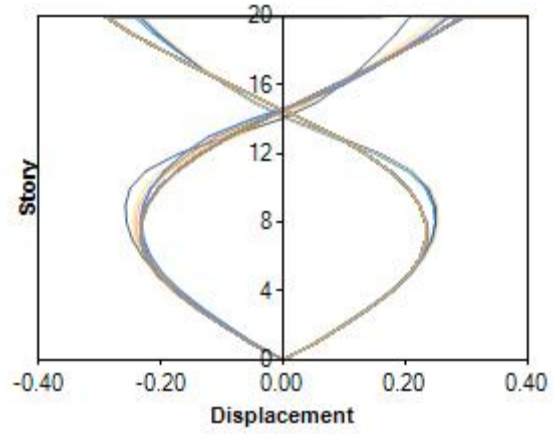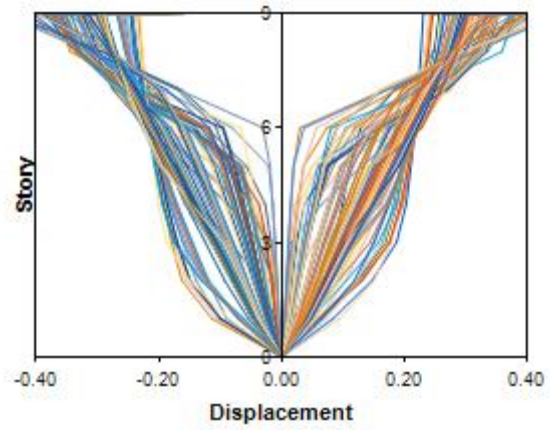
(b) Incremental Mode Shapes for LA28
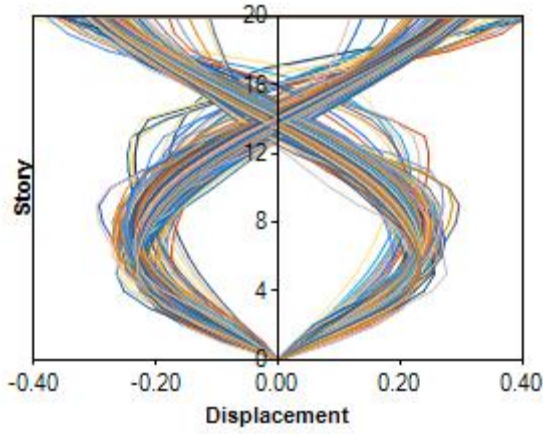
(c) Incremental Mode Shapes for LA29
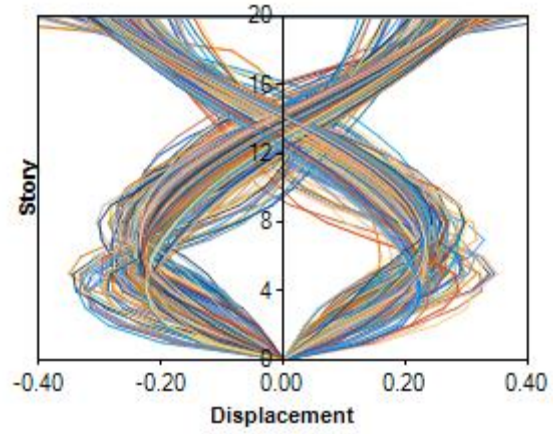
(d) Incremental Mode Shapes for LA30
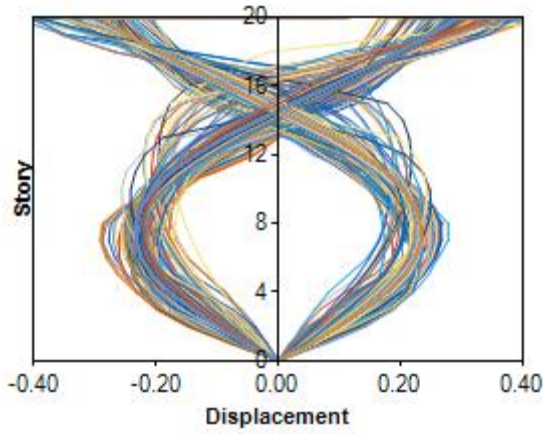
(e) Incremental Mode Shapes for LA31
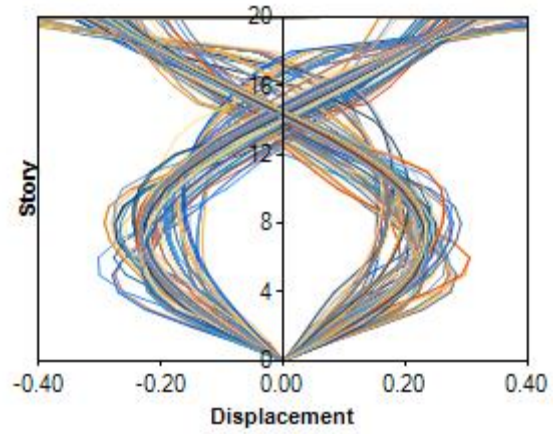
(f) Incremental Mode Shapes for LA32

Figure 6. Incremental Second Mode shapes of the SAC 20-Story Rigid Frame under LA27 to LA32
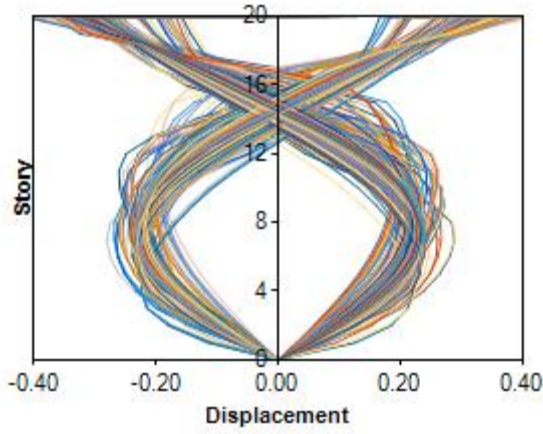
(a) Incremental Mode Shapes for LA33
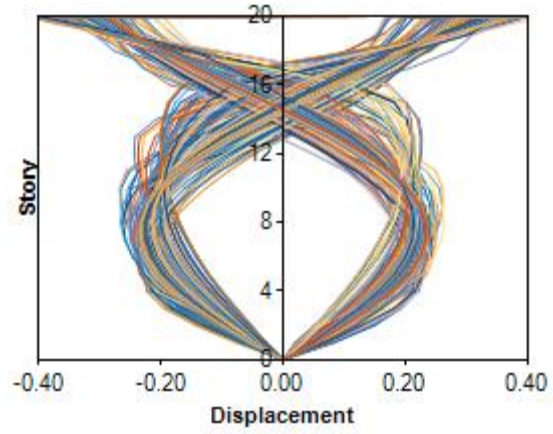
(b) Incremental Mode Shapes for LA34
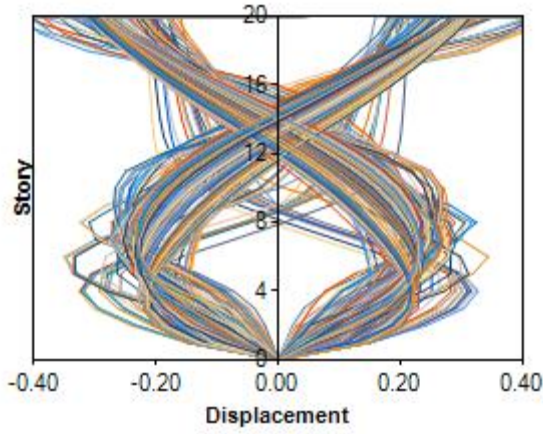
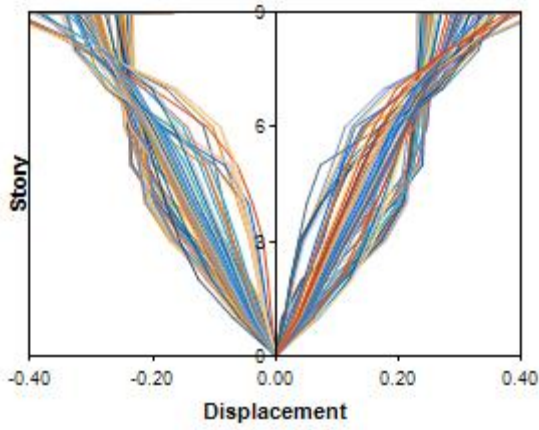(c) Incremental Mode Shapes for LA35
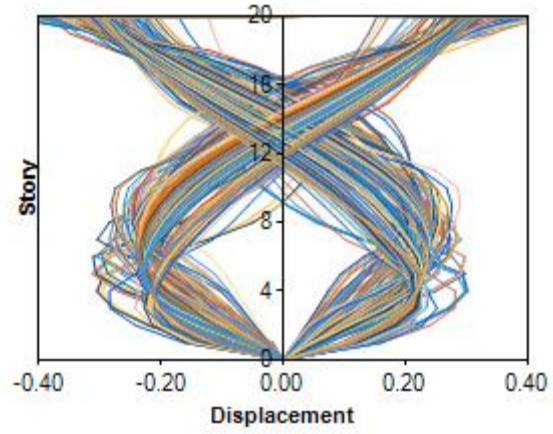
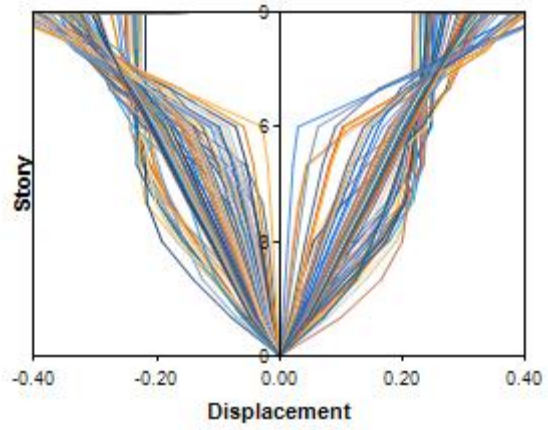(d) Incremental Mode Shapes for LA36
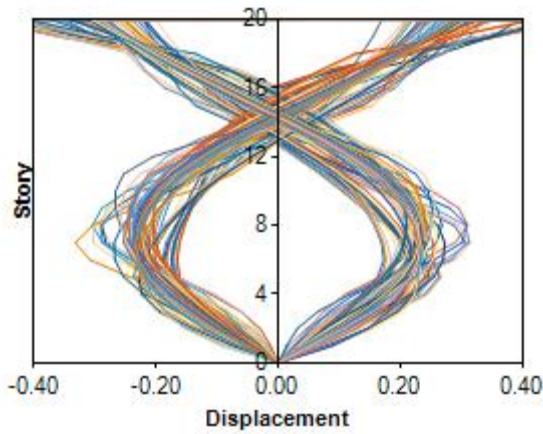
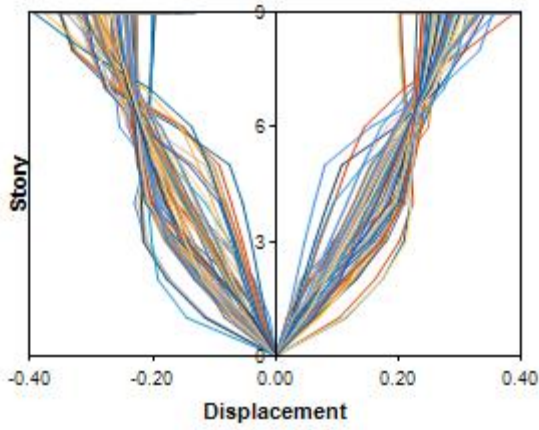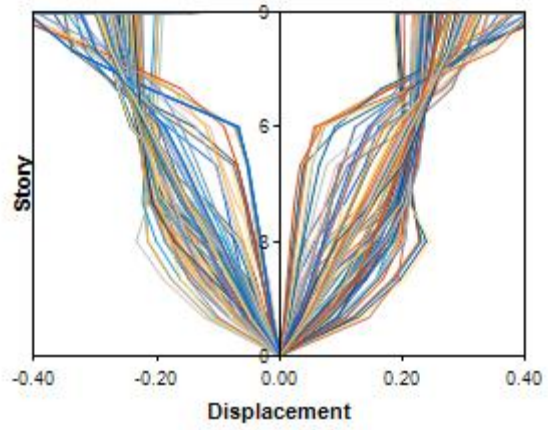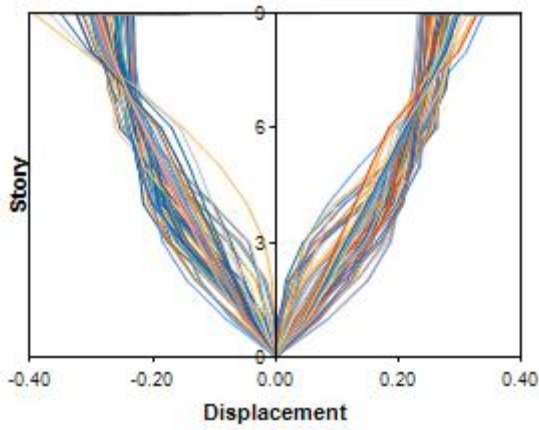(e) Incremental Mode Shapes for LA37
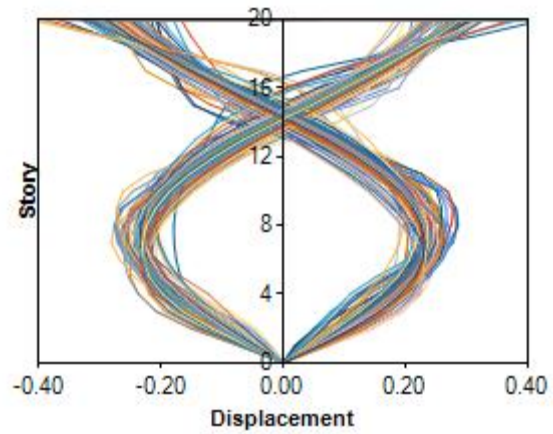
(f) Incremental Mode Shapes for LA38

Figure 7. Incremental Second Mode shapes of the SAC 20-Story Rigid Frame under LA33 to LA38
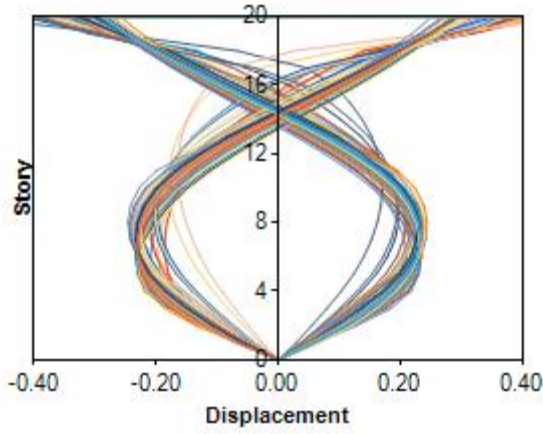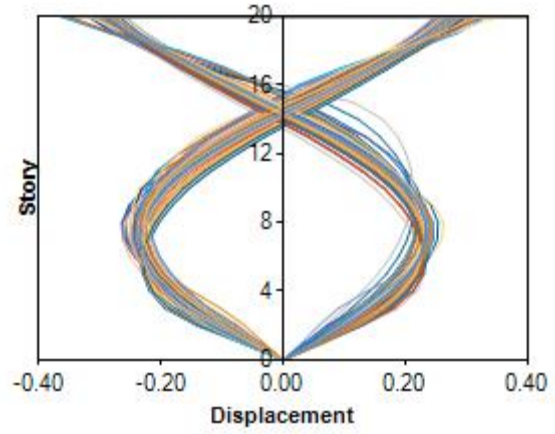
(a) Incremental Mode Shapes for LA39   (b) Incremental Mode Shapes for LA40

Figure 8. Incremental Second Mode shapes of the SAC 20-Story Rigid Frame under LA39 to LA40
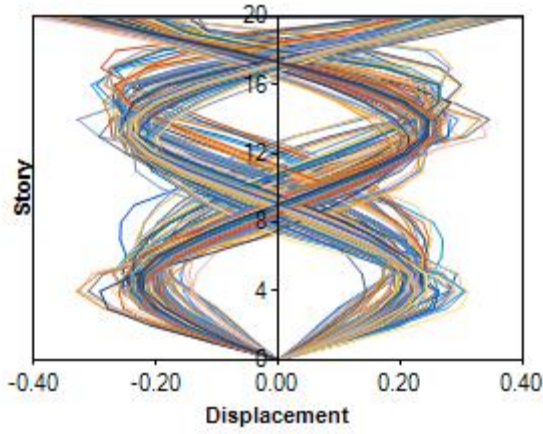
(a) Incremental Mode Shapes for LA21   (b) Incremental Mode Shapes for LA22
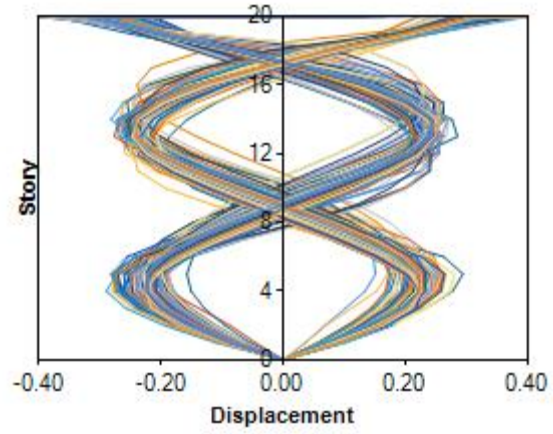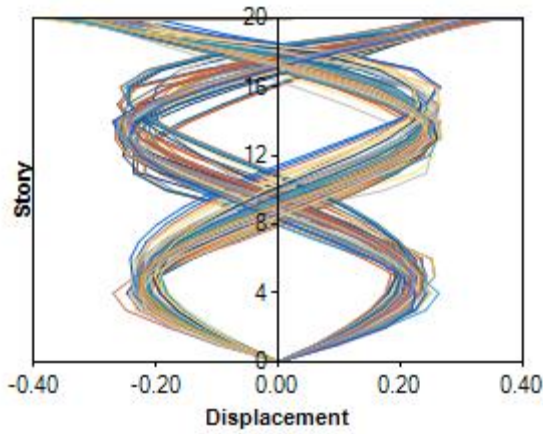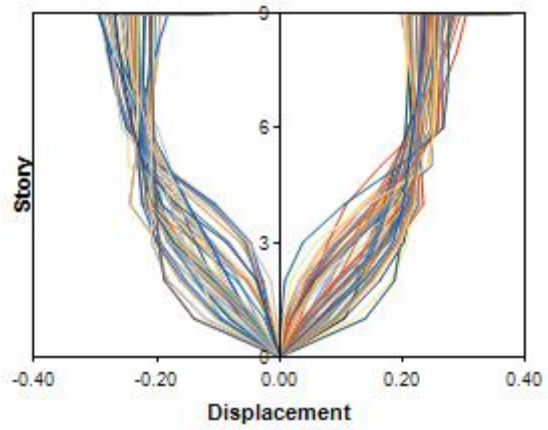
(c) Incremental Mode Shapes for LA23   (d) Incremental Mode Shapes for LA24
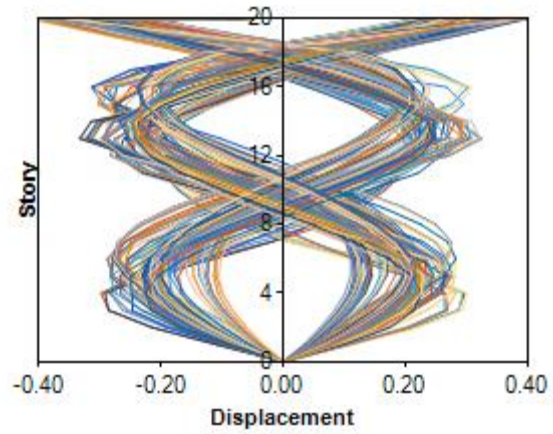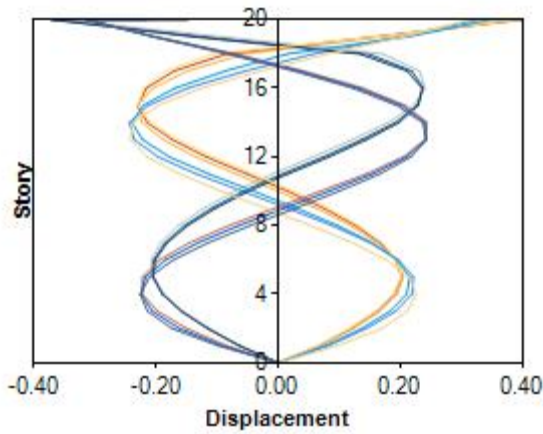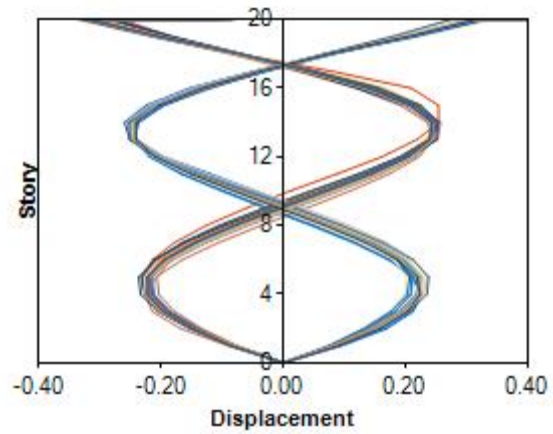
(e) Incremental Mode Shapes for LA25   (f) Incremental Mode Shapes for LA26

Figure 9. Incremental Third Mode shapes of the SAC 20-Story Rigid Frame under LA21 to LA26
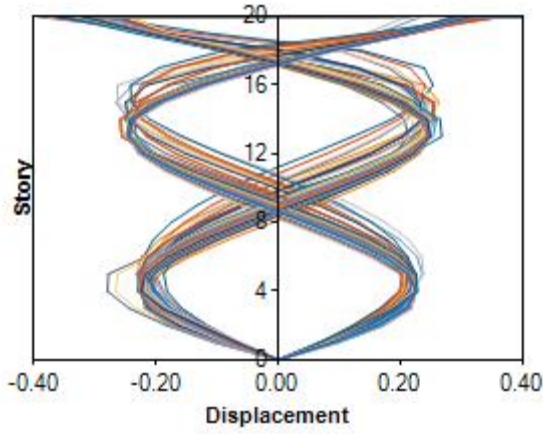
(a) Incremental Mode Shapes for LA27
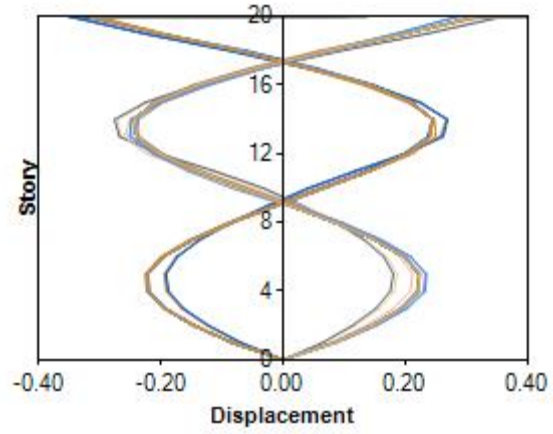
(b) Incremental Mode Shapes for LA28
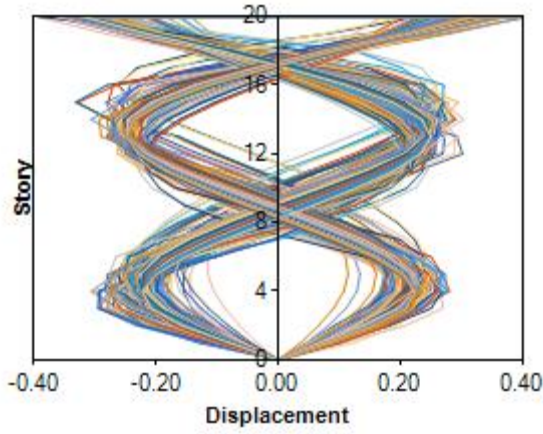
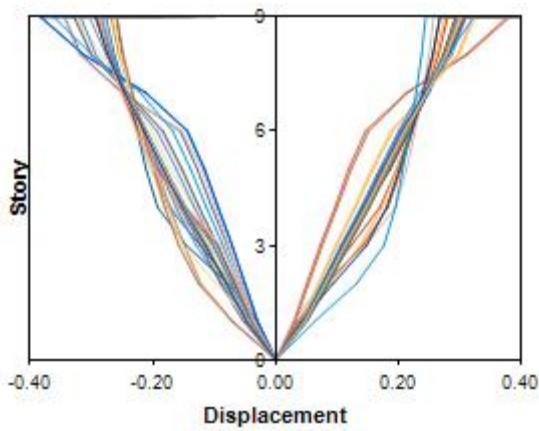(c) Incremental Mode Shapes for LA29
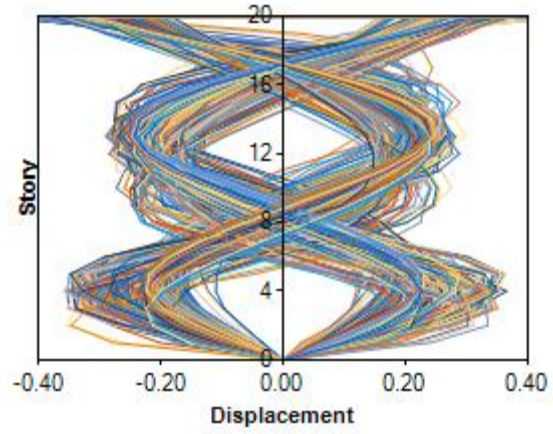
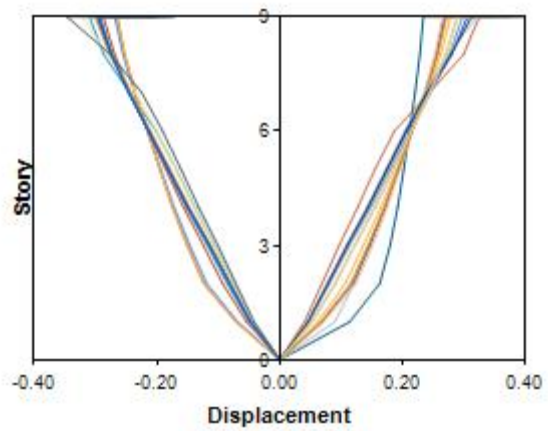(d) Incremental Mode Shapes for LA30
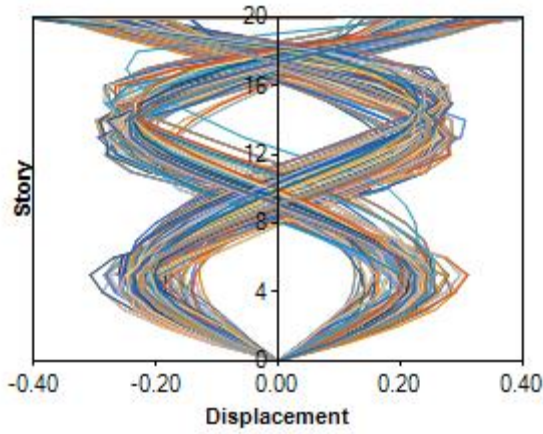
(e) Incremental Mode Shapes for LA31
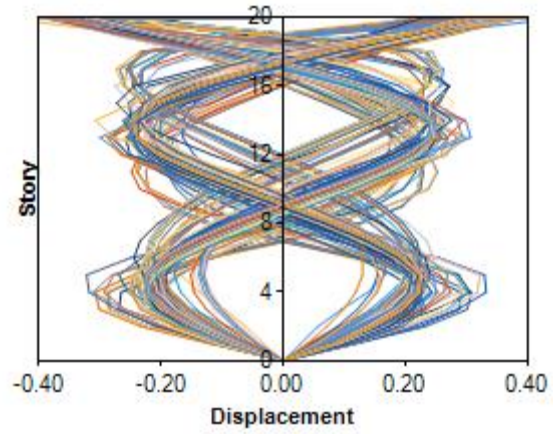
(f) Incremental Mode Shapes for LA32

Figure 10. Incremental Third Mode shapes of the SAC 20-Story Rigid Frame under LA27 to LA32
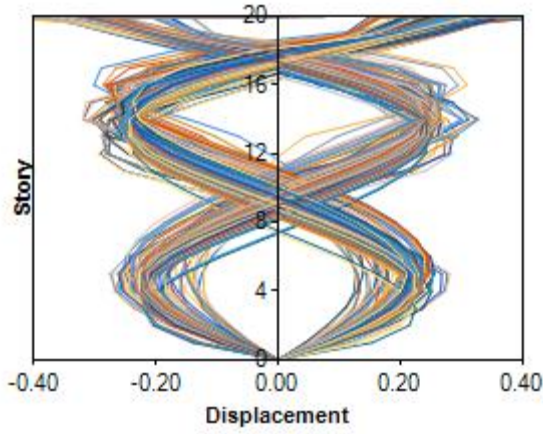
(a) Incremental Mode Shapes for LA33
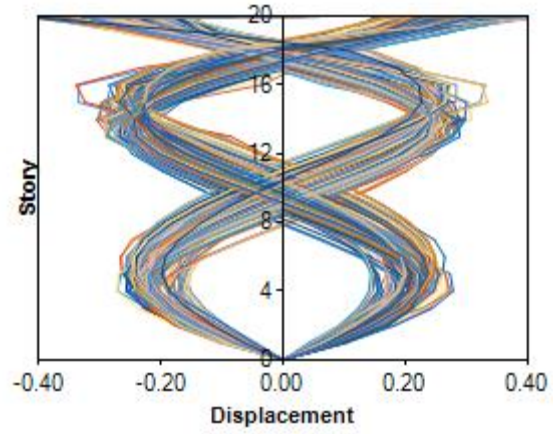
(b) Incremental Mode Shapes for LA34
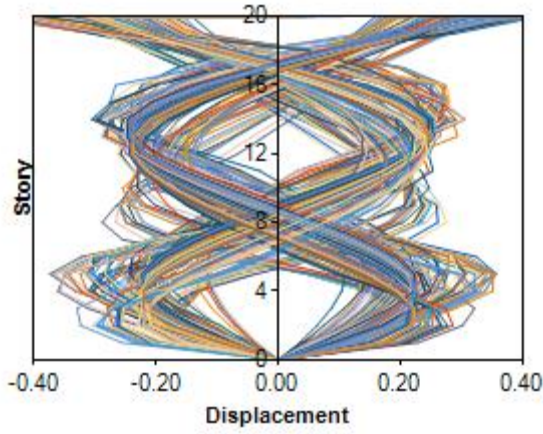
(c) Incremental Mode Shapes for LA35
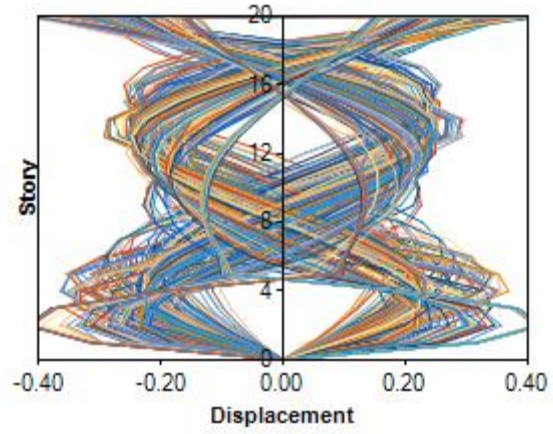
(d) Incremental Mode Shapes for LA36
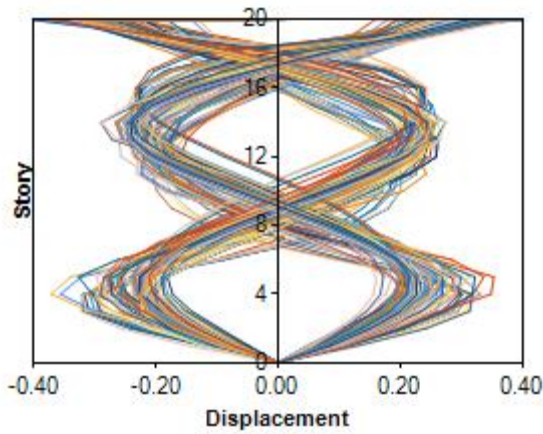
(e) Incremental Mode Shapes for LA37
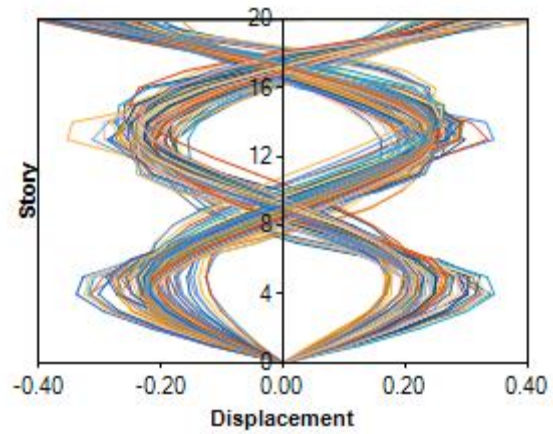
(f) Incremental Mode Shapes for LA38

Figure 11. Incremental Third Mode shapes of the SAC 20-Story Rigid Frame under LA33 to LA38

244

(a) Incremental Mode Shapes for LA39   (b) Incremental Mode Shapes for LA40
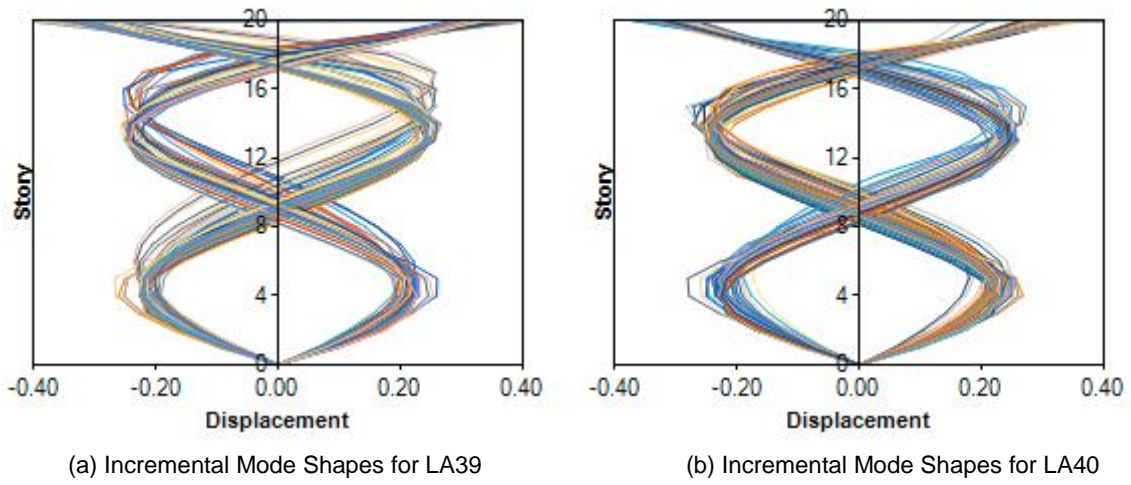
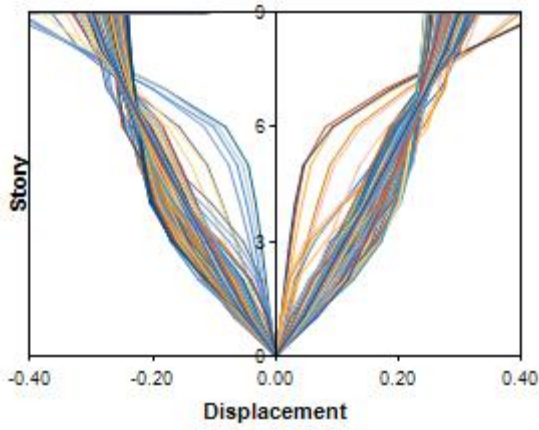Figure 12. Incremental Third Mode shapes of the SAC 20-Story Rigid Frame under LA39 to LA40
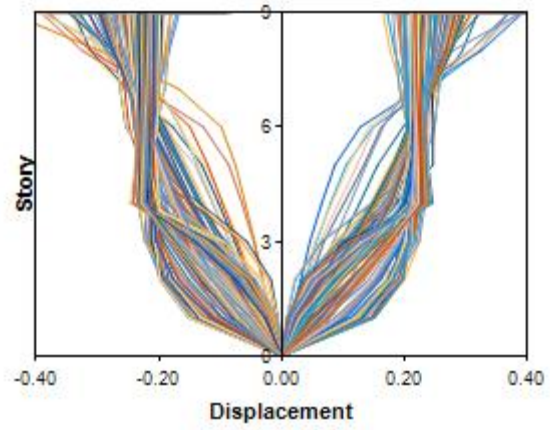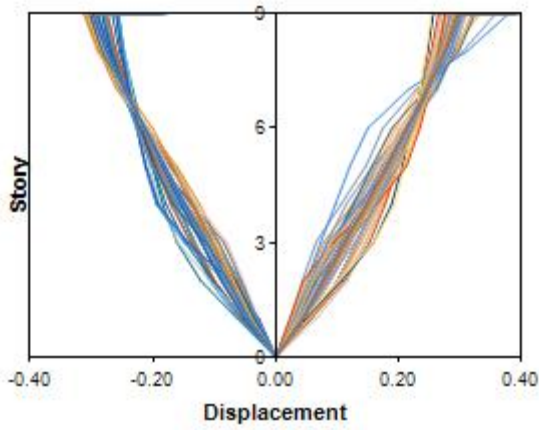
(a) Incremental Mode Shapes for LA21
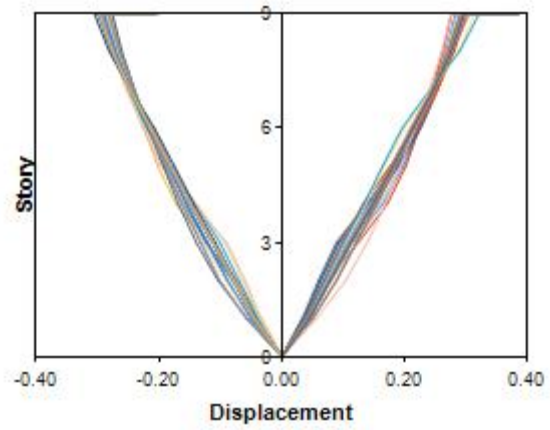
(b) Incremental Mode Shapes for LA22

(c) Incremental Mode Shapes for LA23

(d) Incremental Mode Shapes for LA24

(e) Incremental Mode Shapes for LA25

(f) Incremental Mode Shapes for LA26
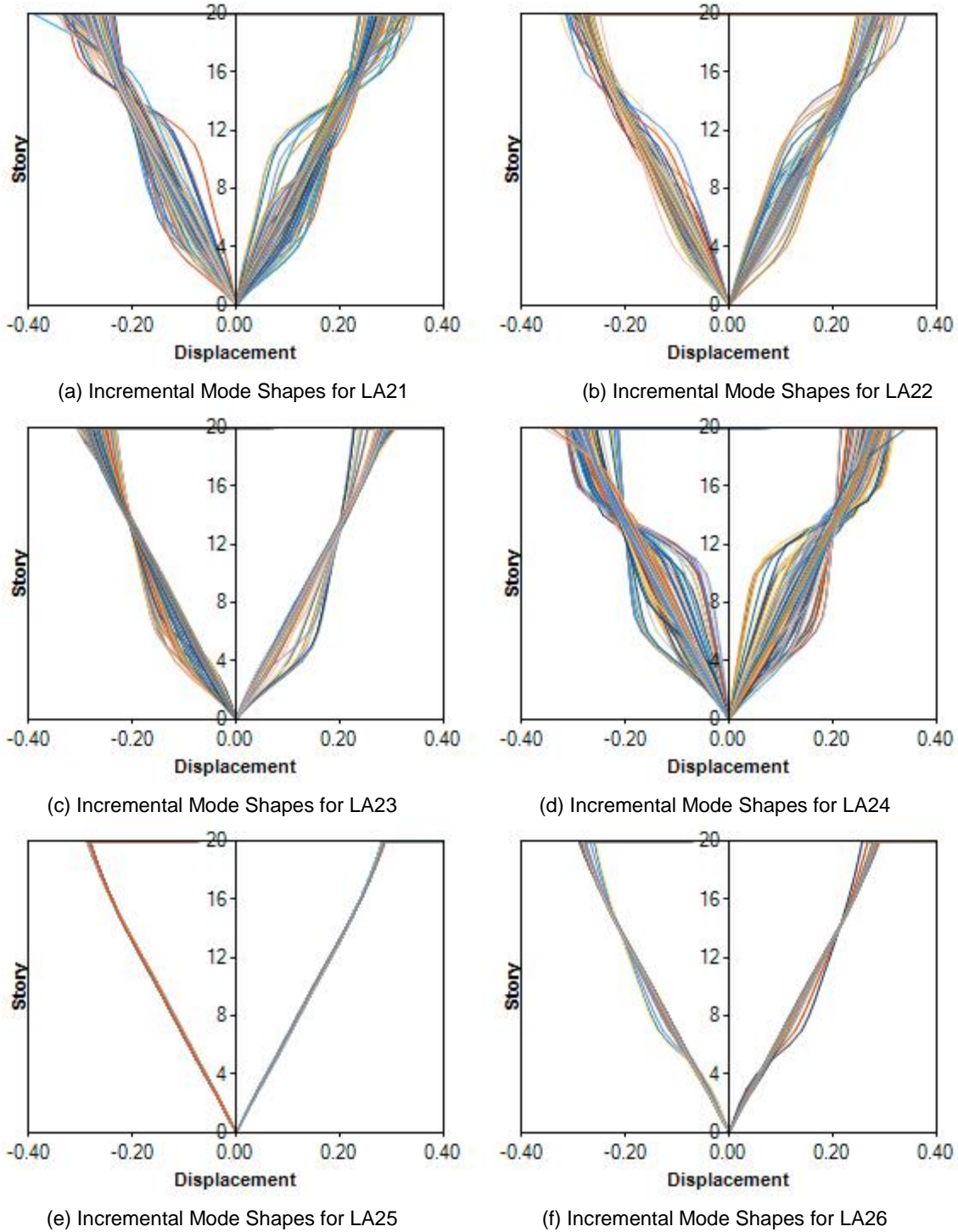
Figure 13. Incremental First Mode shapes of the HSAC20-4 Frame under LA21 to LA26
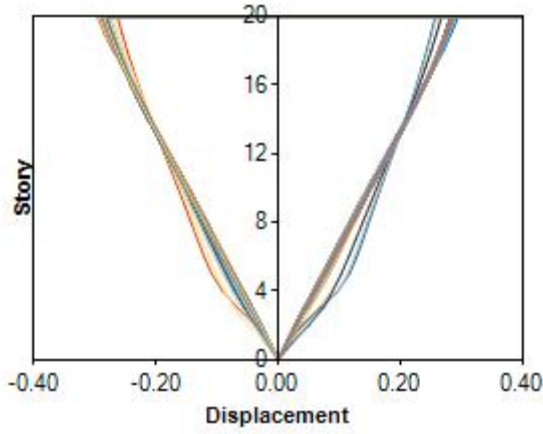
(a) Incremental Mode Shapes for LA27
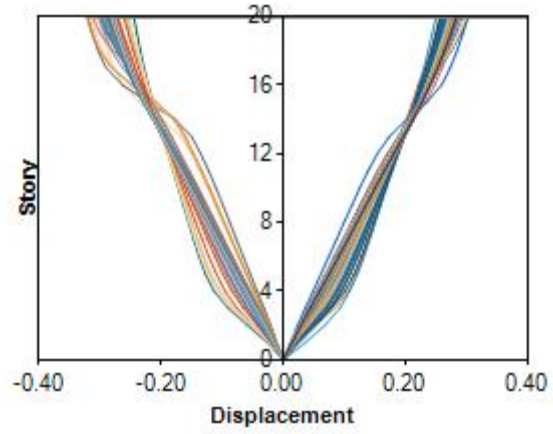
(b) Incremental Mode Shapes for LA28
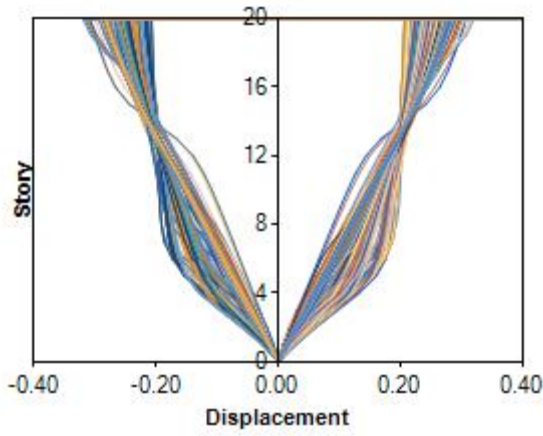
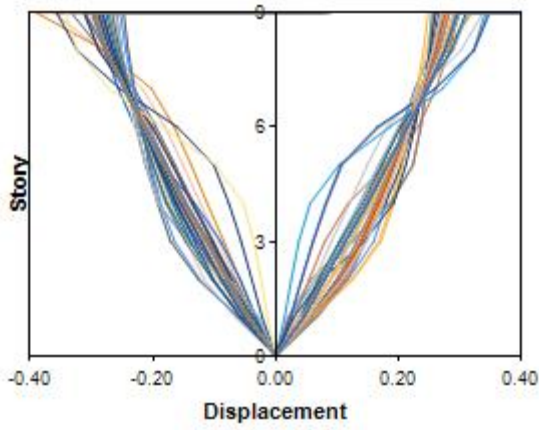(c) Incremental Mode Shapes for LA29
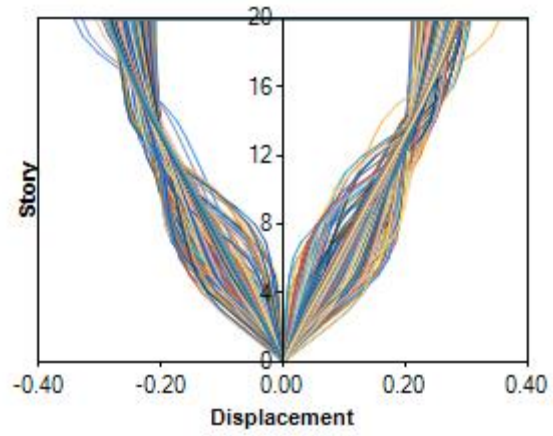
(d) Incremental Mode Shapes for LA30
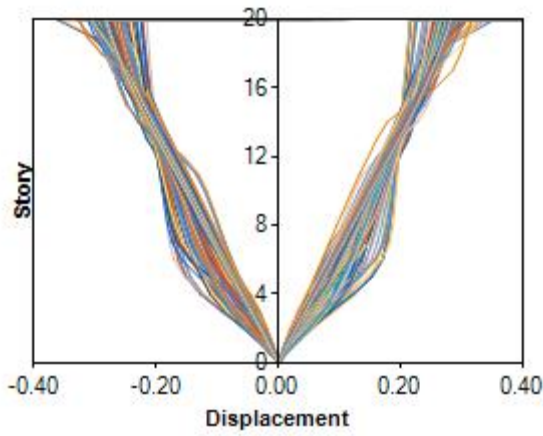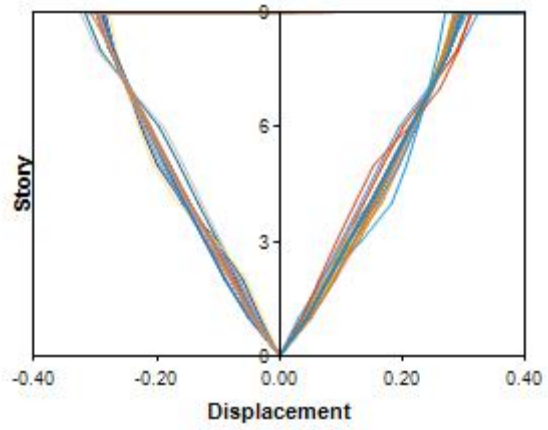
(e) Incremental Mode Shapes for LA31
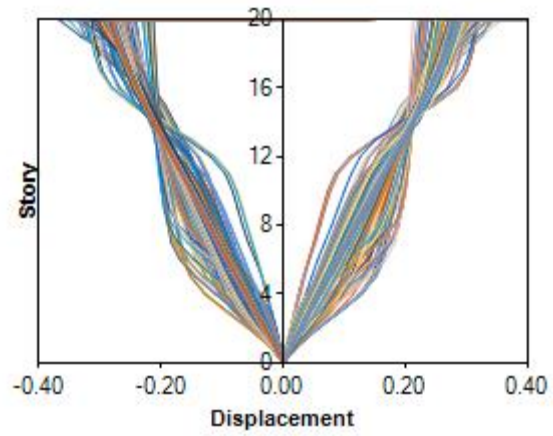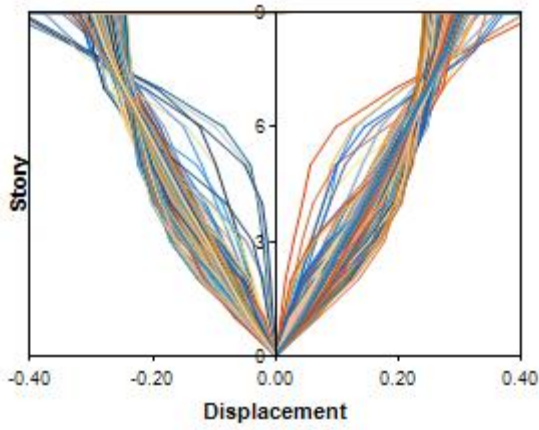
(f) Incremental Mode Shapes for LA32

Figure 14. Incremental First Mode shapes of the HSAC20-4 Frame under LA27 to LA32
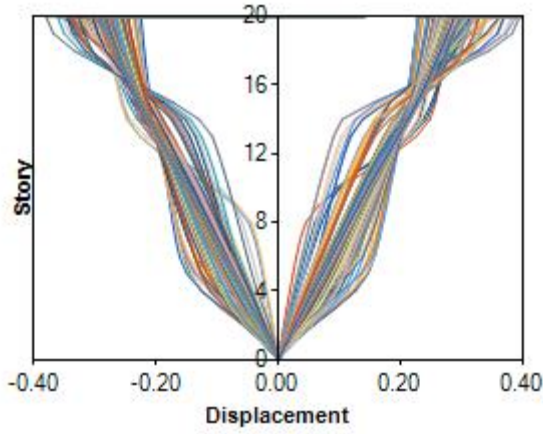
(a) Incremental Mode Shapes for LA33
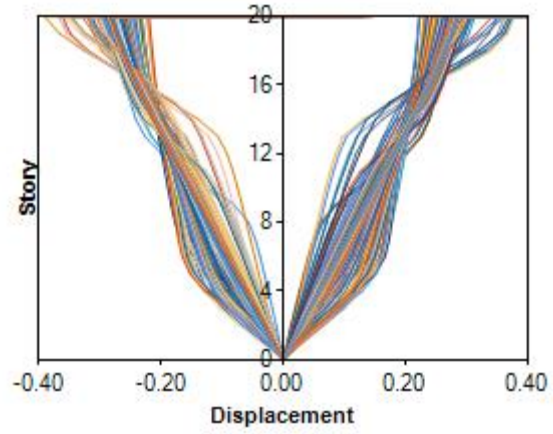
(b) Incremental Mode Shapes for LA34
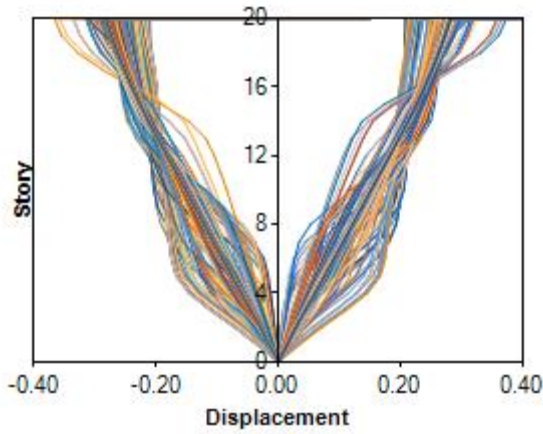
(c) Incremental Mode Shapes for LA35
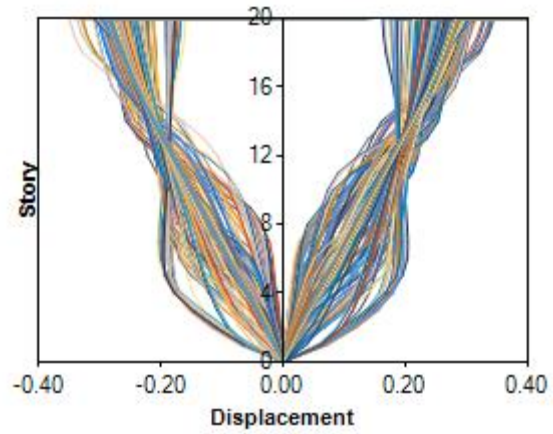
(d) Incremental Mode Shapes for LA36
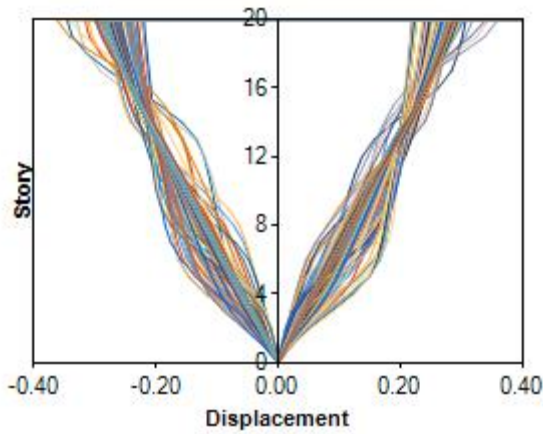
(e) Incremental Mode Shapes for LA37
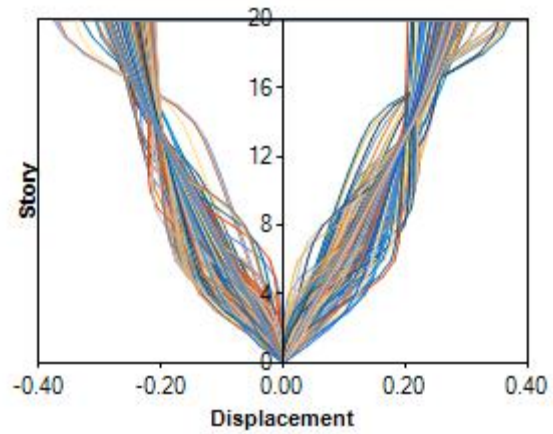
(f) Incremental Mode Shapes for LA38

Figure 15. Incremental First Mode shapes of the HSAC20-4 Frame under LA33 to LA38
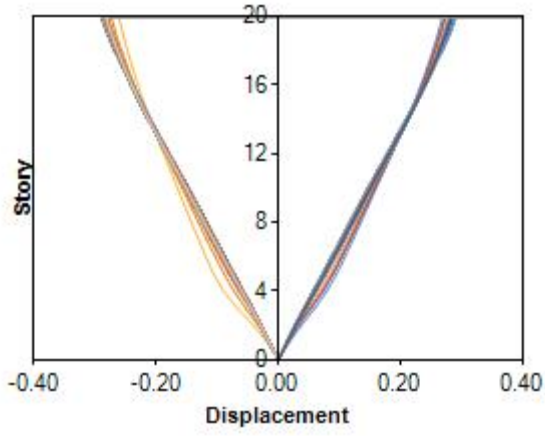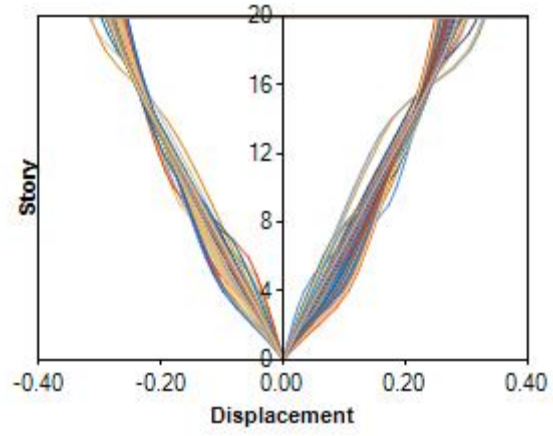
(a) Incremental Mode Shapes for LA39 (b) Incremental Mode Shapes for LA40

Figure 16. Incremental First Mode shapes of the HSAC20-4 Frame under LA39 to LA40
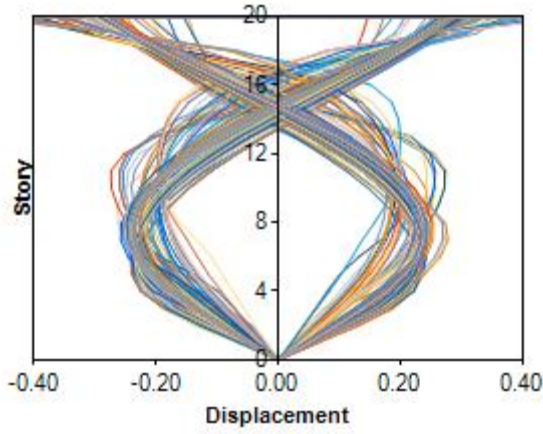
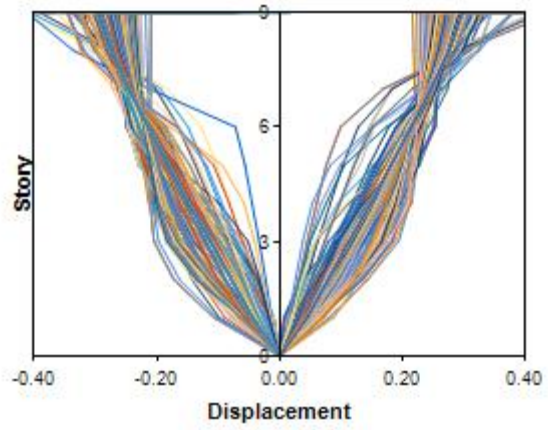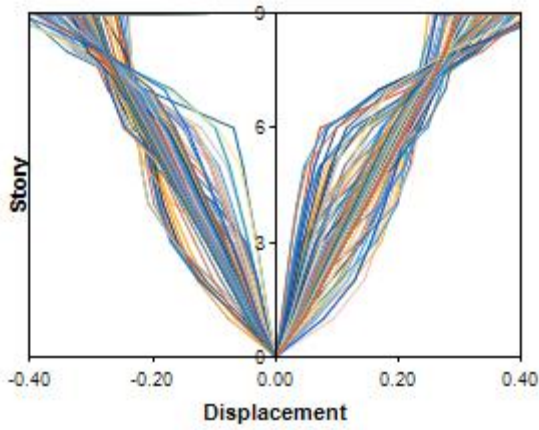(a) Incremental Mode Shapes for LA21
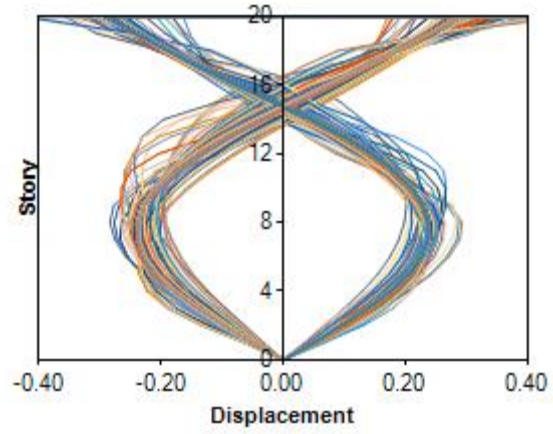
(b) Incremental Mode Shapes for LA22
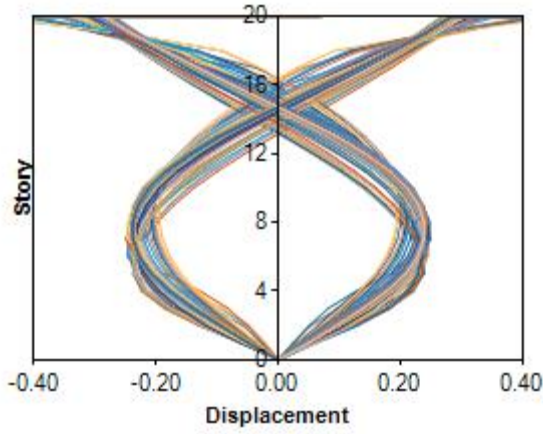
(c) Incremental Mode Shapes for LA23
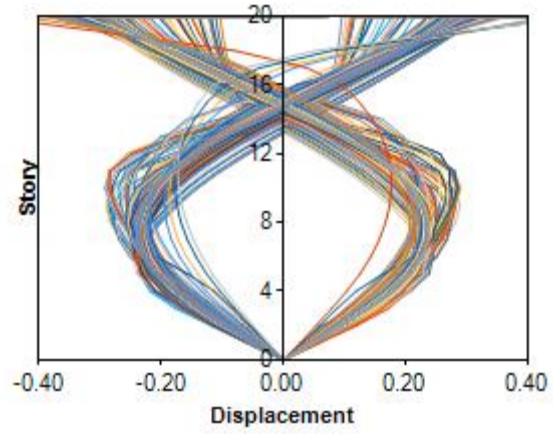
(d) Incremental Mode Shapes for LA24
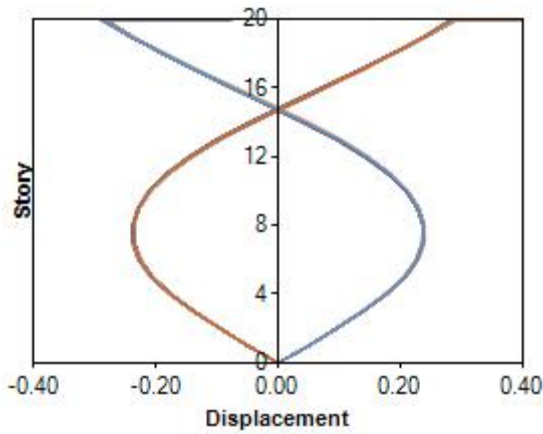
(e) Incremental Mode Shapes for LA25
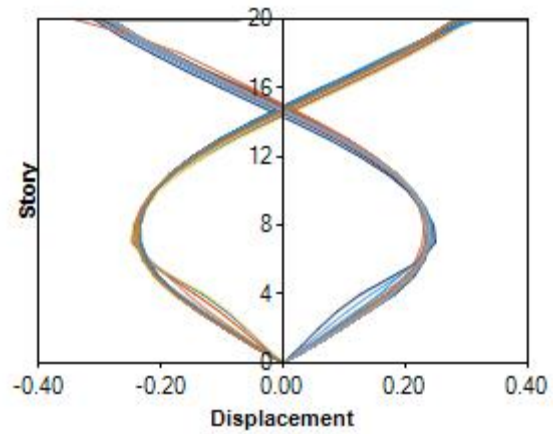
(f) Incremental Mode Shapes for LA26

Figure 17. Incremental Second Mode shapes of the HSAC20-4 Frame under LA21 to LA26
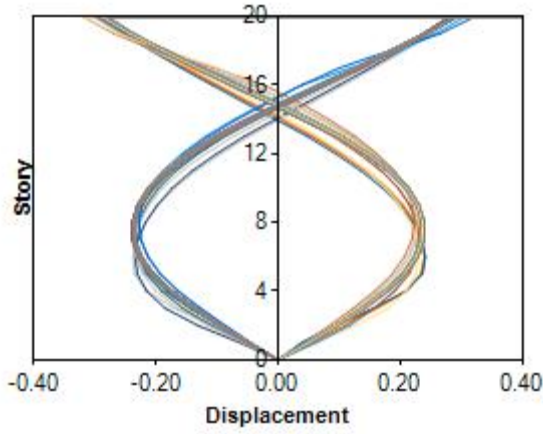
(a) Incremental Mode Shapes for LA27
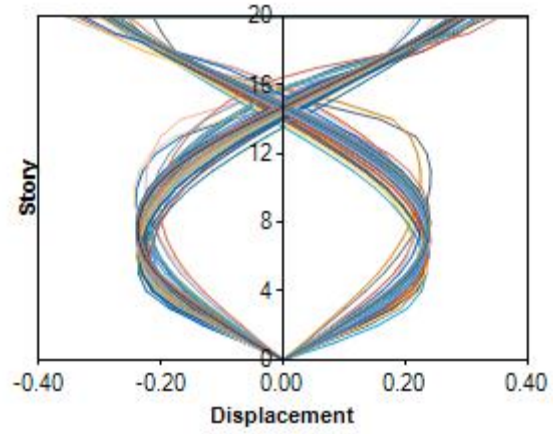
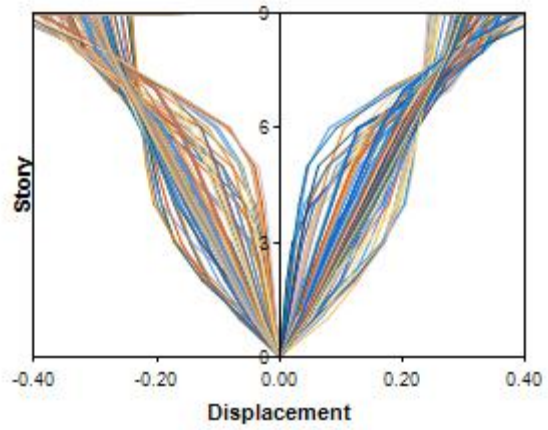(b) Incremental Mode Shapes for LA28
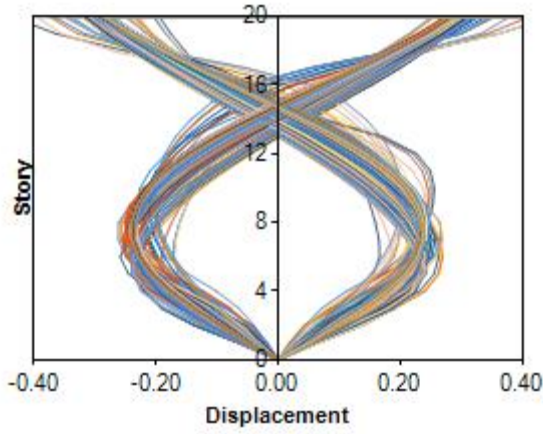
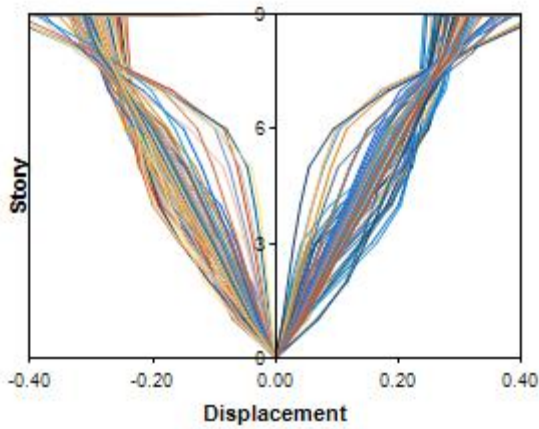(c) Incremental Mode Shapes for LA29
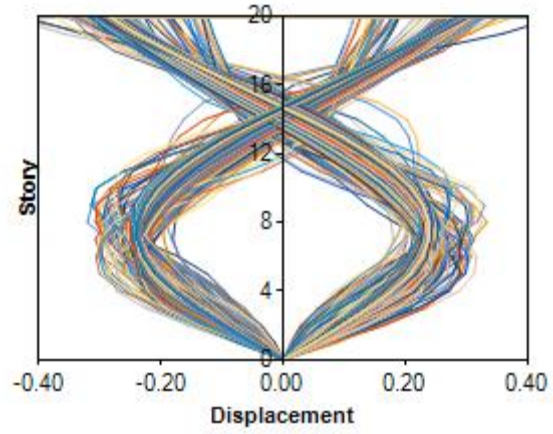
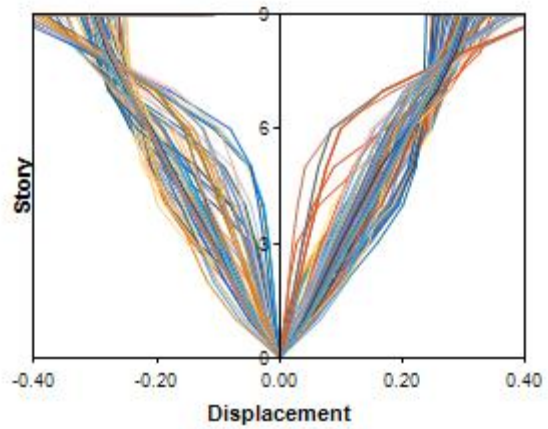(d) Incremental Mode Shapes for LA30
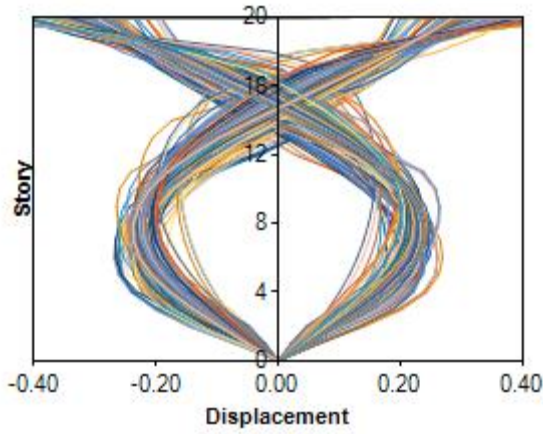
(e) Incremental Mode Shapes for LA31
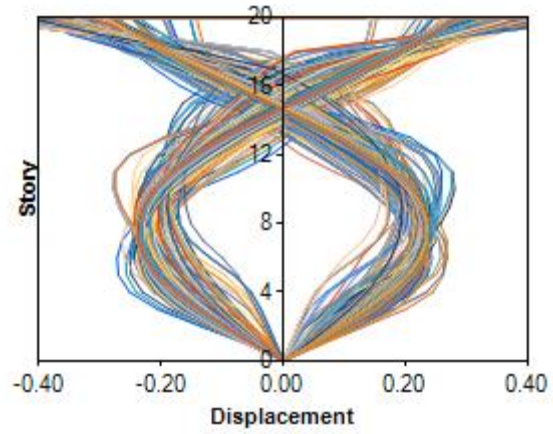
(f) Incremental Mode Shapes for LA32

Figure 18. Incremental Second Mode shapes of the HSAC20-4 Frame under LA27 to LA32
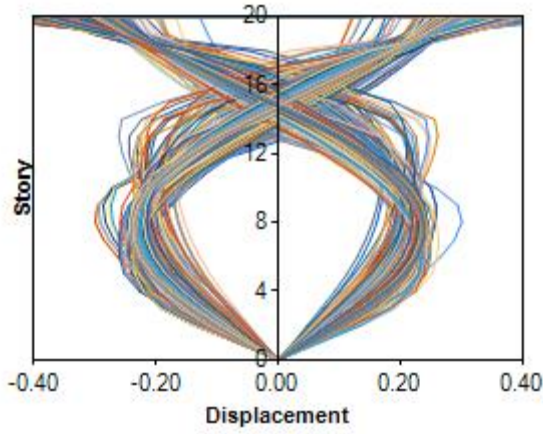
(a) Incremental Mode Shapes for LA33
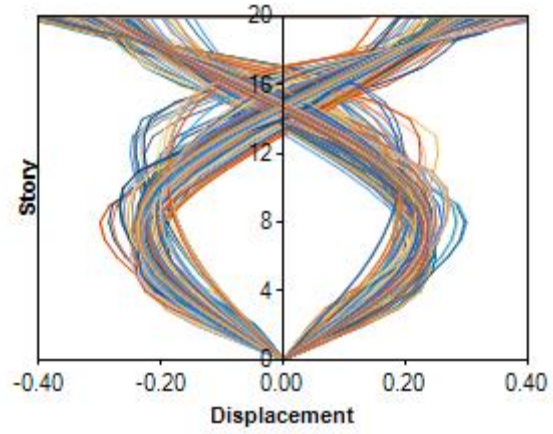
(b) Incremental Mode Shapes for LA34
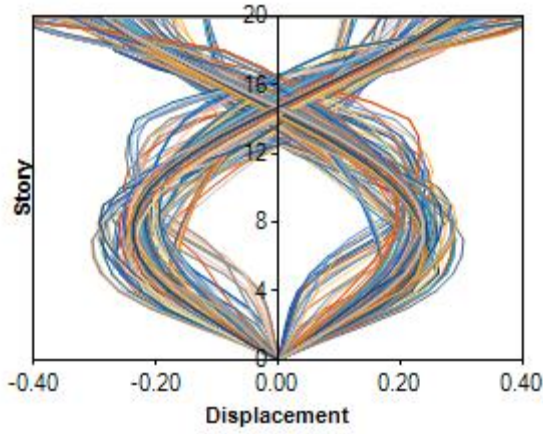
(c) Incremental Mode Shapes for LA35
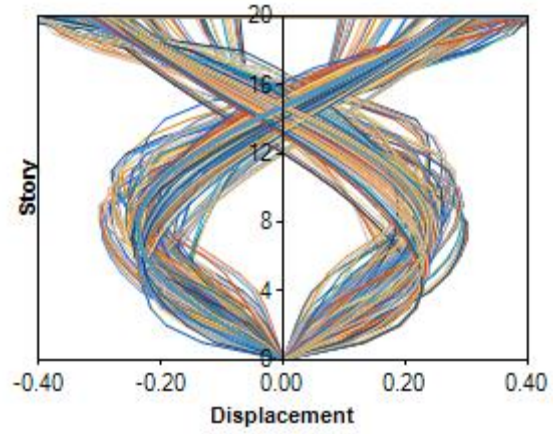
(d) Incremental Mode Shapes for LA36
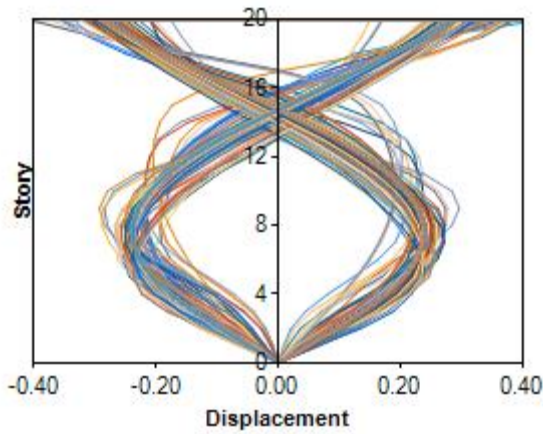
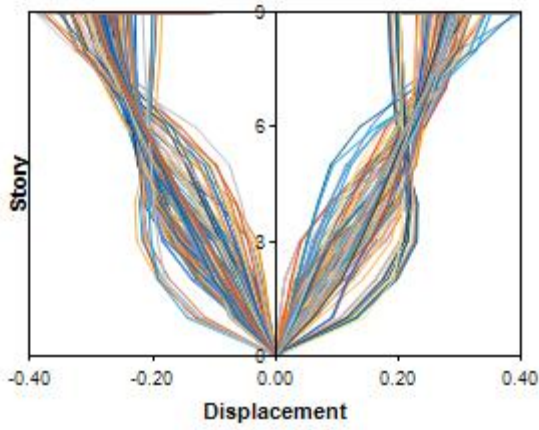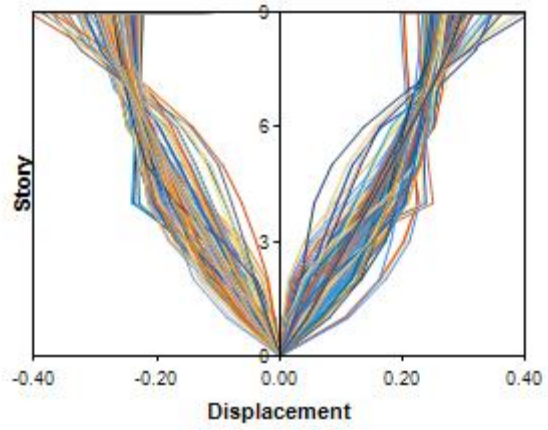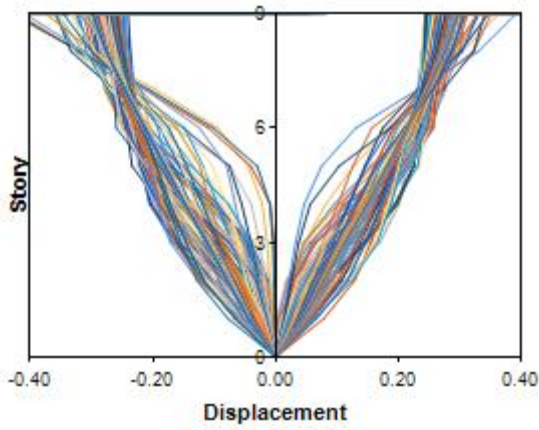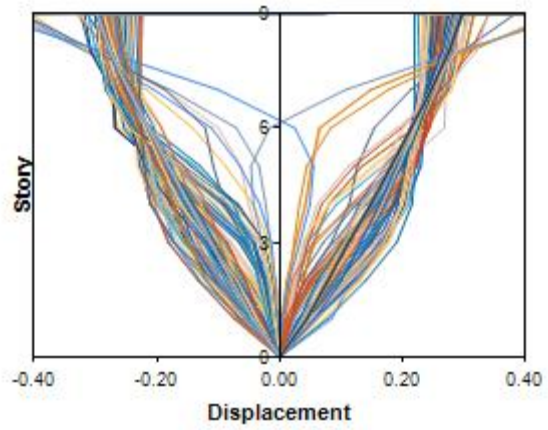(e) Incremental Mode Shapes for LA37
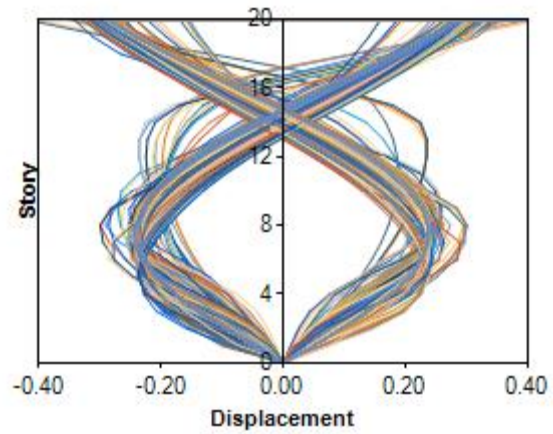
(f) Incremental Mode Shapes for LA38

Figure 19. Incremental Second Mode shapes of the HSAC20-4 Frame under LA33 to LA38
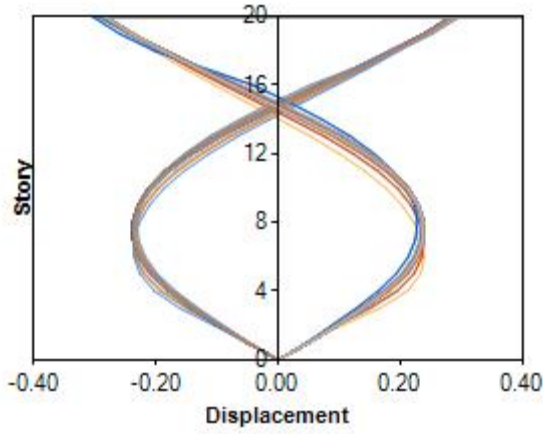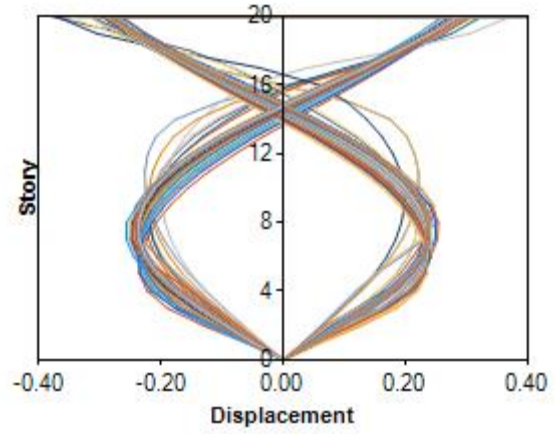
(a) Incremental Mode Shapes for LA39   (b) Incremental Mode Shapes for LA40

Figure 20. Incremental Second Mode shapes of the HSAC20-4 Frame under LA39 to LA40
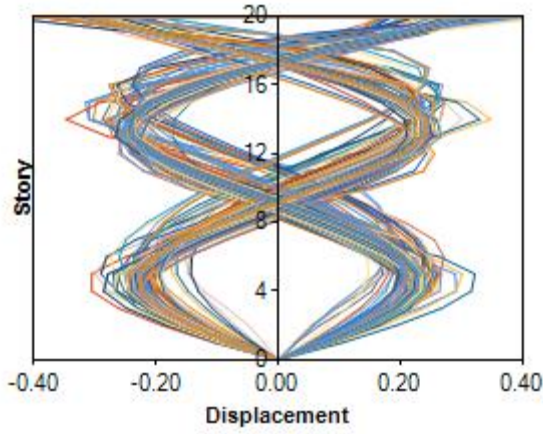
(a) Incremental Mode Shapes for LA21
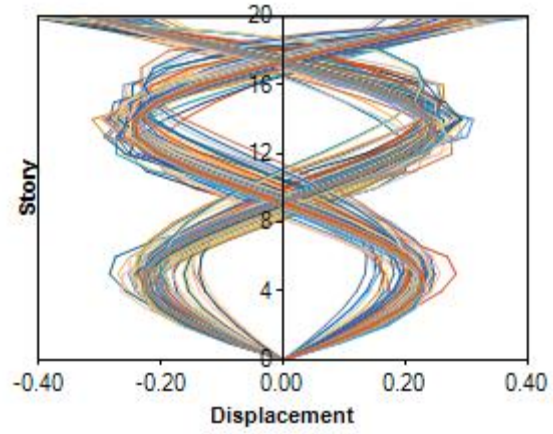
(b) Incremental Mode Shapes for LA22
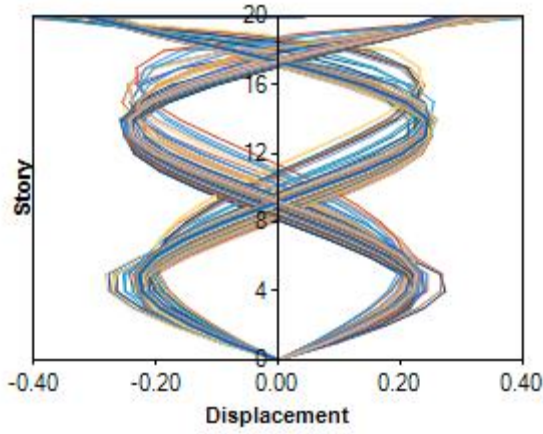
(c) Incremental Mode Shapes for LA23
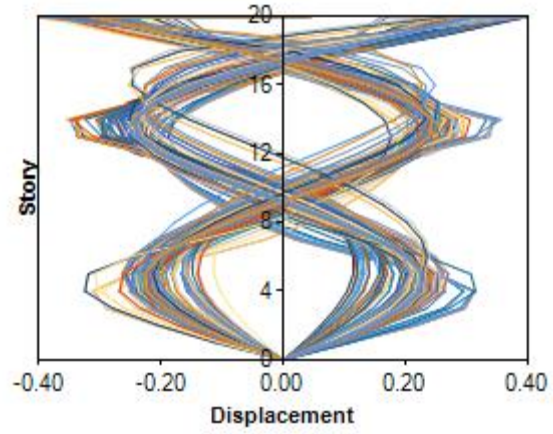
(d) Incremental Mode Shapes for LA24
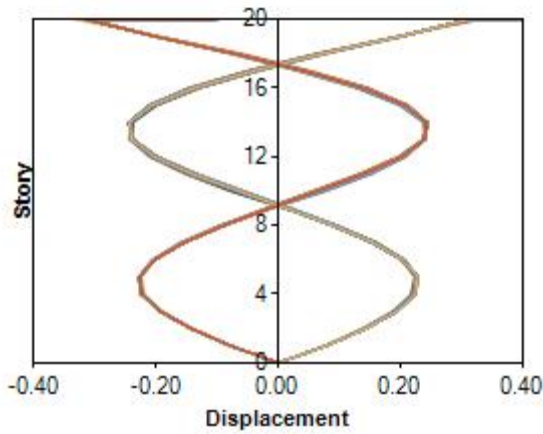
(e) Incremental Mode Shapes for LA25
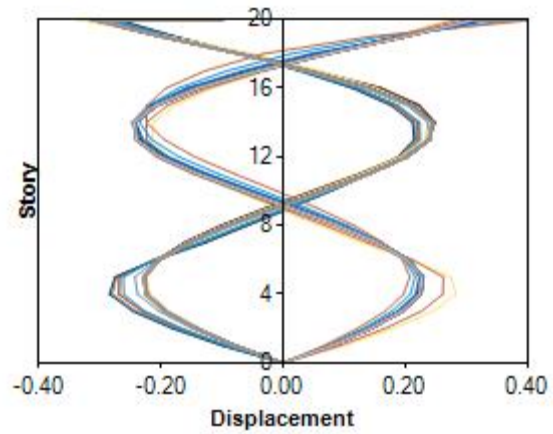
(f) Incremental Mode Shapes for LA26

Figure 21. Incremental Third Mode shapes of the HSAC20-4 Frame under LA21 to LA26
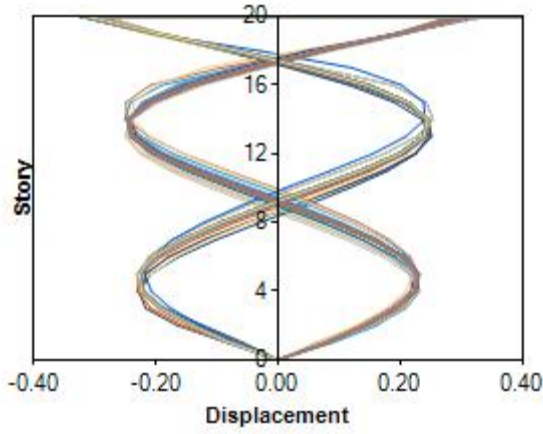
(a) Incremental Mode Shapes for LA27
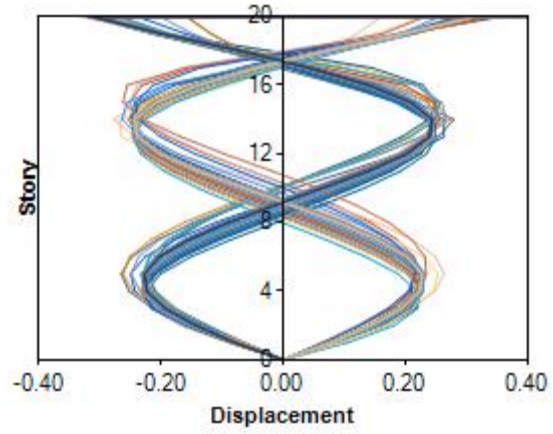
(b) Incremental Mode Shapes for LA28
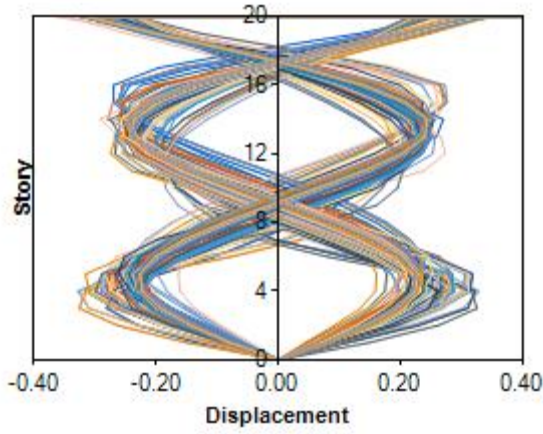
(c) Incremental Mode Shapes for LA29
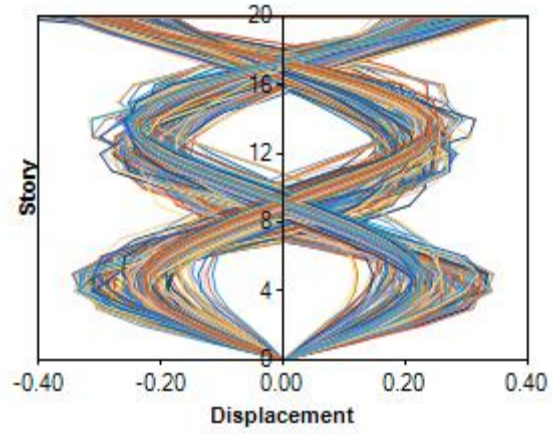
(d) Incremental Mode Shapes for LA30
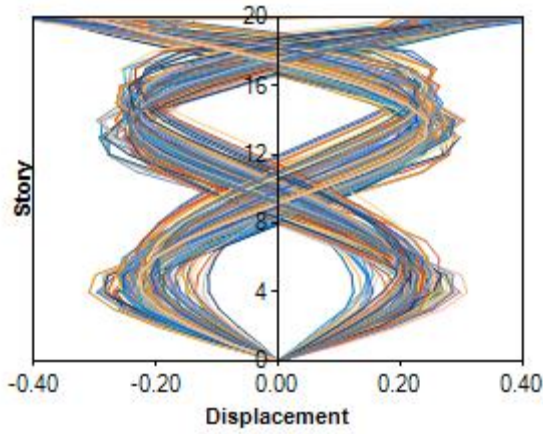
(e) Incremental Mode Shapes for LA31
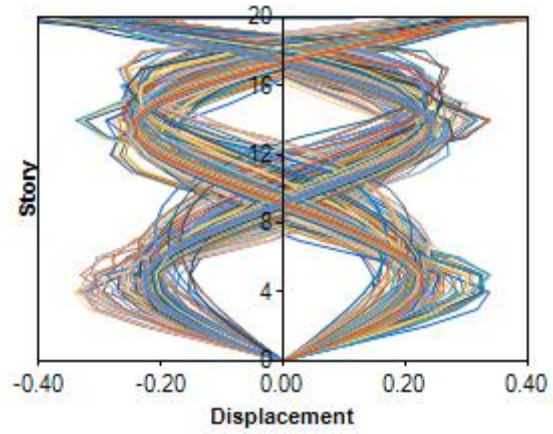
(f) Incremental Mode Shapes for LA32

Figure 22. Incremental Third Mode shapes of the HSAC20-4 Frame under LA27 to LA32
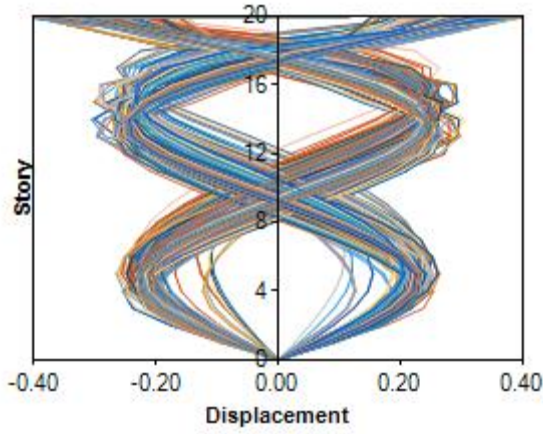
(a) Incremental Mode Shapes for LA33
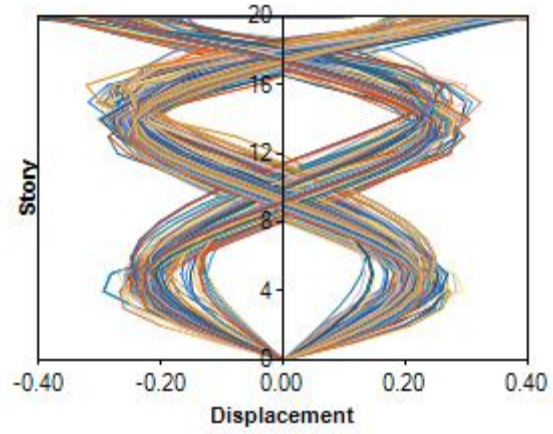
(b) Incremental Mode Shapes for LA34
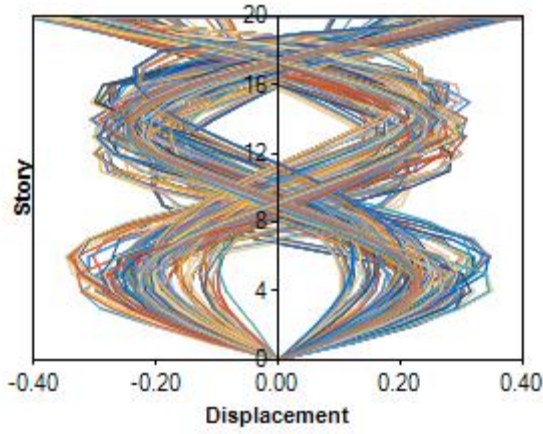
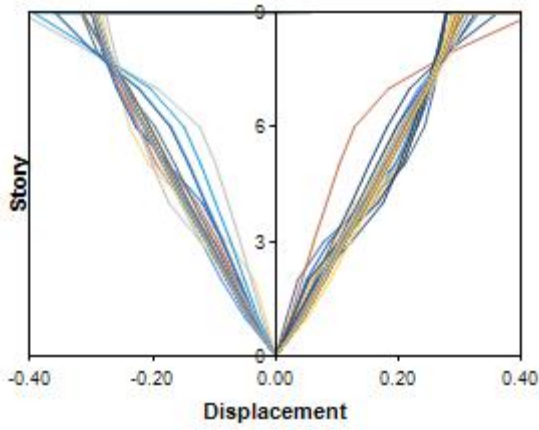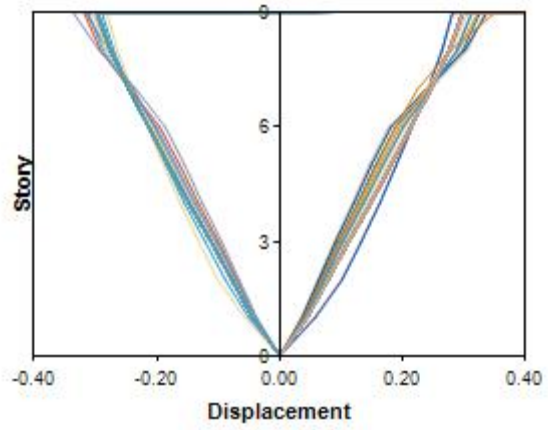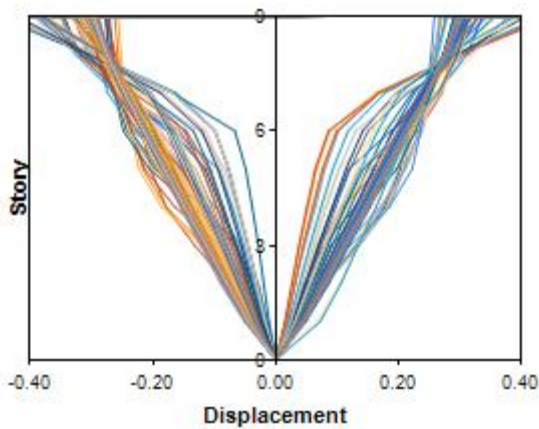(c) Incremental Mode Shapes for LA35
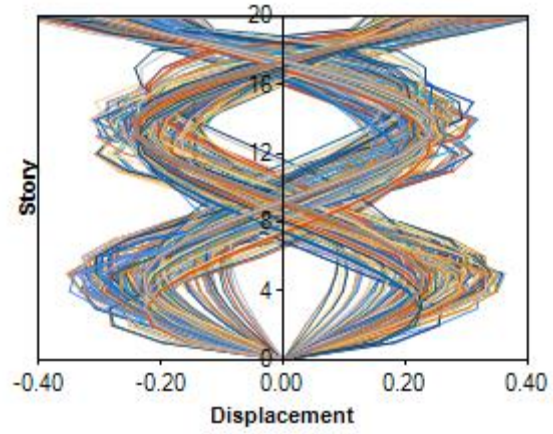
(d) Incremental Mode Shapes for LA36
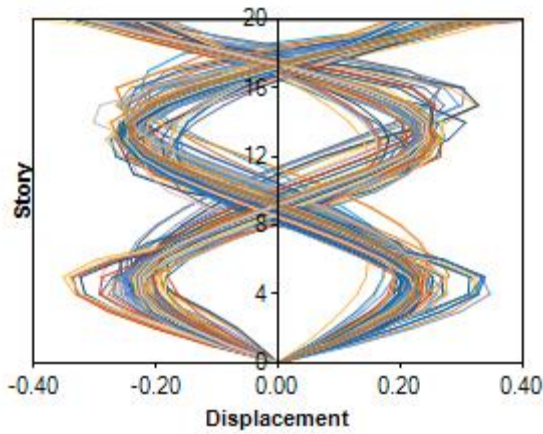
(e) Incremental Mode Shapes for LA37
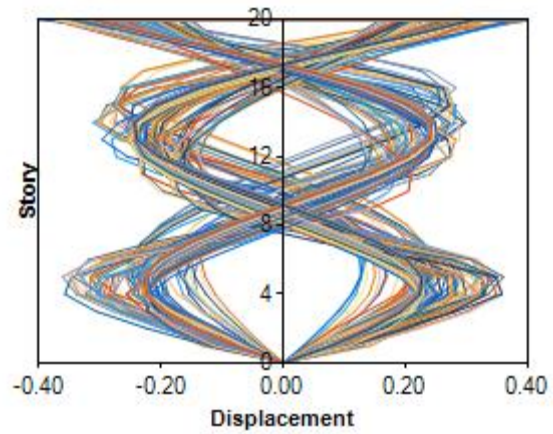
(f) Incremental Mode Shapes for LA38

Figure 23. Incremental Third Mode shapes of the HSAC20-4 Frame under LA33 to LA38
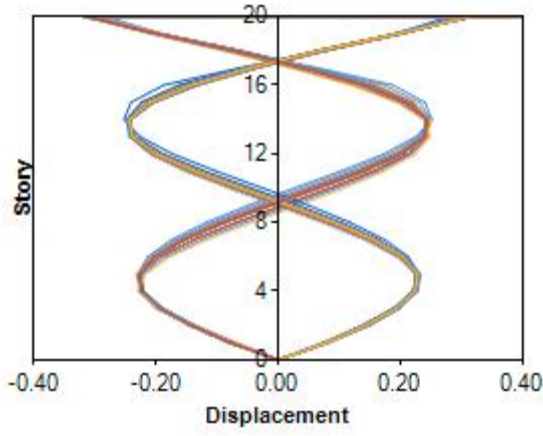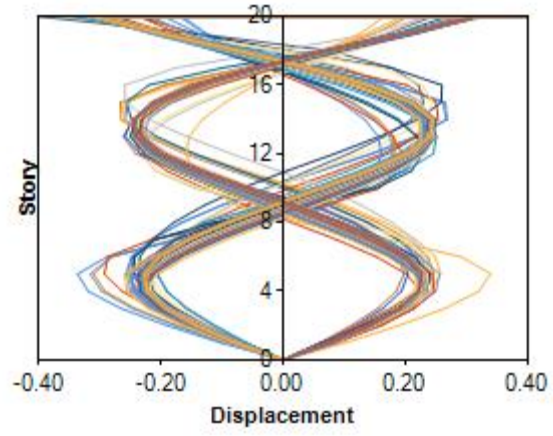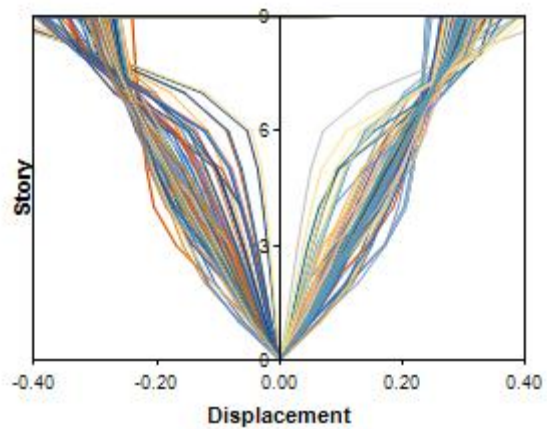
(a) Incremental Mode Shapes for LA39   (b) Incremental Mode Shapes for LA40

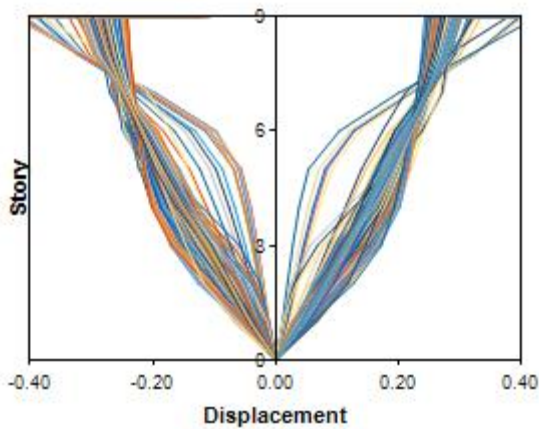Figure 24. Incremental Third Mode shapes of the HSAC20-4 Frame under LA39 to LA40
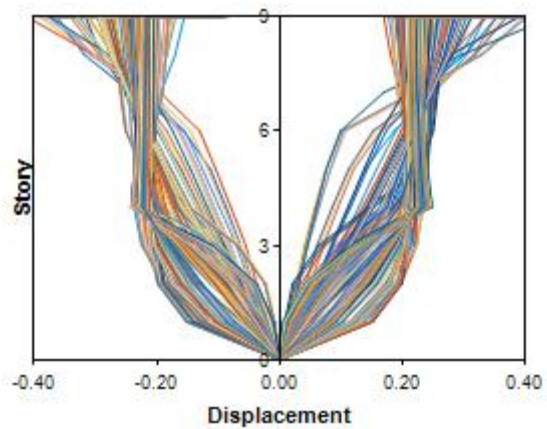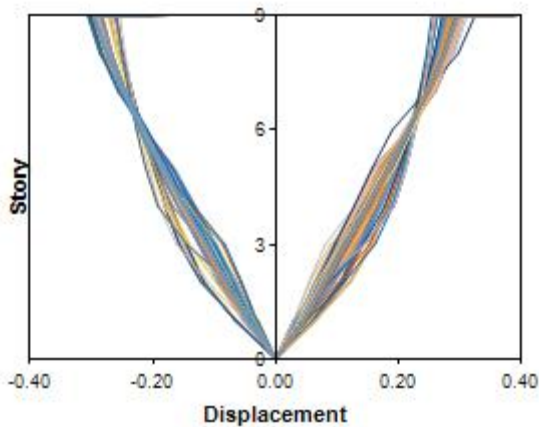
257

(a) Incremental Mode Shapes for LA21
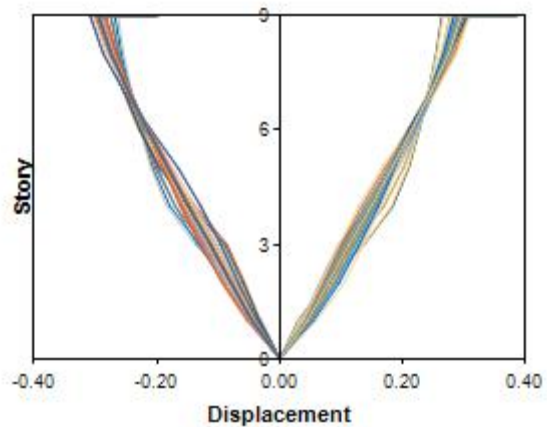
(b) Incremental Mode Shapes for LA22

(c) Incremental Mode Shapes for LA23

(d) Incremental Mode Shapes for LA24

(e) Incremental Mode Shapes for LA25

(f) Incremental Mode Shapes for LA26
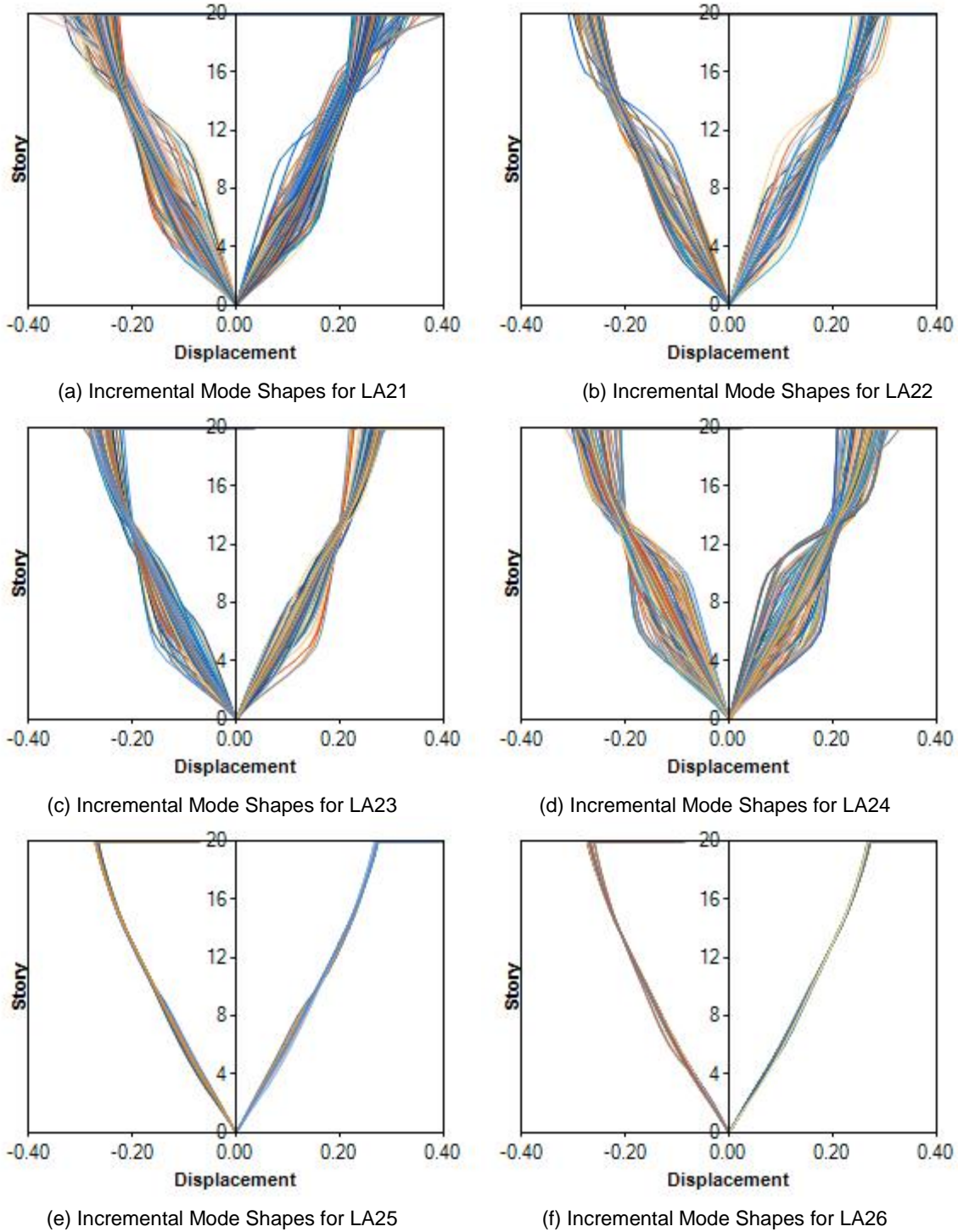
Figure 25. Incremental First Mode shapes of the HSAC20-5 Frame under LA21 to LA26
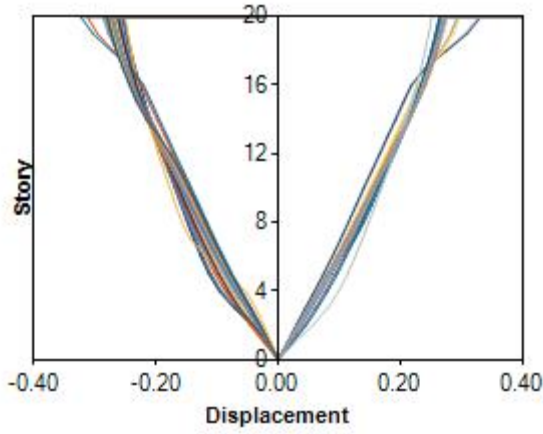
(a) Incremental Mode Shapes for LA27
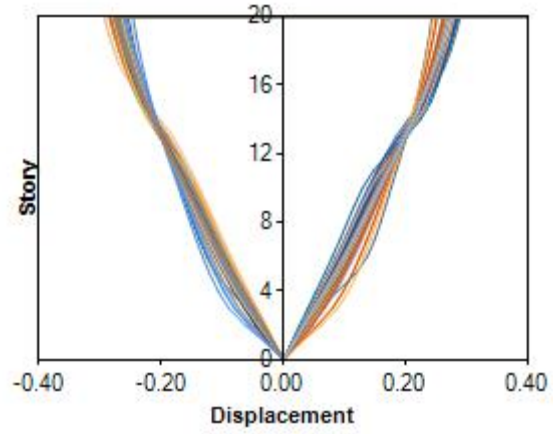
(b) Incremental Mode Shapes for LA28
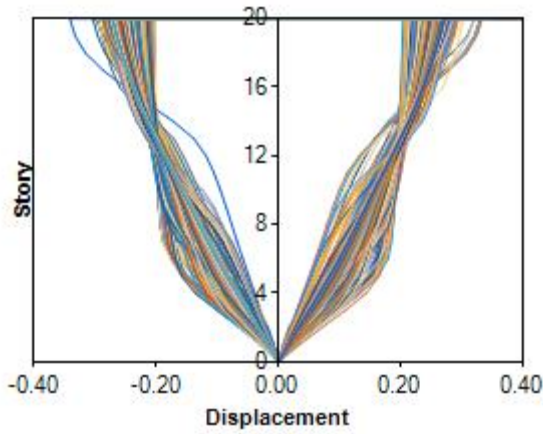
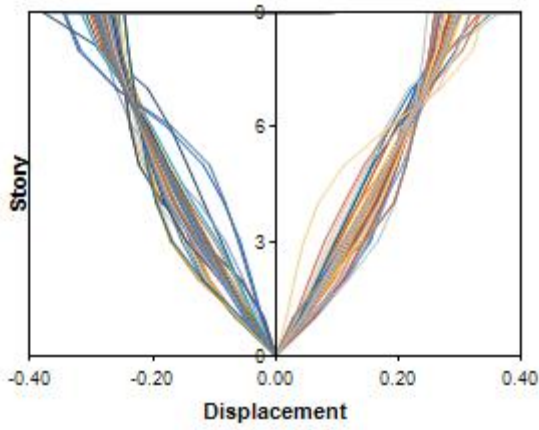(c) Incremental Mode Shapes for LA29
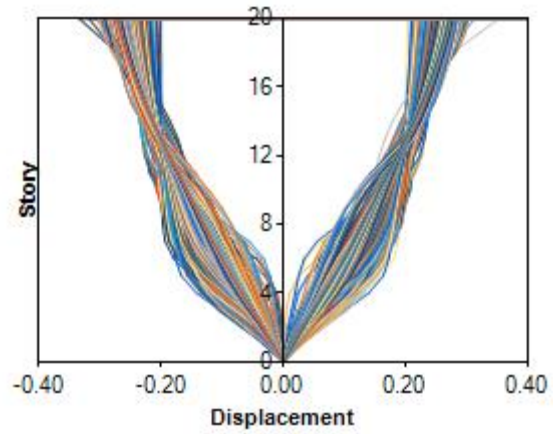
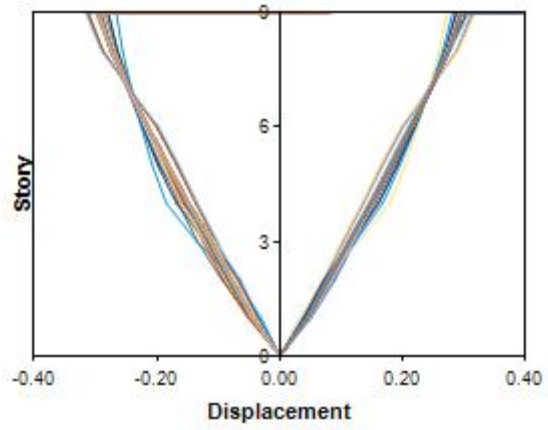(d) Incremental Mode Shapes for LA30
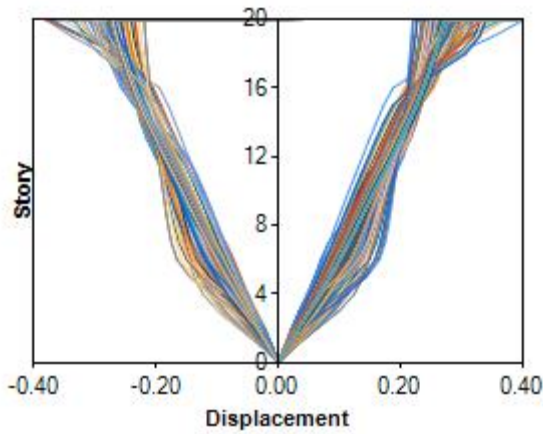
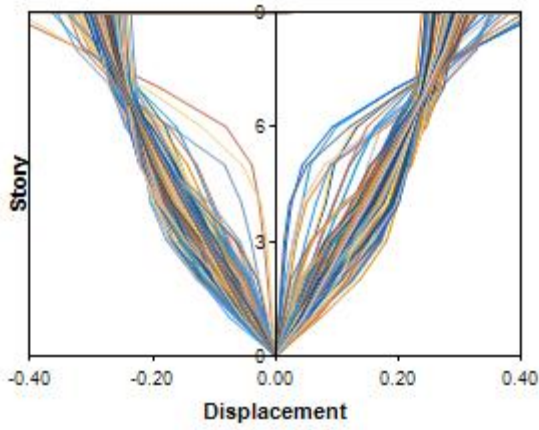(e) Incremental Mode Shapes for LA31
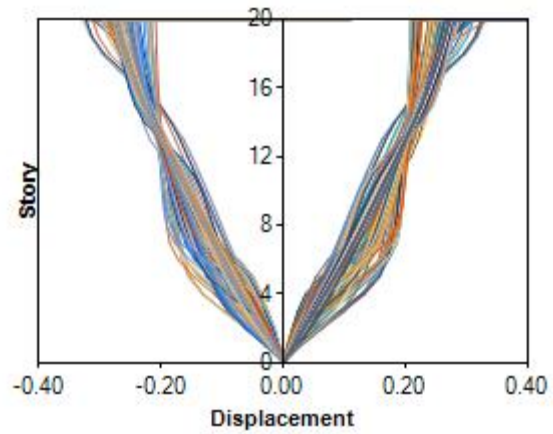
(f) Incremental Mode Shapes for LA32

Figure 26. Incremental First Mode shapes of the HSAC20-5 Frame under LA27 to LA32
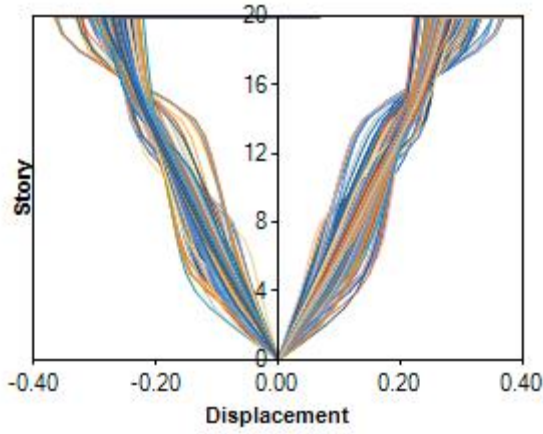
(a) Incremental Mode Shapes for LA33
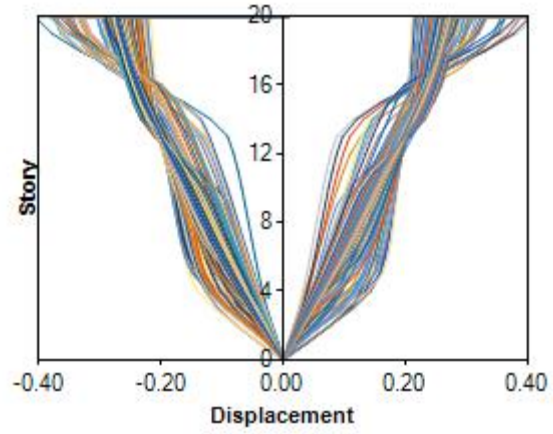
(b) Incremental Mode Shapes for LA34
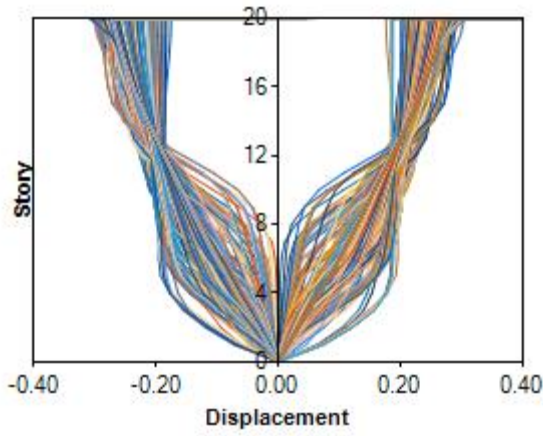
(c) Incremental Mode Shapes for LA35
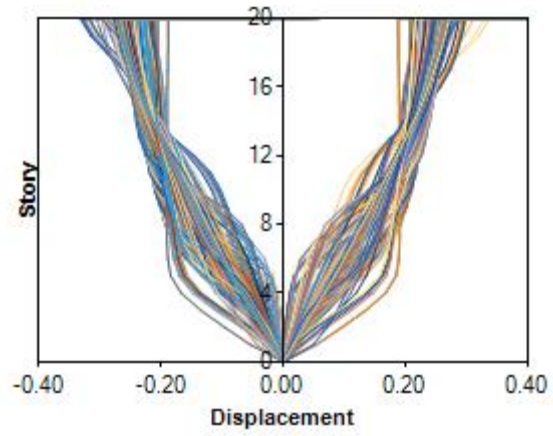
(d) Incremental Mode Shapes for LA36
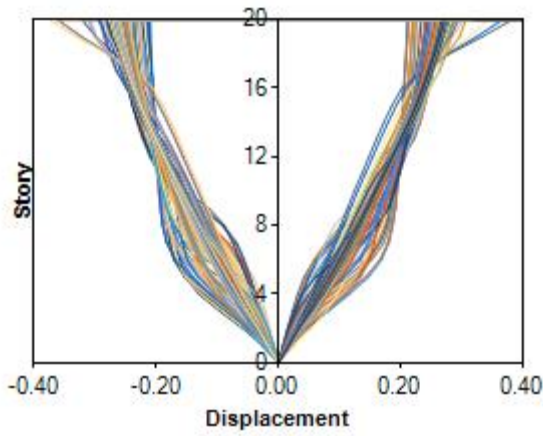
(e) Incremental Mode Shapes for LA37
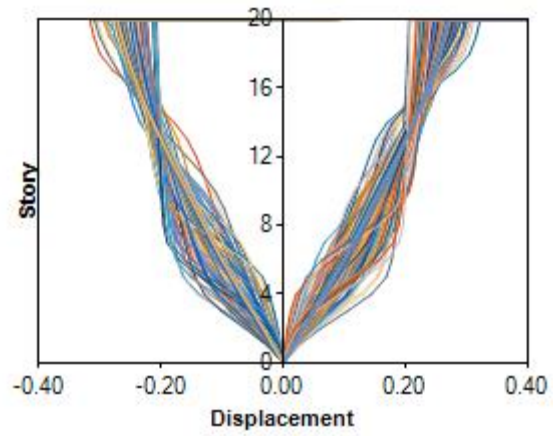
(f) Incremental Mode Shapes for LA38

Figure 27. Incremental First Mode shapes of the HSAC20-5 Frame under LA33 to LA38
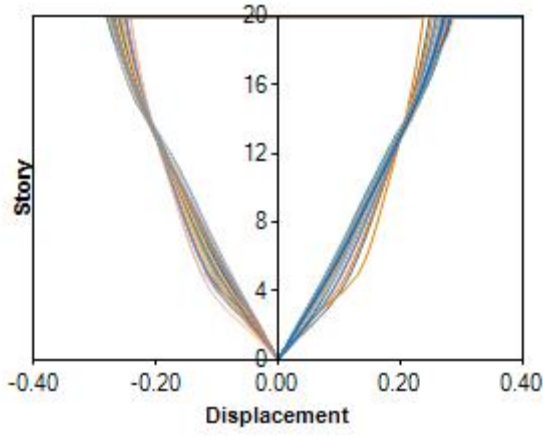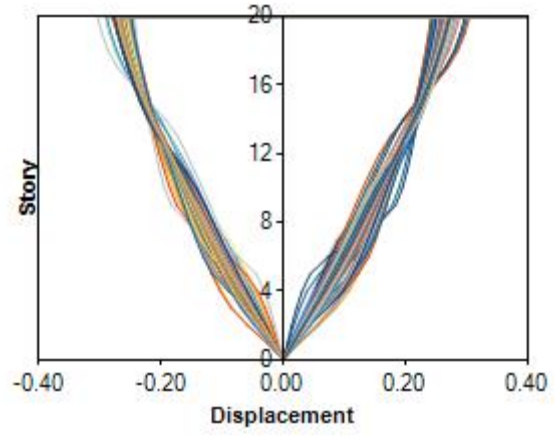
(a) Incremental Mode Shapes for LA39   (b) Incremental Mode Shapes for LA40

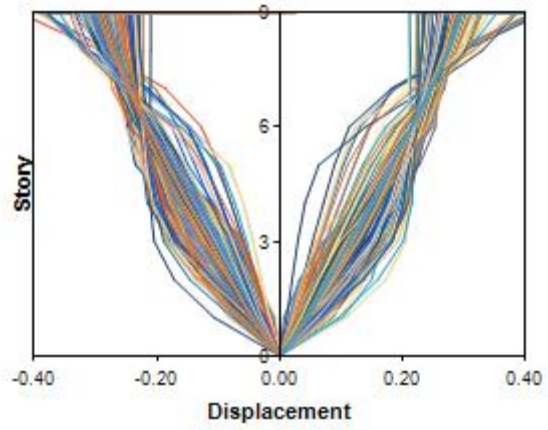Figure 28. Incremental First Mode shapes of the HSAC20-5 Frame under LA39 to LA40
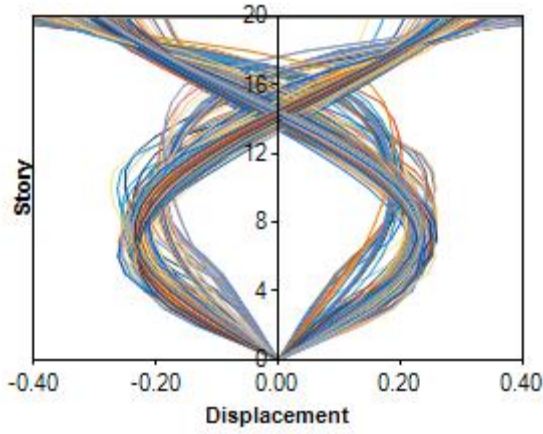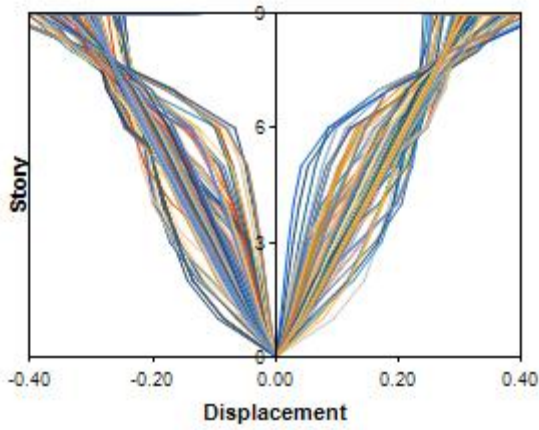
(a) Incremental Mode Shapes for LA21
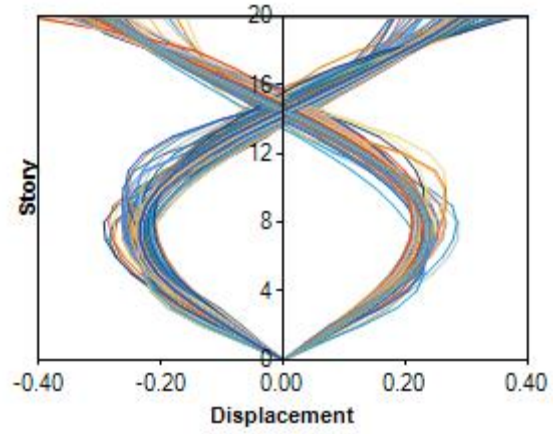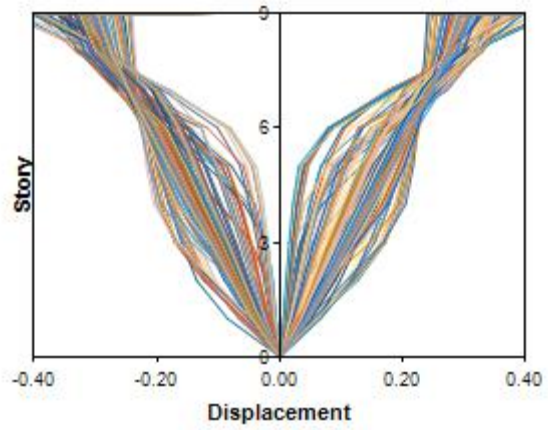
(b) Incremental Mode Shapes for LA22
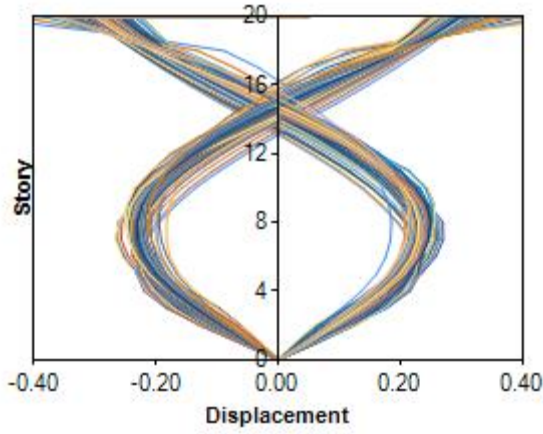
(c) Incremental Mode Shapes for LA23
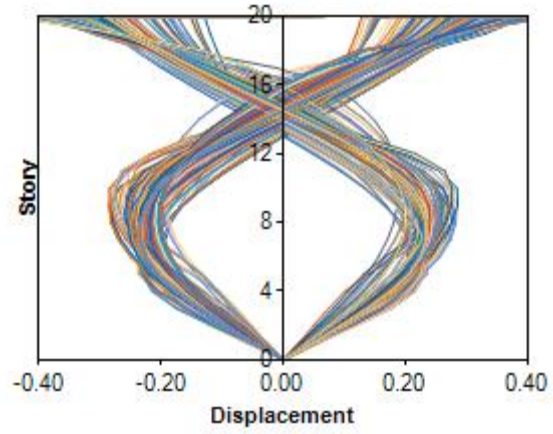
(d) Incremental Mode Shapes for LA24
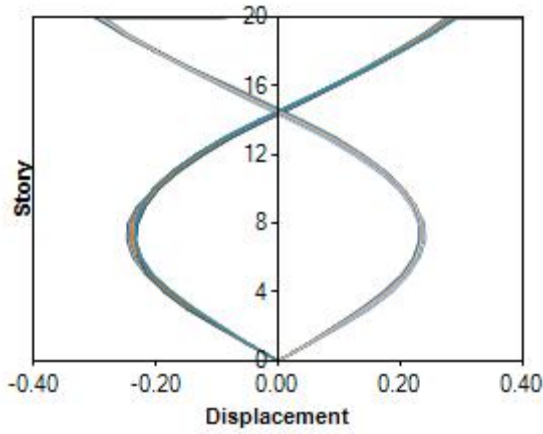
(e) Incremental Mode Shapes for LA25
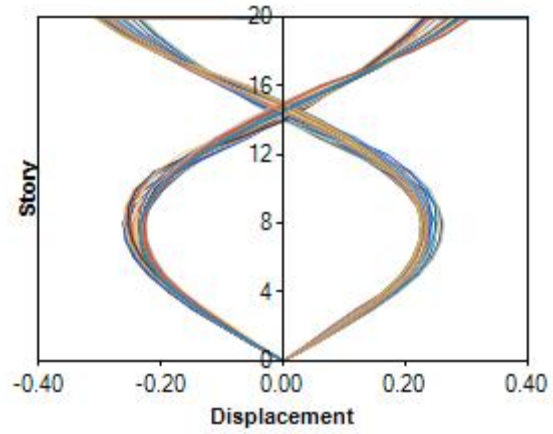
(f) Incremental Mode Shapes for LA26

Figure 29. Incremental Second Mode shapes of the HSAC20-5 Frame under LA21 to LA26
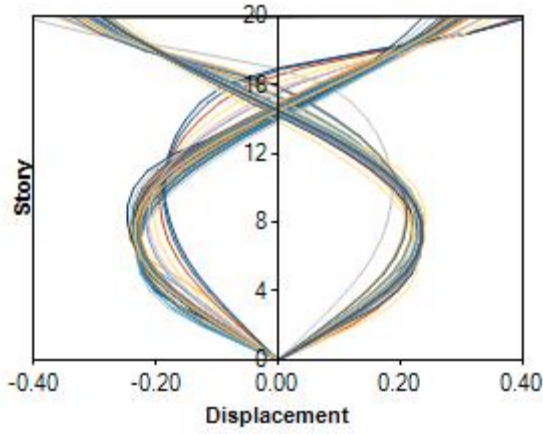
(a) Incremental Mode Shapes for LA27
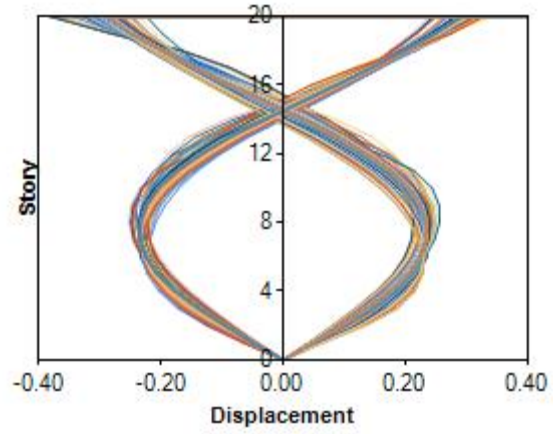
(b) Incremental Mode Shapes for LA28
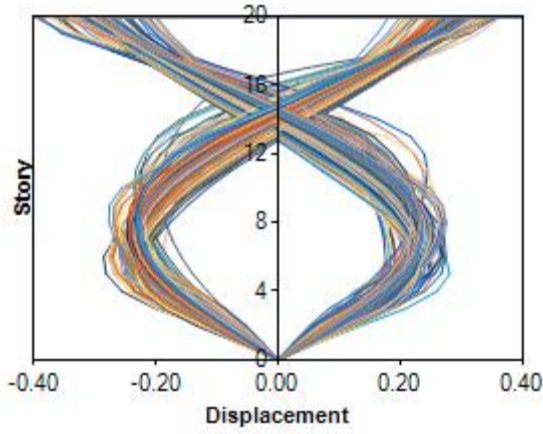
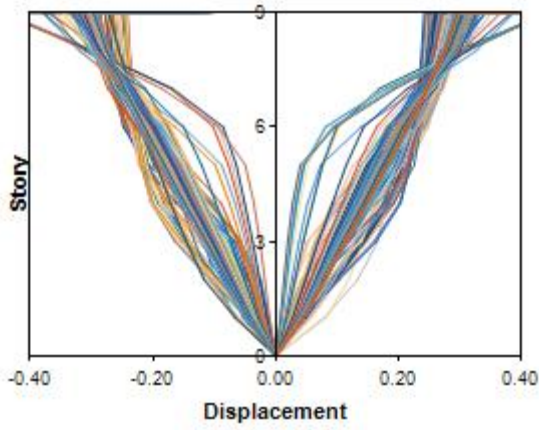(c) Incremental Mode Shapes for LA29
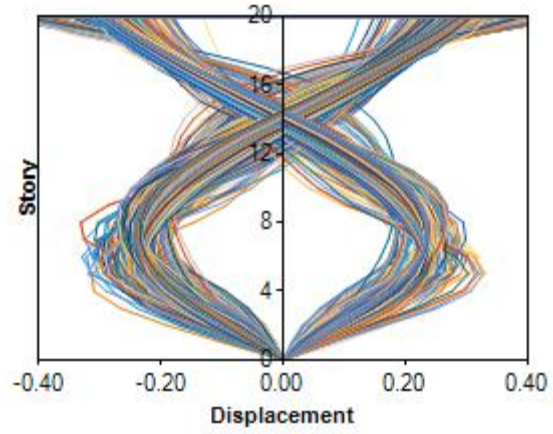
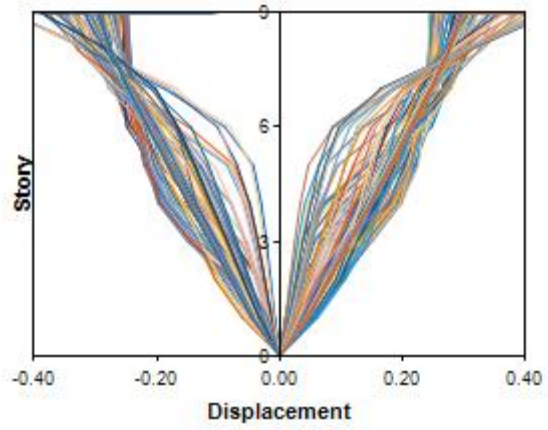(d) Incremental Mode Shapes for LA30
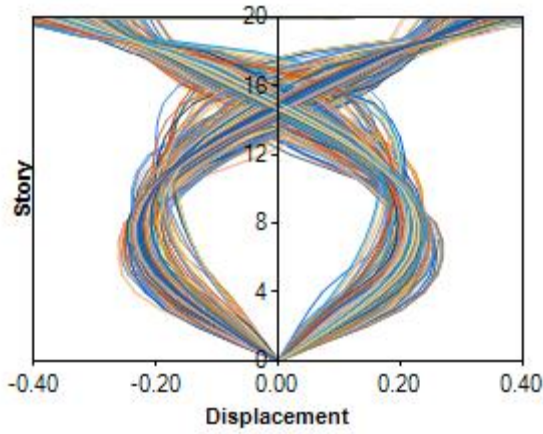
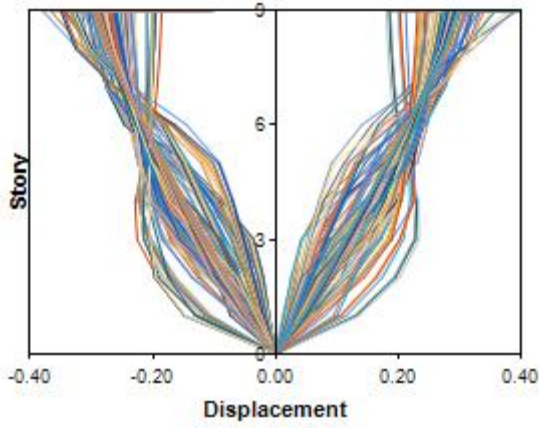(e) Incremental Mode Shapes for LA31
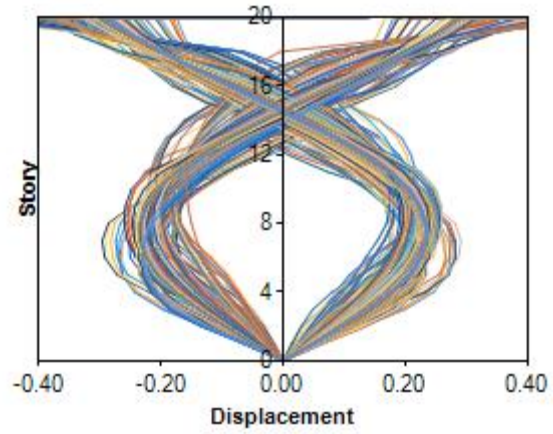
(f) Incremental Mode Shapes for LA32

Figure 30. Incremental Second Mode shapes of the HSAC20-5 Frame under LA27 to LA32
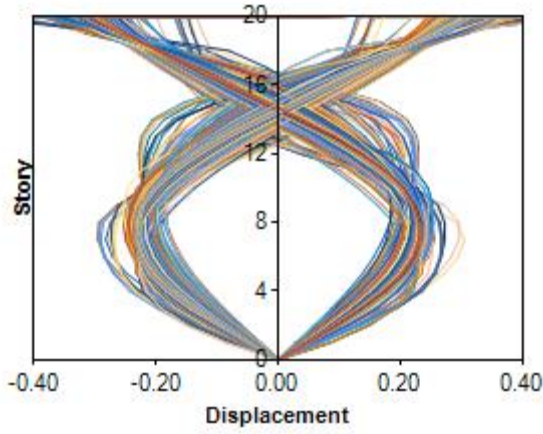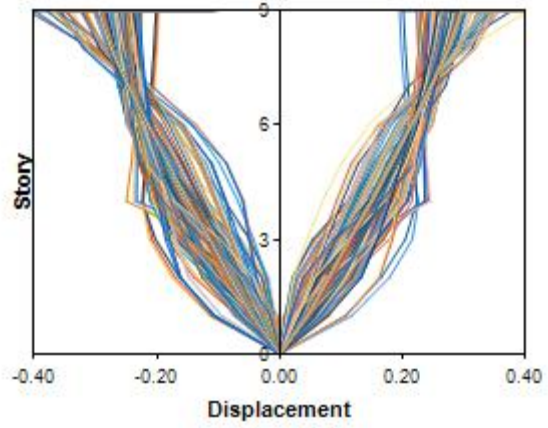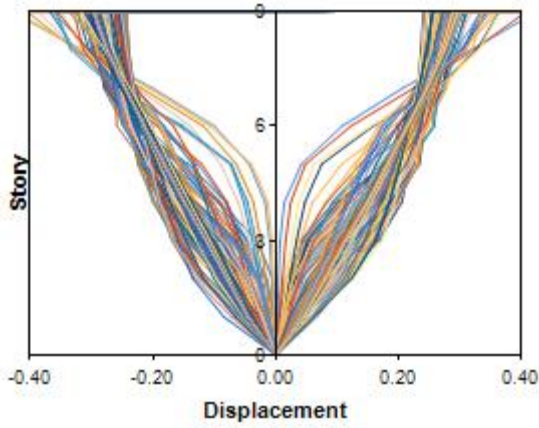
(a) Incremental Mode Shapes for LA33
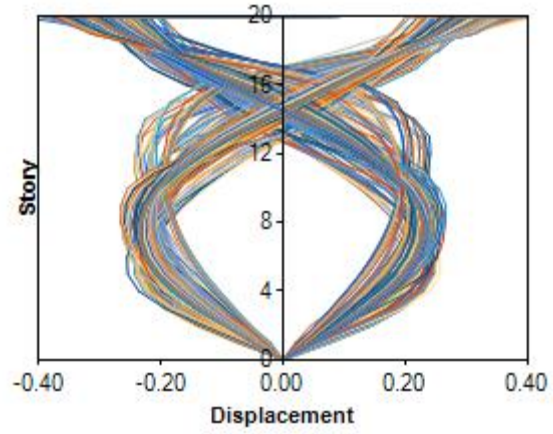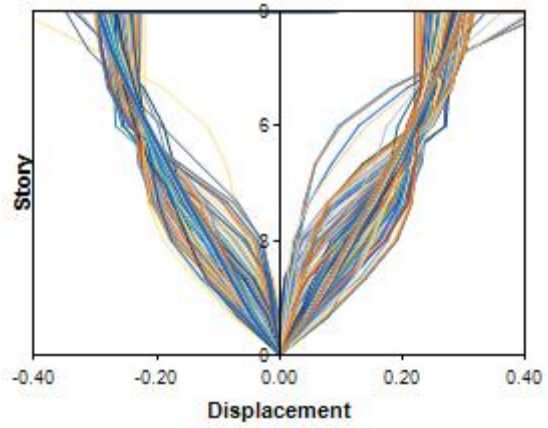
(b) Incremental Mode Shapes for LA34
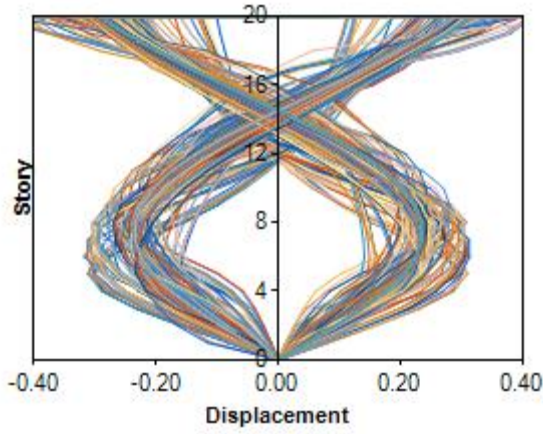
(c) Incremental Mode Shapes for LA35
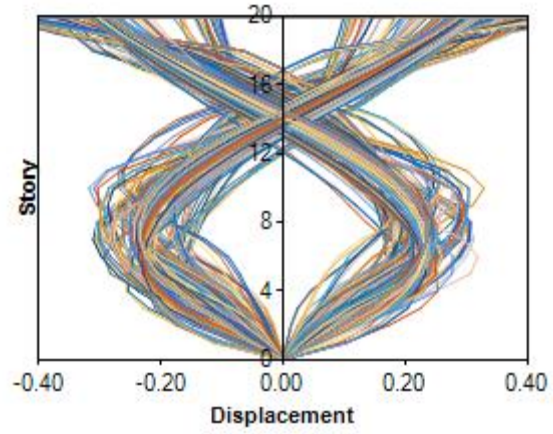
(d) Incremental Mode Shapes for LA36
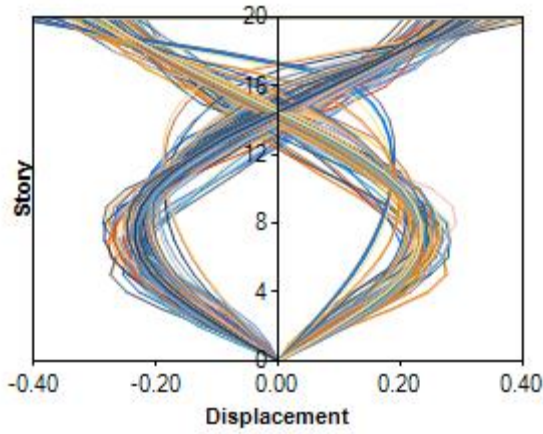
(e) Incremental Mode Shapes for LA37
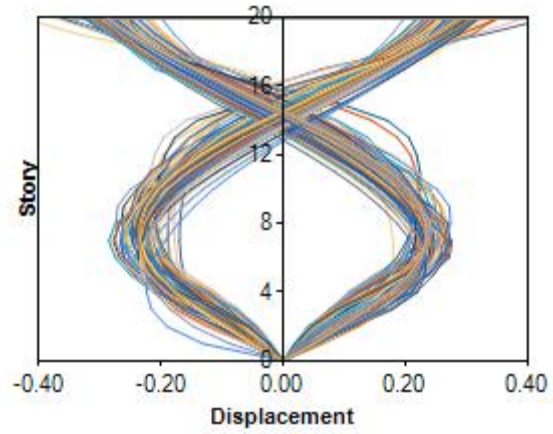
(f) Incremental Mode Shapes for LA38

Figure 31. Incremental Second Mode shapes of the HSAC20-5 Frame under LA33 to LA38
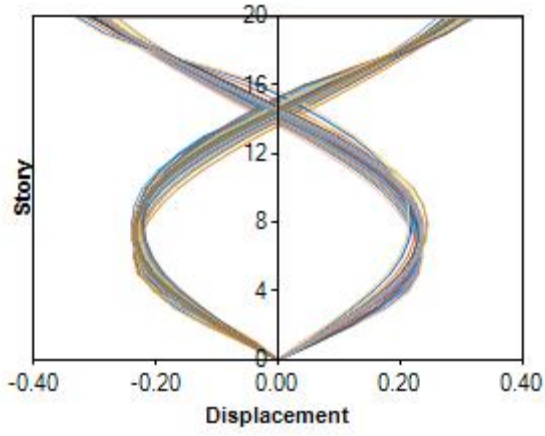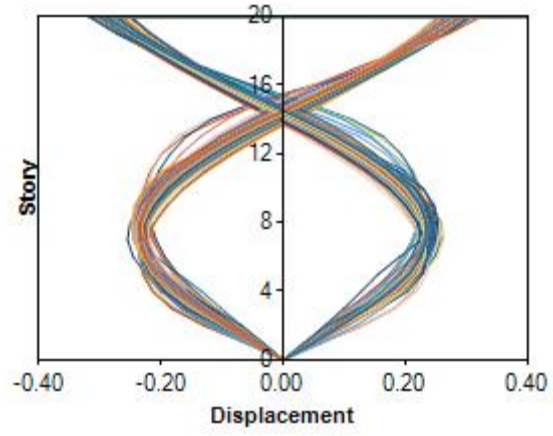
(a) Incremental Mode Shapes for LA39   (b) Incremental Mode Shapes for LA40

Figure 32. Incremental Second Mode shapes of the HSAC20-5 Frame under LA39 to LA40
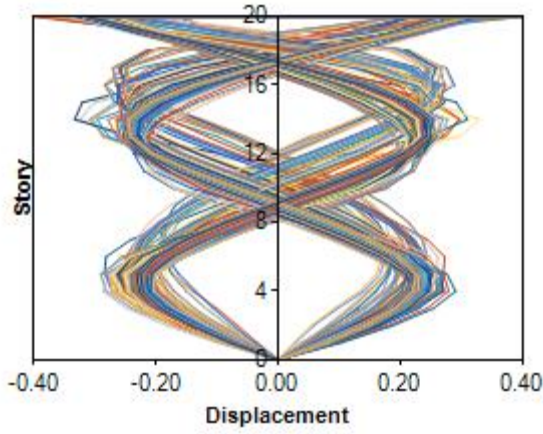
(a) Incremental Mode Shapes for LA21
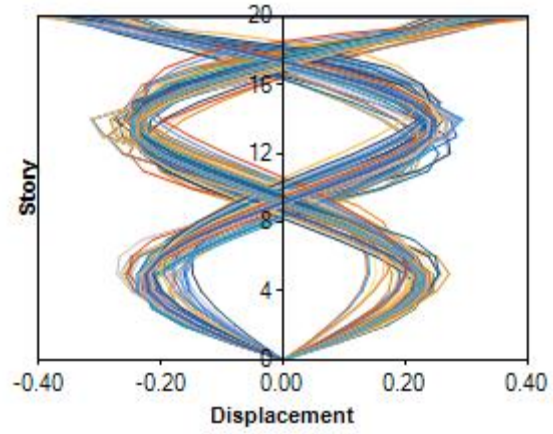
(b) Incremental Mode Shapes for LA22
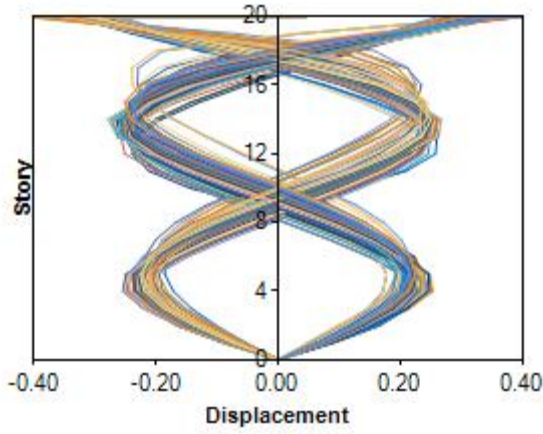
(c) Incremental Mode Shapes for LA23
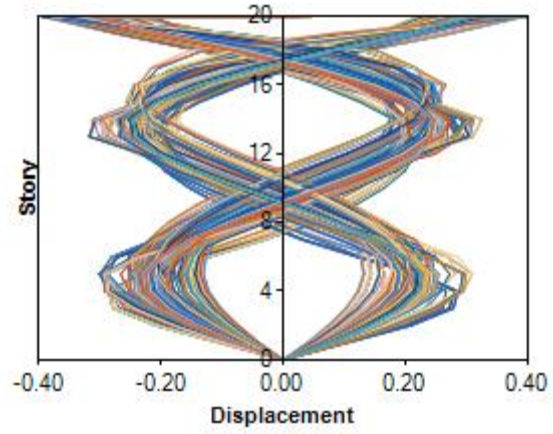
(d) Incremental Mode Shapes for LA24
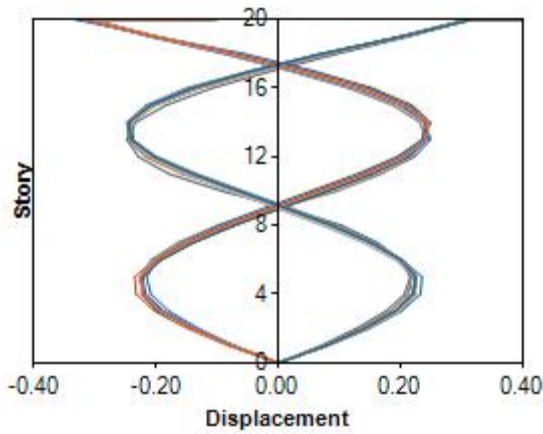
(e) Incremental Mode Shapes for LA25
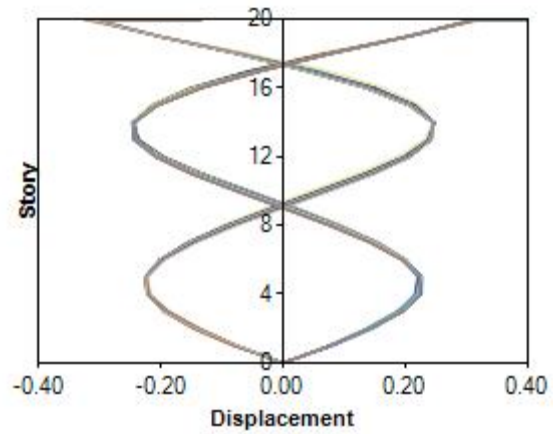
(f) Incremental Mode Shapes for LA26

Figure 33. Incremental Third Mode shapes of the HSAC20-4 Frame under LA21 to LA26
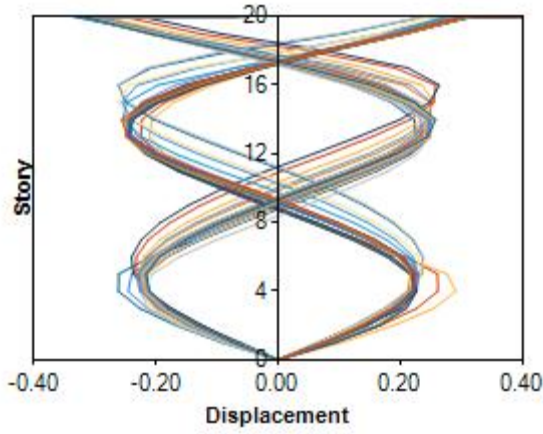
(a) Incremental Mode Shapes for LA27
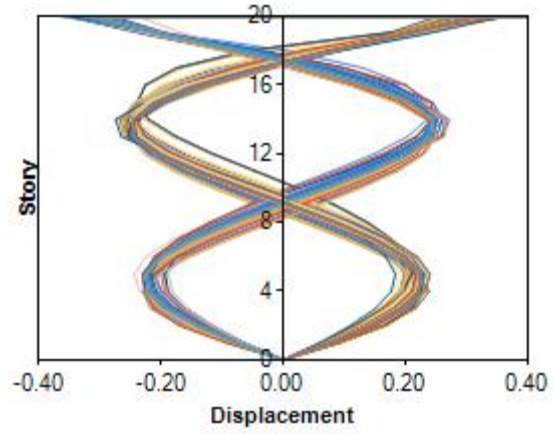
(b) Incremental Mode Shapes for LA28
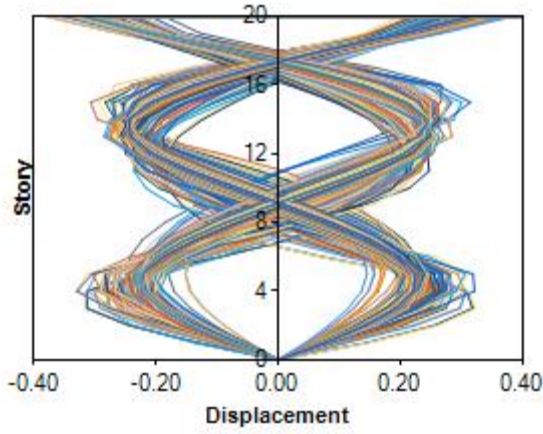
(c) Incremental Mode Shapes for LA29
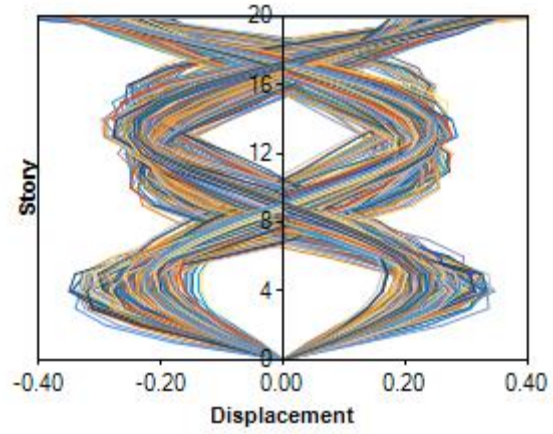
(d) Incremental Mode Shapes for LA30
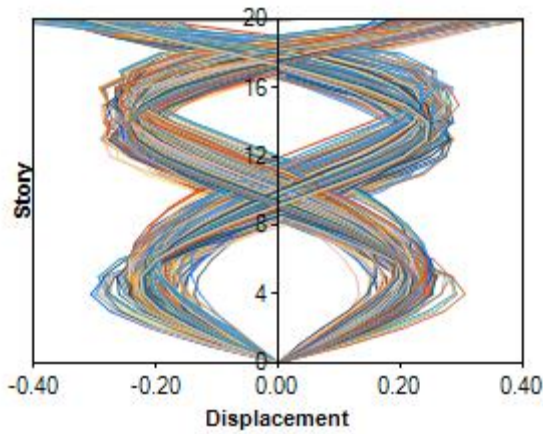
(e) Incremental Mode Shapes for LA31
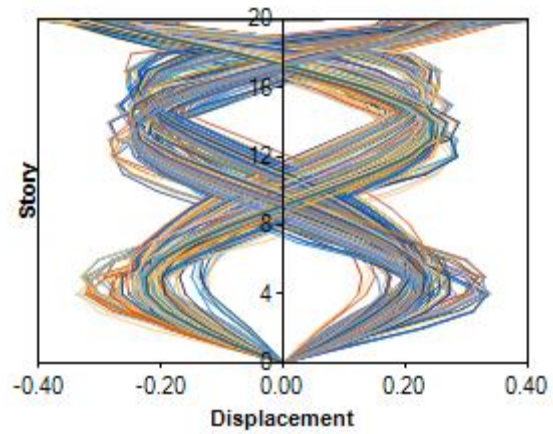
(f) Incremental Mode Shapes for LA32

Figure 34. Incremental Third Mode shapes of the HSAC20-4 Frame under LA27 to LA32
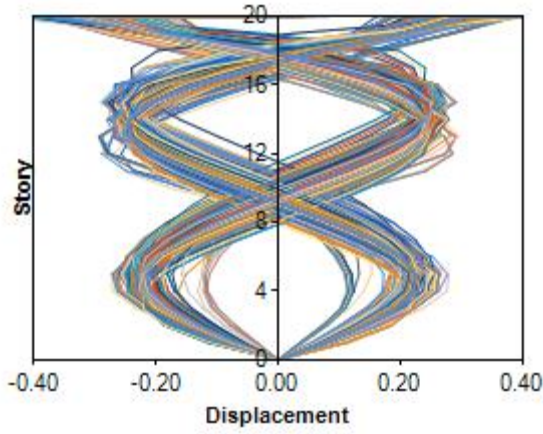
(a) Incremental Mode Shapes for LA33
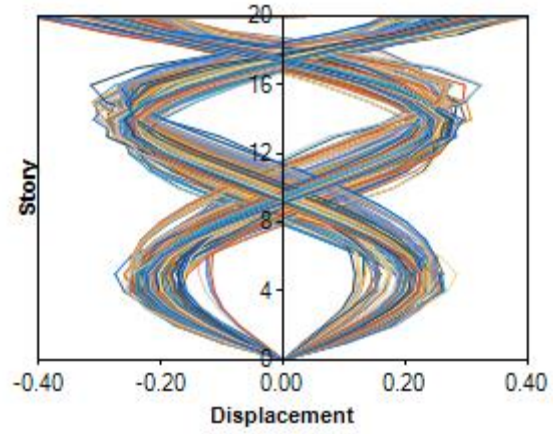
(b) Incremental Mode Shapes for LA34
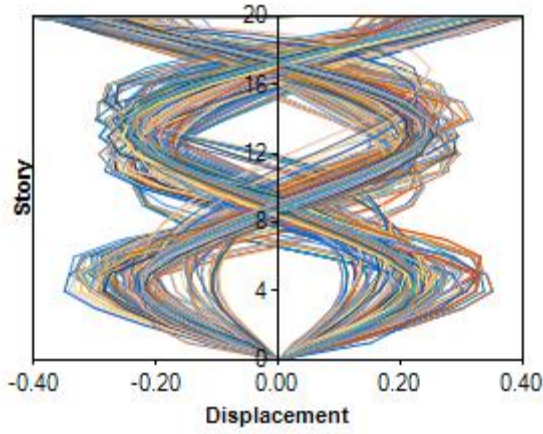
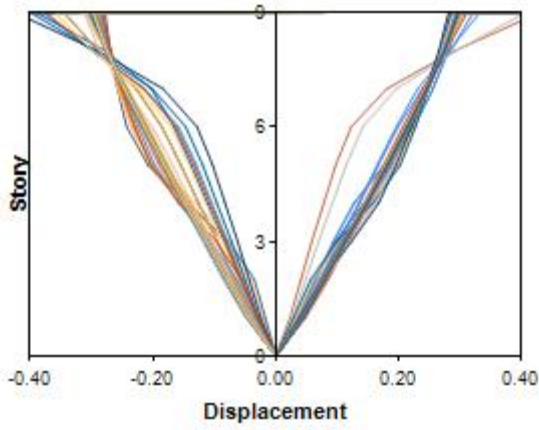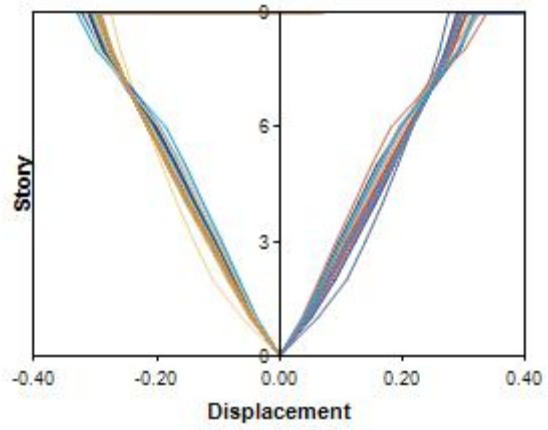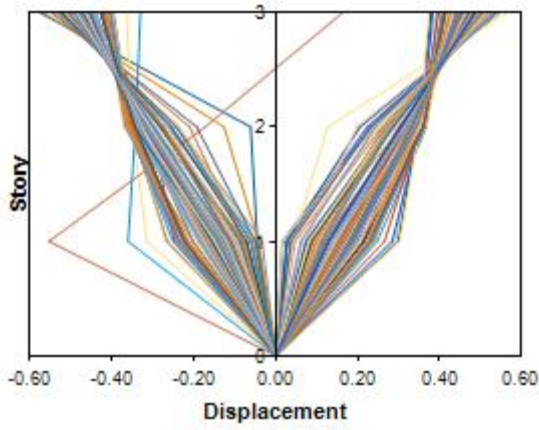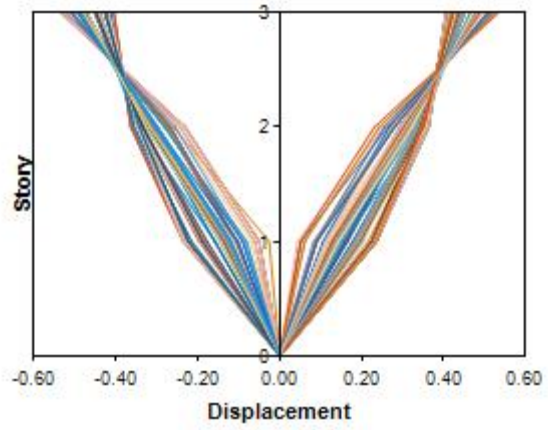(c) Incremental Mode Shapes for LA35
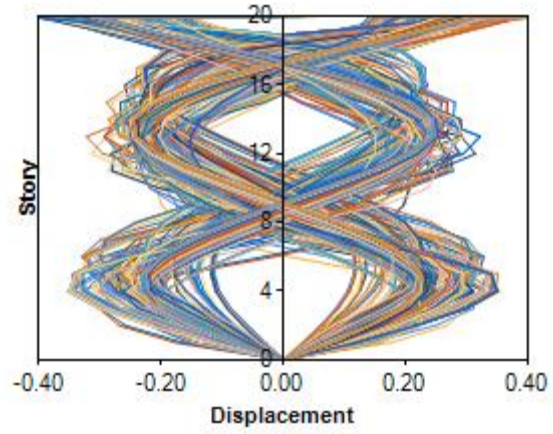
(d) Incremental Mode Shapes for LA36
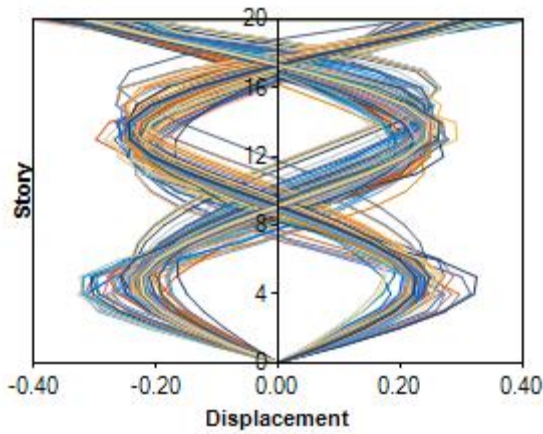
(e) Incremental Mode Shapes for LA37
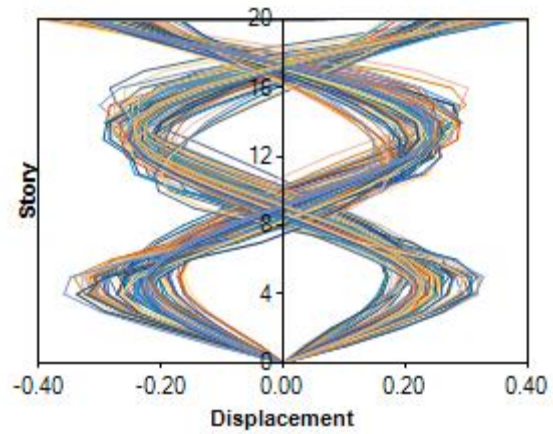
(f) Incremental Mode Shapes for LA38

Figure 35. Incremental Third Mode shapes of the HSAC20-4 Frame under LA33 to LA38
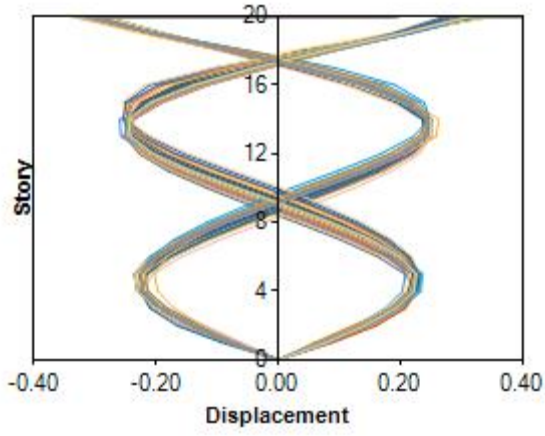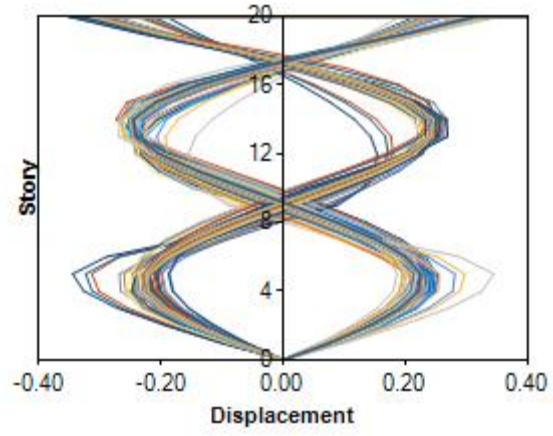
(a) Incremental Mode Shapes for LA39   (b) Incremental Mode Shapes for LA40

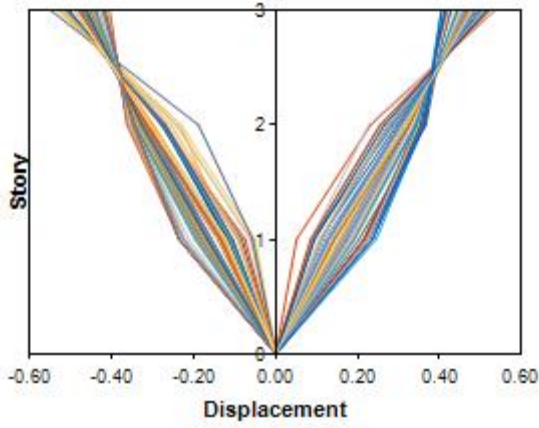Figure 36. Incremental Third Mode shapes of the HSAC20-4 Frame under LA39 to LA40
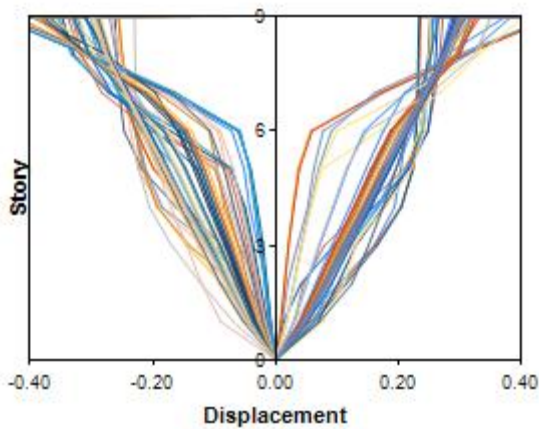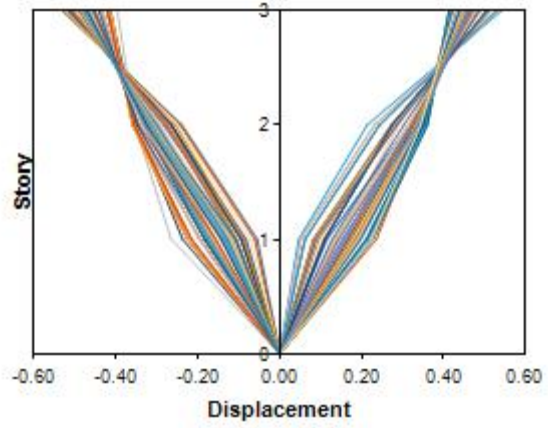
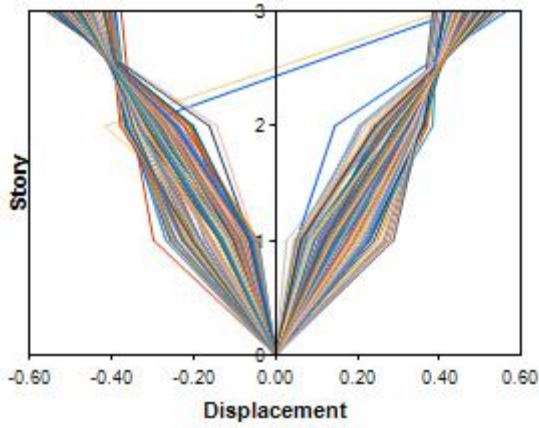(a) Incremental Mode Shapes for LA21
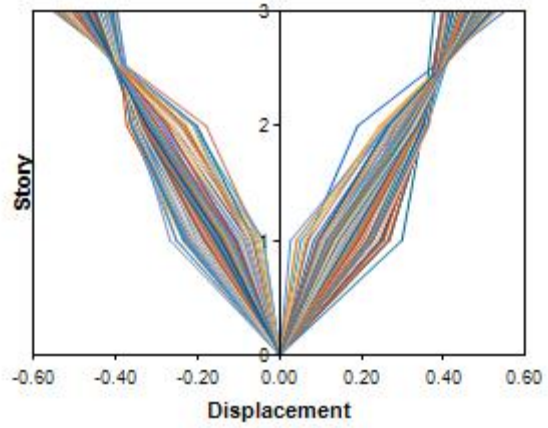
(b) Incremental Mode Shapes for LA22

(c) Incremental Mode Shapes for LA23
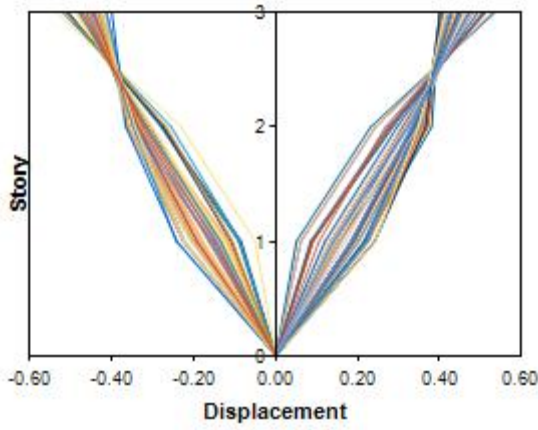
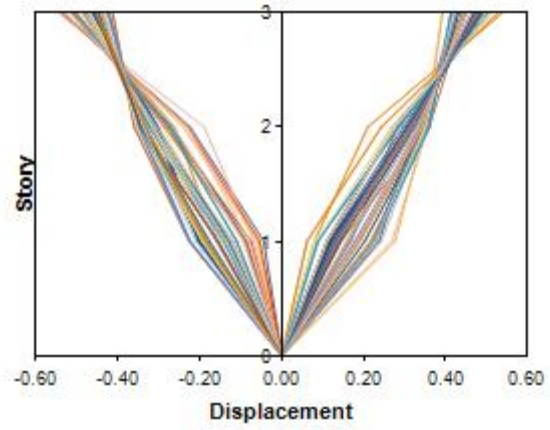(d) Incremental Mode Shapes for LA24

(e) Incremental Mode Shapes for LA25

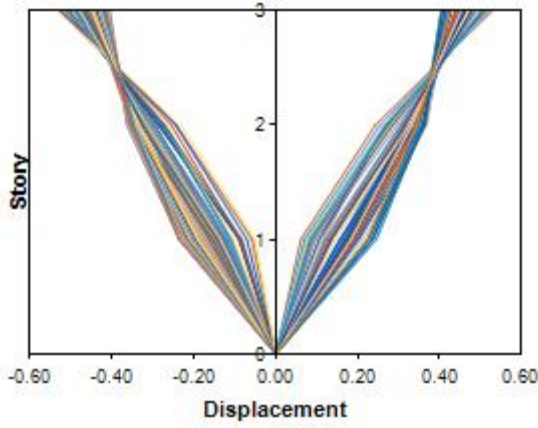(f) Incremental Mode Shapes for LA26

Figure 37. Incremental First Mode shapes of the SAC 9-Story Rigid Frame under LA21 to LA26

(a) Incremental Mode Shapes for LA27

(b) Incremental Mode Shapes for LA28

(c) Incremental Mode Shapes for LA29

(d) Incremental Mode Shapes for LA30

(e) Incremental Mode Shapes for LA31

(f) Incremental Mode Shapes for LA32

Figure 38. Incremental First Mode shapes of the SAC 9-Story Rigid Frame under LA27 to LA32

271

(a) Incremental Mode Shapes for LA33

(b) Incremental Mode Shapes for LA34

(c) Incremental Mode Shapes for LA35

(d) Incremental Mode Shapes for LA36

(e) Incremental Mode Shapes for LA37

(f) Incremental Mode Shapes for LA38

Figure 39. Incremental First Mode shapes of the SAC 9-Story Rigid Frame under LA33 to LA38

(a) Incremental Mode Shapes for LA39   (b) Incremental Mode Shapes for LA40

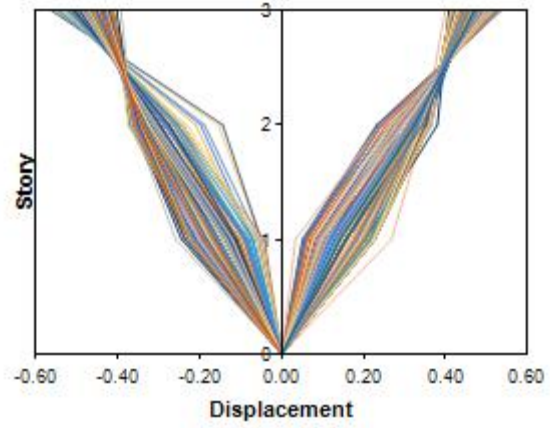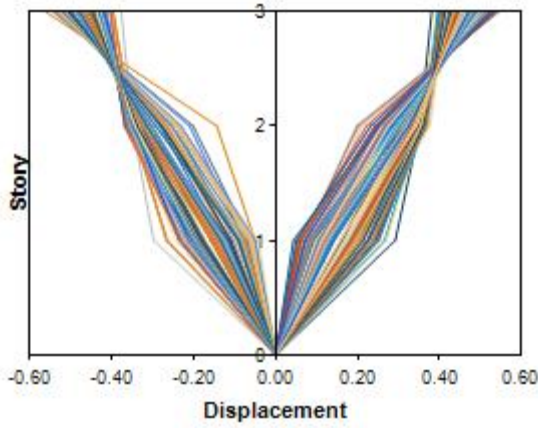Figure 40. Incremental First Mode shapes of the SAC 9-Story Rigid Frame under LA39 to LA40
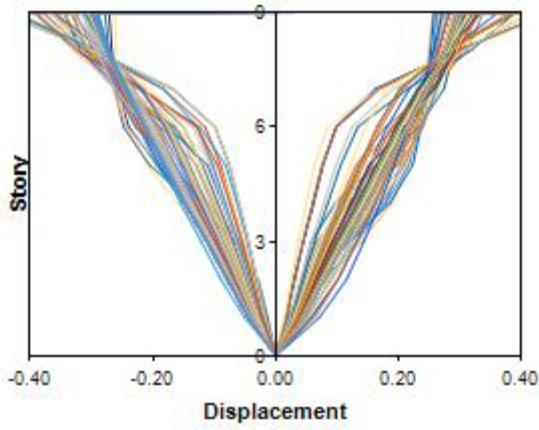
(a) Incremental Mode Shapes for LA21
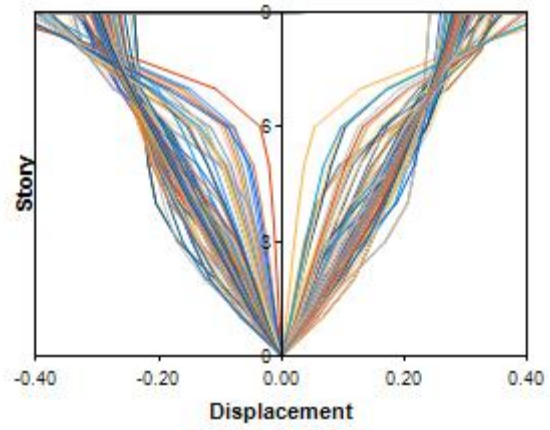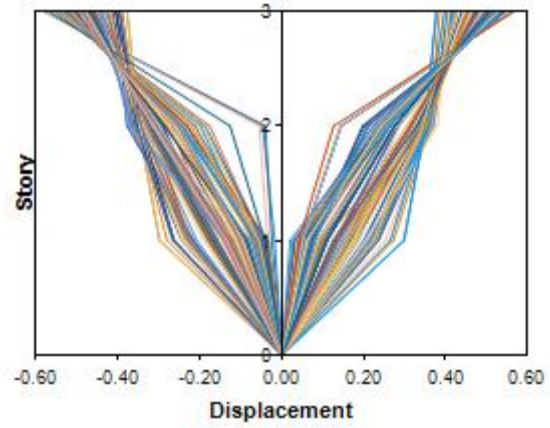
(b) Incremental Mode Shapes for LA22

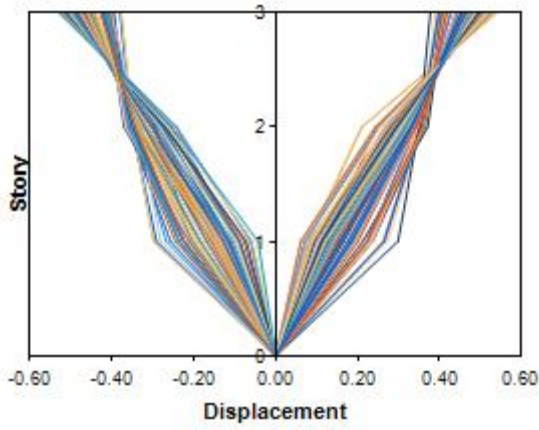(c) Incremental Mode Shapes for LA23

(d) Incremental Mode Shapes for LA24

(e) Incremental Mode Shapes for LA25

(f) Incremental Mode Shapes for LA26

Figure 41. Incremental First Mode shapes of the HSAC9-4 Frame under LA21 to LA26

(a) Incremental Mode Shapes for LA27

(b) Incremental Mode Shapes for LA28

(c) Incremental Mode Shapes for LA29

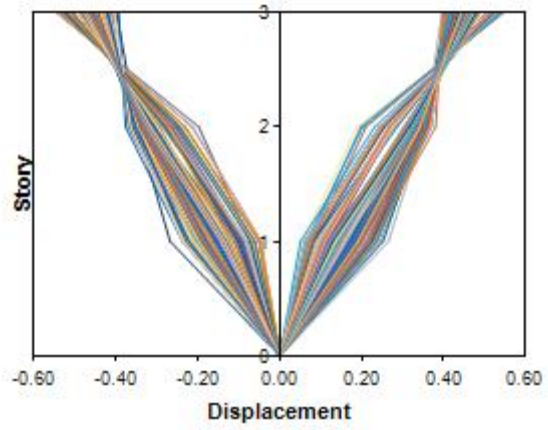(d) Incremental Mode Shapes for LA30

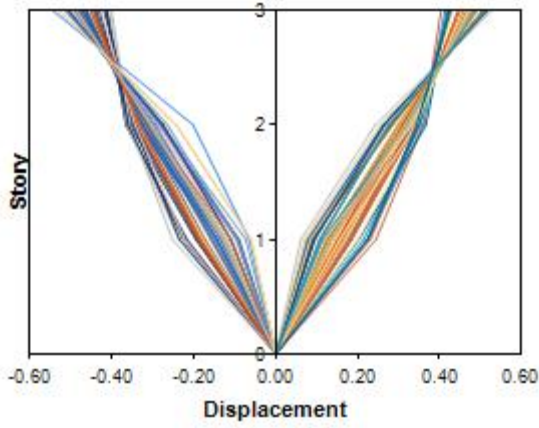(e) Incremental Mode Shapes for LA31

(f) Incremental Mode Shapes for LA32

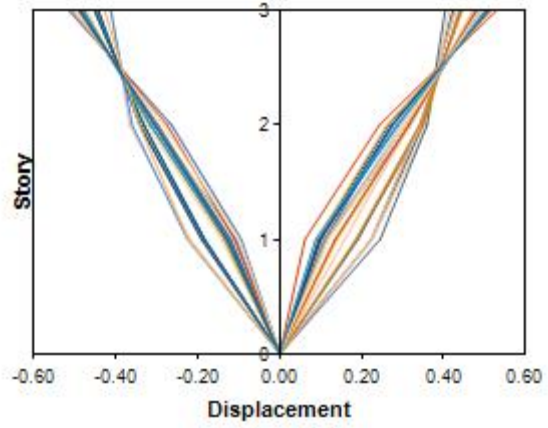Figure 42. Incremental First Mode shapes of the HSAC9-4 Frame under LA27 to LA32
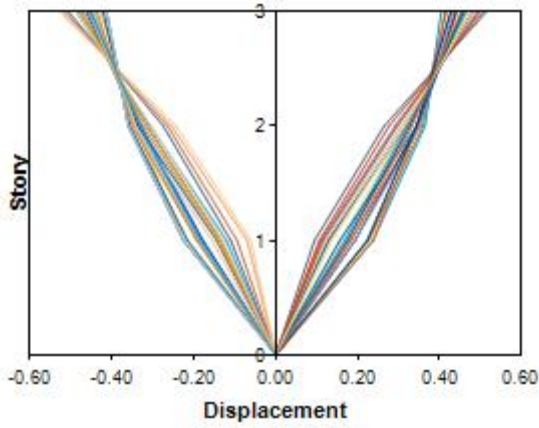
(a) Incremental Mode Shapes for LA33
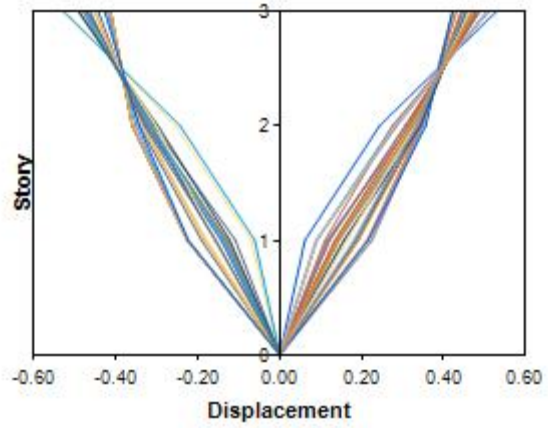
(b) Incremental Mode Shapes for LA34

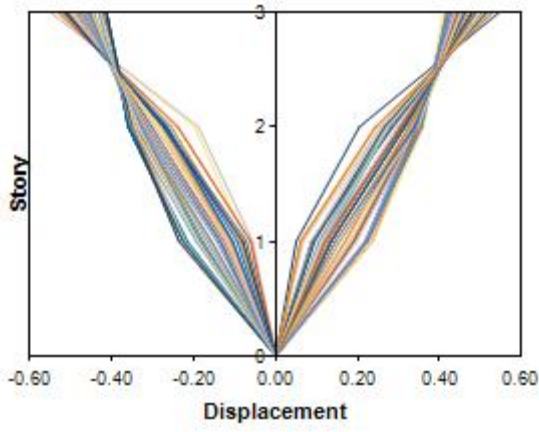(c) Incremental Mode Shapes for LA35

(d) Incremental Mode Shapes for LA36

(e) Incremental Mode Shapes for LA37

(f) Incremental Mode Shapes for LA38

Figure 43. Incremental First Mode shapes of the HSAC9-4 Frame under LA33 to LA38

(a) Incremental Mode Shapes for LA39   (b) Incremental Mode Shapes for LA40

Figure 44. Incremental First Mode shapes of the SAC HSAC9-4 Frame under LA39 to LA40

(a) Incremental Mode Shapes for LA21

(b) Incremental Mode Shapes for LA22

(c) Incremental Mode Shapes for LA23

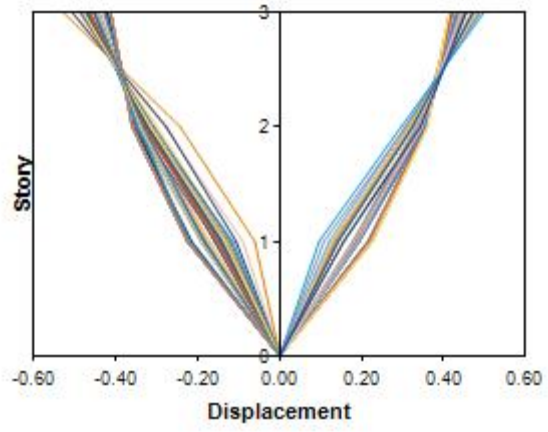(d) Incremental Mode Shapes for LA24

(e) Incremental Mode Shapes for LA25

(f) Incremental Mode Shapes for LA26

Figure 45. Incremental First Mode shapes of the HSAC9-5 Frame under LA21 to LA26

278

(a) Incremental Mode Shapes for LA27

(b) Incremental Mode Shapes for LA28

(c) Incremental Mode Shapes for LA29

(d) Incremental Mode Shapes for LA30

(e) Incremental Mode Shapes for LA31

(f) Incremental Mode Shapes for LA32

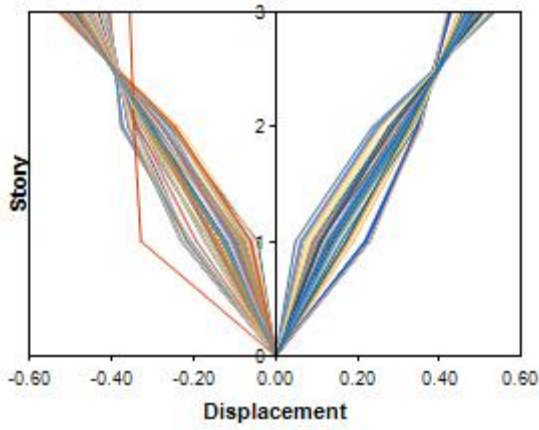Figure 46. Incremental First Mode shapes of the HSAC9-5 Frame under LA27 to LA32
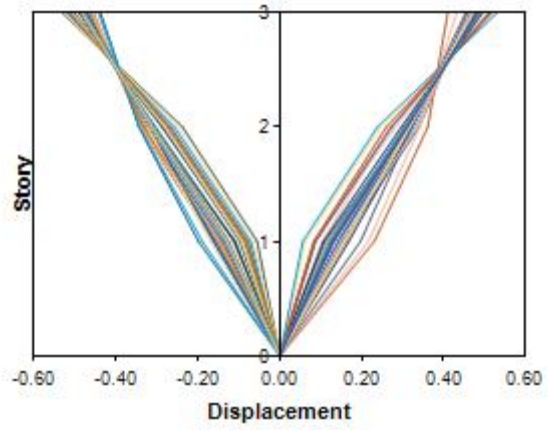
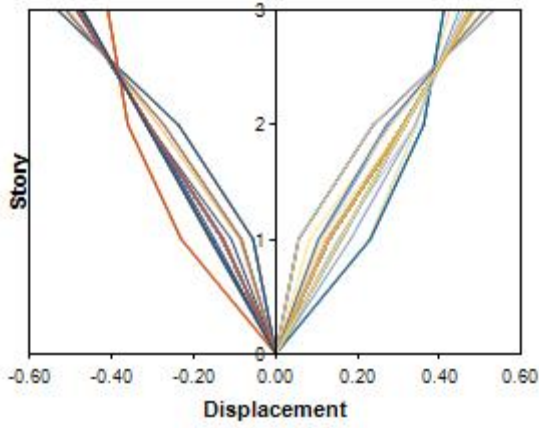(a) Incremental Mode Shapes for LA33

(b) Incremental Mode Shapes for LA34

(c) Incremental Mode Shapes for LA35

(d) Incremental Mode Shapes for LA36

(e) Incremental Mode Shapes for LA37

(f) Incremental Mode Shapes for LA38

Figure 47. Incremental First Mode shapes of the HSAC9-5 Frame under LA33 to LA38

(a) Incremental Mode Shapes for LA39   (b) Incremental Mode Shapes for LA40

Figure 48. Incremental First Mode shapes of the SAC HSAC9-5 Frame under LA39 to LA40
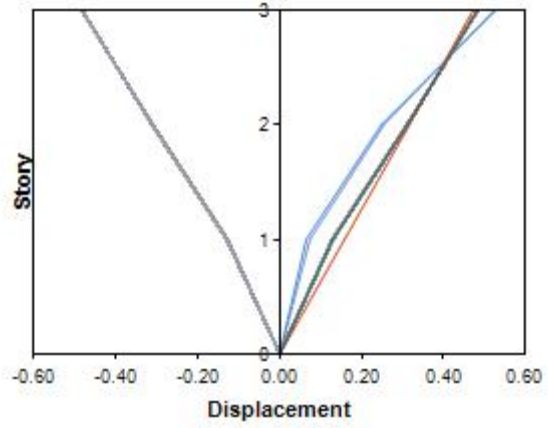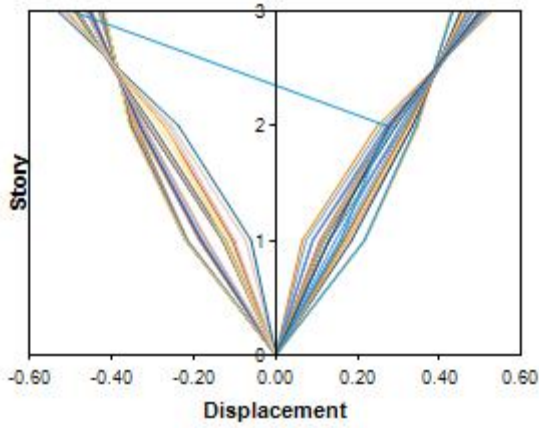
(a) Incremental Mode Shapes for LA21
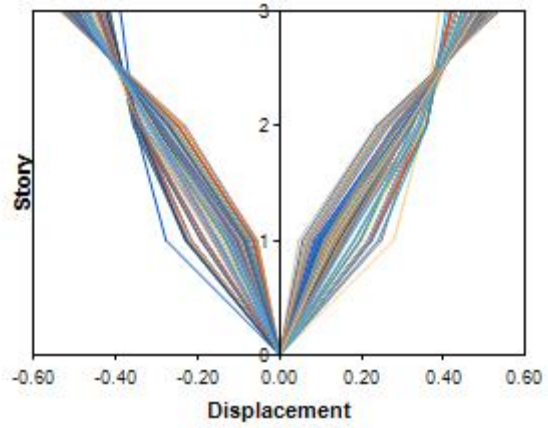
(b) Incremental Mode Shapes for LA22

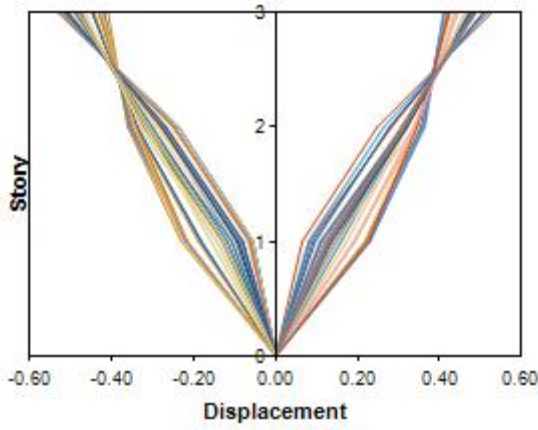(c) Incremental Mode Shapes for LA23

(d) Incremental Mode Shapes for LA24

(e) Incremental Mode Shapes for LA25

(f) Incremental Mode Shapes for LA26

Figure 49. Incremental First Mode shapes of the SAC 3-Story Rigid Frame under LA21 to LA26

(a) Incremental Mode Shapes for LA27

(b) Incremental Mode Shapes for LA28

(c) Incremental Mode Shapes for LA29

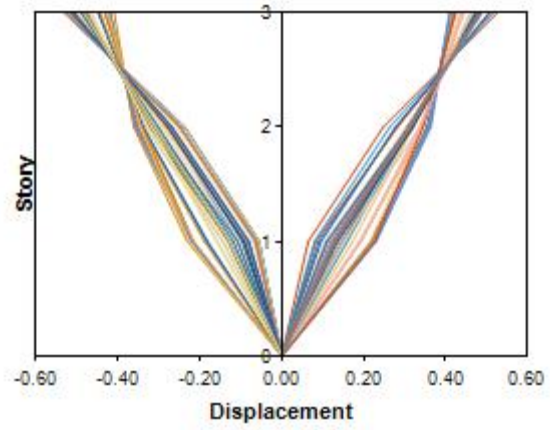(d) Incremental Mode Shapes for LA30

(e) Incremental Mode Shapes for LA31

(f) Incremental Mode Shapes for LA32

Figure 50. Incremental First Mode shapes of the SAC 3-Story Rigid Frame under LA27 to LA32

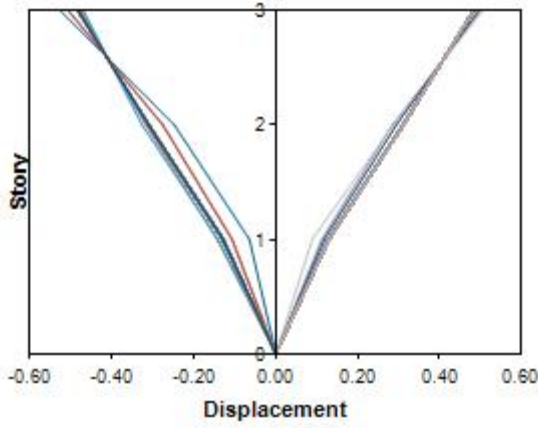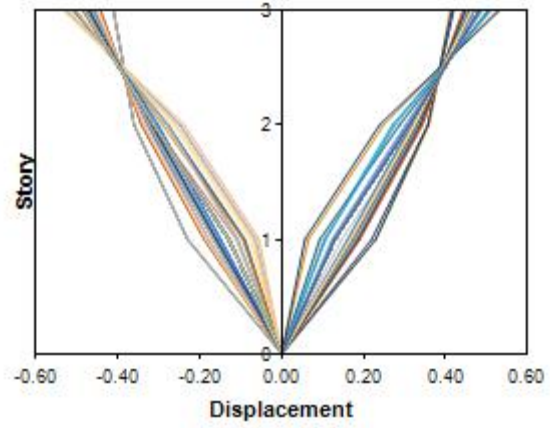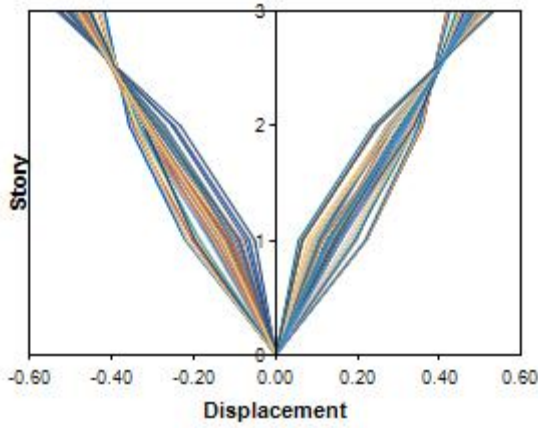(a) Incremental Mode Shapes for LA33

(b) Incremental Mode Shapes for LA34

(c) Incremental Mode Shapes for LA35

(d) Incremental Mode Shapes for LA36

(e) Incremental Mode Shapes for LA37

(f) Incremental Mode Shapes for LA38

Figure 51. Incremental First Mode shapes of the SAC 3-Story Rigid Frame under LA33 to LA38

(a) Incremental Mode Shapes for LA39   (b) Incremental Mode Shapes for LA40

Figure 52. Incremental First Mode shapes of the SAC 3-Story Rigid Frame under LA39 to LA40

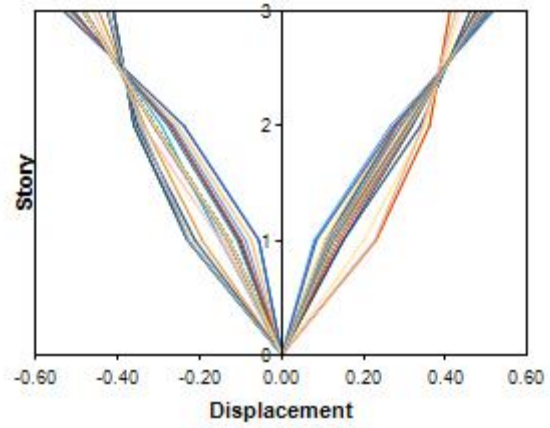(a) Incremental Mode Shapes for LA21

(b) Incremental Mode Shapes for LA22

(c) Incremental Mode Shapes for LA23

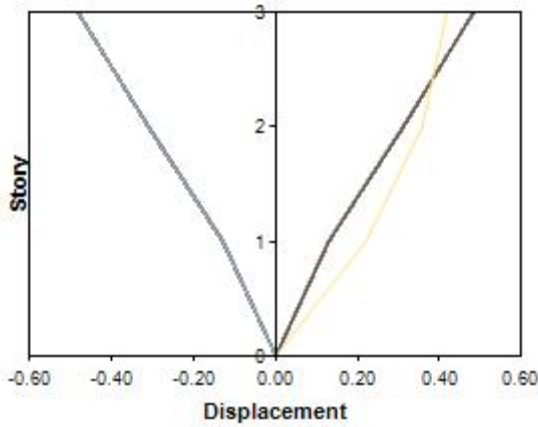(d) Incremental Mode Shapes for LA24

(e) Incremental Mode Shapes for LA25

(f) Incremental Mode Shapes for LA26

Figure 53. Incremental First Mode shapes of the HSAC3-4 Frame under LA21 to LA26

(a) Incremental Mode Shapes for LA27

(b) Incremental Mode Shapes for LA28

(c) Incremental Mode Shapes for LA29

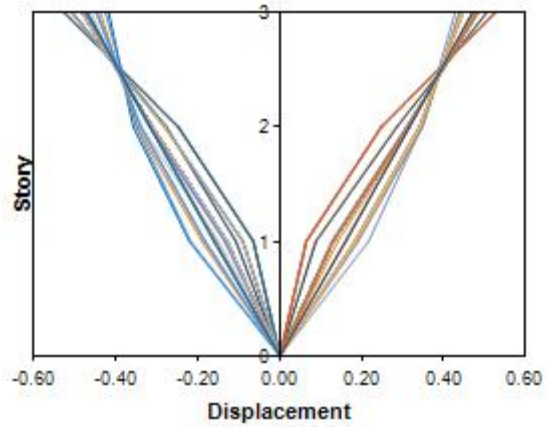(d) Incremental Mode Shapes for LA30

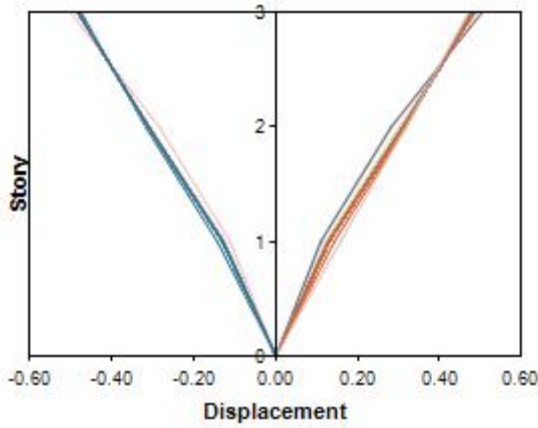(e) Incremental Mode Shapes for LA31

(f) Incremental Mode Shapes for LA32

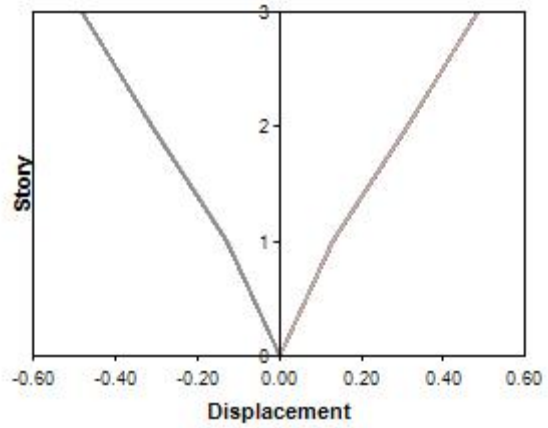Figure 54. Incremental First Mode shapes of the HSAC3-4 Frame under LA27 to LA32

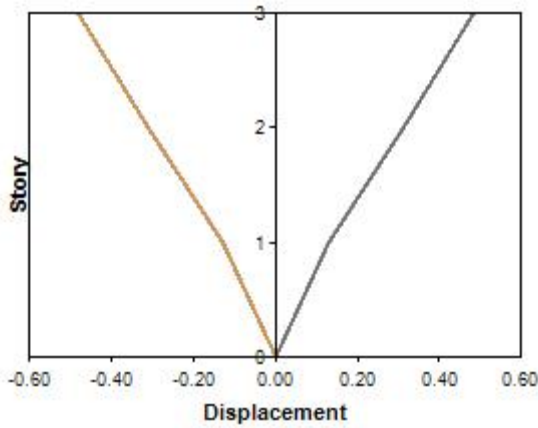(a) Incremental Mode Shapes for LA33
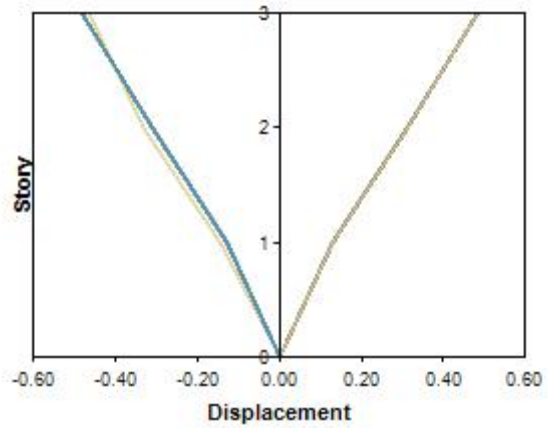
(b) Incremental Mode Shapes for LA34

(c) Incremental Mode Shapes for LA35
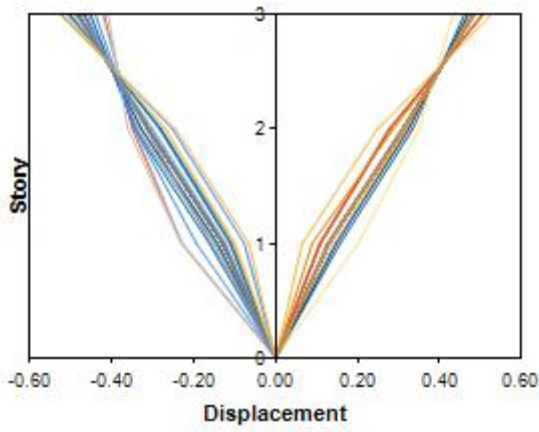
(d) Incremental Mode Shapes for LA36
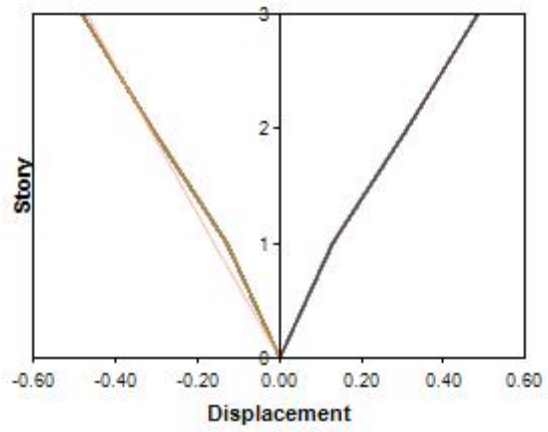
(e) Incremental Mode Shapes for LA37

(f) Incremental Mode Shapes for LA38

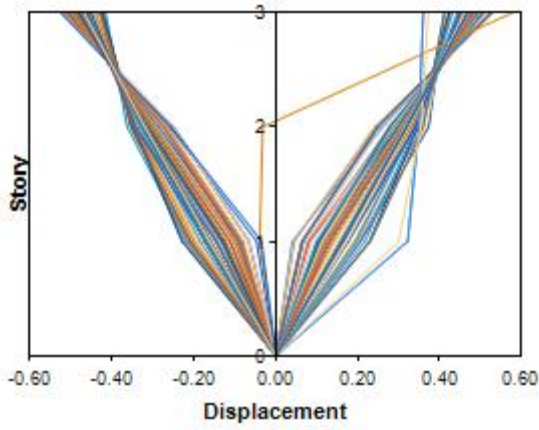Figure 55. Incremental First Mode shapes of the HSAC3-4 Frame under LA33 to LA38

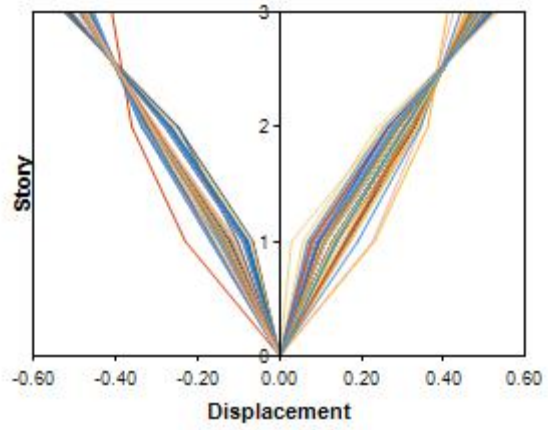(a) Incremental Mode Shapes for LA39   (b) Incremental Mode Shapes for LA40

Figure 56. Incremental First Mode shapes of the SAC HSAC3-4 Frame under LA39 to LA40

(a) Incremental Mode Shapes for LA21

(b) Incremental Mode Shapes for LA22

(c) Incremental Mode Shapes for LA23

(d) Incremental Mode Shapes for LA24

(e) Incremental Mode Shapes for LA25

(f) Incremental Mode Shapes for LA26

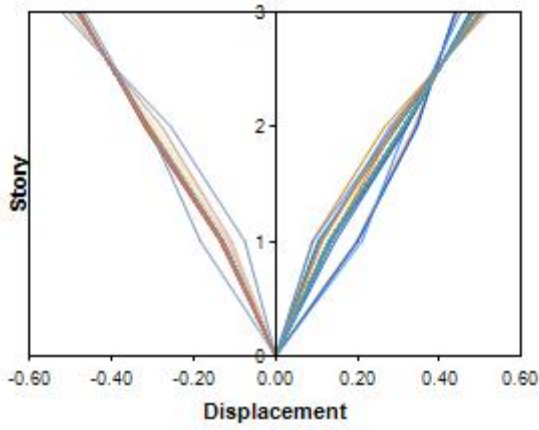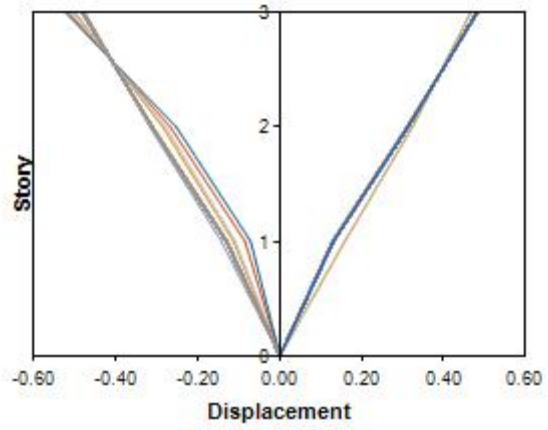Figure 57. Incremental First Mode shapes of the HSAC3-5 Frame under LA21 to LA26

(a) Incremental Mode Shapes for LA27

(b) Incremental Mode Shapes for LA28

(c) Incremental Mode Shapes for LA29

(d) Incremental Mode Shapes for LA30

(e) Incremental Mode Shapes for LA31

(f) Incremental Mode Shapes for LA32

Figure 58. Incremental First Mode shapes of the HSAC3-5 Frame under LA27 to LA32
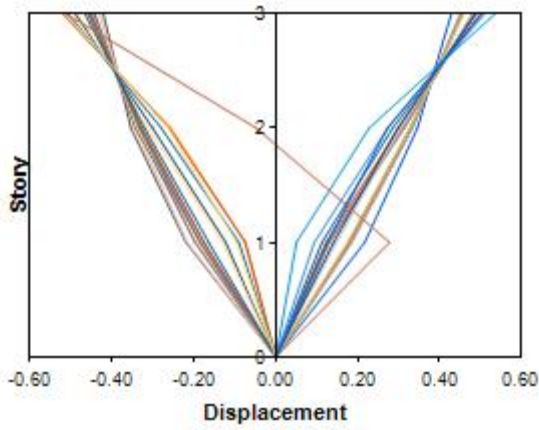
291

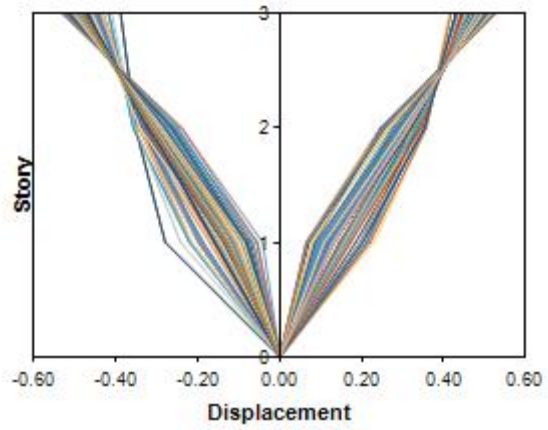(a) Incremental Mode Shapes for LA33

(b) Incremental Mode Shapes for LA34

(c) Incremental Mode Shapes for LA35

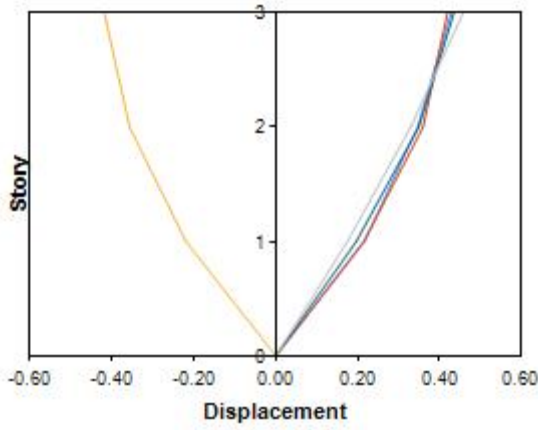(d) Incremental Mode Shapes for LA36
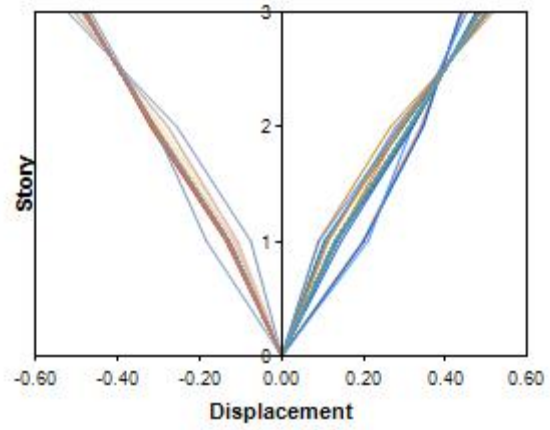
(e) Incremental Mode Shapes for LA37
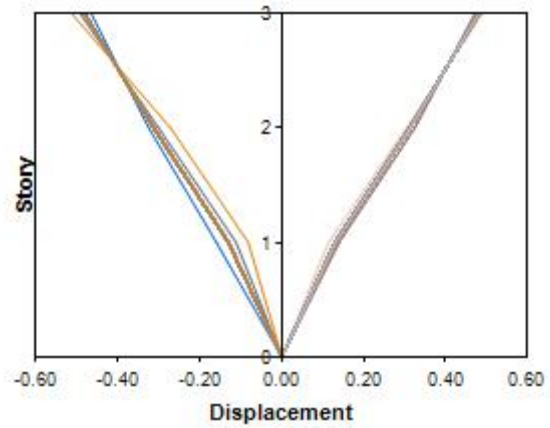
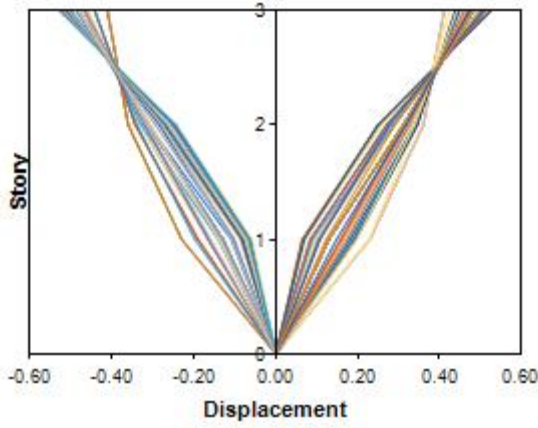(f) Incremental Mode Shapes for LA38

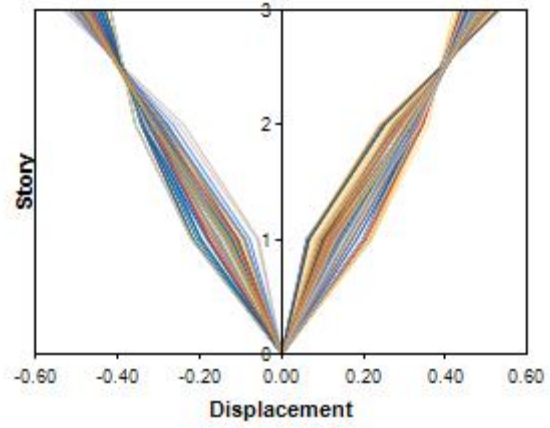Figure 59. Incremental First Mode shapes of the HSAC3-5 Frame under LA33 to LA38
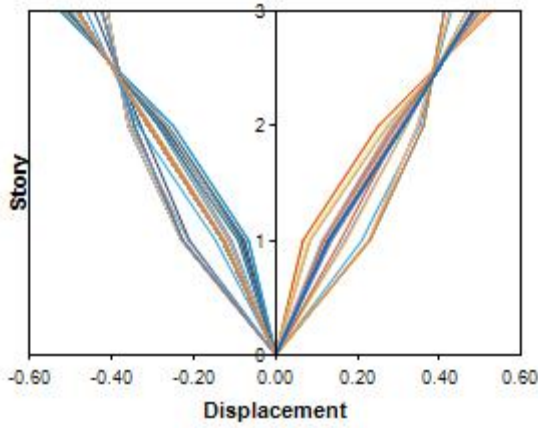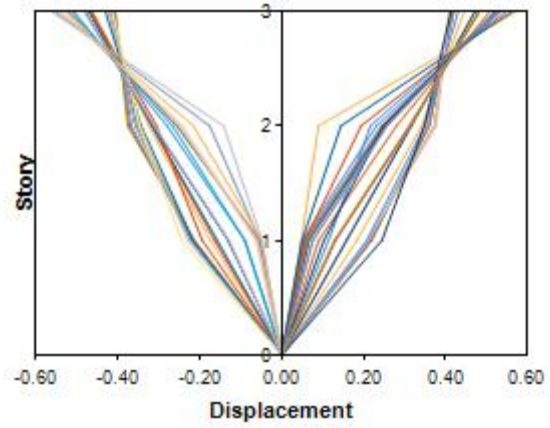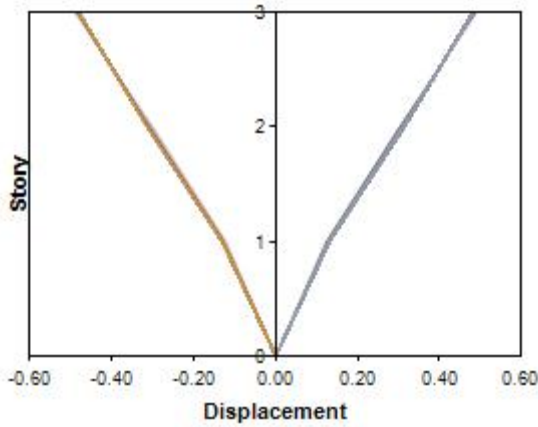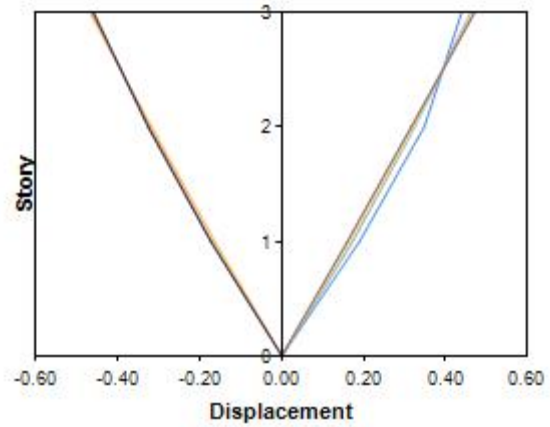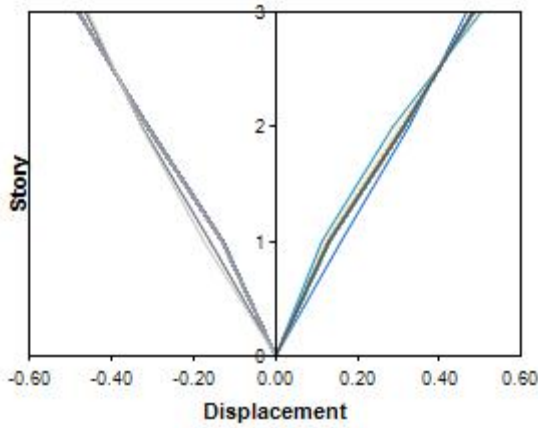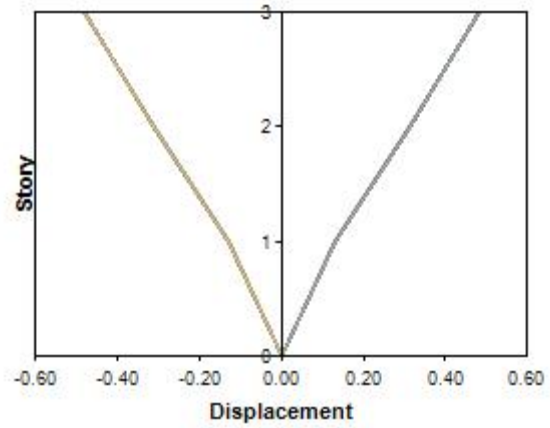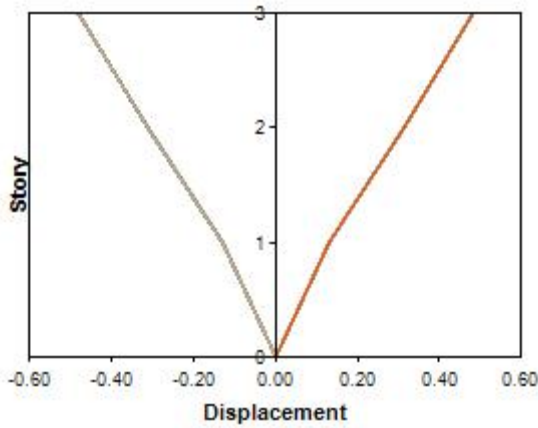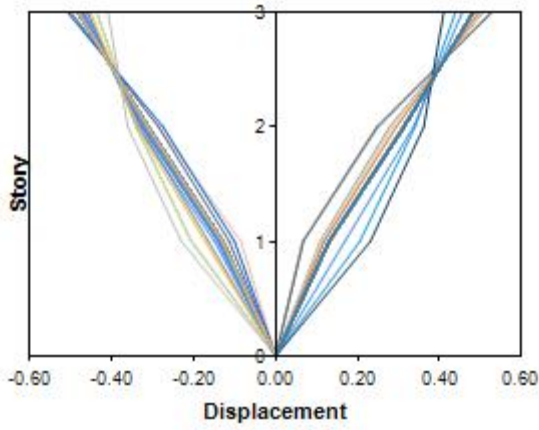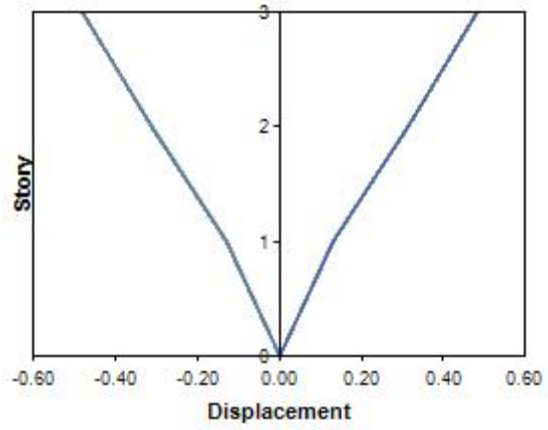
(a) Incremental Mode Shapes for LA39   (b) Incremental Mode Shapes for LA40

Figure 60. Incremental First Mode shapes of the SAC HSAC3-5 Frame under LA39 to LA40

REFERENCES

A. Abolmaali, A.R. Kukreti and H. Razavi, "Hysteresis behavior of semi-rigid double web angle steel connections", Journal of Constructional Steel Research 59 (2003), pp. 1057–1082

Abolmaali, A., Kukreti, A.R., and Razavi, S. H., 2003, "Hysteresis Behavior of Semi-Rigid Double Web Angle Steel Connections," The Journal of Constructional Steel Research, Vol. 59, pp. 1057-1082.

Abolmaali, A., Kukreti, A.R., Motahari, A., and Ghassemieh, M., 2009, "Energy Dissipation Characteristics of Semi-Rigid Connection," The Journal of Constructional Steel Research, Vol. 65, pp. 19-27.

Abolmaali, A., Matthys, J.H., Farooqi, M., and Choi, Y., 2005, "Development of Moment-Rotation Model Equations for Flush End-Plate Connections," The Journal of Constructional Steel Research, Vol. 61, pp. 1595-1612.

Abolmaali, A., Razavi, M., and Radulova, D. ,2012, "On the Concept of Earthquake Resistant Hybrid Steel Frames," The Journal of Constructional Steel Research, Vol. 68, pp. 34-42

Ackroyd, M.H., and Gerstle, KH., 1982, "Behavior of Type 2 Steel Frames," Journal of the Structural Division, ASCE, Vol. 108, No. ST7, pp. 1541-1558.

Ahmed A, Kishi N, Matsuoka K, Komuro M., 2001, "Nonlinear Analysis on Prying of Top-and Seat-Angle connections", Journal of Applied Mechanics, 4:227-36.

Applied Technology Council. 1996b. ATC-40, Seismic Evaluation and Retrofit of Concrete Buildings. Redwood City, CA.

Astaneh, A., Nader, M. N., and Malik, L.,1989. "Cyclic Behavior of Double Angle Connections," Journal of Structural Engineering, ASCE, Vol. 115, No. 5, pp. 1101-1118.

Astaneh-Asl, A., 1995, "Seismic Design of Bolted Steel Moment-Resisting Frames," Steel Tips, Structural Steel Education Council, Moraga, CA, 82 pp.

Astaneh-Asl, A., Nader, M.N., and Harriott, J.D., 1991, "Seismic Behavior and Design Considerations in Semi-Rigid Frames," Proceedings of the 1991 National Steel Construction Conference, AISC.

Bjorhovde, R., Colson, A., and Brozzetti, J., 1990, "Classification System for Beam-to-Column Connections," Journal of Structural Engineering, ASCE, Vol. 116, No. 11.

BSSC. 1997b. NEHRP Guidelines for Seismic Rehabilitation of Buildings, FEMA 273. Washington, D.C.: Federal Emergency Management Agency.

Cosenza, E., DeLuca, A., Faella, C., Inelastic buckling of semi-rigid sway frames, Structural connections: stability and strength, London, Elsevier Applied Science, 1989.

FEMA 273, NEHRP Guidelines for the Seismic Rehabilitation of Buildings. Washington, DC. Federal Emergency Management Agency (FEMA). 2000.

FEMA 356, Prestandard and Commentary for the Seismic Rehabilitation of Buildings. Washington, DC.

Goel SC, Chao S-H. 2008. Performance-Based Plastic Design: Earthquake Resistant Steel Structures. International Code Council: Washington, DC.

Holmes, William T., et al., 2008, "Pacific Earthquake Engineering Research Center."University of California, Berkeley.

Kiamanesh, R., Abolmaali, A, Razavi, M., 2012, "The Effect of the Circular Bolt Pattern on the Behavior of the Extended End-Plate Connection," ASCE Journal of Structural Engineering, accepted October 2012.

Kim, Yosuk, and W-F. Chen. "Design tables for top-and seat-angle with double web-angle connections." ENGINEERING JOURNAL-AMERICAN INSTITUTE OF STEEL CONSTRUCTION 35 (1998): 50-75.

Krishnamurthy, N., 1980, "Modeling and Prediction of Steel Bolted Connection Behavior," Computer and Structure, 11, 75-82

Krishnamurthy, N., and Graddy, D.E., 1976, "Correlation between 2- and 3-Dimensional Finite Element Analysis of Steel Bolted End-Plate Connections," Computer and Structures, Pergamon, 6(4-5/6), 381-389.

Krishnamurthy, N., Huang H. T., Jefferey P. K., and Avery L. K., 1979. "Analytical M-θ Curve for End-Plate Connections," Journal of Structural Division, 105(ST1), 133-145.

Kukreti AR, Biswas P., "Finite element analysis to predict the cyclic hysteretic behavior and failure of end-plate connections", Journal of Computers and Structures 1997; 65(1):127–47.

Kukreti, A. R., Ghassemieh, M., and Murry, T. M. (1990). "Behavior ad Design of Large-Capacity Moment End Plates," Journal of Structural Engineering, ASCE, 116(3), 809-828.

Kukreti, A.R., and Abolmaali, A., 1999, "Moment-Rotation Hysteresis Behavior of Top and Seat Angle Steel Frame Connections," The ASCE Journal of Structural Engineering, Vol. 125, No. 8, pp. 810-820.

Lee S-S, Goel SC., 2001, "Performance-Based design of steel moment frames using target drift and yield mechanism." Research Report no. UMCEE 01-17, Dept. of Civil and Environmental Engineering, University of Michigan, Ann Arbor, MI.

Leelataviwat S, Goel SC, Stojadinovic´ B., 1999, "Toward performance-based seismic design of structures." Earthquake Spectra 15(3): 435–461.

Leelataviwat S, Saewon W, Goel SC., 2007, "An energy based method for seismic evaluation of structures." In Proceedings of Structural Engineers Association of California Convention, SEAOC 2007, Lake Tahoe, CA, September 26–29, 2007; 21–31.

Maison, B. F. & Popov, E. P., 1980, "Cyclic response prediction for braced steel frames." Structural Division, ASCE, 106, No.7 (July 1980) 1401-16.

Manheim, D. N., 1982, "On the design of eccentrically braced frames." DEng thesis, Department of Civil Engineering, University of California, Berkeley, USA.

Moehle, Jack P., 2008, "Performance-based seismic design of tall buildings in the US." The 14th World Conference on Earthquake Engineering.

Moehle, Jack, and Gregory G. Deierlein, 2004, "A framework methodology for performance-based earthquake engineering." Proc. of International Workshop on Performance-Based Design.

Nie J, Cai CS, Wu H, Fan JS, 2006, "Experimental and theoretical study of steel-concrete composite beams with openings in concrete flange," Journal of Engineering Structures

Popov E.P. and Takhirov S.M., 2002, "Bolted Large Seismic Steel Beam-to-Column Connections", Part 1: Experimental Study, Engineering Structures, Journal of Earthquake, Wind and Ocean Engineering.

Popov, Egor P., and Michael D. Engelhardt, 1988, "Seismic eccentrically braced frames." Journal of Constructional Steel Research

Porter, Keith A., 2003, "An overview of PEER's performance-based earthquake engineering methodology." Proc. Ninth International Conference on Applications of Statistics and Probability in Civil Engineering (ICASP9).

Razavi, M., Kiamanesh, R., Abolmaali, A. ,2012, "Computational benchmarks in simulation of cyclic performance of steel connections using three-dimensional nonlinear finite element method," i-manager's Journal on Structural Engineering, Vol. 1, No. 3, September - November 2012, pp 15-25.

SEAOC. 1995. Performance Based Seismic Engineering of Buildings. Vision 2000 Committee, SEAOC: Sacramento, CA.

Structural Engineers Association of California (SEAOC). 1960. Recommended Lateral Force Requirements and Commentary. SEAOC: San Francisco.

Wakabayashi, M., et al., 1974, "Inelastic behavior of full-scale steel frames with and without bracings." Bulletin of the Disaster Prevention Research Institute, Kyoto University, Kyoto, Japan.

BIOGRAPHICAL INFORMATION

Seyed Mohammad Razavi received his BS Degree in Civil Engineering from University of Tehran, Tehran, Iran, in January 2005 and MS Degree in Earthquake Engineering from Sharif University of Technology, Tehran, Iran, in December 2007. He completed his Ph.D. Degree in Civil Engineering/Structures at the University of Texas at Arlington in March 2013.

His research interests include nonlinear finite element analysis, performance-based earthquake engineering, nonlinear analysis of structures, structural stability, and behavior of steel and concrete structures.